

Nucleotide dependence in polymerization and
membrane remodelling by the bacterial actin
MreB5 from Spiroplasma citri

A thesis

Submitted in partial fulfillment of the requirements

Of the degree of
Doctor of Philosophy

By

Vani Pande



20162013

INDIAN INSTITUTE OF SCIENCE EDUCATION AND RESEARCH PUNE

Dedicated to my Parents, Tauji, Taiji and Grandparents

CERTIFICATE

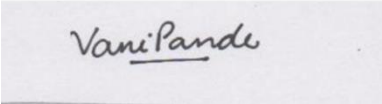
Certified that the work incorporated in the thesis entitled '**Nucleotide dependence in polymerization and membrane remodelling by the bacterial actin MreB5 from *Spiroplasma citri***' submitted by **Vani Pande** was carried out by the candidate, under my supervision. The work presented here or any part of it has not been included in any other thesis submitted previously for the award of any degree or diploma from any other University or institution.


Gayathri Pananghat

Date: 03.04.2023

Declaration

I declare that this written submission represents my ideas in my own words and where others' ideas have been included, I have adequately cited and referenced the original sources. I also declare that I have adhered to all principles of academic honesty and integrity and have not misrepresented or fabricated or falsified any idea/data/fact/source in my submission. I understand that violation of the above will be cause for disciplinary action by the Institute and can also evoke penal action from the sources which have thus not been properly cited or from whom proper permission has not been taken when needed.



Vani Pande

Date: 03.04.2023

Vani Pande

Roll No. 20162013

Acknowledgement

I want to express my deepest gratitude to my advisor Dr. Gayathri Pananghat for giving me the opportunity to work in her lab. I am indebted for her invaluable support and feedback throughout my Ph.D. journey. I could not have undertaken this journey without her guidance, in-depth knowledge of the subject, and constant encouragement. Brainstorming sessions with her have always proved beneficial and helped to sail through my work.

I am incredibly thankful to Dr. Ramanujam Srinivasan and Prof Thomas Pucadyil for collaborating on in vivo and in vitro reconstitution studies. I am highly grateful to Nivedita Mitra, who carried out the in vivo work, and Himani Khurana, for helping with in vitro reconstitution studies.

I would like to sincerely thank my RAC members, Dr. Radha Chauhan, Dr. Sunish Radhakrishnan, and Prof Thomas Pucadyil for providing me their valuable inputs and insightful suggestions during our meetings. I also thank Prof Sai Krishnan Kayarat for the constructive discussions during combined lab group meetings.

I would like to thank the diffraction facilities at IISER Pune and ESRF, Grenoble, for crystal diffraction and data collection. I would also like to thank cryo-EM facilities at IIT Delhi and InStem Bangalore for electron microscopy images acquisition. Special thanks go to Dr. Vinothkumar Kutti Rangunath, Dr. Mamata Bangera, Prof Manideepa Banerjee and her student Kirti for their inputs and help in carrying out electron microscopy experiments. I would also like to thank the IISER Pune Microscopy facility and operators of the HRTEM and the FE-SEM facilities of IISER Pune for helping me perform experiments.

This endeavour would not have been possible without the constant help and support from my past and present lab mates, especially Shrikant, Jyoti, Jaya, Shekhar, Manil, Jazleena, Mrinmayee, Joyeeta, Sukanya, Apurba, Soumyajit, Rinku, Vaishnavi, Kushan, Akhilesh and Puja. I thank them deeply for giving me such wonderful memories of the lab. I am highly grateful to Dr. Shrikant Harne for introducing me to the project and training me in the lab work. I would also like to thank the past and present lab members of Prof Sai Krishnan's lab, especially Mahesh, Sujata, Vishal, Ishtiyag, Vinayak, Pratima, Gyan, Rushik, Nikki, Akhilesh, Akash, Aman, Ashwin and Geetanjali for their help and support. I feel incredibly grateful to work alongside such lovely and warm people in Prof. Sai and Dr. Gayathri's labs. I would like to thank Suman and Rupam from Prof Jayant Udgaonkar's lab for their help with Mass spectrometry.

I would like to recognize the help of IISER Pune Biology office people, Kalpesh, Piyush, Mrinalini, Rupali, Sandeep and Mahesh, for their assistance with various lab-related and official procedures. I am thankful to the department of Biology for providing such a prolific research environment.

I thank the ground floor housekeeping staff for providing a clean working area and carrying out washing and autoclaving for the labs.

I would also like to thank my seniors Ajay, Maithili, Debayan, Yamini, Rupali, Yashaswi, and Yashwant for their constructive inputs and discussions during my Master's semester lab projects.

I would also like to thank Infosys Foundation, SERB- International travel support, and Gordon Research Conferences for providing me the financial assistance for attending the conferences.

I thank Rinku, Sukanya, and Soumyajit for proofreading my thesis.

I could not have undertaken this journey without the constant support and encouragement from my friends and seniors at IISER. I would like to thank my batchmates, especially, Sukanya, Kaveri, Aparna and Manish for their constant support. I am thankful to the friends I made during Drama club rehearsals, morning running sessions, and treks, especially, Shrihar, Sourajit, Netra, Chrisil, Indra, Tumpa, Ravi and Avdhoot. I would like to mention my dearest friend Sukanya who has constantly inspired me and pushed me to become a more confident person. I am always thankful to Mrinmayee for being a humble friend and a great senior. I will also always remember the fun time I spent with my labmates outside the lab and the scientific discussions I had with them during tea time.

I would be remiss in not mentioning my friends from outside IISER, Shriya, Nupur, Sonali, Namrata, Garima, Vasundhara, Vaibhav, and Bhushan, who gave me moral support and encouragement whenever I needed it.

In the end, I am grateful to my parents, siblings, tauji, taiji, and grandparents for their love and blessings. I extend my deepest gratitude to my parents, who gave me the moral support, encouragement, and motivation to accomplish my goals. Lastly, I would like to thank Babba, Nanaji, and Maa Barahi for their countless blessings from above.

Vani

Table of Contents

List of Figures.....	1
List of Tables.....	3
Abbreviations.....	4
Abstract	7
Synopsis	8
Chapter 1: Introduction.....	14
1.1: Bacterial cell shape	15
1.2: Cytoskeleton proteins in cell shape determination	18
1.3: Proteins responsible for bacterial cell shape	24
1.4: Discovery of MreB	25
1.5: MreB and cell shape determination	27
1.5.1: MreB localization and dynamics study.....	27
1.5.2: MreB interaction with the membrane.....	32
1.6: Additional functions of MreB	35
1.7: <i>Spiroplasma</i> as a model organism to study cell shape determination by MreB	36
1.7.1: <i>Spiroplasma</i> : a helical cell-wall less bacterium.....	36
1.7.2: Cell shape determination in <i>Spiroplasma</i>	36
1.8: Cytoskeleton proteins of <i>Spiroplasma</i>	37
1.8.1: Fibril.....	37
1.8.2: MreB.....	39
1.8.3: Recent advances in MreB and Fibril studies of <i>Spiroplasma</i>	39
1.9: Objectives	46
1.10: References	48
Chapter 2: Standardization of purification and structure determination of ScMreB5.....	57
2.1: Introduction	58
2.2: Materials and Methods	59
2.3: Results	66
2.3.1: Expression check standardisation for ScMreB3, ScMreB4 ^{ΔN} and ScMreB5 ^{WT}	66
2.3.2: Purification condition optimization of ScMreBs.....	67
2.3.3: Crystallization and structure determination of ScMreB5.....	70
2.4: Discussion	73
2.5: References	74
Chapter 3: Structural analysis of ScMreB5.....	76
3.1: Introduction	77

3.2: Materials and Methods	78
3.3: Results	81
3.3.1: Features of the crystal structures of ScMreB5	81
3.3.2: Structural basis of K ⁺ ion mediated stability of ScMreB5	84
3.3.3: Protofilament organization of ScMreB5	84
3.3.4: Domain-wise analysis for MreBs.....	86
3.3.5: Nucleotide-binding pocket of ScMreB5	90
3.3.6: Membrane binding sequence of ScMreB5	94
3.3.7: A22 binding pocket of ScMreB5	95
3.4: Discussion	98
3.5: References	100
Chapter 4: ATPase activity and polymerization dynamics of ScMreB5	102
4.1: Introduction	103
4.2: Materials and Methods	104
4.3: Results	107
4.3.1: ATPase activity of ScMreB5 ^{WT} and its mutants.....	107
4.3.2: Light scattering assays	110
4.3.3: Cryo-electron microscopy study	112
4.3.4: ScMreB5 polymerization dynamics study in yeast.....	113
4.3.5: A22 resistance of ScMreB5	114
4.4: Discussion	115
4.5: References	118
Chapter 5: Membrane binding features of ScMreB5	121
5.1: Introduction	122
5.2: Material and methods	123
5.3: Results	128
5.3.1: ScMreB5 binds liposomes	128
5.3.2: ScMreB5 binds to negatively charged lipids	130
5.3.3: C-terminal tail of ScMreB5 facilitates membrane binding.....	130
5.3.4: ScMreB5 activity is stimulated in the presence of liposomes.....	134
5.3.5: ScMreB5 liposome binding is nucleotide-dependent	134
5.4: Discussion	137
5.5: References	138
Chapter 6: Membrane remodelling dynamics of ScMreB5	140
6.1: Introduction	141
6.2: Materials and Methods	142

6.3: Results	151
6.3.1: ScMreB5 can remodel lipid membrane in a nucleotide-dependent manner	151
6.3.2: Visualizing ScMreB5 on a membrane bilayer	155
6.3.3: Mix of ScMreB5 N-terminal GFP and untagged constructs remodels bilayer	159
6.3.4: Electron microscopy of ScMreB5 with liposomes and Supported lipid bilayer (SLB)	161
6.4: Discussion	163
6.5: References	165
Chapter 7: Conclusions and Future prospect	168
7.1: Summary of major findings	169
7.2: Major implications from the work	171
7.3: Future Prospects	174
7.4: References	174
Permissions	176

List of Figures

Figure 1.1: Diversity in bacterial shapes.....	15
Figure 1.2: Peptidoglycan layer of bacteria.	17
Figure 1.3: Schematic of prokaryotic cytoskeleton protein localization.....	18
Figure 1.4: CreS forms constitutive filaments and organizes at the curved region of <i>C.crescentus</i>	19
Figure 1.5: Bactofilin CcmA plays an important role in helical shape determination in <i>Helicobacter pylori</i>	21
Figure 1.6: CetZ is required for rod-shape transition of plate-like archaeal cell <i>Haloferax volcanii</i> . .	22
Figure 1.7: CrvA is required for the curved shape of <i>Vibrio cholerae</i>	23
Figure 1.8: Peptidoglycan synthesis by elongasome and divisome.	25
Figure 1.9: MreB has conserved nucleotide binding pocket and structure similar to actins.....	26
Figure 1.10: MreB localizes as helical filament along the cell length.	29
Figure 1.11: Long helical MreB filaments are not seen under cryo-ET.	29
Figure 1.12: MreB localizes and moves as dynamic patches along the cell length.	31
Figure 1.13: Defining a membrane curvature.	33
Figure 1.14: MreB interacts and deforms the lipid membrane.	34
Figure 1.15: <i>Spiroplasma</i> exhibit helical morphology.	37
Figure 1.16: <i>Spiroplasma</i> Fibril form constitutive filaments.	39
Figure 1.17: Heterologous expression of <i>Spiroplasma</i> MreBs in <i>E.coli</i>	42
Figure 1.18: Heterologous expression of <i>Spiroplasma</i> MreB in synthetic bacterium syn3b.	43
Figure 1.19: Heterologous expression of <i>Spiroplasma</i> MreB in <i>Mycoplasma capricolum</i>	45
Figure 2.1: Expression check profiles of a ScMreBs.	67
Figure 2.2: Purification of ScMreB3 ^{WT}	67
Figure 2.3: Purification optimization for ScMreB5 ^{WT}	69
Figure 2.4: ScMreB5 ^{WT} and its mutants are well folded and elute as monomers.	71
Figure 3.1: Crystal structure of ScMreB5.....	83
Figure 3.2: ScMreB5 is stabilized by KCl and nucleotides.	83
Figure 3.3: ScMreB5 possesses a conserved protofilament assembly compared to other MreBs.	85
Figure 3.4: Domain wise analysis for MreB structures.	87
Figure 3.5: Residues at nucleotide-binding pocket are well conserved in ScMreB5.....	92
Figure 3.6: Nucleotide binding pocket of ScMreB5 is conserved.	92
Figure 3.7: Comparison of active site geometry of ScMreB5 with other MreBs and actins.	93
Figure 3.8: Membrane binding region of ScMreB5.....	95
Figure 3.9: Structure and sequence comparison of A22 binding site in ScMreB5.	97

Figure 3.10: Docking A22 does not lead to the binding at the A22 site in ScMreB5.	98
Figure 4.1: ScMreB5 is an active ATPase.	108
Figure 4.2: ScMreB5 ^{WT} polymerizes without addition of nucleotide.	111
Figure 4.3: ScMreB5 filaments form double-protofilament assemblies independent of nucleotide hydrolysis.	112
Figure 4.4: A22 does not inhibit the filament formation of N-terminal GFP tagged ScMreB5 expressed in yeast.	115
Figure 4.5: Mechanism of ATP dependence of MreB function.	117
Figure 5.1: Design of PLiMAP assay (Proximity-based labeling of membrane-associated proteins)	125
Figure 5.2: ScMreB5 binds liposomes.	129
Figure 5.3: ScMreB5 binding is modulated by charged lipids.	132
Figure 5.4: Electrostatic potential surface of ScMreB5 double protofilament model.	133
Figure 5.5: Liposome stimulates ScMreB5 ^{WT} ATPase activity.	133
Figure 5.6: ScMreB5 binding to liposomes is nucleotide-dependent.	136
Figure 6.1: Schematic of preparing SMrT (Supported Membrane Tubes) and SLB (Supported lipid bilayer) templates.	144
Figure 6.2: Constructs for visualizing ScMreB5 on membrane.	146
Figure 6.3: ScMreB5 remodels supported membrane nanotubes (SMrT) in nucleotide dependent manner.	153
Figure 6.4: ScMreB5 remodels lipid bilayer in the presence of different nucleotides.	154
Figure 6.5: Purification profile and liposome pelleting assay of fusion construct and untagged ScMreB5.	157
Figure 6.6: Visualizing ScMreB5 on the Supported lipid bilayer.	159
Figure 6.7: Visualizing ScMreB5 ^{UT} mediated remodelling of Supported lipid bilayer.	160
Figure 6.8: Visualizing ScMreB5 ^{UT} and ScMreB5 ^{Nt-GFP} mix mediated remodelling of supported lipid bilayer.	160
Figure 6.9: ScMreB5 ^{WT} can bind and deform liposomes.	162
Figure 6.10: FE-SEM of ScMreB5 ^{WT} on SLBs show remodelled bilayer structures	163
Figure 7.1: Schematic of Glu-mediated subdomain conformational change.	171
Figure 7.2: Schematic of nucleotide-dependent differential binding and remodelling of the membrane.	173

List of Tables

Table 1.1: Morphological diversity in bacteria	16
Table 1.2: Constructs and microscopy experiments used that determined the helical organization of MreB	27
Table 1.3: Constructs and microscopy experiments used that determined the patch like organization of MreB	30
Table 2.1: List of primers and clones	60
Table 2.2: Crystallization conditions of ScMreB5 in different nucleotide states	65
Table 2.3: Calculations for ADP standards for the plot (in Figure 2.3 E)	70
Table 2.4: Calculations for determining the percentage of bound ADP.....	70
Table 2.5: Data collection and refinement statistics table	72
Table 3.1: RMSD values of each subdomain upon domain-wise superposition of ScMreB5 structures	82
Table 3.2: Subdomain wise comparison of ScMreB5 structures with other MreBs.....	87
Table 3.3: Subdomain angular movement and distance difference for MreBs	88
Table 3.4: Sequence percentage identity with ScMreB5.....	90
Table 3.5: Comparison of RMSD values of A22 binding loop of CcMreB, double protofilament (PDB ID: 4CZJ) with other structures	96
Table 4.1: List of primers and clones obtained	106
Table 4.2: Kinetic parameters for ScMreB5 ^{WT} from Michaelis –Menten plot.....	109
Table 4.3: Comparison of ATPase activity for different MreBs	109
Table 5.1: Comparison of S.citri lipid composition with E.coli.....	128
Table 6.1: List of primers and clones/inserts generated	146
Table 6.2: Summary of the effects of different nucleotide states on ScMreB5 remodelling of lipid tubes	153
Table 6.3: Summary of the effects of different nucleotide states on ScMreB5 remodelling of supported lipid bilayers.....	155
Table 6.4: Summary of the trials done for ScMreB5 visualization over supported lipid bilayer	156

Abbreviations

% mol	mole percent
μm	Micrometer
μM	Micromolar
Å	Angstrom
A22	S-(3,4-dichlorobenzyl) isothiourea
A ₂₈₀	Absorbance at 280 nm
A ₄₈₈	Absorbance at 488 nm
ADP	Adenosine diphosphate
ADP-AIF _x	Adenosine diphosphate- Aluminum Flouride _x
AMP-PNP	Adenosine 5'-(β,γ-imido)triphosphate
ATP	Adenosine triphosphate
ATPase	ATP hydrolase
<i>B.subtilis</i>	<i>Bacillus subtilis</i>
BDPE	BODIPY-diazirine phosphatidylethanolamine
BSA	Bovine Serum Albumin
<i>C.crescentus</i>	<i>Caulobacter crescentus</i>
CHAPS	3-((3-cholamidopropyl) dimethylammonio) -1-propanesulfonate
CL	Cardiolipin
CPS/microamps	Count per second per microamperes

DHPE	1,2-dihexadecanoyl-sn-glycero-3-phosphoethanolamine
DOPC	1,2-dioleoyl-sn-glycero-3-phosphocholine
DOPG	1,2-dioleoyl-sn-glycero-3-phospho-(1'-rac-glycerol)
DTT	Dithiothreitol
<i>E.coli</i>	<i>Escherichia coli</i>
FRET	Fluorescence resonance energy transfer
<i>H.pylori</i>	<i>Helicobacter pylori</i>
<i>H.volcanii</i>	<i>Haloferax volcanii</i>
kDa	kilo Dalton
k _{obs}	Observed turnover number
L	Litre
LB	Luria Bertani
LSS	N-Lauroyl Sarcosine sodium
M ⁻¹ cm ⁻¹	per Molar per cm
MgCl ₂	Magnesium chloride
mL	millilitre
mM	millimolar
nm	nanometre
OD ₆₀₀	Optical density at 600 nm
PDB	Protein data bank
PE	Phosphatidyl ethanolamine
PEG	Polyethylene glycol

RMSD	Root Mean Square Deviation
RT-PCR	Real Time-Polymerase chain reaction
<i>S.citri</i>	<i>Spiroplasma citri</i>
<i>S.eriocheris</i>	<i>Spiroplasma eriocheris</i>
SDC	Sodium Deoxycholate
SLB	Supported Lipid Bilayer
SM	Sphingomyelin
SMrT	Supported membrane tubes
<i>T.maritima</i>	<i>Thermotoga maritima</i>

Abstract

MreB, the bacterial ancestor of eukaryotic actin, determines the shape of most of the rod-shaped bacteria. Until now, functional studies for MreBs have been carried out for cell-walled rod-shaped bacteria. MreB filaments are said to assist rod shape by their circumferential movement, which is dependent on the peptidoglycan synthesis machinery. However, the role of filament dynamics of MreB polymerization for conferring rod shape is unknown. *Spiroplasma* is a helical cell-wall-less bacterium, which maintains its cell shape in the absence of cell wall synthesis machinery. Recently, we have shown that MreB5, one of the five MreB paralogs of the cell-wall less bacterium *Spiroplasma citri* (ScMreB5) is essential for helical shape and motility of the organism. My Ph.D. work aims to characterize ScMreB5 using structural, biochemical, and in vitro reconstitution approach, with a goal to understand the fundamental principles of shape determination by MreB. Structurally, we show that features such as protofilament organization and nucleotide binding pocket are well conserved in ScMreB5. We also demonstrate that filament dynamics of the ATPase deficient mutant ScMreB5^{E134A} is compromised. Thus, the catalytic Glu134 plays a dual role, firstly, by sensing ATP bound state of MreB for filament assembly and secondly, assisting ATP hydrolysis leading to filament disassembly. Interestingly, membrane binding of ScMreB5 is mediated via charge-based interaction and is also dependent on the nucleotide state of the protein. We report that ScMreB5 under different nucleotide conditions can remodel lipid bilayer and lipid tubes. This remodeling ability is dependent on the conformational cycle as it goes through the steps of ATP hydrolysis and nucleotide exchange. Our results are indicative of an allosteric effect of the nucleotide-binding site on membrane binding. Thus, ScMreB5 functions as a prototype to understand membrane remodelling by MreBs independent of the cell-wall synthesis machinery.

Synopsis

Nucleotide dependence in polymerization and membrane remodelling by the bacterial actin MreB5 from *Spiroplasma citri*

Name: Vani Pande

Registration number: 20162013

Supervisor: Dr. Gayathri Pananghat

Department: Biology, IISER Pune, India

Program: Integrated PhD

Date of registration: August 2016

The bacterial world comprises different shape and sizes of cells. The cell shape in bacteria is defined by the cell-wall, peptidoglycan. MreB, a prokaryotic actin homolog plays an important role in cell shape maintenance in most of the non-spherical cell-walled bacteria. The genetic studies on bacteria such as *Escherichia coli*, *Bacillus subtilis* and *Caluobacter crescentus* have shown that the deletion of *mreb* genes leads to loss of rod shape and eventual lysis of the organism (Kawai et al., 2009; Kruse et al., 2005). These results indicate that MreB plays a pivotal role in cell shape determination and maintenance in bacteria.

The first crystal structure of MreB to be determined was of *Thermotoga maritima* (van den Ent et al., 2001). It revealed that the key features, such as subdomain organization and ATP binding pocket of MreB is very similar to actin, despite having a low sequence identity. The protofilament organization within the crystal packing and nucleotide-dependent polymerization features are also conserved. The functional form of MreB is a straight double protofilament of antiparallel orientation, in contrast to actins that are helical double protofilament of parallel orientation. The polymerization dynamics of MreB has been studied through light scattering assays and electron microscopy. The critical concentration of polymerization is determined to be in a range of 1-2 μM for *E.coli* and *T.maritima* (van den Ent et al., 2001; Nurse and Mariani, 2013). However, the role of filament dynamics of MreB polymerization for conferring rod shape is unknown. *In vivo* studies have demonstrated that small patches of MreB filaments assemble beneath the cell membrane and further recruits the cell wall synthesis machinery (Garner et al., 2011). Thus, MreB acts as a moving rail road track on which cell wall synthesis machinery assembles, thus locally leading to cell wall insertion.

Filaments of MreB can sense and generate membrane curvature. Membrane binding is facilitated by the presence of hydrophobic loop (Gram-positive bacteria) and N-terminal amphipathic helix (Gram-negative and Gram-positive bacteria) (Salje et al., 2011). This kind of interaction is in conjunction with the antiparallel arrangement of the double filaments as both the membrane binding region are on the same side of the double-protofilament. MreB is localized along the lateral edge of the rod shape cells. In these edges there exist local areas of positive and negative curvatures (Ursell et al., 2014). MreB tends to recognize such local curvatures of the cell body and gets localized in the areas of highest principal curvature (Ursell et al., 2014; Hussain et al., 2018).

Until now, most of the MreB-related studies were carried out deciphering the role in cell-wall mediated cell shape determination in model bacteria like *Thermotoga maritima*, *Bacillus subtilis*, *Escherichia coli*, etc. The bacterial genus *Spiroplasma* can maintain a helical shape without a cell wall (Trachtenberg, 1998). It has five copies of MreB and a Fibril cytoskeleton protein (Takahashi et al., 2020). The organism achieves its motility by using internal cytoskeleton. One of the proposed models from cryo electron tomography study on *S.melliferum* revealed a flat monolayer membrane bound filaments. These filaments were arranged alternately as thick and thin filaments. The thick outer ribbon (5-6 filaments) comprised Fibril protein (Kürner et al., 2005). In the middle of this ribbon, around 9 thinner filaments were observed. These thin filaments are predicted to be MreB filaments. It has been proposed that the hydrolytic activity of MreB filaments in the middle of this ribbon bundle can help in the helical motility of bacteria. Recent work from our lab have shown that MreB5, one of the five MreB paralogs (ScMreB5), is essential for helical shape and motility of the organism (Harne et al., 2020). Following this, recent work of *Spiroplasma* MreBs and Fibril has highlighted the role of internal cytoskeleton in the motility and cell shape of the organism (Masson et al., 2021; Lartigue et al., 2022; Kiyama et al., 2022). This altogether proposes a new role for MreB: involvement in organism motility and cell shape maintenance.

One of the approaches towards understanding the role of multiple MreBs in shape determination and motility in *Spiroplasma* is through structural and biochemical analysis. The goal of my thesis is to characterize ScMreB5 of *Spiroplasma citri* in order to understand the mechanism by which it determines the helical shape of the organism. To achieve this aim, I have divided my thesis into the following objectives that are put as chapters:

Chapter 1: Introduction

This chapter summarizes the existing literature on MreB for its role in the bacterial cell shape determination by cell-wall synthesis machinery. Further studies on MreB from cell-wall less bacteria *Spiroplasma* have been discussed that proposes the role and function of multiple MreBs in helicity and motility generation.

Chapter 2: Standardization of purification and structure determination of ScMreB5

This chapter describes the optimization of purification and crystal structure determination of ScMreB5 in two nucleotide states ADP and AMP-PNP (PDB ID: 7BVZ and 7BVY). Purification optimization showed that presence of KCl in buffer increases the protein stability. ScMreB5 was successfully purified in a monomeric state without the addition of excess ADP which was earlier used to prevent protein precipitation. Structure determination of ScMreB5 in ADP and AMP-PNP condition was later followed.

Chapter 3: Structural analysis of ScMreB5

In this chapter structural and sequence comparison was performed with known structures of cell-walled bacterial MreBs and one known structure of MreB from cell-wall less bacteria *S.eriocheris* as well as actins. Structural comparison with other MreBs and actins show conservation of structural features for ScMreB5. Sequence based analysis revealed conservation of ATP hydrolysis residues that are later characterized in chapter 4 for their ATPase activity. A thorough analysis of the domain angle and dihedral angle movement show an eventual decrease in subdomain angle as the protein transitions to a functional double antiparallel protofilament state. Our sequence and structural based analysis for membrane binding region in ScMreB5 shows the presence of hydrophobic loop and a unique extended and positively charged C-terminal tail, both of which could contribute to the membrane binding. Analysing the A22 binding pocket of ScMreB5, it is hypothesized that the protein could be resistant to the polymerization inhibitor A22.

Chapter 4: ATPase activity and polymerization dynamics of ScMreB5

In chapter 4, we carry out the ATPase activity and polymerization dynamics study of ScMreB5 and its mutants. Our ATPase activity for the wildtype and hydrolysis mutant show that the protein is an active ATPase and the mutants are deficient in ATP hydrolysis. Our cryo-EM and light scattering assay show that ScMreB5 can undergo polymerization without the requirement of nucleotide hydrolysis. We have also carried out polymerization dynamics

study in collaboration with Dr. Srinivasan Ramanujam, (NISER Bhubaneswar), expressing GFP fusion ScMreB5 and ATP hydrolysis mutant ScMreB5^{E134A} in yeast *S.pombe*. We show that Glu134 is important for filament dynamics and filament bundling in ScMreB5.

Chapter 5: Membrane binding features of ScMreB5

In this chapter we have determined the membrane binding ability of ScMreB5. We found that ScMreB5 binds to the membrane by a novel mode, which is a charge-based interaction. Unlike for other MreBs where binding is via hydrophobic interaction, our data hypothesize a surface-level interaction for ScMreB5, that involves both charge based as well as hydrophobicity mediated interaction. We further show that ScMreB5 membrane binding is driven by the nucleotide state.

Chapter 6: Membrane remodelling dynamics of ScMreB5

In this chapter we show that like other cell-walled MreBs, ScMreB5 is also able to deform liposomes. Further, we provide the evidence of membrane remodelling ability of ScMreB5 in different nucleotide states. This part of work is done with in collaboration with Prof. Thomas Pucadyil (IISER, Pune). Based on our results from the bilayer and lipid tubes, we hypothesize that the conformational changes accompanying the ATP hydrolysis cycle could drive the membrane remodelling by ScMreB5 filaments.

Chapter 7: Conclusions and Future Prospects

In this chapter, summarize the major findings arising from this work. We propose a model where the ATP hydrolytic cycle of MreB filaments would modulate membrane binding and remodelling. We also discuss the future prospects for *Spiroplasma* MreB protein and the work that can be done to decipher their functions.

List of publications:

Harne, S., S. Duret, **V. Pande**, M. Bapat, L. Béven, and P. Gayathri. 2020. MreB5 Is a Determinant of Rod-to-Helical Transition in the Cell-Wall-less Bacterium *Spiroplasma*. *Curr. Biol.* 30:4753-4762.e7. doi:10.1016/j.cub.2020.08.093.

Pande, V., N. Mitra, S.R. Bagde, R. Srinivasan, and P. Gayathri. 2022. Filament organization of the bacterial actin MreB is dependent on the nucleotide state. *J. Cell Biol.* 221:e202106092. doi:10.1083/jcb.202106092.

Vani Pande and Gayathri Pananghat. “Heterologous expression, purification optimization and structure determination of *S.citri* MreB5” (To be communicated to Bio-protocol).

Vani Pande, Himani Khurana, Thomas Pucadyil, Gayathri Pananghat. “Nucleotide dependent membrane remodelling by bacterial actin MreB” (Manuscript under preparation).

Vani Pande and Gayathri Pananghat “ Domain-wise analysis of bacterial actin MreB structures.’ (Manuscript under preparation)

References:

van den Ent, F., L.A. Amos, and J. Löwe. 2001. Prokaryotic origin of the actin cytoskeleton. *Nature*. 413:39–44. doi:10.1038/35092500.

Garner, E.C., R. Bernard, W. Wang, X. Zhuang, D.Z. Rudner, and T. Mitchison. 2011. Coupled, Circumferential Motions of the Cell Wall Synthesis Machinery and MreB Filaments in *B. subtilis*. *Science*. 333:222–225. doi:10.1126/science.1203285.

Harne, S., S. Duret, V. Pande, M. Bapat, L. Béven, and P. Gayathri. 2020. MreB5 Is a Determinant of Rod-to-Helical Transition in the Cell-Wall-less Bacterium *Spiroplasma*. *Current Biology*. doi:10.1016/j.cub.2020.08.093.

Hussain, S., C.N. Wivagg, P. Szwedziak, F. Wong, K. Schaefer, T. Izoré, L.D. Renner, M.J. Holmes, Y. Sun, A.W. Bisson-Filho, S. Walker, A. Amir, J. Löwe, and E.C. Garner. 2018. MreB filaments align along greatest principal membrane curvature to orient cell wall synthesis. *eLife*. 7:e32471. doi:10.7554/eLife.32471.

Kawai, Y., K. Asai, and J. Errington. 2009. Partial functional redundancy of MreB isoforms, MreB, Mbl and MreBH, in cell morphogenesis of *Bacillus subtilis*. *Molecular Microbiology*. 73:719–731. doi:10.1111/j.1365-2958.2009.06805.x.

Kiyama, H., S. Kakizawa, Y. Sasajima, Y.O. Tahara, and M. Miyata. 2022. Reconstitution of a minimal motility system based on *Spiroplasma* swimming by two bacterial actins in a synthetic minimal bacterium. *Science Advances*. 8:eabo7490. doi:10.1126/sciadv.abo7490.

Kruse, T., J. Bork-Jensen, and K. Gerdes. 2005. The morphogenetic MreBCD proteins of *Escherichia coli* form an essential membrane-bound complex. *Mol. Microbiol.* 55:78–89. doi:10.1111/j.1365-2958.2004.04367.x.

Kürner, J. 2007. Cryo – Electron Tomography Reveals the Cytoskeletal Structure of *Spiroplasma melliferum*. *Science*. 436:436–439. doi:10.1126/science.1104031.

Kürner, J., A.S. Frangakis, and W. Baumeister. 2005. Cryo-Electron Tomography Reveals the Cytoskeletal Structure of *Spiroplasma melliferum*. *Science*. 307:436–438. doi:10.1126/science.1104031.

Lartigue, C., B. Lambert, F. Rideau, Y. Dahan, M. Decossas, M. Hillion, J.-P. Douliez, J. Hardouin, O. Lambert, A. Blanchard, and L. Béven. 2022. Cytoskeletal components can turn wall-less spherical bacteria into kinking helices. *Nat Commun*. 13:6930. doi:10.1038/s41467-022-34478-0.

- Masson, F., X. Pierrat, B. Lemaitre, and A. Persat. 2021. The wall-less bacterium *Spiroplasma poulsonii* builds a polymeric cytoskeleton composed of interacting MreB isoforms. *iScience*. 24:103458. doi:10.1016/j.isci.2021.103458.
- Nurse, P., and K.J. Mariani. 2013. Purification and characterization of *Escherichia coli* MreB protein. *Journal of Biological Chemistry*. 288:3469–3475. doi:10.1074/jbc.M112.413708.
- Salje, J., F. van den Ent, P. de Boer, and J. Löwe. 2011. Direct Membrane Binding by Bacterial Actin MreB. *Molecular Cell*. 43:478–487. doi:10.1016/j.molcel.2011.07.008.
- Takahashi, D., I. Fujiwara, and M. Miyata. 2020. Phylogenetic origin and sequence features of MreB from the wall-less swimming bacteria *Spiroplasma*. *Biochemical and Biophysical Research Communications*. 533:638–644. doi:10.1016/j.bbrc.2020.09.060.
- Trachtenberg, S. 1998. Mollicutes — Wall-less Bacteria with Internal Cytoskeletons. 256:244–256.
- Ursell, T.S., J. Nguyen, R.D. Monds, A. Colavin, G. Billings, N. Ouzounov, Z. Gitai, J.W. Shaevitz, and K.C. Huang. 2014. Rod-like bacterial shape is maintained by feedback between cell curvature and cytoskeletal localization. *Proceedings of the National Academy of Sciences*. 111:E1025–E1034. doi:10.1073/pnas.1317174111.

Chapter 1: Introduction

1.1: Bacterial cell shape

From early times, bacteria were firstly classified based on shape. In nature, bacteria exist in a variety of shapes, ranging from spheres to rods (Fig 1.1 A) (Yang et al., 2016). Rod shape further attains different curvatures, generating curved and helical cells (Fig 1.1.A). Bacteria also have pili and flagella, which aid in their movement. Such additional characteristics of the form are important for efficient motility, which offers advantages in survival and colonisation. (Fig 1.1 B). Moreover, many bacteria can undergo shape changes during their life cycle and course of evolution (Fig 1.1.C) (Veyrier et al., 2015). This kind of morphological diversity is summarized in the table 1.1.

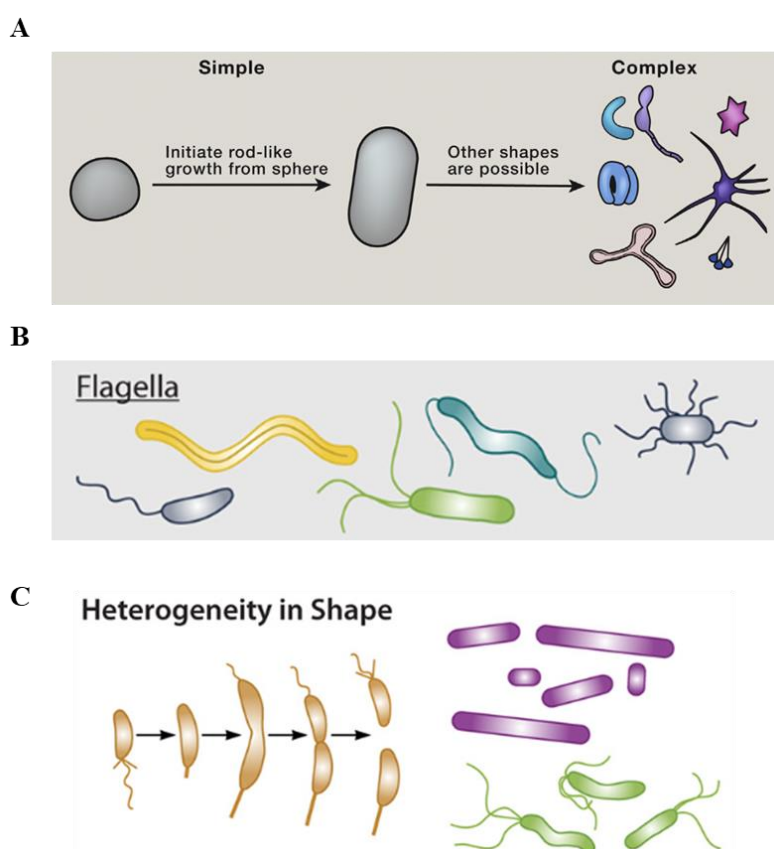


Figure 1.1: Diversity in bacterial shapes.

(A) Bacteria come in different cell shapes. The simplest cell is a spherical cell which further evolved to rod. Rod shape cells further diversify to curved, helical, and branched shapes. Image adapted from Shi et al., 2018. (B) Motility appendages such as flagella provide a survival advantage. Image adapted from Yang et al., 2016. (C) Asymmetric growth and division can generate shape heterogeneity. This can contribute to motility, and colonization and enhance adaptation to varying environments. Image adapted from Yang et al., 2016.

Table 1.1: Morphological diversity in bacteria

Morphological variation	Organism	Functional Consequence
Curved	<i>C.crescentus</i> <i>V.cholerae</i>	Surface colonization
Helical	<i>Helicobacter pylori</i> <i>Spirochetes sp.</i>	Motility in viscous solution
Filamentation	<i>Streptococcus pneumoniae</i> Uropathogenic <i>Escherichia coli</i>	Cell survival, Antibiotic resistance, Host cell attachment
Cell surface minimization	<i>Streptococcus pneumoniae</i> <i>Salmonella typhimurium</i>	Cell survival within host
Bacterial appendages	<i>Helicobacter pylori</i> <i>C.crescentus</i> <i>Campylobacter jejuni</i>	Motility and Nutrient uptake

The structural integrity to the bacterial cell shape is provided by cell-wall peptidoglycan (Scheffers and Pinho, 2005). Peptidoglycan (PG) is made from the repeating unit of a disaccharide (N-acetylglucosamine GlcNAc, and N-acetylmuramic acid, MurNAc) and with a short pentapeptide attached to GlcNAc (Fig 1.2 A). The repeating unit of the glycan strand undergoes transpeptidation with the other strand (Desmarais et al., 2013). This generates a rigid meshwork of crosslinked glycan strands that provides a structural frame to the cell and prevents lysis due to osmotic stress. A purified peptidoglycan sacculi is able to retain the shape of the bacterial cell from which it is purified (Goodwin and Shedlarski, 1975; de Pedro et al., 1997). Gram-positive bacteria have multiple layers of peptidoglycan along with other structural components (e.g., wall teichoic acids), compared to Gram-negative bacteria with a thin layer of peptidoglycan sandwiched between inner and outer membrane (Lovering et al., 2012; Typas et al., 2011) (Fig 1.2 B). The peptidoglycan strands arrange circumferentially within the cell as an irregular lattice (Yang et al., 2016). As the new layer of peptidoglycan gets inserted the older layer migrates upwards and faces the cell surface. Autolytic activity at the cell surface causes the peptidoglycan material to hydrolyze, allowing continued cell enlargement (Doyle et al., 1988). Different cell shapes of bacteria result from asymmetric deposition of peptidoglycan at different regions of the cell surface. Peptidoglycan synthesis

and cell shape determination are both interlinked. Several studies on bacterial cell shape have shown that the changes in the cell shape are linked to proteins responsible for peptidoglycan synthesis (Graham et al., 2021).

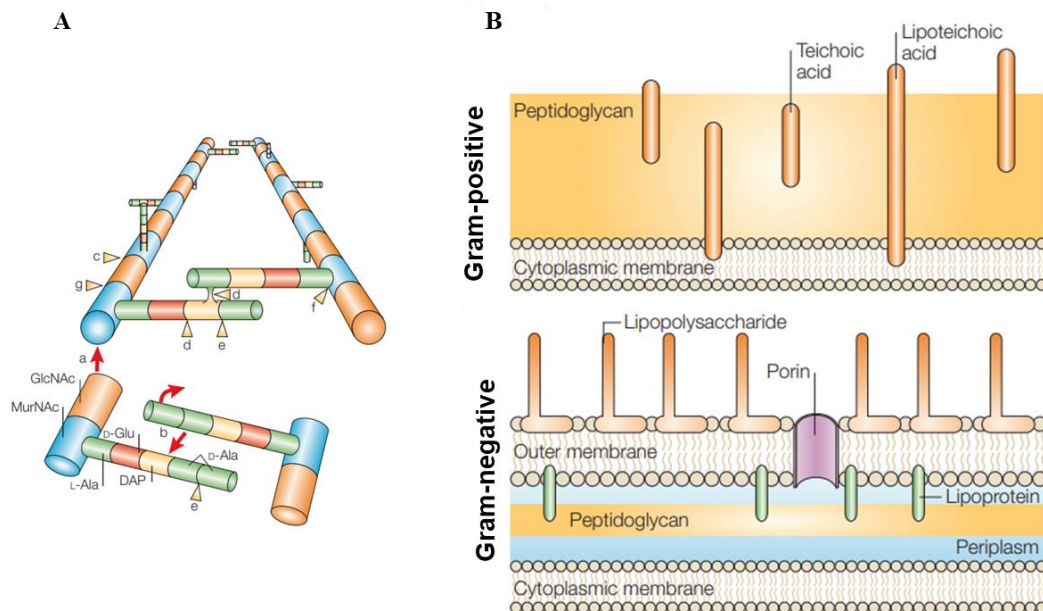


Figure 1.2: Peptidoglycan layer of bacteria.

(A) Chemistry of peptidoglycan synthesis. Repeating disaccharide subunits (MurNAc and GlcNAc) form a strand. The pentapeptides are attached to MurNAc and get crosslinked to adjacent strand by peptide cross-bridges. Diaminopimelic acid (DAP) in the pentapeptide undergoes crosslinking. The red arrows show peptidoglycan synthesis and cross-linking. The yellow arrowheads show the hydrolytic activity of transglycosylase and transpeptidase. (B) Gram-positive and Gram-negative bacterial cell walls. The gram-positive cell wall has thick multi-layered peptidoglycan. Teichoic acid and lipoteichoic acids are linked to peptidoglycan. In Gram-negative bacteria, the peptidoglycan is thin-layered and located at the periplasmic space. An additional outer layer is present in Gram-negative bacteria that has molecules such as lipopolysaccharide. Images are adapted from Cabeen and Jacobs-Wagner, 2005.

1.2: Cytoskeleton proteins in cell shape determination

Cytoskeleton proteins play and perform diverse functions in bacteria. Many of them are homologous to eukaryotic actin and tubulins (Wagstaff and Löwe, 2018). This include cell division; FtsZ, FtsA, DNA segregation; ParM, TubZ, intracellular compartment organizer; MamK, PopZ and cell shape determination; MreB, CreS, CcmA, Fibril, CetZ (Fig 1.3) (Wagstaff and Löwe, 2018). Some bacterial cytoskeleton proteins are like intermediate filaments, forming filaments without co-factors (Ausmees et al., 2003). Some of the bacterial cytoskeleton proteins determining bacterial cell shape are discussed here:

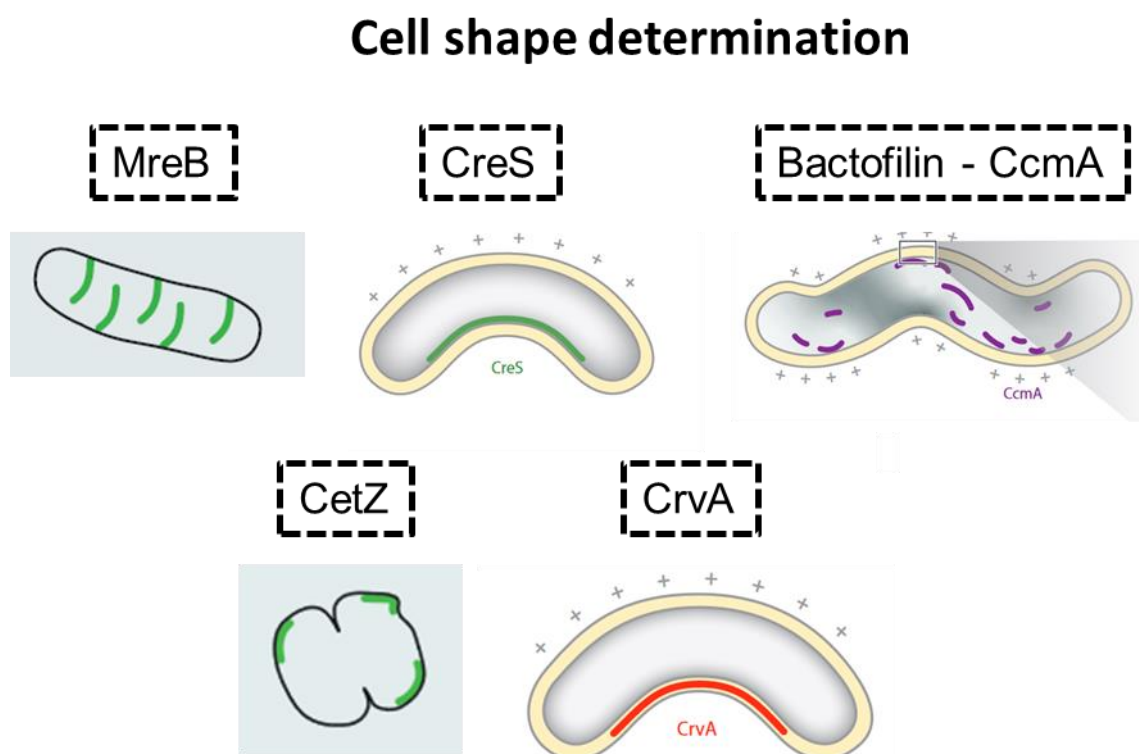


Figure 1.3: Schematic of prokaryotic cytoskeleton protein localization.

Various cell shape-determining proteins, MreB, CreS, CcmA, CetZ and CrvA, are responsible for generating and maintaining various bacterial cell shape. These protein interacts with peptidoglycan synthesis machinery and regulates cell-wall deposition in different regions of the bacterial cell. Images adapted from Wagstaff and Löwe, 2018 and Taylor et al., 2019.

MreB: MreB is a prokaryotic actin homolog (Esue et al., 2004; van den Ent et al., 2001). It is found in most of the non-spherical cell-walled bacteria. MreB has been widely studied and is the first prokaryotic protein to be determined for its role in cell shape determination (Bork et al., 1992). The detailed function and characteristics of MreB is discussed in the sections below.

CreS: Crescentin (CreS) is a bacterial equivalent of eukaryotic intermediate filament. It forms constitutive filaments that organize at the concave cytoplasmic face (negative membrane curvature) of *C. crescentus* (Fig 1.3 and Fig 1.4 A) (Charbon et al., 2009). In the absence of CreS, the curved *C. crescentus* cells form straight rods (Fig 1.4 B) (Ausmees et al., 2003). In vitro, CreS can form long filaments (Fig 1.4 C). CreS is divided into three domains: the head domain and the tripartite IF-like domain with short linker sequences between the coiled-coil domain and the tail domain (Fig 1.4 D) (Cabeen et al., 2011). Each domain has a specific role in the function and assembly of CreS (Cabeen et al., 2011). Both MreB and CreS function to maintain the curved shape of *C. crescentus*. This feature is reminiscent of actins and intermediate filaments determining the cell shape within eukaryotes together.

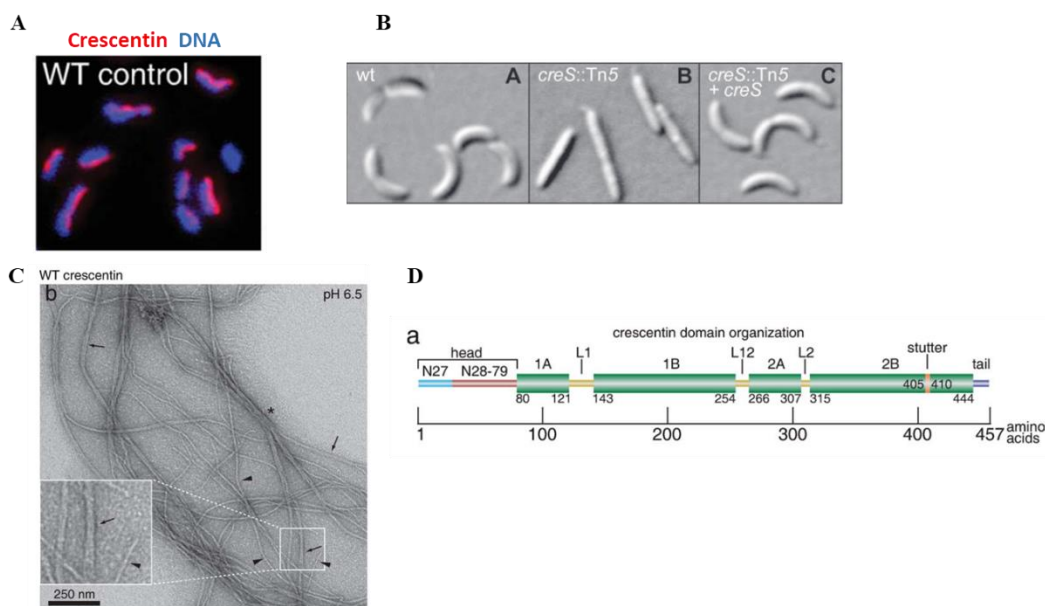


Figure 1.4: CreS forms constitutive filaments and organizes at the curved region of *C. crescentus*.

(A) Anti-crescentin immunofluorescence (red) shows the filament localization at the bacteria's negative curvature. Scale bar= 2 μ m. Images adapted from Cabeen et al., 2011. (B) Transposon-mediated inactivation of *creS* leads to the loss of curved shape in *C. crescentus*. Image adapted from Ausmees et al., 2003. Scale bar= 2 μ m. (C) Filaments of *CreS* using negative staining electron microscopy. Width of a single filament is 8-10 nm,

arrowheads and pair of filament width is 17-20 nm, black arrows. Images adapted from Cabeen et al., 2011 **(D)** Domain organization of CreS. Head, tail and stutter domains are labeled. The coiled-coil region is shown as green boxes with which are separated by linker L1, L 12 and L2. Image adapted from Cabeen et al., 2011.

Bactofilin: Bactofilins are found in diverse varieties of cell-walled bacteria. They can undergo nucleotide-independent polymerization, hence forms constitutive polymers (Lin and Thanbichler, 2013). All the bactofilins possess a characteristic DUF583 domain (bactofilin domain) that is flanked by unstructured N and C – terminal sequences (Fig 1.5 A and B) (Lin and Thanbichler, 2013). Many of the bacteria also possess multiple paralogs of bactofilin. Bactofilins have been hypothesized to be involved in various cellular functions (Deng et al., 2019) . One of the most important functions is regulating the cell morphogenesis. Bactofilins from *Caulobacter crescentus*, *Helicobacter pylori*, and *Myxococcus xanthus* has been widely studied for their role in regulating bacterial cell shape by interacting with a protein involved in peptidoglycan synthesis. Consider an example of *Helicobacter pylori*, a pathogenic bacteria with a characteristic helical shape (Jackson et al., 2020). It has a single bactofilin, CcmA, localized at the positive membrane curvature regions of the helical cells (Fig 1.3 and Fig 1.5 E) (Sichel et al., 2022). Deletion of *ccmA* results in curved cells (Fig 1.5 C). *In vitro*, CcmA forms filaments of different architecture, such as helical, lattice, and single filaments (Fig 1.5 D). CcmA interacts with cell shape determining proteins in *H.pylori*, Csd5 and Csd7, and together regulates the localization of peptidoglycan synthesis at the positive gaussian curvature (Fig 1.5 E). In *H.pylori*, it has been hypothesized that both CcmA and MreB function locally at positive and negative gaussian curvature to maintain peptidoglycan synthesis activity (Taylor et al., 2020).

CetZ: CetZ belongs to tubulin superfamily of proteins (Duggin et al., 2015). It is an archaeal tubulin homolog. Unlike FtsZ, which is required for cell division in bacteria, CetZ plays an important role in determining cell shape and motility (Duggin et al., 2015). While FtsZ localizes at the mid cell as a ring, CetZ localizes as spots or patches near the cell envelope, division furrow throughout the cytoplasm (Fig 1.3 and Fig 1.6 A). The first crystal structure of CetZ (CetZ1 and CetZ2) was solved from *Haloferax volcanii*. The structure revealed that it had the conserved FtsZ/tubulin core (Fig 1.6 B). CetZ2 bound to GTP γ S showed a straight protofilament assembly, indicating the cytoskeleton function of CetZ (Fig 1.6 C). Most of the studies on CetZ have been carried out on *Haloferax volcanii*. *H.volcanii* cells have

pleomorphic plate-like morphology which transition to rod shape under different conditions where motility is required. CetZs have two orthologs CetZ1 and CetZ2. CetZ1 has recently been shown to play major role in motility and cell shape (Fig 1.6 D) (Brown and Duggin, 2023). Deletion of *cetZ1* resulted in loss of motility, attributed to loss of rod shape.

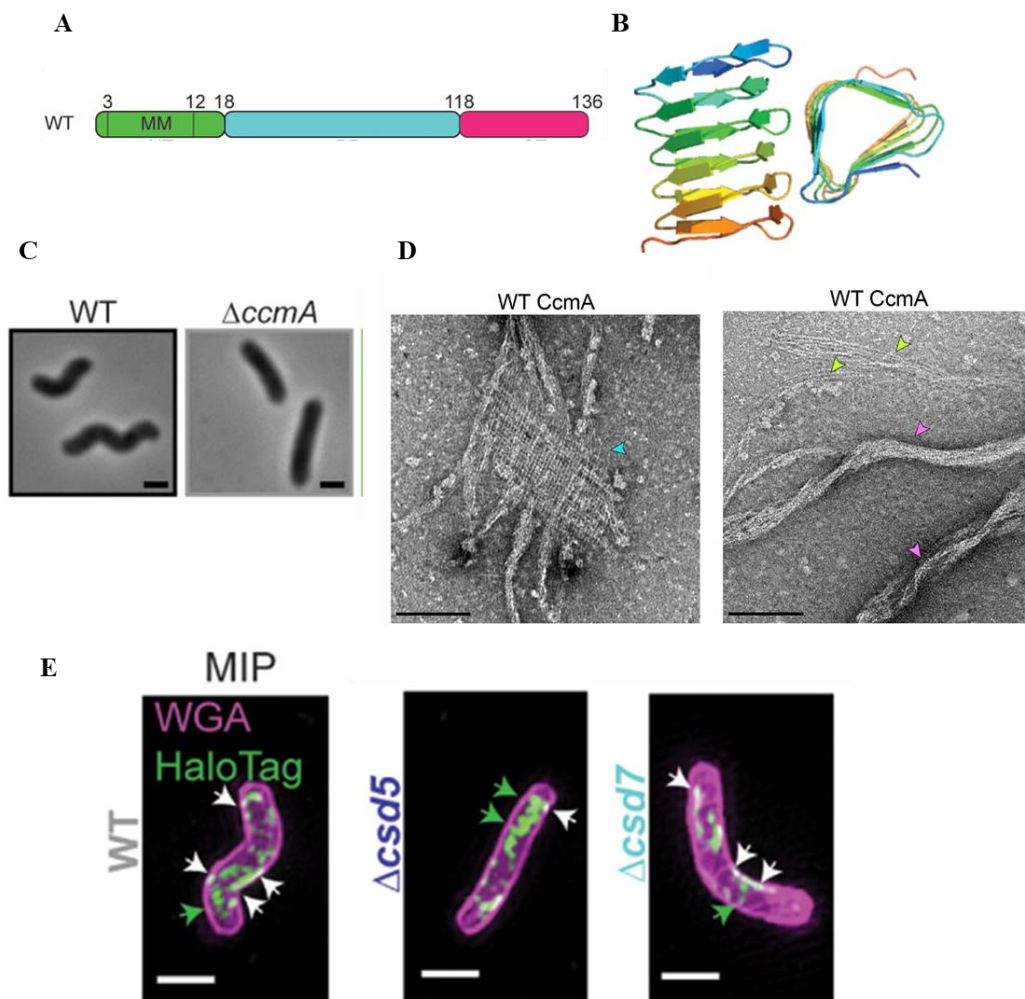


Figure 1.5: Bactofilin CcmA plays an important role in helical shape determination in *Helicobacter pylori*.

(A) Domain organization of CcmA bactofilin. Residues 18 – 118 constitute the bactofilin domain. It is flanked by an N-terminal region containing a putative membrane binding motif (MM, residues 3 – 12). The C-terminal region spans from 118 – 136 residues. Both the N and the C- terminal regions are unstructured. Image adapted from Sichel et al., 2022. (B) Model of bactofilin domain of CcmA that forms right-handed, three-sided, β – helix. The model is generated by RoseTTAFold. Image adapted from Sichel et al., 2022. (C) Phase contrast images of wildtype and *ccmA* truncated construct show loss of helicity in the absence of CcmA protein. Scale bar= 1 μ m. Image adapted from Sichel et al., 2022. (D) Negative staining transmission electron micrographs showing long CcmA filaments forms lattice (blue

arrowheads) and helical bundles (pink arrowheads) and individual filaments (yellow arrowheads). Scale bar = 100 nm. Image adapted from Taylor et al., 2020. **(E)** Maximum intensity projection of *H. pylori* cells that are labelled with wheat germ agglutinin (WGA) to label the cell wall (magenta) and a ligand JF549 that labels HaloTag-CcmA (green). The co-localization signal is seen as white pixel. In both $\Delta csd5$ and $\Delta csd7$ background, the cells lose helical shape and less or no co-localization signal for HaloTag-CcmA with the cell envelope is observed. Csd5 and Csd7 are required for CcmA function. Scale bar = 1 μ m. Image adapted from Sichel et al., 2022.

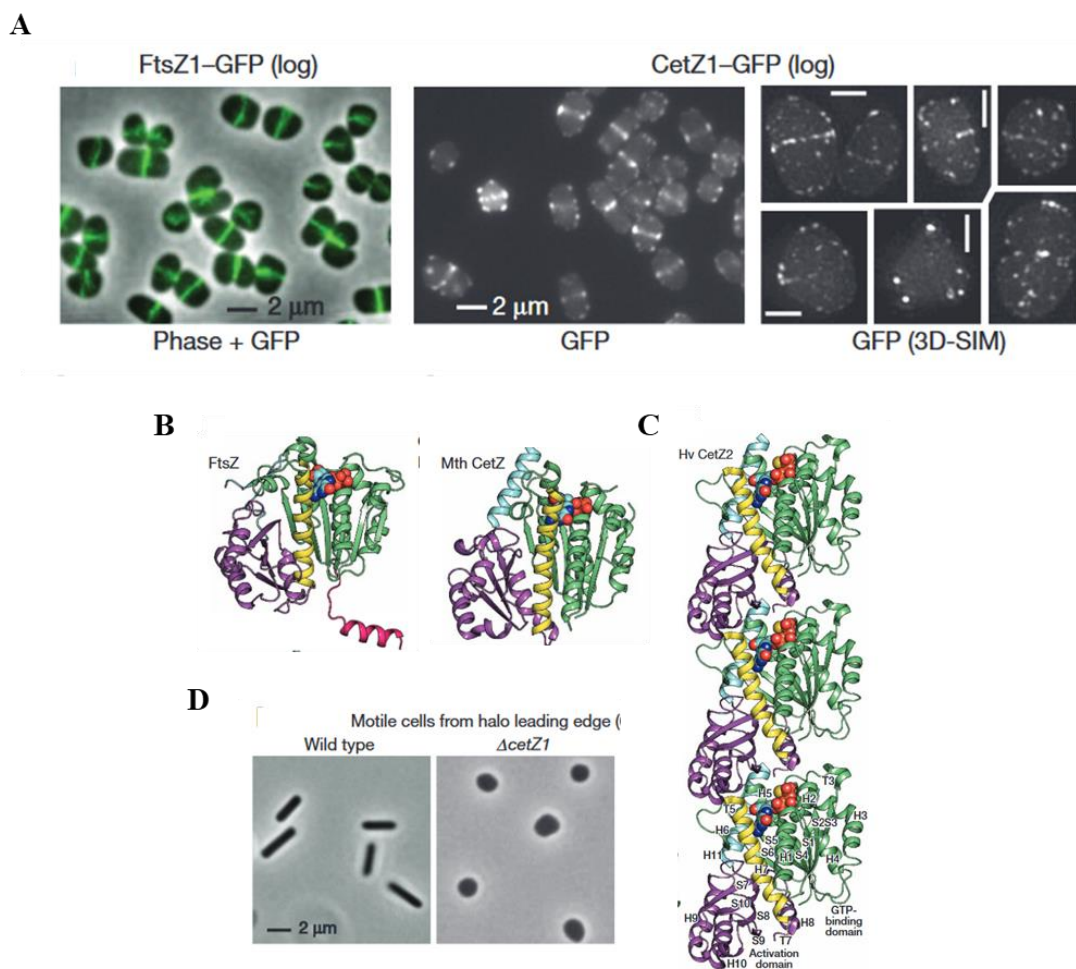


Figure 1.6: CetZ is required for rod-shape transition of plate-like archaeal cell *Haloferax volcanii*.

(A) CetZ and FtsZ show differences in the localization pattern in plate like *H. volcanii* cells. Here FtsZ1-GFP show ring at the mid cell. CetZ1-GFP is seen throughout the cytoplasm, as spots near cell envelop and at the mid cell. Scale bar = 1 μ m. **(B)** Crystal structure comparison of FtsZ (PDB ID 1FSZ) and CetZ (*Methanosaeta thermophila*) showing high structural similarity. **(C)** Straight protofilament organization of CetZ2-GTP- γ S in the crystal packing. **(D)** Deletion of *cetZ1* from the rod shape *H. volcanii* leads to loss of rod shape to plate-like morphology. Scale bar = 2 μ m. All the images adapted from Duggin et al., 2015.

Crv proteins: CrvA and CrvB are the cell shape determining protein of *V.chloerae* that promotes cell curvature (Martin et al., 2021). *V. cholerae* is a notorious pathogen whose curved shape is responsible for the motility and infectivity within the host. Both CrvA and CrvB are essential for the vibrioid shape of the organism; deletion of *crvA* and *crvB* was shown to generate rod shape cells (Fig 1.7 A). CrvA and CrvB filaments co-localize at the negative curvature of the cell within the periplasm and interact with the peptidoglycan (Fig 1.3 and Fig 1.7 B) (Bartlett et al., 2017). Interestingly, CrvA and CrvB are sufficient to break the symmetry and generate curved cells when heterologously expressed in *E. coli*, *C. crescentus*, *Pseudomonas aeruginosa* (Martin et al., 2021).

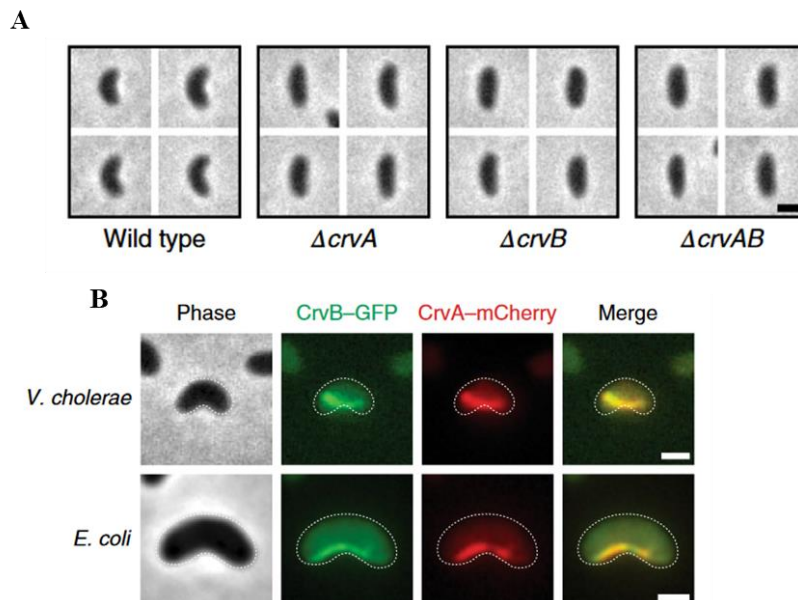


Figure 1.7: CrvA is required for the curved shape of *Vibrio cholerae*.

(A) In the absence of *crvA*, *crvB*, and *crvAB* the cells lose the curved shape as seen for the wildtype *V.cholerae*. Scale bar = 1 μ m. (B) CrvA-GFP and CrvB-GFP co-localize at the negative curvature in the *V.cholerae* cell at the periplasm. Scale bar = 1 μ m. All the images are adapted from Martin et al., 2021.

1.3: Proteins responsible for bacterial cell shape

Peptidoglycan synthesis is carried out by two types of machinery, elongasome and divisome (Szwedziak and Löwe, 2013). Elongasome functions at the length of the rod-shaped cell and carry out peptidoglycan synthesis for maintaining cell shape throughout the life cycle.

Divisome assembles and functions during cell division for septum synthesis at the constriction site (Szwedziak and Löwe, 2013). Both types of machinery share a few common proteins, MraY, MurG and MurJ, mainly required for synthesizing and transporting peptidoglycan (Egan et al., 2020). MraY and MurG synthesize Lipid II (GlcNAc-MurNAc-pentapeptide subunit linked to a polyisoprenoid) (de Kruijff et al., 2008). MurJ transports Lipid II across the cell membrane. Most research on bacterial cell elongation by peptidoglycan synthesis has used rod-shaped bacteria, such as *E. coli*. (Garde et al., 2021). This section focuses on the proteins that make up the elongasome machinery and their function in the formation of rod shapes. Three sets of proteins that form elongasome are mentioned below:

- Scaffold proteins: Cytoskeleton proteins such as MreB
- Cytoplasmic and Inner membrane proteins: Precursor synthesis (MraY and MurG), Flippases (MurJ/RodA), Associated protein (e.g. RodZ), PG synthesis activators
- Peptidoglycan modifiers: PG-Synthases (PBP1 and PBP2), Carboxypeptidase, Endopeptidase

Scaffold protein, MreB, in bacteria provides a platform for peptidoglycan synthesis machinery. The cytoplasmic precursor proteins are mainly involved in synthesizing peptidoglycan precursors. Flippases are involved in transporting the lipidated precursor to the periplasm. The peptidoglycan modifiers elongate the glycan strands, carry out peptide crosslink, and digest the old peptidoglycan strands to insert new peptidoglycan. The schematic of both the elongasome and divisome are shown in the Fig 1.8.

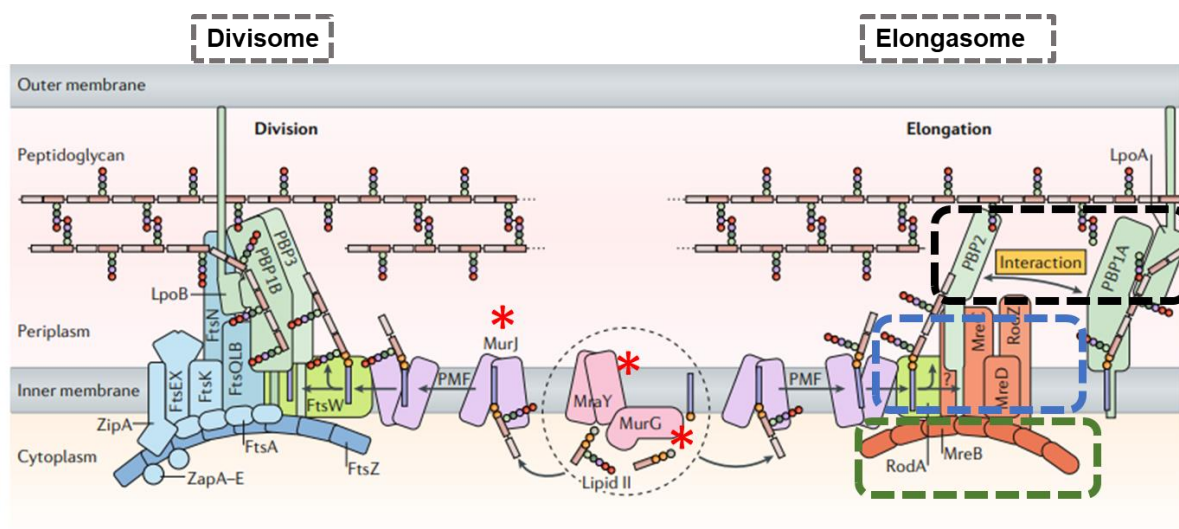


Figure 1.8: Peptidoglycan synthesis by elongasome and divisome.

Schematic showing multiprotein complex for peptidoglycan synthesis during cell division (by Divisome) and cell elongation (by Elongasome). Proteins common to both the types of machinery are marked with a red asterisk. In the elongasome machinery, a scaffold protein, inner membrane proteins, and peptidoglycan modifiers are highlighted with green, blue, and black boxes. Image adapted from Egan et al., 2020 .

1.4: Discovery of MreB

mreb gene was first isolated in the year 1987 from spherical *E.coli* cells. This strain had mutations at the 71 min region of *E.coli* chromosome map. This region was defined as *mre* (murein formation cluster e) and composed *mreC*, *rodY*, *envB* and *mreb*. Complementation study showed the role of this region in rod shape determination and sensitivity to amidinopenicillin, mecillinam (Wachi et al., 1987). Later on, in the year 1992, bioinformatics and sequence analysis showed that MreB had five conserved motifs of the ATPase domains as for actins, hexokinase and chaperone Hsp70 (Fig 1.9 A) (Bork et al., 1992). This analysis predicted that MreB, FtsA, and StbA had a similar subdomain (I and II) tertiary structure, the same ATP binding pocket, and the ability for interdomain hinge motion during state changes (Bork et al., 1992). In 2001, in vivo study of MreB and Mbl protein in *B.subtilis* showed that both proteins were responsible for rod shape (Jones et al., 2001). Filaments of MreB and Mbl were also seen as helical filaments encircling the *B.subtilis* cells (Jones et al., 2001). Finally,

the first crystal structure of MreB from *Thermotoga maritima* was solved for apo- and AMP-PNP bound states (Fig 1.9 B) (van den Ent et al., 2001). The key features, such as subdomain

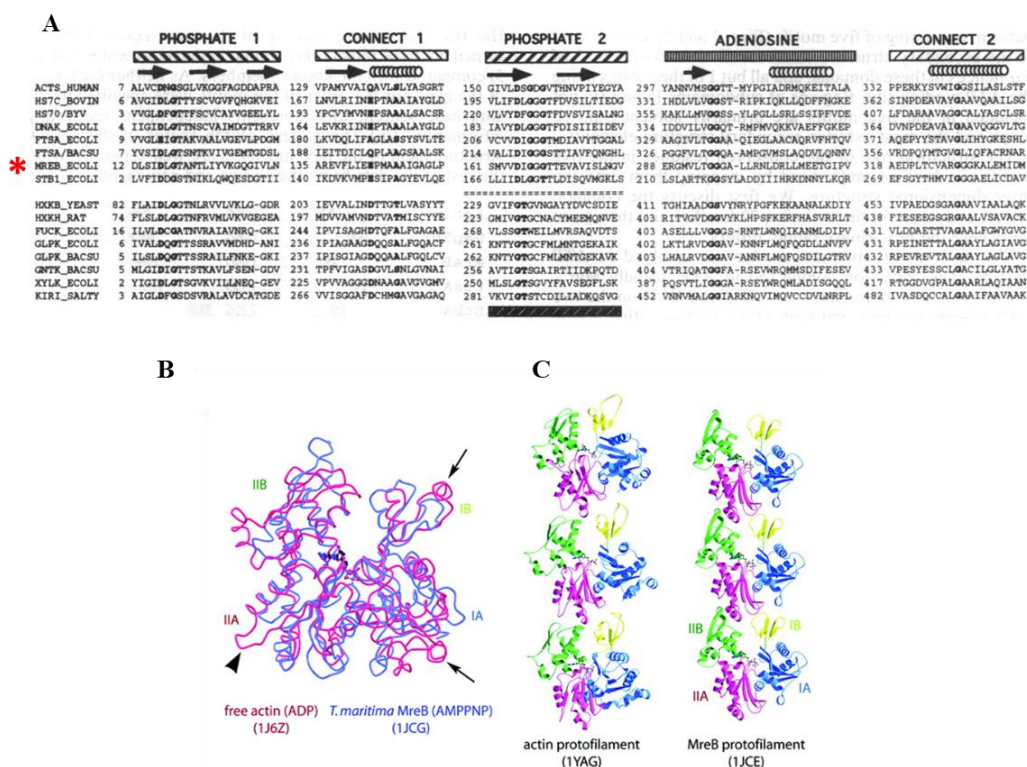


Figure 1.9: MreB has conserved nucleotide binding pocket and structure similar to actins.

(A) Multiple sequence alignment of the representatives of the hsp70 family proteins.

Sequence of MreB from *E.coli* is highlighted with red asterisk. MreB has the conserved motif responsible for ATP binding and hydrolysis. Image adapted from Bork et al., 1992. (B)

Superposed structures of MreB from *Thermotoga maritima* and actin are essentially the same fold. (C) Single protofilament organization of actin and MreB are similar. Images B and

C are adapted from Carballido-López, 2006.

organization and ATPase binding pocket, were very similar in the three-dimensional structure. The protofilament organization within the crystal packing and nucleotide-dependent polymerization features were similar to actin (Fig 1.9 C).

Most of the non-spherical cell-walled bacteria have a single copy of the *mreb* gene.

Interestingly, *B.subtilis* have three copies of *mreb*, *mrebh* and *mbl* with some redundant function (Kawai et al., 2009a). However, there are other phylogenetic order within bacteria that does not have MreB but are still able to maintain the rod shape (Cameron et al., 2015; Brown et al., 2012). The examples are:

1. Gram-positive Actinomycetales (that includes *Streptomyces*, *Mycobacterium spp.* and *Corynebacterium spp.*)
2. Gram-negative Rhizobiales (that includes *Brucella spp.* and *Bartonella spp.*, and *Agrobacterium tumefaciens*)

In these cases, the cell undergoes polar growth rather than growth along the side walls.

1.5: MreB and cell shape determination

1.5.1: MreB localization and dynamics study

To understand the function of MreB, firstly, MreB localization studies within cell-walled bacteria were carried out. Most of these studies came from model Gram-negative bacteria, *E.coli* and *C.crescentus*, and Gram-positive bacteria *B.subtilis*. Since deleting the native *mreb* gene compromised the survival of the cell (Fig 1.10 A) , most of the studies came by expressing *mreb* under an inducible promoter from a plasmid in an *mreb* depleted strains (Jones et al., 2001; Figge et al., 2004; Shih et al., 2003; Defeu Soufo and Graumann, 2006). Table 1.2 and 1.3 shows different constructs and imaging techniques used for locating MreB in the three organisms.

Table 1.2: Constructs and microscopy experiments used that determined the helical organization of MreB

Organism	MreB construct	Type of Microscopy
<i>E.coli</i>	N- terminus-YFP	Epifluorescence (Imaging done near the central plane of the cell)
<i>B.subtilis</i>	- N- terminus-GFP	Immunofluorescence Epifluorescence (Imaging done near the central plane of the cell)
<i>C.crescentus</i>	-	Immunofluorescence

Chapter 1: Introduction

Fluorescence microscopy of the bacteria showed that the MreB formed helical filaments (Fig 1.10 B). These helical filaments spanned the entire bacterial length. Using the GFP-MreB of *B.subtilis*, time-lapse imaging also captured the filament dynamics. Filaments of MreB could move around the entire cell circumference in 50-60 secs at an average speed of 0.07 $\mu\text{m/s}$, for actin it was reported to $\sim 1 \mu\text{m/s}$ (Mogilner and Oster, 2003). Interestingly, a similar kind of study for the peptidoglycan synthesis machinery proteins such as PBPs, MreC, MreD, etc, also showed a helical pattern of organization (Fig 1.10 C) (Leaver and Errington, 2005; Kawai et al., 2009b). Even the pattern of new cell-wall insertion visualized using fluorescently tagged vancomycin and ramoplannin, was similar to the helical filament pattern of MreB (Tiyanont et al., 2006). Thus, based on these results, it was concluded that MreB would function as a long helical scaffold for peptidoglycan synthesis machinery proteins. Hence, until 2010, it was believed that MreB forms long helical filaments that have a role in cell shape. Later on, these conclusions were disregarded due to the identification of artefacts of imaging and fusion constructs used in the previous localization studies (Table 1.2).

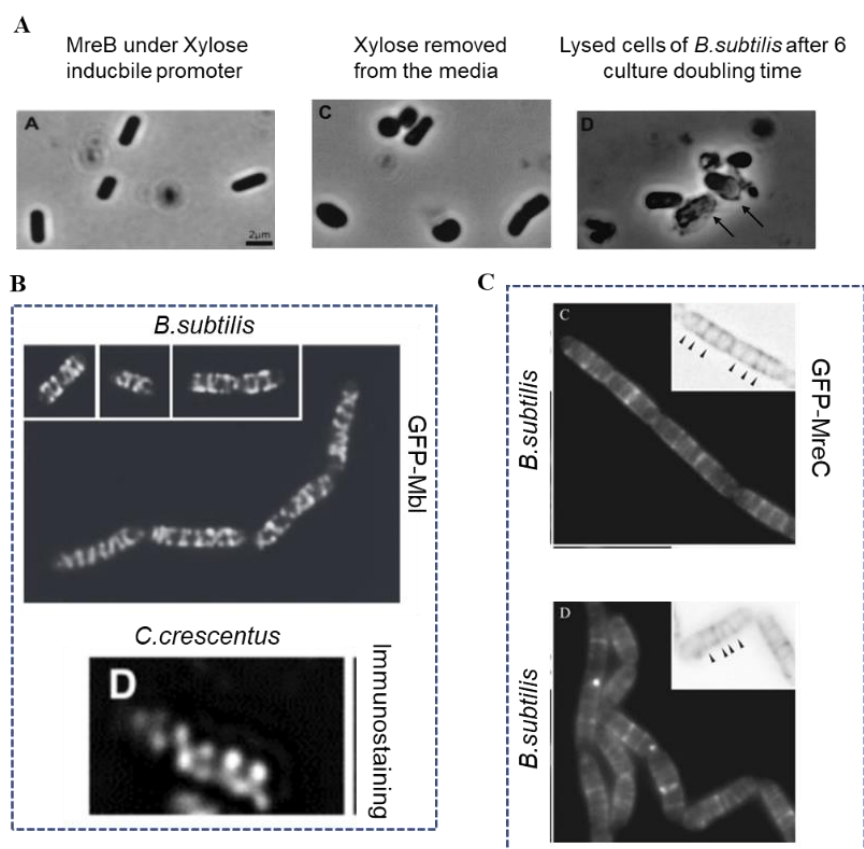


Figure 1.10: MreB localizes as helical filament along the cell length.

(A) Inhibition of MreB expression, which is under xylose inducible promoter, leads to lysis of *B.subtilis* cells. Scale bar = 2 μm . Image adapted from Jones et al., 2001. (B) Fluorescence microscopy shows the localization of MreB and Mbl (MreB-like protein) as helical or coiled shapes along the long axis of the cell for both *B.subtilis* (Mbl) and *C.crescentus* (MreB). Scale bar = 2 μm . Images are adapted from Carballido-López, 2006; Figge et al., 2004. (C) Peptidoglycan machinery proteins MreC and MreD also show helical localization as MreB and Mbl of *B.subtilis*. Scale bar = 5 μm . Images are adapted from Leaver and Errington, 2005.

Later on, cryo-electron tomography (cryo-ET) and cryo-fluorescence light microscopy coupled with cryo-ET on six different bacterial species (*E.coli*, *B.subtilis* and *C.crescentus*, *V.cholerae*, *Borrelia burgdorferi* and *Acetonea longum*) were done to visualize the organization of MreB helical filament. Surprisingly, such long helical MreB scaffold was absent beneath the cell membrane (Fig 1.11 A) (Swulius et al., 2011). Instead, filament length, >80 nm, which corresponded to MreB, were observed (Fig 1.11 B).

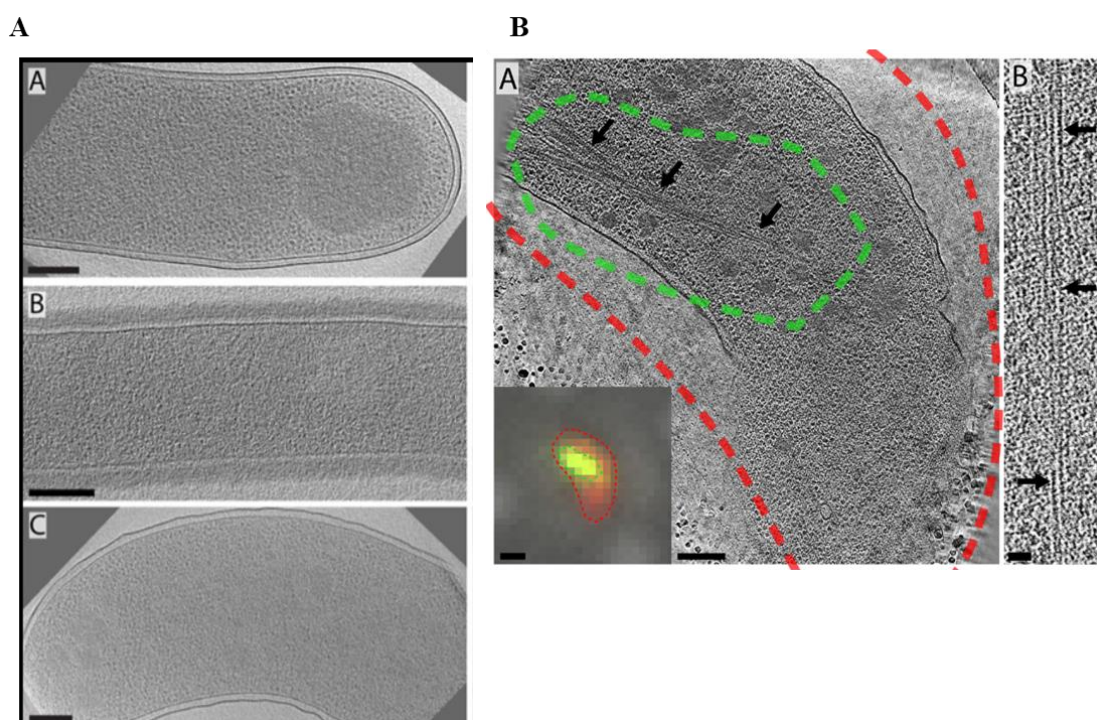


Figure 1.11: Long helical MreB filaments are not seen under cryo-ET.

(A) Tomographic slices of *E.coli*, *B.subtilis* and *V.cholerae* which show periplasmic edge of inner membrane to 13 nm into cytoplasm. No long helical filaments of MreB are observed. Scale bars = 200 nm (B) Tomographic slice of *V.cholerae* overexpressing GFP-MreB, inset corresponds to the cryo-fLM of the same cell. The GFP signal from cryo-fLM colocalize with

the cytoplasmic MreB filament bundles. Scale bar of cryo-fLM = 1 μm and tomographic slice = 200 nm. All the images are adapted from Swulius et al., 2011.

Further, Total internal reflection fluorescence microscopy (TIRFM), super-resolution microscopy and improved imaging analysis and software determined MreB localization and dynamics. These studies were carried out for *E.coli*, *B.subtilis* and *C.crescentus*. The type of construct and microscopy methods used are summarized in Table 1.3. MreB formed discrete dynamic patches (Fig 1.12 A). These dynamic patches rotated almost circumferentially perpendicular to the longitudinal axis of the cell. The movement of these patches was bi-directional, in contradiction to the earlier observation of MreB filament treadmilling (Kim et al., 2006). Cryo-EM and crystal structure studies, later on, showed the antiparallel filament organization for MreB which implied that treadmilling feature was not a possibility for MreBs (Fig 1.12 B) (van den Ent et al., 2014; Harne et al., 2020a; Salje et al., 2011; Takahashi et al., 2023).

Table 1.3: Constructs and microscopy experiments used that determined the patch like organization of MreB

Organism	MreB construct	Type of Microscopy	MreB filament velocity (nm/s) or mean square displacement value ($\mu\text{m}^2/\text{s}$)
<i>E.coli</i>	RFP sandwich construct	Epifluorescence (Imaging near the bottom plane of the cell)	$6.7 \pm 2.7 \text{ nm/s}$
<i>B.subtilis</i>	N- terminus-GFP	TIRFM with particle tracking	$\sim 50 \text{ nm/s}$
<i>C.crescentus</i>	N-terminus-YFP	Transmission and epifluorescence microscopy for tracking single molecule fluorescence	$1.11 \pm 0.18 \mu\text{m}^2/\text{s}$

It was also further shown that movement of MreB patches was independent of polymerization dynamics. Treating the cells with polymerization inhibiting drug, A22 did not affect the

velocity of the moving MreB puncta (van Teeffelen et al., 2011; Kim et al., 2006). In addition to this, the hydrolysis mutant of MreB also did not affect the MreB motion (Fig 1.12 C)

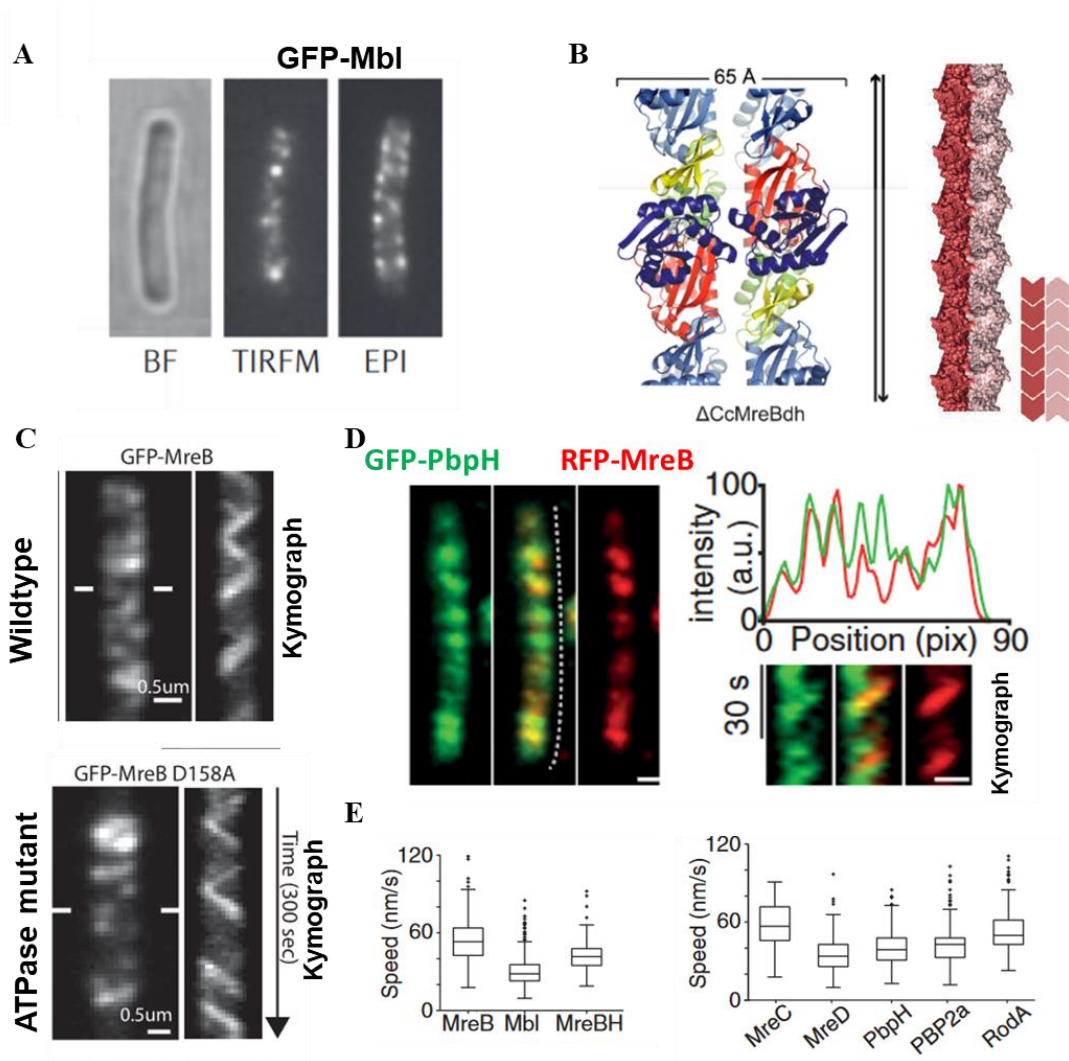


Figure 1.12: MreB localizes and moves as dynamic patches along the cell length.

(A) TIRFM and epifluorescence microscopy of GFP-Mbl of *B. subtilis* cells shows localization in patches. Scale bar = 1 μm . Image is adapted from Domínguez-Escobar et al., 2011. (B) Double protofilament organization of MreB from the crystal structure of *C. crescentus* (PDB ID: 4CZJ). The protofilament are antiparallel in orientation as seen from the schematic. Images are adapted from van den Ent et al., 2014; Wagstaff and Löwe, 2018. (C) ATP hydrolysis mutant GFP-MreB D158A shows similar localization and dynamics as the wildtype GFP-MreB in *B. subtilis*. Scale bar = 0.5 μm . Image is adapted from Garner et al., 2011. (D) Peptidoglycan machinery protein GFP-PbpH colocalizes with the RFP-MreB. The dynamics of movement also show co-localization as seen from the kymograph. Scale bar = 1 μm . (E) The speed of the processive movement of MreB paralogs (MreB, Mbl and

MreBH) is similar to proteins involved in peptidoglycan synthesis (MreC, MreD, PbpH, PBP2a and RodA). Images in D and E adapted from Domínguez-Escobar et al., 2011.

(Garner et al., 2011). These studies collectively proposed that the hydrolysis and the polymerization of MreB filaments do not determine the MreB motion.

Co-localization studies for peptidoglycan machinery proteins such as PbpH, MreC and MreD from *B. subtilis* were further carried out. These proteins co-localize with the rotating MreB patches and moved with similar velocity (Fig 1.12 D and E). (Domínguez-Escobar et al., 2011; Garner et al., 2011). MreB motion was also shown to be governed by the cell-wall synthesizing events of transpeptidation and transglycosylation. Drug targeting specific transpeptidase, PBP2, reduced the MreB motion (van Teeffelen et al., 2011). Both these findings showed that cell wall synthesis is required for MreB rotation. Thus, MreB would function as a regulator for cell growth but not as a platform that defines the whole cell shape.

1.5.2: MreB interaction with the membrane

Lipid membranes are dynamic in nature. The shape taken by the lipid membranes defines the shape of the cell and the organelles. Membrane shape is determined by the concept of principal curvature. Every surface has two principal curvatures in perpendicular directions. This is measured at the two intercept lines between the planes and the curved surface. The radii of the circular fragments R_1 and R_2 are called principal radii, and their inverse are called principal curvatures (Fig 1.13 A) (Zimmerberg and Kozlov, 2006). In terms of size, a curvature can be large or small. If the radius of curvature (R) is larger than the thickness of the membrane (d), $R \gg d$ then the membrane curvature is considered to be small, and if R is almost equal to 'd' then the membrane curvature is considered to be large. In terms of

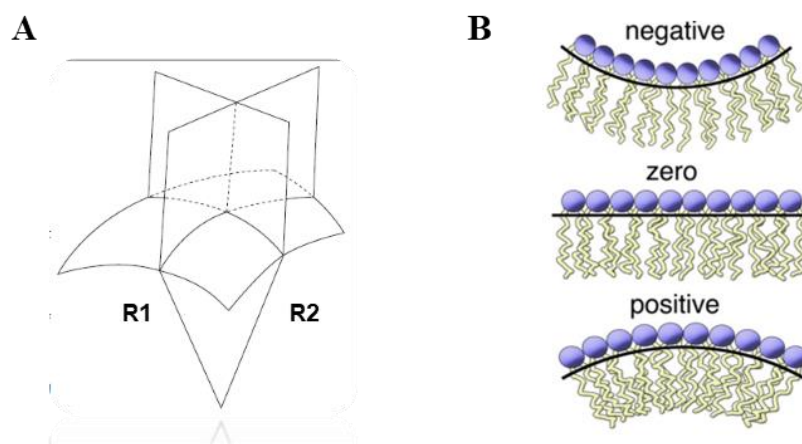


Figure 1.13: Defining a membrane curvature.

(A) Principal radii (R1 and R2) for a curved membrane surface. Image adapted from Zimmerberg and Kozlov, 2006. (B) Different curvatures of a membrane based on its orientation. Image adapted from Brown, 2012.

orientation, a curvature can be positive, negative or zero (Fig 1.13 B). This is determined by the curve directionality towards or away relative to the volume contained by the membrane (Zimmerberg and Kozlov, 2006).

Cryo-EM and crystal structures of MreB have revealed that it forms antiparallel double protofilaments (Fig 1.12 B). These filaments can directly bind to the lipid monolayer (van den Ent et al., 2014) (Fig 1.14 A). Structure and sequence analysis of MreB from *T. maritima*, *E. coli*, *C. crescentus* has revealed the presence of membrane binding region of MreB. These membrane binding regions are N-terminal amphipathic helix in Gram-negative bacteria and hydrophobic loop in the Gram-positive and Gram-negative bacteria (Fig 1.14 B). The antiparallel orientation of the filaments facilitates exposure of the membrane binding regions on the same face of the MreB double protofilament. The initial direct membrane binding ability of MreB filaments came from the study of *T. maritima* MreB (TmMreB). Membrane binding was determined through: (a) liposome pelleting assay with the purified wildtype TmMreB and hydrophobic loop mutants and (b) Cryo-electron microscopy of TmMreB filaments in the presence of ATP. Hence, it was established that MreB can bind to the membrane via the hydrophobic loop. Later on, cryo EM visualization of liposomes enclosing MreB filaments showed that in the presence of ATP, MreB filaments can sense and generate curvature. Filaments enclosed within a liposome showed three localization features (Fig 1.14 C), (a) Single filaments were organized throughout the spherical region of the liposomes, (b) Filaments arranged in bundles are organized perpendicular to the long axis of the tube generated from the liposomes, (c) No binding of the MreB filaments was observed over the small liposome surface that enclosed within the larger liposomes.

MreB is localized along the cylindrical region of the rod shape cells. In these regions there exist local areas of positive and negative curvatures (Ursell et al., 2014). MreB tends to recognize such local curvature of the cell body and gets localized in the areas of highest principal curvature (Ursell et al., 2014; Hussain et al., 2018), thus localizing perpendicular to the cell axis in a rod-shaped cell. By quantifying MreB enrichment (localization of fluorescent MreB) as a function of cell geometry (cell contour), it was reported that the maximal enrichment were

at the regions of negative contour curvature along the lateral edge of the cell. Minimum localization was at positive contour curvature (cell poles) (Fig 1.14 D). MreB filaments tend to bend liposomes (Salje et al., 2011) and this bent MreB filament has a radius of curvature of 200 nm. This curvature of MreB was used to model how the filament would

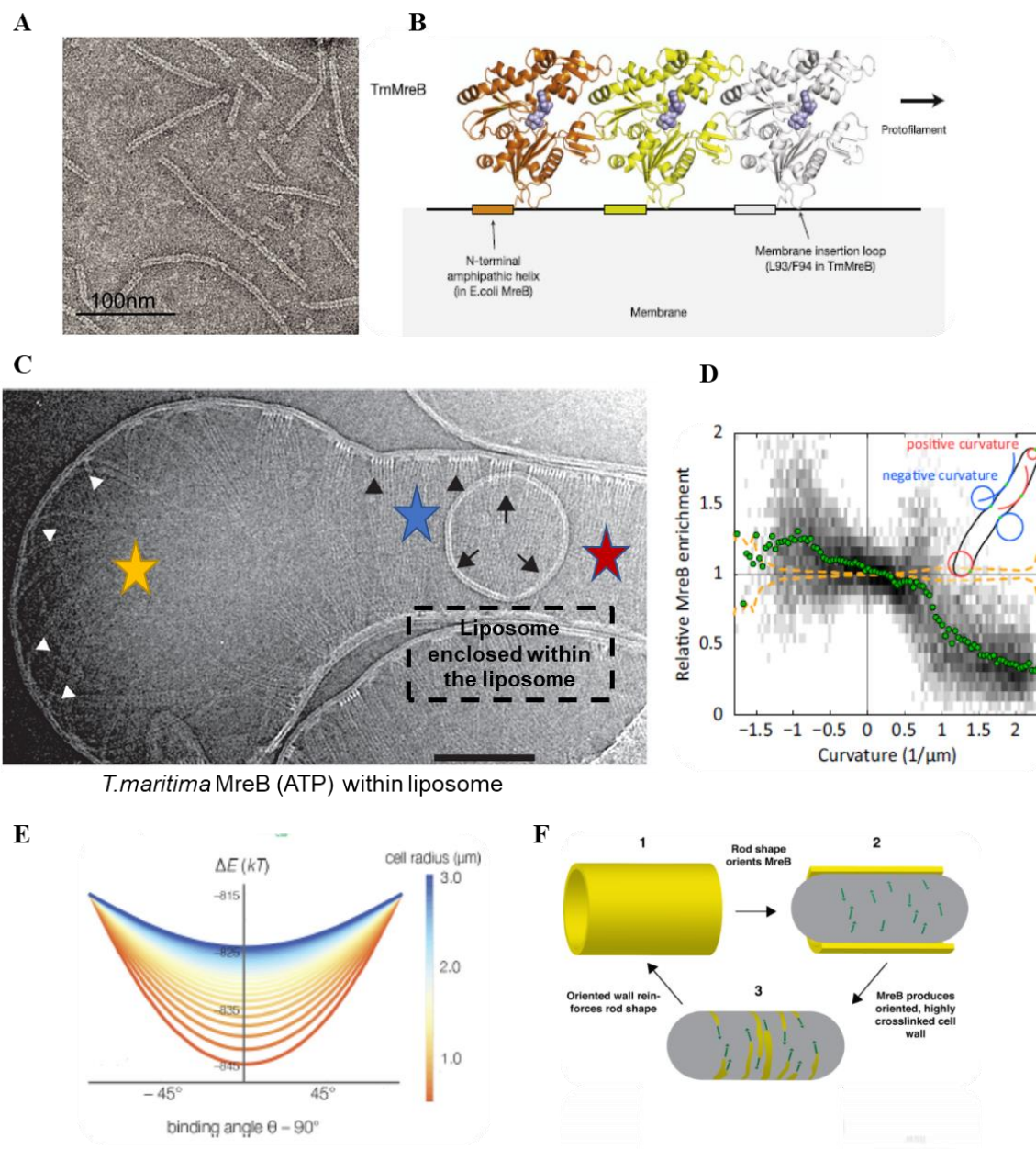


Figure 1.14: MreB interacts and deforms the lipid membrane.

(A) Cryo-EM of MreB filaments of *C. crescentus* MreB-ATP over a lipid monolayer. Scale bar = 100 nm. Image adapted from van den Ent et al., 2014. (B) Schematic showing the membrane binding face of MreB protofilament and the regions involved in membrane binding. These are a hydrophobic loop and an amphipathic helix. Image adapted from Salje et al., 2011. (C) Cryo-EM of MreB filaments enclosed within a liposome show membrane

deformations. Non-uniform distribution of individual filaments is observed in the spherical part of the liposome (yellow star). Circumferential orientation of MreB bundles is observed in the tubulated region of the liposome (red star). No filament binding is observed over the liposome surface that is enclosed within the larger liposome. Scale bar = 100 nm. Image adapted from Hussain et al., 2018. **(D)** Relative enrichment of MreB as a function of membrane curvature. Green dots depict mean enrichment. Image adapted Ursell et al., 2014. **(E)** Plot showing change in total energy upon MreB membrane interaction. Change in total energy is minimum when the filaments are perpendicular to the longitudinal axis of the cell. Image adapted from Hussain et al., 2018. **(F)** Model depicting MreB orientation along the rod that provide a single curved axis for MreB orientation. Image adapted from Hussain et al., 2018.

bind to the cell membrane, which has a radius of curvature of 1 μm . Modelling showed total change in the free energy is minimized when the orientation of the filament is at the highest principal curvature that might maximize membrane interactions (Fig 1.14 E). Experimental evidence further suggested that the MreB filaments orient circumferentially, in two possible ways: (a) filaments deform to the membrane (in cells due to high osmotic pressure) and (b) membrane deforms to the filament (in liposomes due to low osmotic pressure). MreB filament alignment to the greatest membrane curvature facilitates the positioning of peptidoglycan synthesis machinery, thus further reinforcing the rod shape (Fig 1.14 F).

1.6: Additional functions of MreB

Apart from playing a role in cell shape maintenance in non-spherical bacteria, studies on MreB have shown its role in chromosome segregation, motility, and division. In *C. crescentus* and *E. coli*, MreB plays an essential role in the separation of the origin of replication, *oriC* (Kruse and Gerdes, 2005; Gitai et al., 2005).

Chlamydomonas reinhardtii are spherical shaped bacteria that harbour MreB, which is typically exclusive to non-spherical bacteria. It lacks essential division proteins like FtsZ. In such bacteria, MreB is suggested to be involved in divisome machinery by interacting and tethering biosynthesis of lipid II (Gaballah et al., 2011).

In *Myxococcus xanthus* MreB functions in gliding motility of the organism. Through interaction with the small Ras like GTPase MglA-GTP, MreB stimulates the formation of a motility complex at the leading pole (Treuner-Lange et al., 2015). MreB would function as a scaffold for the gliding motors (Agl-Glt complex) while the gliding machinery drives the

MreB filament (Fu et al., 2018). Recent studies on MreBs from *Spiroplasma* have shed light on their role in the organism's kink-based motility. This is discussed in detail in the next sections.

1.7: *Spiroplasma* as a model organism to study cell shape determination by MreB

1.7.1: *Spiroplasma*: a helical cell-wall less bacterium

Spiroplasma are helical bacteria that are classified under Mollicutes (Fig 1.15 A). The class Mollicutes have evolved from the phylum Firmicutes, which includes *Bacillus* and *Clostridium*. It has a polarized morphology with a tapered end and a rounded end. They measure around 150 nm in width and 2-10 μm in length. They are known to be associated with the plant diseases such as citrus stubborn and corn stunt diseases. Many *Spiroplasma* species discovered have been shown to infect plants and insect vectors. *Spiroplasma* exhibit reduced genome size of a range 0.7-2.2 megabase pairs (Vera-Ponce León et al., 2021) owing to the parasitic lifestyle of the bacteria. It lacks genes involved in cell-wall synthesis, motility appendages, and chemotaxis (two-component regulatory system genes) from its genome. It exhibits chemotaxis (towards sugars and some amino acids) and viscotatic behaviour (Daniels et al., 1980). The absence of cell-wall would provide an advantage to evade the host innate immune response through peptidoglycan recognition proteins (Royet et al., 2011). The characteristic helical shape provides *Spiroplasma* a larger surface area for nutrient uptake, host cell attachment etc. Electron microscopy revealed the absence of any motility appendages such as flagella and pili. But still *Spiroplasma* exhibit motility by alternating between left and right helicity through the viscous medium, with swimming speed up to 5 $\mu\text{m/s}$ (Sasajima and Miyata, 2021; Shaevitz et al., 2005; Daniels et al., 1980). This kind of motility is called as kinking motility. Motility might be an essential survival strategy for the parasitic lifestyle of *Spiroplasma*. Motility in *Spiroplasma* would help in infection and evading the immune system within the host tissue.

1.7.2: Cell shape determination in *Spiroplasma*

The helical shape has shown to be important in *Spiroplasma* motility. One example that shows this link comes from a serotype of *Spiroplasma citri* called ASP-I (Townsend et al., 1977), which is non-helical and does not exhibit motility either (Fig 1.15 B). However, *scm1* mutant of *Spiroplasma* is helical but non-motile. This further indicates that helicity and motility machinery might have some common and uncommon proteins driving this machinery.

Research since 1970 on *Spiroplasma* has led to the discovery and study of cytoskeletal proteins. Cytoskeletal proteins are hypothesized to be involved in the cell shape determination and motility of *Spiroplasma*. Genetic, proteomic, and electron microscopy studies have revealed the presence of cytoskeleton proteins Fibril and MreBs (Fig 1.15 C) which are discussed below.

1.8: Cytoskeleton proteins of *Spiroplasma*

1.8.1: Fibril

In 1974 (Williamson, 1974), Fibril protein was first isolated from *Spiroplasma* upon treatment with detergent. Preliminary characterization of Fibril protein was further carried out in 1980 (Townsend et al., 1980), showing that it formed filaments with subunit repeat of 3.5 nm diameter, axial repeat of 8.5 nm, molecular weight of 55000 ± 550 Daltons (Fig 1.16 A). A polymerization-depolymerization study using ATP in dialysis and treatment with colchicine showed that these treatments did not affect the filaments, unlike features of actin and microtubules respectively. Fibril protein forms constitutive filaments without polymerization–depolymerization activity. Two cryo-electron tomography studies on *Spiroplasma melliferum* revealed the presence of flat ribbon-like structure running along the

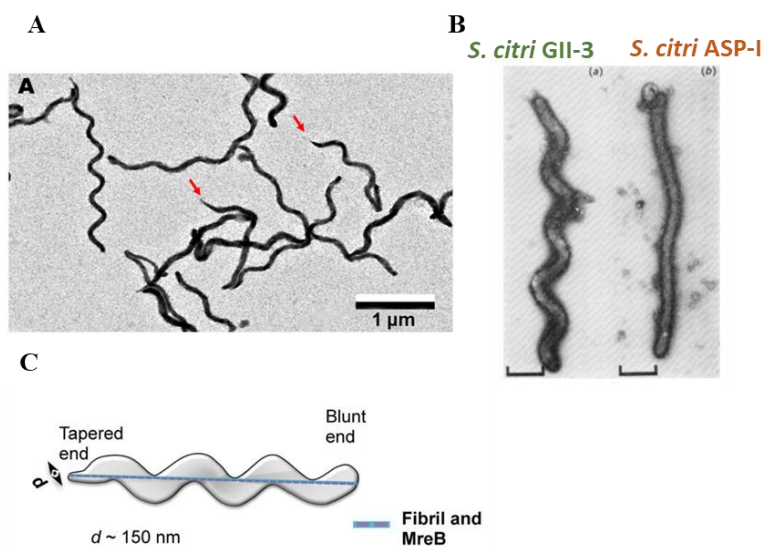


Figure 1.15: *Spiroplasma* exhibit helical morphology.

(A) Field image of intact *Spiroplasma eriocheris* cells. Scale bar = 1 μm. Image adapted from Takahashi et al., 2020 . (B) Negatively stained electron microscopy images of *S. citri* GII-3 (wildtype; helical, motile) and *S. citri* ASP-I (mutant; non-helical, non-motile). Scale bar = 0.5 μm. Image adapted from Townsend et al., 1977. (C) Schematic of *Spiroplasma* cell with

rounded/blunt and tapered end. Internal cytoskeleton protein runs along the shortest path between the cell poles. Image adapted from (Harne et al., 2020b).

helical path of the cell (Fig 1.16 B). Based on subunit repeat distance and subunit width, the ribbon was hypothesised to consist of two types of filament (Trachtenberg et al., 2008; Kürner et al., 2005). One of the filament populations was successfully isolated further and confirmed by proteomic approaches to be made of Fibril filament. Thus, Fibril is a part of the internal cytoskeleton of *Spiroplasma* that follows the geodetic line underneath the cell membrane. Recently, structure determination of Fibril filaments using electron microscopy of the negatively stained sample was carried out (Fig 1.16 C and D). The structure agreed with the previous work but did not display any subunit contraction and expansion of Fibril (Kürner, 2007; Cohen-Krausz et al., 2011). The fibril filament was shown to be composed of two oval rings with a connecting cylindrical part, the size of subunit was 8.7 nm length (Sasajima et al., 2022) (Fig 1.16 D). Each Fibril unit is slightly twisted with respect to the next unit. This generates a slight positive curvature (by the cylindrical part) in the filament (Fig 1.16 D). Due to which Fibril might align with the cell membrane. It has now been hypothesized that Fibril determines cell helicity (Sasajima et al., 2022; Lartigue et al., 2022). However, it is still unknown what force cause the change in helicity during *Spiroplasma* motility.

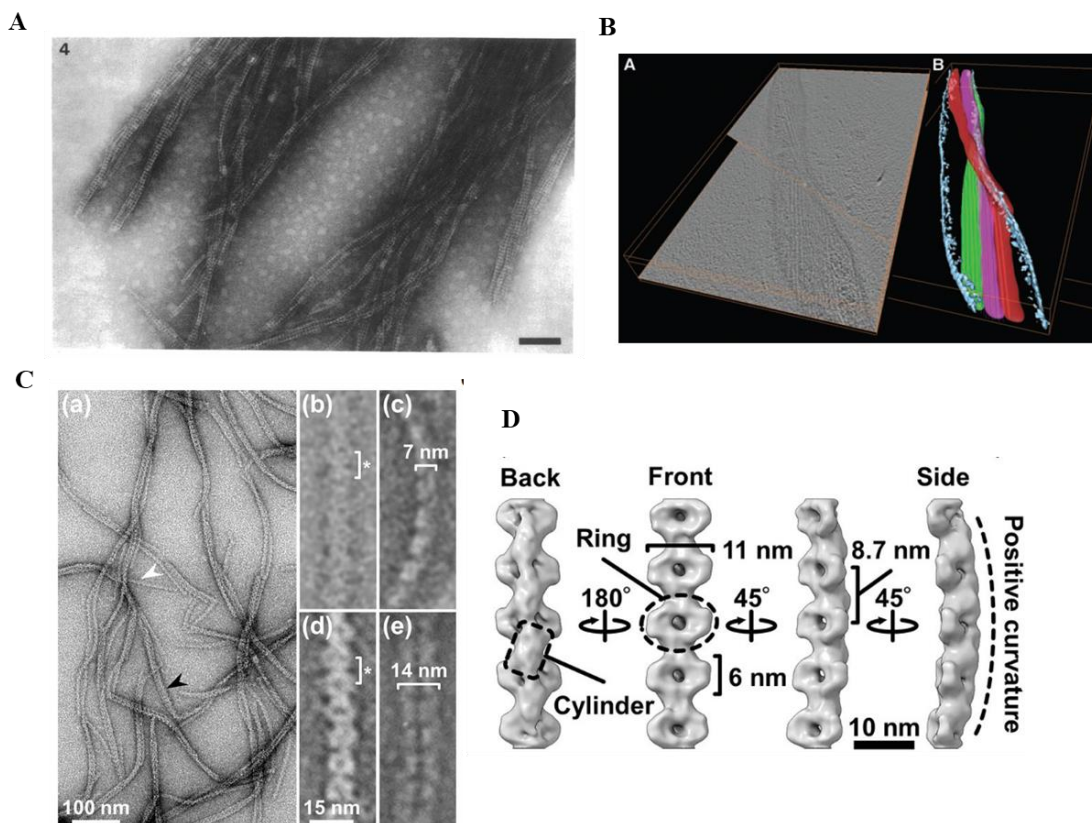


Figure 1.16: *Spiroplasma* Fibril form constitutive filaments.

(A) First time purified *Spiroplasma* Fibril proteins. Scale bar = 100 nm. Image adapted from (Townsend et al., 1980). (B) Cryo-electron tomography of *Spiroplasma melliferum* showing internal cytoskeleton beneath the cell membrane. A simplified 3-D representation show the red and green ribbon corresponding to Fibril and the purple ribbon is hypothesized to be MreB filament. Image adapted from (Kürner et al., 2005). (C) Negative stain image of purified Fibril filament, white arrow shows single strand and black arrowhead shows a double stranded filament (a). Front and side view of single stranded filament are shown in (b) and (d). Front and side view of double stranded filament are shown in (c) and (e). (D) Front, back and side conformation of Fibril filament generated by 3-D refinement in RELION software. Images are adapted from (Sasajima et al., 2022).

1.8.2: MreB

Most of the non-spherical cell-walled bacteria have at least a single copy of *mreB* gene. However, *Spiroplasma* species, as well as other helical mollicutes such as *Haloplasma*, have at least five paralogs of *mreB* gene. Different *mreB* paralogs have pairwise sequence identities in the range of 33-74% (Harne et al., 2020a; Miyata et al., 2020). Cryoelectron-tomography studies (as discussed for Fibril in the above section), revealed the presence of a second population of filaments in the ribbon running beneath the cell membrane (Fig 1.16 B). However, these filaments could not be isolated. Based on the subunit repeat length and width, which had been obtained from the *T.maritima* MreB crystal structure, these filaments might be MreB filaments. Studies of MreBs of cell-walled bacteria show that they undergo nucleotide dependent polymerization, hydrolyse ATP as well as interact with the lipid membrane. Thus, MreB in *Spiroplasma*, as proposed from the cryo-electron tomography studies (Trachtenberg et al., 2008; Kürner et al., 2005), postulates the role of MreB in conferring cell shape and motility by the polymerization dynamics of MreB. A few studies on multiple MreBs have been reported recently and are discussed below.

1.8.3: Recent advances in MreB and Fibril studies of *Spiroplasma*

Role of MreBs in *Spiroplasma* motility and helicity determination came from a recent study from our lab on *S.citri*, a plant pathogen (Harne et al., 2020a). Sequencing revealed a truncation in the *mreB5* gene in a naturally occurring non-helical, non-motile ASP-I strain of *S.citri*. A comparative proteomic study further showed the absence of MreB5 expression in the strain. When *mreB5* was expressed through a plasmid under the control of *tuf* promoter, the ASP-I phenotype switched to a helical shape exhibiting the characteristic kinking

motility. Thus, MreB5 was shown to be a major driver for helicity and motility in *S.citri*. Biochemical characterization showed it to undergo nucleotide-dependent filament dynamics (Pande et al., 2022). It was able to bind the membrane. MreB5 was able to form antiparallel double protofilaments as observed for other cell-walled MreBs. Thus, together this suggested that conserved structural features of MreB5 could have the divergent functional significance of helicity and motility determination. The exact mechanism of MreB5 function remains to be elucidated.

Subsequently, structure determination and biochemical characterization of MreBs (MreB3 and MreB5) of *S.eriocheris* followed. Structures of MreB3 and MreB5 filaments showed characteristic antiparallel assembly. However, the filament organization differed; where MreB3 formed individual separated filaments, filaments of MreB5 were organized as sheets in a given condition. Also, both proteins differ in the polymerization and ATP hydrolytic rate. These differences probably signify the different role of the proteins for determining the helicity and motility of *Spiroplasma*.

Due to limited genetic engineering tools and inefficient recombination machinery of *Spiroplasma* due to the conversion of *recA* to a pseudogene (Marais et al., 1996), gene inactivation studies have been unsuccessful. Heterologous expression in *Escherichia coli* (Masson et al., 2021), *Mycoplasma capricolum* (Lartigue et al., 2022) and synthetic bacterium, JCVI-syn3.0 (Kiyama et al., 2022) has been reported for the five MreBs and Fibril proteins. These studies with their major conclusions are discussed below:

- Lemaitre and co-workers (Masson et al., 2021) heterologously expressed three isoforms of MreBs :1, 2 and 3 of *S.poulsonii* in the *E.coli*. In *E.coli* MreB isoforms polymerized into distinctive filamentous structures (Fig 1.17 A). Only MreB2 fusion construct formed mobile filaments. MreBs were co-expressed in different combinations of GFP-tagged and untagged proteins. Each isoform affected the polymerization of the other in a complex network of interactions (Fig 1.17 B) (Masson et al., 2021). Co-immuno precipitation study with mass spectrometry and co-polymerization study revealed specific interactions between the MreBs and Fibril. Along with interaction between MreB isoforms, MreB1 and Fibril were observed. A model was hypothesized based on the interaction studies where, (a) MreB2 could act as a regulator of *S.poulsonii* motility, (b) MreB1 and MreB3 might serve as membrane anchors with the Fibril. Together the three cytoskeleton proteins will function to

generate the *Spiroplasma*-like shape and motility. Although the heterologous study can help in understanding the function of each MreBs, it has several caveats, such as protein tagging and other *E.coli* proteins that might interact with *Spiroplasma* MreBs. Hence, confirmation of such intricate level of interactions need to be confirmed by genetic and visualization studies in the *Spiroplasma*.

- Miyata and co-workers (Kiyama et al., 2022) reconstituted *Spiroplasma* motility and helicity in JCVI-syn3B (syn3B). syn3B is a synthetic bacterium with a minimal gene set, faster growth rate compared to *Spiroplasma*, and genome manipulation possibility. It has a spherical morphology. Seven genes (*fib*, 5 *mrebs* and one non-annotated gene) of *S. eriocheris* were incorporated into the syn3B genome under the *tuf* promoter. Expression of these genes led to morphological changes in syn3B cells. Around 13 % of the population also exhibited helical shape and kinking swimming motility similar to wild type *Spiroplasma* cells. This construct is called as syn3Bsw. When expression of 1 out of 6 genes was hampered sequentially from syn3Bsw, no drastic phenotypic changes occurred except for MreB5. There was a significant increase in the helical width and the absence of kinking motility in the absence of MreB5. Lastly, 10 pairs of MreB protein combinations were analyzed for their motility and helical shape. Five MreBs were divided into three groups, MreB2 and MreB5, MreB1 and MreB4, and MreB3, based on their sequence similarity (Fig 1.18 A). MreB from each group was expressed in combination with the other group. Only cells with MreB5 paired with the MreB1 and MreB4, exhibited helix formation and movement similar to syn3Bsw (Fig 1.18 A and B). Only two MreBs, each from one group, were sufficient for syn3Bsw motility and helical shape. To understand the role of Fibril, Fibril was incorporated into the MreB5-MreB4 construct. Very subtle morphological and motility changes occurred, which were insignificant (Fig 1.18 C). Hence, this study indicated that the helix formation and force generation for swimming requires MreB interactions. The authors proposed a theoretical model where two MreBs from the two groups (MreB1/4 and MreB2/5) would generate force like in a bimetallic strip. This force would be transmitted further to Fibril filament (Fig 1.18 D). Together, these three proteins will function to generate the kinking motility in *Spiroplasma*.

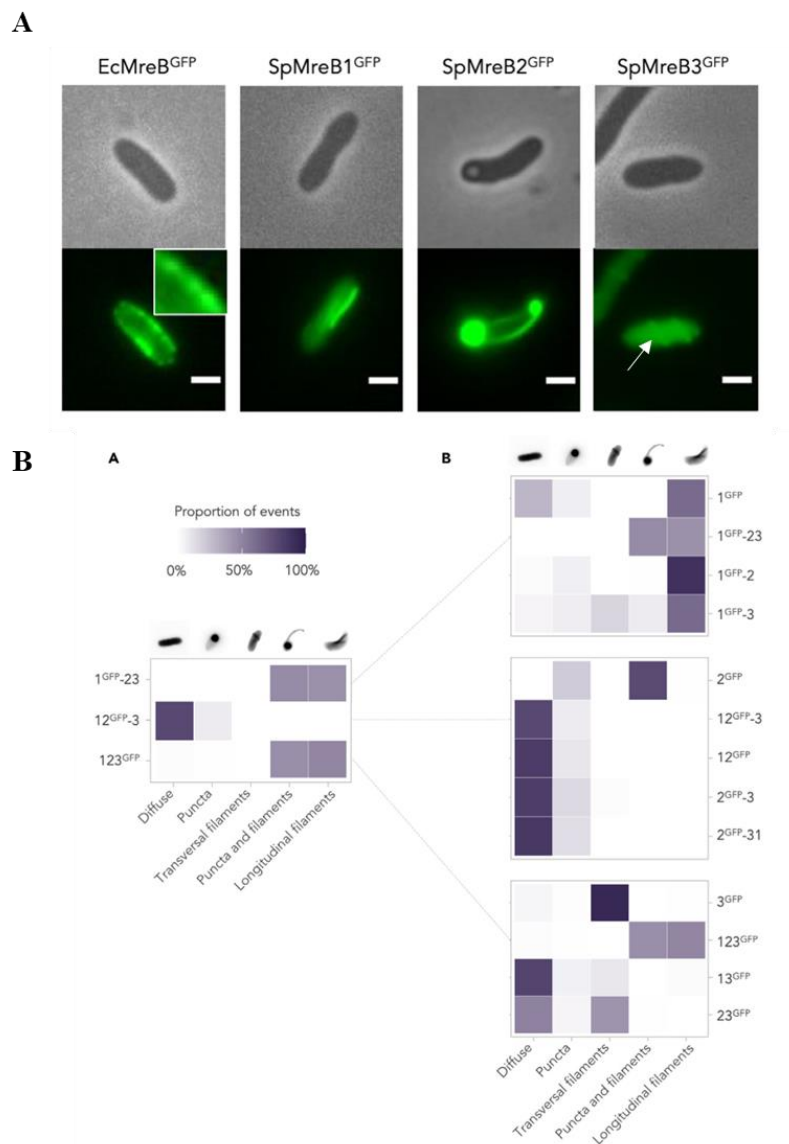


Figure 1.17: Heterologous expression of *Spiroplasma* MreBs in *E. coli*.

(A) GFP tagged MreB1, MreB2 and MreB3 are able to form filaments in *E. coli* expression system. MreB1 longitudinal filaments, MreB2 forms both puncta and filaments and MreB3 forms transversal filaments (white arrow). Scale bar = 2 μm (B) Co-expression of GFP-tagged MreBs with the other two untagged MreBs shows that MreB interaction regulates polymerization. The difference in the proportion of filaments patterns can be observed for different combinations. All the images are adapted from Masson et al., 2021.

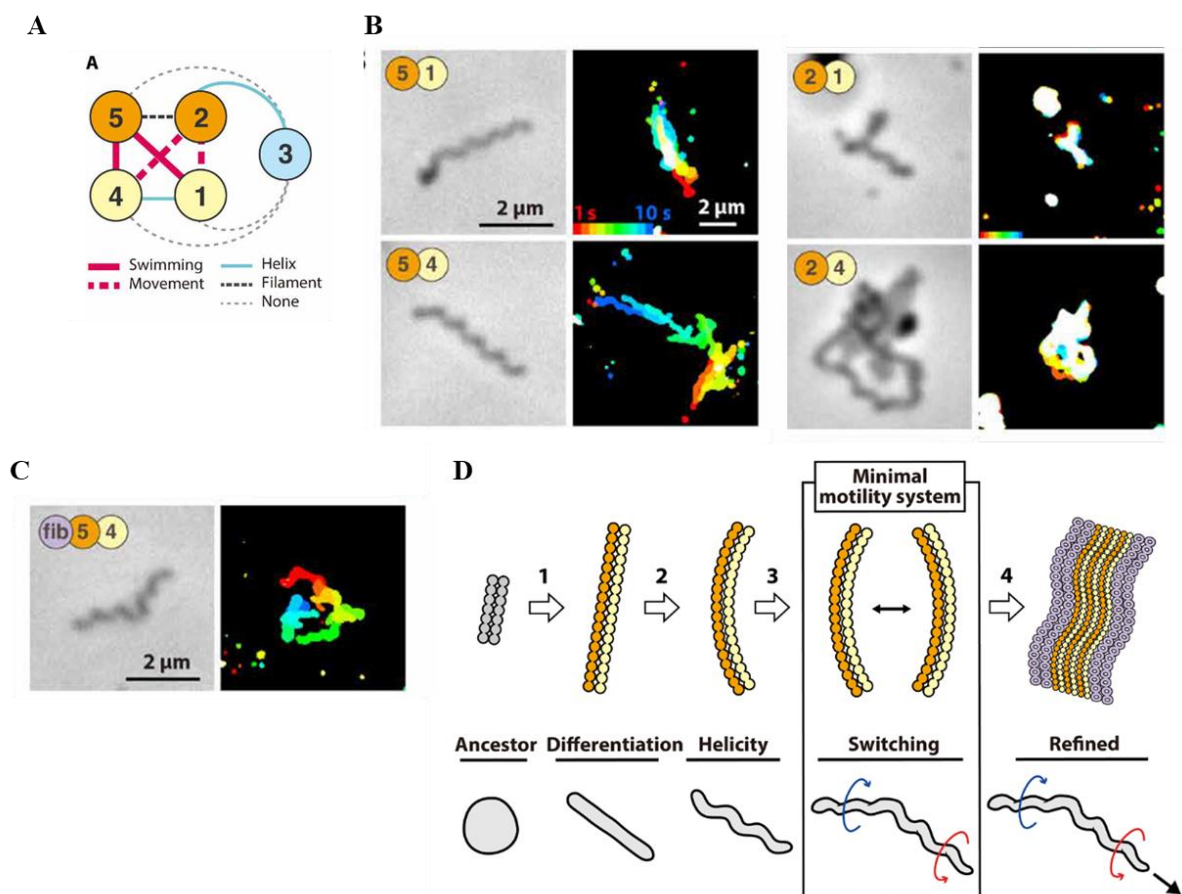


Figure 1.18: Heterologous expression of *Spiroplasma* MreB in synthetic bacterium syn3b.

(A) Schematic of MreB combinations with the three protein groups (orange, yellow and blue). The characters observed by expressing these *mreb* combinations are shown by lines. Red solid line is filamentous and helical cells with swimming motility. Red dotted line represents filamentous and helical with only movements. Blue solid line represents filamentous and helical with no movements. Black dotted lines represent filamentous and cells with no helicity and movement. (B) Phase contrast microscopy showing syn3B cells expressing MreBs in pairs from the groups (2,5) and (1,4). Motility and helical shape is observed for 5-1 and 5-4. Only helical and filamentous cell with no motility is observed for 2-1 and 2-4. Scale bar = 2 μ m. (C) syn3B cells expressing MreB4, MreB5 and Fibril show no difference in helicity and motility. (D) Model showing the development and mechanism of *Spiroplasma* swimming. Swimming may be acquired in four steps. (1) Differentiation of cell-walled bacterial MreB in two classes which acquired different characters through evolution. (2) Small differences in filament properties led to curvature generation and, eventually, the helicity of heterogeneous filaments. (3) Changes in filament length causes ATP hydrolysis that induces changes in curvature, causing kinks. (4) The swimming motility

became more defined with other MreBs, Fibril, and other cell factors. All the images are adapted from (Kiyama et al., 2022).

- Another group (Lartigue et al., 2022) reconstituted *Spiroplasma* motility and helicity by heterologously expressing *mreb* (1-5) and *fib* gene in *Mycoplasma capricolum* (Mcap). *M. capricolum* has spherical morphology and does not have *mreB* in the genome (Fig 1.19 A). Expressing all the *mreb*s and *fib* together resulted in helical morphology and kinking motility to the Mcap cells (Fig 1.19 A). However, the helical pitch was significantly different from *S. citri*. In addition to that, the kink-based propulsion did not provide directional motility to the Mcap^{*mreb1-5, fib*} cells. This indicated that other *Spiroplasma* components might be required for directed cell movement in addition to cytoskeleton protein. When only *fib* was expressed in Mcap cell (Mcap^{*fib*}), the cells remained spherical. Hence, *fib* did not confer to helicity and motility. In addition, Mcap cells expressing only *mreb* genes (Mcap^{*mreb1-5*}) were helical and motile but the propagation of kinks was affected. Hence, although *mreb* provided the helicity and kinking motility, but for the efficient propagation of kinks, *fib* would be required. Mass spectrometry analysis of Mcap^{*mreb1-5, fib*} showed that MreB1 and MreB5 were most abundant. Co-expressing *mreb5-fib* and *mreb1-fib* showed that the *mreb5-fib* had helicity and kinking motility (Fig 1.19 B), whereas the latter had helices with no motility (Fig 1.19 B). MreB5 represented the minimal requirement for the cell to attain helical pitch mimicking *S. citri* and motility. Cryo-electron tomography further showed the association of expressed MreB and Fibril protein to the cytoplasmic membrane (Fig 1.19 C). The authors propose a model in which MreB5 will facilitate the localization of Fibril and MreB1 onto the membrane. Together, MreB5 and MreB1 will generate the force by ATP hydrolysis. Fibril will carry out the transmission of force through the propagation of kink along the cell body.

These studies show that MreB paralogs function as a major driver for *Spiroplasma* helicity. Out of all MreBs, MreB5 has a major role in driving the helicity and motility along with Fibril. MreB1 might function along with Fibril and MreB5 in driving motility. Both the MreBs might provide the required force for propagation of kinks by Fibril filaments. In general, at least two MreBs and Fibril protein are required to generate a minimal motility system that closely resembles *Spiroplasma* helical shape and motility. Hence, studying these

five MreBs and Fibril in a heterologous system has increased our understanding of how, in the absence of cell-wall the MreBs can function to determine the helical shape and motility. The helical shape of the organism might be required for the motility by internal cytoskeleton protein.

There are a number of areas that are still yet to be explored for *Spiroplasma* MreBs and Fibril with respect to shape, such as

1. How these MreBs expressions are regulated within the *Spiroplasma* life cycle.
2. Do the functions of MreBs of same group overlap, and can they co-polymerize.
3. Function of morphologically distinct ends of *Spiroplasma*.
4. Regulation of MreB and Fibril dynamics during cell division.

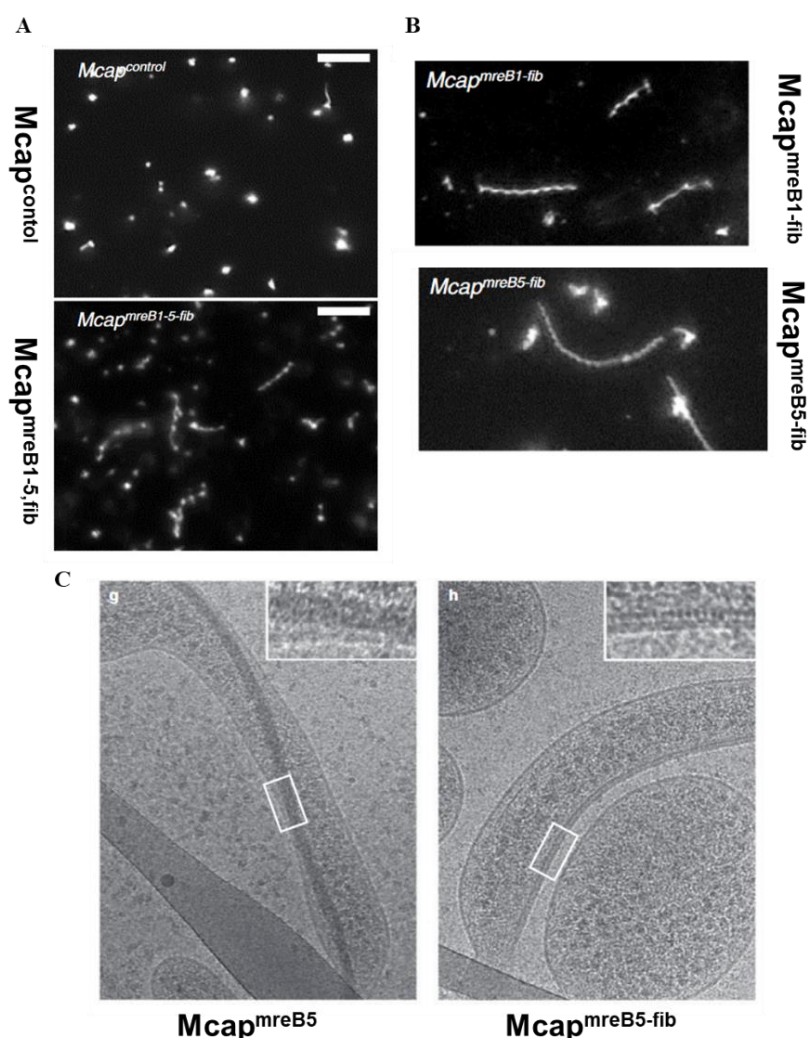


Figure 1.19: Heterologous expression of *Spiroplasma* MreB in *Mycoplasma capricolum*

(A) Expression of MreB(1-5) and Fib in *M. capricolum* leads to helicity and swimming motility to non-motile spherical *M. capricolum* cells. Scale bar = 10 μm . (B) Co-expression of

MreB1-Fibril or MreB5-Fibril is sufficient to cause helicity to *M.capricolum* cells. Scale bar = 5 μ m. (C) Cryo-electron tomography shows the formation of cytoskeleton filaments beneath the cell membrane of *M.capricoulm* cells. Scale bar = 100 nm, Inset scale bar = 20 nm. Images are adapted from Lartigue et al., 2022 .

1.9: Objectives

Studies of MreB function, including cell shape regulation, cell division and motility, have been reported for cell-walled bacteria. MreB function has always been in conjunction with the peptidoglycan synthesis machinery (Kawai et al., 2009b; Dye et al., 2011; Defeu Soufo and Graumann, 2006; Mauriello et al., 2010). Antiparallel double-protofilament form of MreB filaments implies the absence of treadmilling which is a conserved feature for actins. However, the role of nucleotide hydrolysis in polymerization is not understood. Polymerization properties such as polymerization rate, filament-filament interaction and nucleotide binding and ATP hydrolysis role in driving polymerization are unknown for MreB. Studies have shown the membrane interaction and curvature sensing ability of MreB is important for cell shape maintenance. However, the role of ATP hydrolysis and conformational change that would occur during the hydrolytic cycle is not well understood. Recently, a number of studies for non-spherical shape determination in the absence of cell wall have started to come up. These studies, as discussed in the previous section, show the role of multiple MreBs in helical shape and motility determination.

The main aim of my thesis is to decipher the role of the nucleotide state of MreB in determining filament organization and membrane binding. For this, I have chosen MreB5 of *Spiroplasma citri* (ScMreB5). Characterizing ScMreB5 which functions independently of cell wall synthesis machinery, will help identify conserved mechanisms and signatures for MreB function. I have used structural, biochemical and *in-vitro* reconstitution approaches to understand ScMreB5 functioning. The following goals, which are discussed as chapters, make up this work.

1. Purification condition optimization of ScMreB5. This followed by crystallization and structure determination of the protein in the ADP and AMP-PNP bound state.
2. Analysis of ScMreB5 ADP and AMP-PNP bound structure. This involves determining residues essential for ATP hydrolysis, polymerization interface, membrane binding, and A22 drug binding. The study also includes the structural

comparison of the subdomains and ATP binding pocket with other available structures of MreBs from cell-walled and cell-wall-less bacteria and actins.

3. Biochemical characterization of ScMreB5 wildtype, ATPase mutants and polymerization mutants. This includes comparative ATP hydrolysis and light scattering studies of ScMreB5 wildtype and its mutants. An analysis of the polymerization dynamics using yeast expression is also carried out. To visualize filaments of ScMreB5 in different nucleotide states, cryo-electron microscopy has also been performed.
4. Characterization of membrane-ScMreB5 interaction for the wildtype and membrane binding mutants. Further, the role of nucleotide state in determining membrane binding is characterized. Liposome pelleting assays are performed for the this work.
5. ScMreB5-membrane remodelling studies are done on lipid tubes and planar bilayers. Membrane remodelling has been visualized under different nucleotide conditions. Electron microscopy of the liposome and MreBs are also performed to visualize filaments and membrane deformation.

1.10: References

- Ausmees, N., J.R. Kuhn, and C. Jacobs-Wagner. 2003. The Bacterial Cytoskeleton: An Intermediate Filament-Like Function in Cell Shape. *Cell*. 115:705–713. doi:10.1016/S0092-8674(03)00935-8.
- Bartlett, T.M., B.P. Bratton, A. Duvshani, A. Miguel, Y. Sheng, N.R. Martin, J.P. Nguyen, A. Persat, S.M. Desmarais, M.S. VanNieuwenhze, K.C. Huang, J. Zhu, J.W. Shaevitz, and Z. Gitai. 2017. A Periplasmic Polymer Curves *Vibrio cholerae* and Promotes Pathogenesis. *Cell*. 168:172-185.e15. doi:10.1016/j.cell.2016.12.019.
- Bork, P., C. Sander, and A. Valencia. 1992. An ATPase domain common to prokaryotic cell cycle proteins, sugar kinases, actin, and hsp70 heat shock proteins. *Proc. Natl. Acad. Sci.* 89:7290–7294. doi:10.1073/pnas.89.16.7290.
- Brown, H.J., and I.G. Duggin. 2023. Diversity and Potential Multifunctionality of Archaeal CetZ Tubulin-like Cytoskeletal Proteins. *Biomolecules*. 13:134. doi:10.3390/biom13010134.
- Brown, M.F. 2012. Curvature forces in membrane lipid-protein interactions. *Biochemistry*. 51:9782–9795. doi:10.1021/bi301332v.
- Brown, P.J.B., M.A. de Pedro, D.T. Kysela, C. Van der Henst, J. Kim, X. De Bolle, C. Fuqua, and Y.V. Brun. 2012. Polar growth in the Alphaproteobacterial order Rhizobiales. *Proc. Natl. Acad. Sci.* 109:1697–1701. doi:10.1073/pnas.1114476109.
- Cabeen, M.T., H. Herrmann, and C. Jacobs-Wagner. 2011. The domain organization of the bacterial intermediate filament-like protein crescentin is important for assembly and function. *Cytoskelet. Hoboken Nj*. 68:205–219. doi:10.1002/cm.20505.
- Cabeen, M.T., and C. Jacobs-Wagner. 2005. Bacterial cell shape. *Nat. Rev. Microbiol.* 3:601–610. doi:10.1038/nrmicro1205.
- Cameron, T.A., J.R. Zupan, and P.C. Zambryski. 2015. The essential features and modes of bacterial polar growth. *Trends Microbiol.* 23:347–353. doi:10.1016/j.tim.2015.01.003.
- Carballido-López, R. 2006. The bacterial actin-like cytoskeleton. *Microbiol. Mol. Biol. Rev. MMBR*. 70:888–909. doi:10.1128/MMBR.00014-06.

Charbon, G., M.T. Cabeen, and C. Jacobs-Wagner. 2009. Bacterial intermediate filaments: in vivo assembly, organization, and dynamics of crescentin. *Genes Dev.* 23:1131–1144. doi:10.1101/gad.1795509.

Cohen-Krausz, S., P.C. Cabahug, and S. Trachtenberg. 2011. Monomeric, Tetrameric, and Fibrillar Organization of Fib: The Dynamic Building Block of the Bacterial Linear Motor of *Spiroplasma melliferum* BC3. *J. Mol. Biol.*

Daniels, M.J., J.M. Longland, and J. Gilbert. 1980. Aspects of Motility and Chemotaxis in Spiroplasmas. *Microbiology.* 118:429–436. doi:10.1099/00221287-118-2-429.

Defeu Soufo, H.J., and P.L. Graumann. 2006. Dynamic localization and interaction with other *Bacillus subtilis* actin-like proteins are important for the function of MreB. *Mol. Microbiol.* 62:1340–1356. doi:10.1111/j.1365-2958.2006.05457.x.

Deng, X., A.G. Llamazares, J. Wagstaff, V.L. Hale, G. Cannone, S.H. McLaughlin, D. Kureisaite-Ciziene, and J. Löwe. 2019. The structure of bactofilin filaments reveals their mode of membrane binding and lack of polarity. *Nat. Microbiol.* 4:2357–2368. doi:10.1038/s41564-019-0544-0.

Desmarais, S.M., M.A. De Pedro, F. Cava, and K.C. Huang. 2013. Peptidoglycan at its peaks: how chromatographic analyses can reveal bacterial cell-wall structure and assembly. *Mol. Microbiol.* 89:1–13. doi:10.1111/mmi.12266.

Domínguez-Escobar, J., A. Chastanet, A.H. Crevenna, V. Fromion, R. Wedlich-Söldner, and R. Carballido-López. 2011. Processive Movement of MreB-Associated Cell Wall Biosynthetic Complexes in Bacteria. *Science.* 333:225–228. doi:10.1126/science.1203466.

Doyle, R.J., J. Chaloupka, and V. Vinter. 1988. Turnover of cell walls in microorganisms. *Microbiol. Rev.* 52:554–567. doi:10.1128/mr.52.4.554-567.1988.

Duggin, I.G., C.H.S. Aylett, J.C. Walsh, K.A. Michie, Q. Wang, L. Turnbull, E.M. Dawson, E.J. Harry, C.B. Whitchurch, L.A. Amos, and J. Löwe. 2015. CetZ tubulin-like proteins control archaeal cell shape. *Nature.* 519:362–365. doi:10.1038/nature13983.

Dye, N.A., Z. Pincus, I.C. Fisher, L. Shapiro, and J.A. Theriot. 2011. Mutations in the nucleotide binding pocket of MreB can alter cell curvature and polar morphology in *Caulobacter*. *Mol. Microbiol.* 81:368–394. doi:10.1111/j.1365-2958.2011.07698.x.

Egan, A.J.F., J. Errington, and W. Vollmer. 2020. Regulation of peptidoglycan synthesis and remodelling. *Nat. Rev. Microbiol.* 18:446–460. doi:10.1038/s41579-020-0366-3.

van den Ent, F., L.A. Amos, and J. Löwe. 2001. Prokaryotic origin of the actin cytoskeleton. *Nature.* 413:39–44. doi:10.1038/35092500.

van den Ent, F., T. Izoré, T.A.M. Bharat, C.M. Johnson, and J. Löwe. 2014. Bacterial actin MreB forms antiparallel double filaments. *eLife.* doi:10.7554/eLife.02634.

Esue, O., M. Cordero, D. Wirtz, and Y. Tseng. 2004. The Assembly of MreB, a Prokaryotic Homolog of Actin*. doi:10.1074/jbc.M410298200.

Figge, R.M., A.V. Divakaruni, and J.W. Gober. 2004. MreB, the cell shape-determining bacterial actin homologue, co-ordinates cell wall morphogenesis in *Caulobacter crescentus*. *Mol. Microbiol.* 51:1321–1332. doi:10.1111/j.1365-2958.2003.03936.x.

Fu, G., J.N. Bandaria, A.V. Le Gall, X. Fan, A. Yildiz, T. Mignot, D.R. Zusman, and B. Nan. 2018. MotAB-like machinery drives the movement of MreB filaments during bacterial gliding motility. *Proc. Natl. Acad. Sci.* 115:2484–2489. doi:10.1073/pnas.1716441115.

Gaballah, A., A. Kloeckner, C. Otten, H.-G. Sahl, and B. Henrichfreise. 2011. Functional Analysis of the Cytoskeleton Protein MreB from *Chlamydomonas reinhardtii*. *PLOS ONE.* 6:e25129. doi:10.1371/journal.pone.0025129.

Garde, S., P.K. Chodiseti, and M. Reddy. 2021. Peptidoglycan: Structure, Synthesis, and Regulation. *EcoSal Plus.* 9. doi:10.1128/ecosalplus.ESP-0010-2020.

Garner, E.C., R. Bernard, W. Wang, X. Zhuang, D.Z. Rudner, and T. Mitchison. 2011. Coupled, Circumferential Motions of the Cell Wall Synthesis Machinery and MreB Filaments in *B. subtilis*. *Science.* 333:222–225. doi:10.1126/science.1203285.

Gitai, Z., N.A. Dye, A. Reisenauer, M. Wachi, and L. Shapiro. 2005. MreB actin-mediated segregation of a specific region of a bacterial chromosome. *Cell.* 120:329–341. doi:10.1016/j.cell.2005.01.007.

Goodwin, S.D., and J.G. Shedlarski. 1975. Purification of cell wall peptidoglycan of the dimorphic bacterium *Caulobacter crescentus*. *Arch. Biochem. Biophys.* 170:23–36. doi:10.1016/0003-9861(75)90094-6.

Graham, C.L.B., H. Newman, F.N. Gillett, K. Smart, N. Briggs, M. Banzhaf, and D.I. Roper. 2021. A Dynamic Network of Proteins Facilitate Cell Envelope Biogenesis in Gram-Negative Bacteria. *Int. J. Mol. Sci.* 22:12831. doi:10.3390/ijms222312831.

Harne, S., S. Duret, V. Pande, M. Bapat, L. Béven, and P. Gayathri. 2020a. MreB5 Is a Determinant of Rod-to-Helical Transition in the Cell-Wall-less Bacterium Spiroplasma. *Curr. Biol.* doi:10.1016/j.cub.2020.08.093.

Harne, S., P. Gayathri, and L. Béven. 2020b. Exploring Spiroplasma Biology: Opportunities and Challenges. *Front. Microbiol.* 11.

Hussain, S., C.N. Wivagg, P. Szwedziak, F. Wong, K. Schaefer, T. Izoré, L.D. Renner, M.J. Holmes, Y. Sun, A.W. Bisson-Filho, S. Walker, A. Amir, J. Löwe, and E.C. Garner. 2018. MreB filaments align along greatest principal membrane curvature to orient cell wall synthesis. *eLife.* 7:e32471. doi:10.7554/eLife.32471.

Jackson, L.K., B. Potter, S. Schneider, M. Fitzgibbon, K. Blair, H. Farah, U. Krishna, T. Bedford, R.M.P. Jr, and N.R. Salama. 2020. Helicobacter pylori diversification during chronic infection within a single host generates sub-populations with distinct phenotypes. *PLOS Pathog.* 16:e1008686. doi:10.1371/journal.ppat.1008686.

Jones, L.J.F., R. Carballido-López, and J. Errington. 2001. Control of Cell Shape in Bacteria: Helical, Actin-like Filaments in Bacillus subtilis. *Cell.* 104:913–922. doi:10.1016/S0092-8674(01)00287-2.

Kawai, Y., K. Asai, and J. Errington. 2009a. Partial functional redundancy of MreB isoforms, MreB, Mbl and MreBH, in cell morphogenesis of Bacillus subtilis. *Mol. Microbiol.* 73:719–731. doi:10.1111/j.1365-2958.2009.06805.x.

Kawai, Y., R.A. Daniel, and J. Errington. 2009b. Regulation of cell wall morphogenesis in Bacillus subtilis by recruitment of PBP1 to the MreB helix. *Mol. Microbiol.* 71:1131–1144. doi:10.1111/j.1365-2958.2009.06601.x.

Kim, S.Y., Z. Gitai, A. Kinkhabwala, L. Shapiro, and W.E. Moerner. 2006. Single molecules of the bacterial actin MreB undergo directed treadmilling motion in Caulobacter crescentus. 103:10929–10934.

Kiyama, H., S. Kakizawa, Y. Sasajima, Y.O. Tahara, and M. Miyata. 2022. Reconstitution of a minimal motility system based on Spiroplasma swimming by two bacterial actins in a synthetic minimal bacterium. *Sci. Adv.* 8:eabo7490. doi:10.1126/sciadv.abo7490.

de Kruijff, B., V. van Dam, and E. Breukink. 2008. Lipid II: a central component in bacterial cell wall synthesis and a target for antibiotics. *Prostaglandins Leukot. Essent. Fatty Acids.* 79:117–121. doi:10.1016/j.plefa.2008.09.020.

Kruse, T., and K. Gerdes. 2005. Bacterial DNA segregation by the actin-like MreB protein. *Trends Cell Biol.* 15:343–345. doi:10.1016/j.tcb.2005.05.002.

Kürner, J. 2007. Cryo – Electron Tomography Reveals the Cytoskeletal Structure of Spiroplasma melliferum. *Science.* 436:436–439. doi:10.1126/science.1104031.

Kürner, J., A.S. Frangakis, and W. Baumeister. 2005. Cryo-Electron Tomography Reveals the Cytoskeletal Structure of Spiroplasma melliferum. *Science.* 307:436–438. doi:10.1126/science.1104031.

Lartigue, C., B. Lambert, F. Rideau, Y. Dahan, M. Decossas, M. Hillion, J.-P. Douliez, J. Hardouin, O. Lambert, A. Blanchard, and L. Béven. 2022. Cytoskeletal components can turn wall-less spherical bacteria into kinking helices. *Nat. Commun.* 13:6930. doi:10.1038/s41467-022-34478-0.

Leaver, M., and J. Errington. 2005. Roles for MreC and MreD proteins in helical growth of the cylindrical cell wall in Bacillus subtilis. *Mol. Microbiol.* 57:1196–1209. doi:10.1111/j.1365-2958.2005.04736.x.

Lin, L., and M. Thanbichler. 2013. Nucleotide-independent cytoskeletal scaffolds in bacteria. *Cytoskeleton.* 70:409–423. doi:10.1002/cm.21126.

Lovering, A.L., S.S. Safadi, and N.C.J. Strynadka. 2012. Structural Perspective of Peptidoglycan Biosynthesis and Assembly. *Annu. Rev. Biochem.* 81:451–478. doi:10.1146/annurev-biochem-061809-112742.

Marais, A., J.M. Bove, and J. Renaudin. 1996. Characterization of the recA gene regions of Spiroplasma citri and Spiroplasma melliferum. *J. Bacteriol.* 178:7003–7009.

- Martin, N.R., E. Blackman, B.P. Bratton, K.J. Chase, T.M. Bartlett, and Z. Gitai. 2021. CrvA and CrvB form a curvature-inducing module sufficient to induce cell-shape complexity in Gram-negative bacteria. *Nat. Microbiol.* 6:910–920. doi:10.1038/s41564-021-00924-w.
- Masson, F., X. Pierrat, B. Lemaitre, and A. Persat. 2021. The wall-less bacterium *Spiroplasma poulsonii* builds a polymeric cytoskeleton composed of interacting MreB isoforms. *iScience.* 24:103458. doi:10.1016/j.isci.2021.103458.
- Mauriello, E.M.F., F. Mouhamar, B. Nan, A. Ducret, D. Dai, D.R. Zusman, and T. Mignot. 2010. Bacterial motility complexes require the actin-like protein, MreB and the Ras homologue, MglA. *EMBO J.* 29:315–326. doi:10.1038/emboj.2009.356.
- Miyata, M., R.C. Robinson, T.Q.P. Uyeda, Y. Fukumori, S. Fukushima, S. Haruta, M. Homma, K. Inaba, M. Ito, C. Kaito, K. Kato, T. Kenri, Y. Kinoshita, S. Kojima, T. Minamino, H. Mori, S. Nakamura, D. Nakane, K. Nakayama, M. Nishiyama, S. Shibata, K. Shimabukuro, M. Tamakoshi, A. Taoka, Y. Tashiro, I. Tulum, H. Wada, and K. Wakabayashi. 2020. Tree of motility – A proposed history of motility systems in the tree of life. *Genes Cells.* 25:6–21. doi:10.1111/gtc.12737.
- Mogilner, A., and G. Oster. 2003. Polymer motors: pushing out the front and pulling up the back. *Curr. Biol. CB.* 13:R721-733. doi:10.1016/j.cub.2003.08.050.
- Pande, V., N. Mitra, S.R. Bagde, R. Srinivasan, and P. Gayathri. 2022. Filament organization of the bacterial actin MreB is dependent on the nucleotide state. *J. Cell Biol.* 221:e202106092. doi:10.1083/jcb.202106092.
- de Pedro, M.A., J.C. Quintela, J.V. Höltje, and H. Schwarz. 1997. Murein segregation in *Escherichia coli*. *J. Bacteriol.* 179:2823–2834. doi:10.1128/jb.179.9.2823-2834.1997.
- Royet, J., D. Gupta, and R. Dziarski. 2011. Peptidoglycan recognition proteins: modulators of the microbiome and inflammation. *Nat. Rev. Immunol.* 11:837–851. doi:10.1038/nri3089.
- Salje, J., F. van den Ent, P. de Boer, and J. Löwe. 2011. Direct Membrane Binding by Bacterial Actin MreB. *Mol. Cell.* 43:478–487. doi:10.1016/j.molcel.2011.07.008.
- Sasajima, Y., T. Kato, T. Miyata, A. Kawamoto, K. Namba, and M. Miyata. 2022. Isolation and structure of the fibril protein, a major component of the internal ribbon for *Spiroplasma* swimming. *Front. Microbiol.* 13.

Sasajima, Y., and M. Miyata. 2021. Prospects for the Mechanism of Spiroplasma Swimming. *Front. Microbiol.* 12:706426. doi:10.3389/fmicb.2021.706426.

Scheffers, D.-J., and M.G. Pinho. 2005. Bacterial Cell Wall Synthesis: New Insights from Localization Studies. *Microbiol. Mol. Biol. Rev.* 69:585–607. doi:10.1128/MMBR.69.4.585-607.2005.

Shaevitz, J.W., J.Y. Lee, and D.A. Fletcher. 2005. Spiroplasma Swim by a Processive Change in Body Helicity. *Cell.* 122:941–945. doi:10.1016/j.cell.2005.07.004.

Shi, H., B.P. Bratton, Z. Gitai, and K.C. Huang. 2018. How to Build a Bacterial Cell: MreB as the Foreman of E. coli Construction. *Cell.* 172:1294–1305. doi:10.1016/j.cell.2018.02.050.

Shih, Y.-L., T. Le, and L. Rothfield. 2003. Division site selection in Escherichia coli involves dynamic redistribution of Min proteins within coiled structures that extend between the two cell poles. *Proc. Natl. Acad. Sci.* 100:7865–7870. doi:10.1073/pnas.1232225100.

Sichel, S.R., B.P. Bratton, and N.R. Salama. 2022. Distinct regions of H. pylori's bactofilin CcmA regulate protein–protein interactions to control helical cell shape. *eLife.* 11:e80111. doi:10.7554/eLife.80111.

Swulius, M.T., S. Chen, H. Jane Ding, Z. Li, A. Briegel, M. Pilhofer, E.I. Tocheva, S.R. Lybarger, T.L. Johnson, M. Sandkvist, and G.J. Jensen. 2011. Long helical filaments are not seen encircling cells in electron cryotomograms of rod-shaped bacteria. *Biochem. Biophys. Res. Commun.* 407:650–655. doi:10.1016/j.bbrc.2011.03.062.

Szwedziak, P., and J. Löwe. 2013. Do the divisome and elongasome share a common evolutionary past? *Curr. Opin. Microbiol.* 16:745–751. doi:10.1016/j.mib.2013.09.003.

Takahashi, D., I. Fujiwara, and M. Miyata. 2020. Phylogenetic origin and sequence features of MreB from the wall-less swimming bacteria Spiroplasma. *Biochem. Biophys. Res. Commun.* 533:638–644. doi:10.1016/j.bbrc.2020.09.060.

Takahashi, D., M. Miyata, and I. Fujiwara. 2023. Assembly properties of Spiroplasma MreB involved in swimming motility. 2023.01.26.525654. doi:10.1101/2023.01.26.525654.

Taylor, J.A., B.P. Bratton, S.R. Sichel, K.M. Blair, H.M. Jacobs, K.E. DeMeester, E. Kuru, J. Gray, J. Biboy, M.S. VanNieuwenhze, W. Vollmer, C.L. Grimes, J.W. Shaevitz, and N.R.

Salama. 2020. Distinct cytoskeletal proteins define zones of enhanced cell wall synthesis in *Helicobacter pylori*. *eLife*. 9:e52482. doi:10.7554/eLife.52482.

Taylor, J.A., S.R. Sichel, and N.R. Salama. 2019. Bent Bacteria: A Comparison of Cell Shape Mechanisms in Proteobacteria. *Annu. Rev. Microbiol.* 73:457–480. doi:10.1146/annurev-micro-020518-115919.

van Teeffelen, S., S. Wang, L. Furchtgott, K.C. Huang, N.S. Wingreen, J.W. Shaevitz, and Z. Gitai. 2011. The bacterial actin MreB rotates, and rotation depends on cell-wall assembly. *Proc. Natl. Acad. Sci.* 108:15822–15827. doi:10.1073/PNAS.1108999108.

Tiyanont, K., T. Doan, M.B. Lazarus, X. Fang, D.Z. Rudner, and S. Walker. 2006. Imaging peptidoglycan biosynthesis in *Bacillus subtilis* with fluorescent antibiotics. *Proc. Natl. Acad. Sci.* 103:11033–11038. doi:10.1073/pnas.0600829103.

Townsend, R., D.B. Archer, and K.A. Plaskitt. 1980. Purification and preliminary characterization of *Spiroplasma fibrils*. *J. Bacteriol.* 142:694–700. doi:10.1128/jb.142.2.694-700.1980.

Townsend, R., P.G. Markham, K.A. Plaskitt, and M.J. Daniels. 1977. Isolation and Characterization of a Non-Helical Strain of *Spiroplasma citri*. *J. Gen. Microbiol.* 100:15–21. doi:10.1099/00221287-100-1-15.

Trachtenberg, S., L.M. Dorward, V.V. Speransky, H. Jaffe, S.B. Andrews, and R.D. Leapman. 2008. Structure of the Cytoskeleton of *Spiroplasma melliferum* BC3 and Its Interactions with the Cell Membrane. *J. Mol. Biol.* 378:778–789. doi:10.1016/j.jmb.2008.02.020.

Treuner-Lange, A., E. Macia, M. Guzzo, E. Hot, L.M. Faure, B. Jakobczak, L. Espinosa, D. Alcor, A. Ducret, D. Keilberg, J.P. Castaing, S. Lacas Gervais, M. Franco, L. Søggaard-Andersen, and T. Mignot. 2015. The small G-protein MglA connects to the MreB actin cytoskeleton at bacterial focal adhesions. *J. Cell Biol.* 210:243–256. doi:10.1083/jcb.201412047.

Typas, A., M. Banzhaf, C.A. Gross, and W. Vollmer. 2011. From the regulation of peptidoglycan synthesis to bacterial growth and morphology. *Nat. Rev. Microbiol.* 10:123–136. doi:10.1038/nrmicro2677.

Ursell, T.S., J. Nguyen, R.D. Monds, A. Colavin, G. Billings, N. Ouzounov, Z. Gitai, J.W. Shaevitz, and K.C. Huang. 2014. Rod-like bacterial shape is maintained by feedback between cell curvature and cytoskeletal localization. *Proc. Natl. Acad. Sci.* 111:E1025–E1034. doi:10.1073/pnas.1317174111.

Vera-Ponce León, A., M. Dominguez-Mirazo, R. Bustamante-Brito, V. Higareda-Alvear, M. Rosenblueth, and E. Martínez-Romero. 2021. Functional genomics of a Spiroplasma associated with the carmine cochineals *Dactylopius coccus* and *Dactylopius opuntiae*. *BMC Genomics.* 22:240. doi:10.1186/s12864-021-07540-2.

Veyrier, F.J., N. Biais, P. Morales, N. Belkacem, C. Guilhen, S. Ranjeva, O. Sismeiro, G. Péhau-Arnaudet, E.P. Rocha, C. Werts, M.-K. Taha, and I.G. Boneca. 2015. Common Cell Shape Evolution of Two Nasopharyngeal Pathogens. *PLOS Genet.* 11:e1005338. doi:10.1371/journal.pgen.1005338.

Wachi, M., M. Doi, S. Tamaki, W. Park, S. Nakajima-Iijima, and M. Matsushashi. 1987. Mutant isolation and molecular cloning of mre genes, which determine cell shape, sensitivity to mecillinam, and amount of penicillin-binding proteins in *Escherichia coli*. *J. Bacteriol.* 169:4935–4940. doi:10.1128/jb.169.11.4935-4940.1987.

Wagstaff, J., and J. Löwe. 2018. Prokaryotic cytoskeletons: Protein filaments organizing small cells. *Nat. Rev. Microbiol.* 16:187–201. doi:10.1038/nrmicro.2017.153.

Williamson, D.L. 1974. Unusual Fibrils from the Spirochete-Like Sex Ratio Organism. *J. Bacteriol.* 117:904–906.

Yang, D.C., K.M. Blair, and N.R. Salama. 2016. Staying in Shape: the Impact of Cell Shape on Bacterial Survival in Diverse Environments. *Microbiol. Mol. Biol. Rev. MMBR.* 80:187–203. doi:10.1128/MMBR.00031-15.

Zimmerberg, J., and M.M. Kozlov. 2006. How proteins produce cellular membrane curvature. *Nat. Rev. Mol. Cell Biol.* 7:9–19. doi:10.1038/nrm1784.

Chapter 2: Standardization of purification and structure determination of ScMreB5

Some sections reprinted from: Pande et al., *Journal of Cell Biology*

DOI: [10.1083/jcb.202106092](https://doi.org/10.1083/jcb.202106092)

2.1: Introduction

Structure determination for MreBs has been limited until now due to difficulties in the purification of the monomeric entity of MreBs. Around two decades back, the first structure of MreB was determined from a hyperthermophilic bacteria, *Thermotoga maritima* (van den Ent et al., 2001). Structures of two conformational states were determined, namely apo and AMP-PNP bound *T. maritima* MreB (TmMreB). The crystal packing of both structures displayed a single protofilament assembly. The structures confirmed the well-conserved nucleotide binding pocket for MreB, which was same as other hsp70 families of proteins (eg., actins). Despite having a sequence similarity of less than 25 %, TmMreB displayed a remarkable structural similarity with actin, having four domains (IA, IB, IIA, and IIB) and a conserved nucleotide-binding pocket.

A decade later from the first structure determination, the second MreB structure was determined from a Gram-negative bacterium, *Caulobacter crescentus* (van den Ent et al., 2014). Multiple structures of *C. crescentus* MreB (CcMreB) were solved. These structures were different in their nucleotide-bound state, oligomeric state, etc. Importantly, the crystal structure of CcMreB also revealed the antiparallel double protofilament assembly of MreB. This double protofilament assembly has been observed under cryo-EM earlier (Salje et al., 2011). From the structure, it was confirmed that the antiparallel arrangement of the MreB filament exposes the membrane-binding regions of both filaments on the same side of the protein. A mechanism of structural changes during polymerization was also shown from CcMreB crystal structures that captured the monomeric and polymeric state of the protein in ADP and AMP-PNP bound states. Interestingly, small structural changes at the nucleotide-binding pocket could trigger CcMreB polymerization.

By comparing the monomeric ADP bound structure with the AMP-PNP (ATP analog) bound structure of CcMreB, an initial closure of the domain was observed upon AMP-PNP binding (van den Ent et al., 2014). In a functional double protofilament state, the subdomain IB undergoes a rotation towards the nucleotide-binding cleft that leads to domain closure. This is accompanied by a twist between IA and IIA domains. Interestingly, by comparing monomeric CcMreB AMP-PNP and double protofilament CcMreB AMP-PNP nucleotide-binding pocket, the catalytic residues Glu140 can only coordinate with the catalytic water in the double protofilament state. Thus, the transition from a monomeric state to a double protofilament

polymeric state of MreB facilitates small changes at the nucleotide-binding pocket that positions the catalytic residues to trigger ATP hydrolysis.

Structure determination of MreB from different bacteria is important to understand how the mechanism of polymerization, ATP hydrolysis, and membrane binding differs within bacteria. *Spiroplasma* is a cell-wall-less bacteria, having five homologs of MreB, with varying sequence identities among them (Sasajima and Miyata, 2021; Harne et al., 2020) . Structure determination of these MreB can help in understanding similar and contrasting features of MreB from a cell-walled bacteria. This chapter discusses the over-expression and purification optimization of three out of five of the *S.citri* MreBs. These are ScMreB3^{WT}, ScMreB4^{ΔN} and ScMreB5^{WT}. Out of these three MreBs, the purification of ScMreB5 could be standardized optimally. The structure determination using X-ray crystallography for ScMreB5 in different nucleotide states was further carried out. ScMreB5 characterization is further followed in the course of my Ph.D.

2.2: Materials and Methods

2.2.1: Cloning of ScMreB3^{WT}, ScMreB4^{ΔN}, ScMreB5^{WT} and its mutants:

All *S.citri* *mreB* genes (Uniprot IDs: *mreb3*, Q8VQG3; *mreb4*, Q8VQG3 and *mreb5*, Q8VQG1) were amplified from the genomic DNA (21833; DSMZ) using the primers listed in Table 2.1. The amplified products were cloned into the pHis17 vector (Addgene catalog #78202) between the restriction sites, NdeI and BamHI. Cloning from genomic DNA into pHis17 vector for ScMreB3^{WT}, ScMreB4^{WT} and ScMreB5^{WT} was done by Saket Bagde and Varun Prasad (BS-MS students). The method of restriction-free cloning was used for the same (van den Ent and Löwe, 2006) The resulting constructs have the hexahistidine tag GSHHHHHH at the C-terminal end after the last residue. All the single and double ScMreB5 and ScMreB4 single and double mutants were cloned in the same manner. The list of all the clones generated are given in Table 2.1.

Table 2.1: List of primers and clones

Primer name	Sequence (‘5 → 3’)	Clones generated using the primers (Vector-construct name)
ScM5-f	CTTTAAGAAGGAGATATACATATGAG ACCAGAAACTAGACCATTTATTTC	pHis17-ScMreB5 ^{WT}
ScM5H6-r	GATGATGATGATGATGGGATCCTTTT CTTTTTTTACCTAATGTTGATAATAAT CC	
ScM5W-f	GAATGAAAATGATGAACATTTGGAA GAATGCTATTG	
ScM5-k57a-f	CTATGATATGGTAGGAGCAACACACG GAGATATTAG	pHis17-ScMreB5 ^{K57A}
ScM5-D156-f	GGTCATTTAATCATTGCTATCGGTGG AGGAACAAC	pHis17-ScMreB5 ^{D156A}
ScM5-E134-f	GTTATCATTGAAGAAGCGGCTAAAAT GGCCG	pHis17-ScMreB5 ^{E134A} pRep-ScMreB5 ^{E134A} - NGFP
D12A-f	CCAGAACTAGACCATTTATTTCTCT TGCGTTAGGAACTGCTAATG	pHis17-ScMreB5 ^{D12A}
ScM5-D70-f	GGTAACACCATTAGTAGCGGGAGTTA TCGCAGACATGGAAGCTGCAC	pHis17-ScMreB5 ^{D70A}
ScM5-T161A-f	GGTGGAGGAGCGACTGATTTAGCTAT TATTCATCAGGTG	pHis17-ScMreB5 ^{T161A}
M5-I95A	CAAGAATGAAAATGATGAACGCGTG GAAGAATGCTATTGTATTATTAGC	pHis17-ScMreB5 ^{I95A}
M5-W96A	CAAGAATGAAAATGATGAACATTGC GAAGAATGCTATTGTATTATTAGC	pHis17-ScMreB5 ^{W96A}
M5-IWA	CAAGAATGAAAATGATGAACGCCGC GAAGAATGCTATTGTATTATTAGC	pHis17-ScMreB5 ^{IWA}
ScM5Ct10 del-r	GCTTTTAATGATGATGATGATGATGG GATCCTTTTTCTTGAAAATTATATAA ACC	pHis17-ScMreB5 ^{ΔC10} (Residue range: 326- 335; ‘LLSTLGKKRK’ deleted)
ScM4_del_Nt 7-f	GTTTAACTTTAAGAAGGAGATATACA TATGAAAAAACC GGCTTTCGTTTCTA TGG	pHis17-ScMreB4 ^{ΔN} (Residue range: 2-6; ‘ALFNSA’ deleted)
ScM4-H6-R	GATGATGATGATGATGGGATCCGTAA TTTAATTCCTTTACATGCATTG	
ScM3-F	CTTTAAGAAGGAGATATACATATGGC AATATCAGACGTATTG	
ScM3-H6-R	GATGATGATGGGATCCTCTATTTTTTT TGTTTTTC	pHis17-ScMreB3 ^{WT}
ScM3W-f	CAAAGGTAGCTGATTTATGGAAAAAT GCTATTGTT	

2.2.2: Expression Check and Purification of ScMreB5^{WT}

ScMreB5 wildtype and the mutant constructs cloned in pHis 17 vectors were transformed in the BL21AI strain (Stratagene) of *E.coli*. In the pHis17 vector, the gene of interest to be overexpressed is under the T7 promoter. In the BL21AI strain, the T7 polymerase expression is under the tight regulation of *araBAD* operon (Narayanan et al., 2011). Inducing the transformed culture of BL21AI cells with L-arabinose will lead to overexpression of our gene of interest.

Heat shock method was used to transform the plasmid of wildtype ScMreB5 and its mutant clones into BL21AI cells and spread on LB Agar plate containing ampicillin as the antibiotic. The plate was incubated for 12 hrs at 37 °C. A small culture expression check was performed for checking the overexpression and protein solubility. 3 – 5 colonies were inoculated in 10 mL of LB broth containing 100 µg/mL of ampicillin and incubated under shaking conditions at 37 °C. Once the OD₆₀₀ reached between 0.8 – 1.0, 5 mL of culture was induced with 0.2 % arabinose, The other 5 mL was used as an uninduced culture. Both, the induced culture and uninduced culture were incubated under shaking conditions at 18 °C for 12 hrs. This optimized condition gave the optimal protein expression and solubility. For checking the overexpression and solubility, 5 mL of the induced and the uninduced culture was pelleted down. The pellets were resuspended in 500 µL of the lysis buffer (200 mM NaCl, 50 mL Tris pH 8, and 10% glycerol). Both the resuspensions were sonicated using a probe sonicator (Total time - 1 min; 1 sec ON, 3 sec OFF; 60% Amplitude). Lysed samples from the induced and uninduced were taken out for the gel as the total lysate. The lysates was spun down at 22,000 xg at 4 °C for 20 mins, to obtain the supernatant which contains the soluble fraction of the lysate. The total lysate and supernatant samples were taken for sample preparation for SDS-PAGE. The lysate and the soluble fractions from the induced and the uninduced cultures were loaded onto 12% SDS-PAGE gel. The overexpressed bands from the induced culture (lysate and soluble fractions) were identified.

For purification, 2 L culture of ScMreB5 expressed in BL21AI cells was grown under the conditions as described above. The culture was pelleted down at 4000 xg and the pellet was stored at -80 °C until further use. The pellet was thawed and cells were homogenized in lysis buffer (200 mM NaCl, 50 mM Tris, pH 8, and 10% glycerol) and sonicated (total time - 2 min; 1 sec ON, 3 secs OFF; 60% amplitude, 2 cycles). The lysate was centrifuged at 44,082 xg for 45 mins, 4 °C in JA 25.5 rotor. The supernatant was loaded on a 5 mL Ni-NTA column (HisTrap, GE Healthcare) pre-equilibrated with buffer A (50 mM Tris pH 8, 200 mM NaCl). Hexa-histidine tag present in the C-terminus of the protein facilitated binding to the

Ni-NTA column. Bound protein was eluted using a step gradient of 5 %, 10 %, 20 %, 50 %, and 100 % of buffer B (50 mM Tris pH 8, 200 mM NaCl, and 500 mM imidazole). Fractions containing the purest protein were identified using 12 % SDS-PAGE gel. 1 mM ADP and 1 mM MgCl₂ (final concentrations) were added to those fractions to minimize protein precipitation. The protein was concentrated in 10 kDa molecular weight cut-off concentrators (Sartorius). Imidazole was removed in buffer exchange while concentrating. The final buffer for the protein was 50 mM Tris pH 8, 50 mM NaCl, 1 mM ADP, and 1 mM MgCl₂. After concentration, the protein was aliquoted, flash-frozen and stored at -80°C until further use. This protein was used for all thermal shift assays (for optimizing purification conditions).

After optimizing the buffer condition for protein stability using the thermal shift assay, purification with the optimized conditions was performed similarly as described with the new optimized buffer conditions. 200 mM NaCl in lysis buffer, buffer A and buffer B was replaced with 300 mM KCl. The protein was either subjected to dialysis or size exclusion chromatography post-affinity chromatography. Dialysis was performed post-Ni-NTA elution for the fractions containing the purified protein against buffer A (50 mM Tris pH 8, 300 mM KCl). Size exclusion was performed using either Superdex 75 or 200, (GE Life Sciences column) which was pre-equilibrated with buffer A (300 mM KCl, 50 mM Tris pH 8). Fractions corresponding to the monomeric peak for the protein (checked by the UV absorbance peak at 280 nm) were collected and checked on the 12 % SDS – PAGE gel for their purity. The protein was further concentrated using a 10 kDa molecular weight cutoff concentrator. Concentrated protein was spun at 22,000 xg at 4 °C, aliquoted, and flash frozen. The protein aliquots were stored at – 80°C (in 10 µL aliquots) until further use. It is important to note that there was no addition of ADP and MgCl₂ at any stage of protein purification. The same protocol was followed for purifying all the mutant constructs of ScMreB5 as well.

Analytical size exclusion was performed using Superdex 75 or 200, (GE Life Sciences column) was performed for the protein batches for which only Ni-NTA was performed. Both the wild type and all the ScMreB5 mutants eluted as pure monomers.

2.2.3: Thermal Shift Assay

The thermal shift assay was performed to determine the optimal buffer condition that increases the protein stability and enables us to purify ScMreB5^{WT} without an excess addition of ADP and MgCl₂. The optimized condition will enable us to use the protein for nucleotide-dependent experiments. In thermal shift assay, the melting temperature (T_m) is determined for the protein

as it undergoes denaturation with increasing temperature (Huynh and Partch, 2015). This melting temperature shifts in the presence of any ligand or buffer as it gets more stabilized or destabilized. This will be the read-out for an increase in protein stability in the given condition. The assay is carried out in a 96-well plate and an RT-PCR machine is used. SYPRO orange dye (excitation of 470 nm and emission at 569 nm) is used as a fluorophore. The data for the change in SYPRO fluorescence emission as it binds to the hydrophobic binding pockets of the protein is collected using the FRET channel (excitation at 450-490 nm and emission at 560-580 nm). The raw data of the first derivative of the melting curve $(-dRFU)/dT$ is plotted against temperature. The apex of the graph corresponds to the melting temperature (T_m) for the protein. (Huynh and Partch, 2015; Cimperman and Matulis, 2011)

For ScMreB5, the reaction was set up in a 96-well PCR plate (Bio-Rad) that was sealed with a micro seal (Bio-Rad). 2.6 μ M of protein (ultracentrifuged at 100,000 xg for 25 mins, 4 °C in TLA 120.2) in a total volume of 25 μ l reaction was used in this assay. This protein was in the final buffer: 50 mM Tris pH 8, 50 mM NaCl, 1 mM ADP, and 1 mM MgCl₂. 2 μ l of 50 X SYPRO Orange (Sigma-Aldrich) was added to the reaction after addition of all the components. After the addition of SYPRO Orange, the reaction in the 96-well plate was sealed. The plate was given a quick spin at 4 °C at 3000 xg, to get the reaction to the bottom of the well. The reaction was set up in a Bio-Rad CFX96 Real-Time System. The plate was first incubated in the machine at 4 °C for 10 mins. Subsequently, readings were taken from a temperature range of 4-90 °C with a rise of 0.4 °C every 20 secs. The readings for different conditions were plotted as discussed before.

2.2.4: Expression Check and Purification of ScMreB3^{WT} and ScMreB4^{AN}

ScMreB3^{WT} and ScMreB4^{AN} constructs cloned in the pHis17 vector were transformed in different bacterial expression strains. These expression strains were: BL21AI, BL21DE3, and Rosetta. The heat shock method of transformation was used as described previously. 2- 3 colonies were inoculated in 10 mL LB media containing ampicillin (100 μ g/mL). 34 μ g/mL chloramphenicol was additionally added for the Rosetta cells. The inoculated cultures were incubated at 37 °C under shaking conditions. Once the OD₆₀₀ reached between 0.6 – 0.8, 5 mL of culture was induced with 0.2 % L-arabinose (for BL21AI cells) and 0.5 mM IPTG (for BL21DE3 and Rosetta cells). Post induction, the cultures were incubated under shaking conditions at 18°C for 12 hrs. The expression check for these cultures was performed in the same way as described for ScMreB5. For expression check standardization, different post-

induction temperatures and varying concentrations of arabinose and IPTG were tried similarly. Rosetta strain gave better overexpression for ScMreB3 as well as ScMreB4^{ΔN} (post-induction temperature 18°C), but no solubility was observed. Hence, a detergent screen was performed. Different detergents were incorporated in lysis buffer (300 mM KCl, 50 mM Tris pH 8), such as CHAPS (3-((3-cholamidopropyl) dimethylammonio) -1-propanesulfonate), LSS (N-Lauroyl Sarcosine sodium) and SDC (Sodium Deoxycholate). LSS detergent-solubilized both the proteins, therefore LSS condition was further standardized. Different concentrations of LSS, which has a critical micellar concentration of 14 mM, (1 mM, 3 mM, 5 mM, 10 mM, and 14 mM) were tried for both constructs. The expression check was performed as described previously.

For purifying ScMreB3^{WT}, 2 L transformed Rosetta cell culture was grown. The purification was carried out in the same manner, as described for ScMreB5, the only difference being, the lysis buffer had LSS (50 mM Tris pH 8, 300 mM KCl, 10 % glycerol and 5 mM LSS). Affinity chromatography followed by size exclusion chromatography using Superdex 200 column (using optimized buffer condition of ScMreB5) was performed. The entire protein eluted in the void fraction (checked by the UV absorbance peak at 280 nm) of the column.

2.2.5: Crystallization of ScMreB5

Crystallization trials were attempted for ScMreB5 ADP and AMP-PNP bound states. For both, about 960 conditions of commercially available screens (Molecular dimensions, Hampton Research) were screened, using drop sizes containing 100 nL of protein (4 - 5 mg/mL) and 100 nL of crystallization condition. Initial hits were seen for some of the conditions and were further optimized to get a well-diffracting crystal. Conditions in which well-diffracting crystals were obtained for ScMreB5 (ADP and AMP-PNP) are listed in Table 2.2. The concentration of nucleotide and MgCl₂ used for crystallization was 2 mM each. Crystals were frozen in 20 % glycerol cryoprotectant with the parent conditions in which the crystals were obtained.

Table 2.2: Crystallization conditions of ScMreB5 in different nucleotide states

	ScMreB5 – ADP	ScMreB5 – AMPPNP
Method	Hanging drop Vapour diffusion	Sitting drop Vapour diffusion
Plate Type	24 well	48 well
Temperature (K)	291	291
Construct and Protein concentration	ScMreB5- H6 (5 mg/mL)	ScMreB5- H6 (4 mg/mL)
Buffer composition of protein	200 mM NaCl, 50 mM Tris pH8, 2 mM ADP, 2 mM MgCl ₂	300 mM KCl, 50 mM Tris pH 8, 2 mM AMPPNP, 2 mM MgCl ₂
Composition of reservoir solution	0.15 M Na-K phosphate and 16% PEG 3350, pH 7.8	0.15 M Na-K phosphate and 16% PEG 3350, pH 7.8
Volume and ratio of drop (μL: μL)	1:1	1:1
Volume of the reservoir (mL)	0.5 mL	0.1 mL

2.2.6: Structure determination of ScMreB5

Data for ScMreB5-ADP was collected at the home source, Rigaku MicroMax-007 HF. Crystal diffracted till 2.3 Å. Data reduction was performed using IMOSFLM (Battye et al., 2011), scaling using AIMLESS (Evans and Murshudov, 2013) followed by molecular replacement using PHASER (McCoy et al., 2007). ScMreB5-ADP bound structure was solved using *C.crescentus* MreB (PDB ID- 4CZI) for molecular replacement. All these programs are available in the CCP4 package (Evans and Murshudov, 2013; Potterton et al., 2018). Refinement was carried out in PHENIX (Adams et al., 2010) package and model building was done in *Coot* (Emsley et al., 2010). For ScMreB5- AMPPNP, data was collected at ESRF. Data reduction was performed using DIALS (Winter et al., 2018) and data scaling using AIMLESS (Evans and Murshudov, 2013) in CCP4i2 (Potterton et al., 2018) package.

Figure 2.1: Expression check profiles of a ScMreBs.

(A) Expression check profile of ScMreB3^{WT} and ScMreB4^{ΔN} in the presence of different concentrations of LSS detergent. Both the constructs were expressed in Rosetta bacterial strain. (B) Expression check profile of ScMreB5 expressed in BL21AI cells. “T” corresponds to induced lysate and “S” corresponds to the induced supernatant.

2.3.2: Purification condition optimization of ScMreBs

Purification of ScMreB3^{WT}: ScMreB3^{WT} was purified in the presence of LSS in lysis buffer (300 mM KCl, 50 mM Tris pH8, 10 % glycerol and 5 mM LSS (Fig 2.2 A). The protein came in the void fraction of Superdex 200 (Fig 2.2 B) along with some level of degradation and impurities. This protein could not be used for any biochemical and structural studies. Further standardization of ScMreB3^{WT} purification optimization is to be carried out.

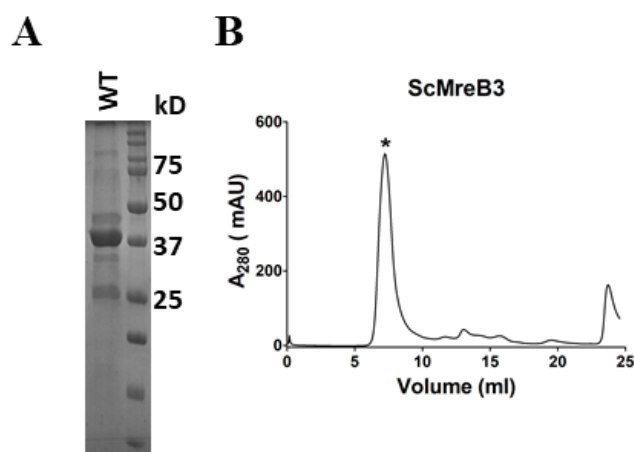


Figure 2.2: Purification of ScMreB3^{WT}.

(A) 12 % SDS-PAGE gel profile of the purified protein post-gel filtration. (B) Superdex 200 gel filtration profile of ScMreB3^{WT}. The protein undergoes degradation post purification as seen from the gel.

Purification optimization of ScMreB5^{WT}: All the constructs of ScMreB5 – H6 were purified using two steps of purification, affinity chromatography followed by size exclusion chromatography. Earlier in the lab ScMreB5 purification was carried out in the presence of an excess of ADP and MgCl₂ (1 mM) in the buffer. The addition of ADP helped in decreasing the amount of precipitation while the protein undergoes concentration. This helped in reducing the amount of precipitation, which otherwise would lead to heavy

precipitation and poor protein yield at the end of purification. But, even this condition would not yield enough protein, and the presence of ADP would hamper the biochemical assays to monitor ATPase activity. Thus, optimization for ScMreB5 purification was carried out. Series of thermal shift assay were performed to determine the optimal buffer condition for protein purification. In a 96-well PCR plate, 2.6 μ M protein was mixed with the buffer conditions to be tested. SYPRO orange was used as a fluorophore that binds to the exposed hydrophobic pockets of the protein as it undergoes denaturation with an increase in temperature. This assay measures the T_m of the protein. When any additive such as salts, buffer, ligand, etc is added to the reaction, the protein changes T_m , which is a readout of the effect of the additive added to the reaction. Different buffer, salt, and pH conditions were tested in this assay.

Changing the salt from NaCl to KCl clearly showed an increase in T_m of around 10 °C with KCl at different salt concentrations (Fig 2.3 A). Finally, a combination of 50 mM Tris pH 8 and 300 mM KCl was chosen as the optimized condition. The protein was purified in this condition without the addition of ADP and MgCl₂. The yield of protein increased from 2 mg to 8 mg from a 2 L of culture pellet. This indicated that the presence of KCl as the salt in the buffer condition increased the solubility to a greater extent such that the overall yield of purification increased. The purified protein was eluted as a homogenous monomeric fraction in the size exclusion chromatography (Fig 2.4 B). Thermal shift assay for the protein in KCl-containing buffer was performed with ADP/ATP and without any nucleotide. The T_m of protein in the absence of nucleotide was around 30 °C and the presence of nucleotide increased the T_m around 47°C for either ADP or ATP addition (Fig. 2.3 C). Thus, as expected, the presence of nucleotide increased the stability of the protein. Additionally, the purified ScMreB5 in the KCl-containing buffer also came bound with ADP as observed from the HPLC (Fig 2.3 D). We further quantified the percentage of bound ADP in the 97 % of the protein had bound ADP. Thus, ScMreB5^{WT} had eluted in the ADP bound state (Fig 2.3 E, Table 2.3 and Table 2.4).

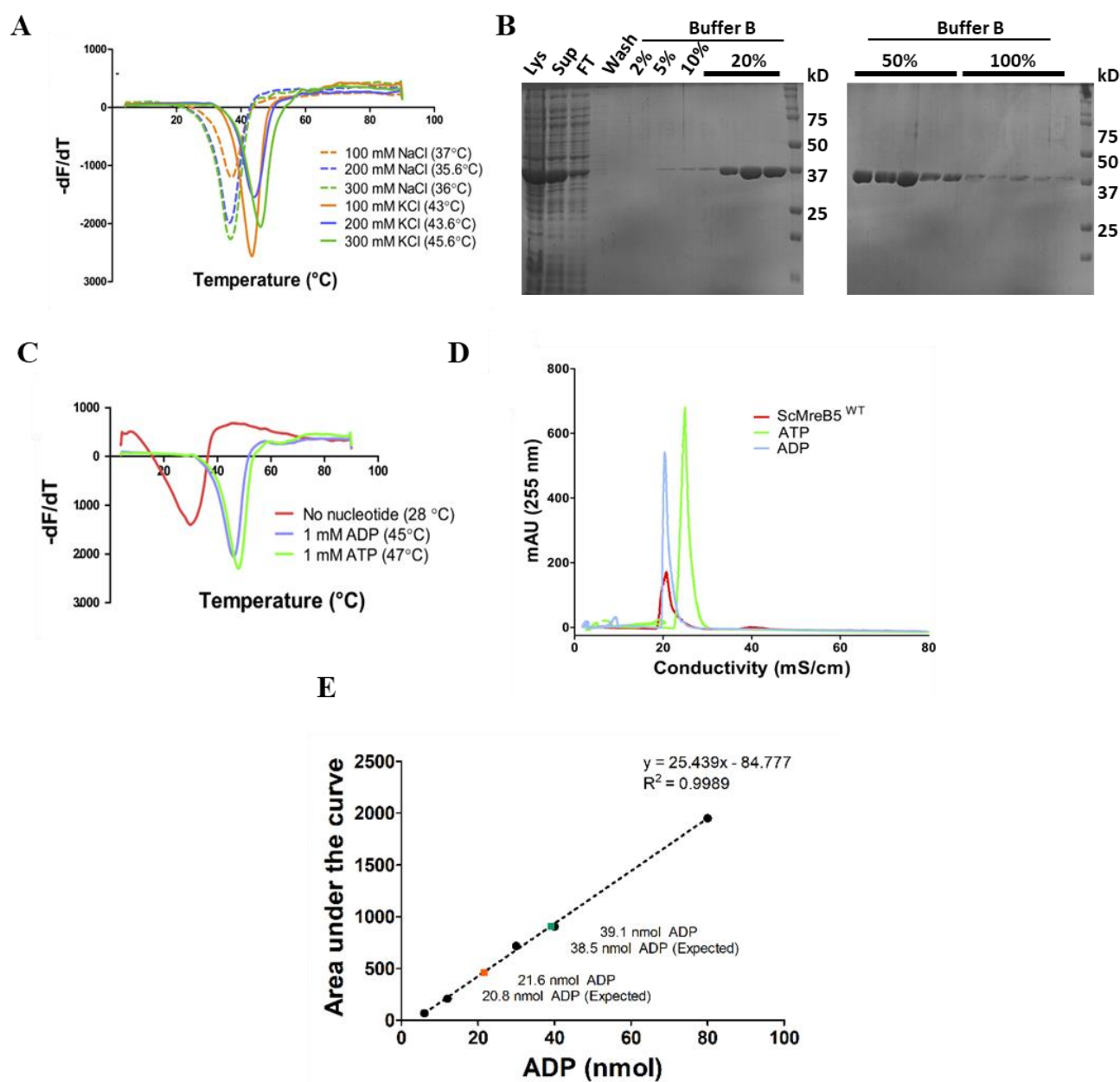


Figure 2.3: Purification optimization for ScMreB5^{WT}.

(A) Melting curve for ScMreB5^{WT} showing T_m for varying concentrations (orange, 100 mM; purple, 200 mM; and green, 300 mM) of NaCl (dotted line) and KCl (solid line). (B) Ni-NTA purification profile of ScMreB5^{WT} purified in the presence of KCl in the buffer. (C) Melting curve for ScMreB5 showing T_m of ScMreB5 without any nucleotide (red), 1 mM ADP (blue), and 1 mM ATP (green). (D) HPLC profile of the supernatant of the denatured ScMreB5^{WT} protein (20 nmol) (red), ADP (blue), and ATP (green). The concentration of nucleotide used in the run was 40 nmol. (E) Standard curve for ADP (in nmol) for determining the unknown ADP concentration from the denatured protein samples (orange, and green points are the two batches of the ScMreB5^{WT} protein).

Table 2.3: Calculations for ADP standards for the plot (in Figure 2.3 E)

ADP (μM)	Volume (μL)	ADP (nmol)	Area under the curve
15	400	6	67.9
30	400	12	209
75	400	30	717
100	400	40	904
200	400	80	1952

Table 2.4: Calculations for determining the percentage of bound ADP

S.No	ScMreB5 ^{WT} (μM)	Volume (μL)	Protein (nmol)	Area under the curve	Bound ADP (nmol)	Protein (nmol)/ADP (nmol)	% Bound ADP
1	55	700	38.5	910.2	39.12	0.983	98.3%
2	99.3	210	20.8	464	21.6	0.963	96.3%

Like ScMreB5^{WT}, all the ScMreB5 mutants were purified in the same manner (Fig 2.4 A). All of the mutants eluted as a monomer as observed from the gel filtration profile of the constructs (Fig 2.4 B and C).

2.3.3: Crystallization and structure determination of ScMreB5

We went ahead to solve the crystal structure of ScMreB5^{WT} in the two nucleotide-bound states ADP and AMP-PNP. Crystallization and X-ray diffraction of ScMreB5^{WT} in the presence of ADP was earlier done in the lab with the protein purified in the presence of excess ADP by Saket. Crystallization of ScMreB5^{WT} in the presence of an excess of AMP-PNP was done with the protein purified in the optimized buffer condition (KCl-containing buffer). Both conditions gave needle-shaped crystals. The crystals of ADP and AMP-PNP ScMreB5^{WT} diffracted to 2.3 Å and 2.5 Å respectively. The data collection table and refinement statistics are provided in the Table 2.5. Calculation of Mathews coefficient indicated the presence of a single molecule in the asymmetric unit in both conditions. After scaling of diffraction data, the structure solution was obtained by molecular replacement using PHASER using MreB from *C. crescentus* (PDB ID: 4CZI).

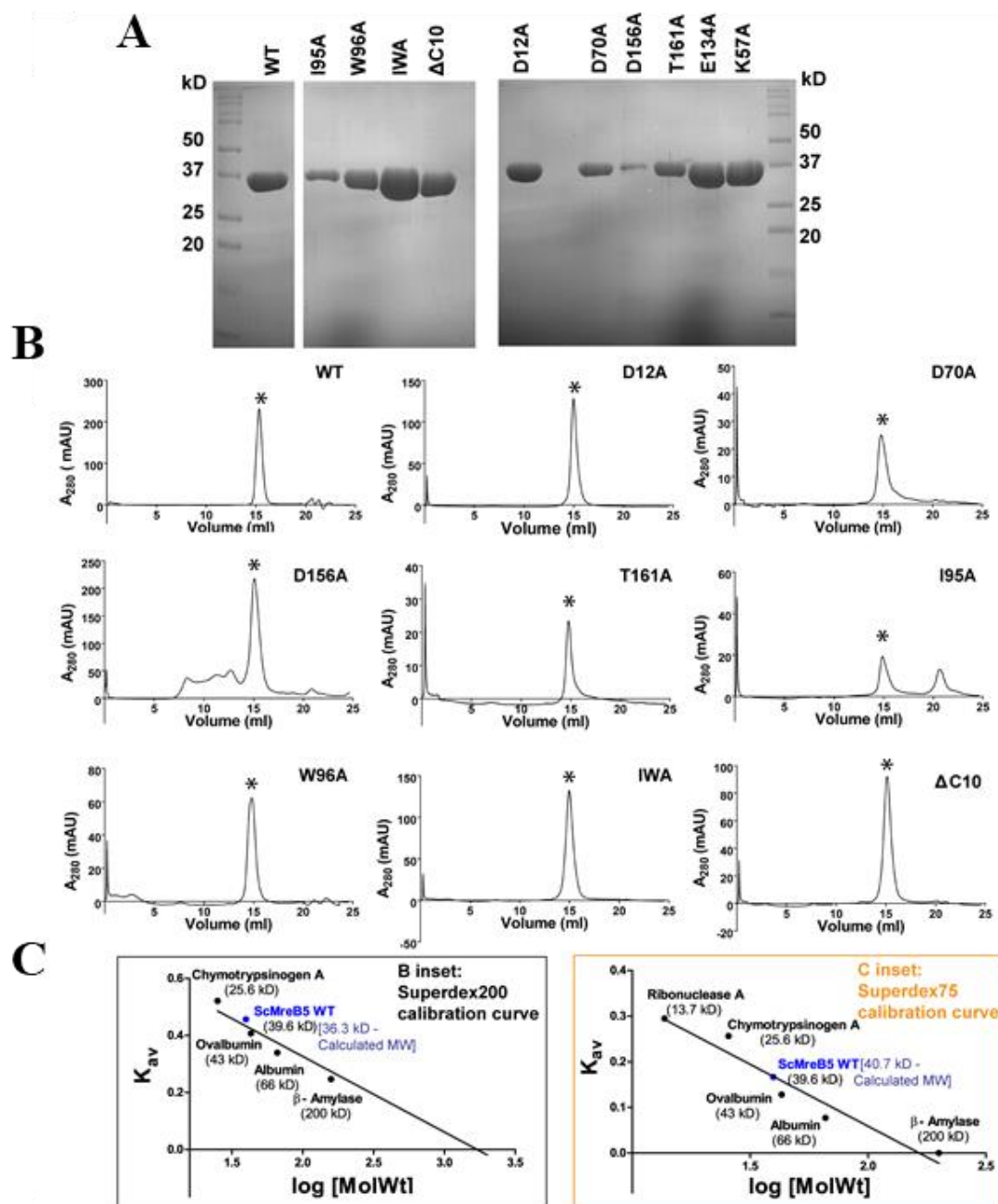


Figure 2.4: ScMreB5^{WT} and its mutants are well folded and elute as monomers.

(A) Representative gels of 12 % SDS-PAGE profile of purified protein samples of ScMreB5^{WT} and the mutant constructs. (B) Analytical size-exclusion chromatography using Superdex 200 for ScMreB5^{WT} (WT); ATPase mutants ScMreB5^{D12A}, ScMreB5^{D70A}, ScMreB5^{D156A}, and ScMreB5^{T161A} (D12A, D70A, D156A, and T161A); and membrane-binding mutants ScMreB5^{I95A}, ScMreB5^{W96A}, ScMreB5^{IWA}, and ScMreB5^{ΔC10A} (I95A, W96A, IWA, and ΔC10) in buffer A (300 mM KCl and 50 mM Tris, pH 8.0) shows a single peak corresponding to monomeric ScMreB5, molecular weight ~38 kD. Peaks (milli absorbance unit [mAU])

corresponding to monomeric protein are marked with asterisk (*). B inset: Calibration curve for size-exclusion chromatography for Superdex 200 using molecular weight standards. The theoretical and estimated molecular weights of ScMreB5^{WT} monomer are mentioned. (C) Size-exclusion chromatography using Superdex 75 for ScMreB5 ATPase mutant ScMreB5^{E134A} (E134A); polymerization mutant ScMreB5^{K57A} (K57A), and ScMreB5 (WT) in buffer A (300 mM KCl and 50 mM Tris, pH 8.0) shows a single peak corresponding to monomeric ScMreB5, molecular weight ~38 kD. Peaks corresponding to monomeric protein are marked with asterisk (*). C inset: Calibration curve for size-exclusion chromatography for Superdex 75 using molecular weight standards. The theoretical and estimated molecular weights of ScMreB5^{WT} monomer are mentioned.

Table 2.5: Data collection and refinement statistics table

Data collection statistics	ScMreB5-ADP	ScMreB5-AMPPNP
Space group	P1	I121
a, b, c (Å)	37.9,41.1,56.3	51.1, 54, 138
α , β , γ (°)	82.3, 74, 80.4	90, 98.18, 90
No. of unique reflections	12584 (1233)	13034 (1461)
Resolution (Å)	40.4- 2.3 (2.38-2.3)	68.7- 2.5 (2.6-2.5)
R _{merge} (%)*	0.12 (0.63)	0.20 (0.89)
R _{pim} (%)*	0.11 (0.52)	0.12 (0.54)
CC _{1/2} *	0.98 (0.48)	0.99 (0.82)
Mean I/ σ I*	6.1 (1.5)	7.0 (2.2)
Completeness (%)*	87.9 (86.2)	98.9 (98.3)
Multiplicity*	(2.1) (2.1)	6.9 (7.1)
Refinement statistics		
Resolution (Å)	36.14-2.3	49.8-2.5
Number of unique reflections (test set)	12580(657)	13181(1322)
R _{work} / R _{free} (%)	22.5/27.2	19.0/24.2
Average B-factor (Å ²)	23.1	26.47
Wilson B-factor (Å ²)	19.2	23.89
RMS deviations	0.002	0.002
Bond lengths (Å)	0.51	0.45
Bond angles (°)		

* Values in parenthesis denote the outer resolution shell

2.4: Discussion

In this chapter, we carried out purification optimization and structure determination of ScMreB5. This is the first reported structure of MreB from a cell wall-less bacteria. To carry out depth biochemical study, we first focused on getting protein in the absence of an excess of ADP. The presence of ADP in the buffer would prevent carrying out nucleotide-dependent experiments for filament-forming protein. But, we also wanted the protein to be stable and functional in the absence of ADP. Hence, we carried out global parameter optimization of the conditions to get a stable and functional protein. This included optimization of buffer agent, pH, and salt. Thermal shift assay was used as a readout of the effect of change in protein stability upon changing different parameters. This assay turned out to be an efficient method for determining the precise condition for ScMreB5, which finally led to the replacement of NaCl salt with KCl salt in the buffer. This helped us in getting a high yield of stable, non – aggregating protein. Interestingly, ScMreB5^{WT} in the KCl condition came as a natively ADP-bound protein, which indicated that the K⁺ ion has a role in stabilizing the bound ADP. The significance of the K⁺ ion was later on determined from the structure which has been discussed in Chapter 3. A detailed structural and sequence analysis has been done in chapter 3.

Purification and expression check optimization for the other two ScMreBs, tend to be difficult, which could indicate a different requirement for stability and purity for ScMreB3 and ScMreB4^{ΔN}. ScMreB3 purification trial indicated that the protein could be undergoing aggregation and/or forming higher-order oligomers which are difficult to separate. A different approach such as changing the position of Hexa-His tag and using a protein solubilizing tag could help in improving the overall protein yield.

2.5: References

- Adams, P.D., P.V. Afonine, G. Bunkóczi, V.B. Chen, I.W. Davis, N. Echols, J.J. Headd, L.W. Hung, G.J. Kapral, R.W. Grosse-Kunstleve, A.J. McCoy, N.W. Moriarty, R. Oeffner, R.J. Read, D.C. Richardson, J.S. Richardson, T.C. Terwilliger, and P.H. Zwart. 2010. PHENIX: A comprehensive Python-based system for macromolecular structure solution. *Acta Crystallogr. D Biol. Crystallogr.* 66:213–221. doi:10.1107/S0907444909052925.
- Battye, T.G.G., L. Kontogiannis, O. Johnson, H.R. Powell, and A.G.W. Leslie. 2011. iMOSFLM: a new graphical interface for diffraction-image processing with MOSFLM. *Acta Crystallogr. D Biol. Crystallogr.* 67:271–281. doi:10.1107/S0907444910048675.
- Cimpmperman, P., and D. Matulis. 2011. Protein thermal denaturation measurements via a fluorescent dye. *Biophys. Approaches Determining Ligand Bind. Biomol. Targets Detect. Meas. Model.* 247–273. doi:10.1039/9781849732666-00247.
- Emsley, P., B. Lohkamp, W.G. Scott, and K. Cowtan. 2010. Features and development of Coot. *Acta Crystallogr. D Biol. Crystallogr.* 66:486–501. doi:10.1107/S0907444910007493.
- van den Ent, F., L.A. Amos, and J. Löwe. 2001. Prokaryotic origin of the actin cytoskeleton. *Nature.* 413:39–44. doi:10.1038/35092500.
- van den Ent, F., T. Izoré, T.A.M. Bharat, C.M. Johnson, and J. Löwe. 2014. Bacterial actin MreB forms antiparallel double filaments. *eLife.* doi:10.7554/eLife.02634.
- van den Ent, F., and J. Löwe. 2006. RF cloning: A restriction-free method for inserting target genes into plasmids. *J. Biochem. Biophys. Methods.* 67:67–74. doi:10.1016/j.jbbm.2005.12.008.
- Evans, P.R., and G.N. Murshudov. 2013. How good are my data and what is the resolution? *Acta Crystallogr. D Biol. Crystallogr.* 69:1204–1214. doi:10.1107/S0907444913000061.
- Harne, S., S. Duret, V. Pande, M. Bapat, L. Béven, and P. Gayathri. 2020. MreB5 Is a Determinant of Rod-to-Helical Transition in the Cell-Wall-less Bacterium Spiroplasma. *Curr. Biol.* doi:10.1016/j.cub.2020.08.093.
- Huynh, K., and C.L. Partch. 2015. Analysis of protein stability and ligand interactions by thermal shift assay. *Curr. Protoc. Protein Sci.* 79:28.9.1-28.9.14. doi:10.1002/0471140864.ps2809s79.

McCoy, A.J., R.W. Grosse-Kunstleve, P.D. Adams, M.D. Winn, L.C. Storoni, and R.J. Read. 2007. Phaser crystallographic software. *J. Appl. Crystallogr.* 40:658–674.

doi:10.1107/S0021889807021206.

Narayanan, A., M. Ridilla, and D.A. Yernool. 2011. Restrained expression, a method to overproduce toxic membrane proteins by exploiting operator–repressor interactions. *Protein Sci. Publ. Protein Soc.* 20:51–61. doi:10.1002/pro.535.

Potterton, L., J. Agirre, C. Ballard, K. Cowtan, E. Dodson, P.R. Evans, H.T. Jenkins, R. Keegan, E. Krissinel, K. Stevenson, A. Lebedev, S.J. McNicholas, R.A. Nicholls, M. Noble, N.S. Pannu, C. Roth, G. Sheldrick, P. Skubak, J. Turkenburg, V. Uski, F. Von Delft, D. Waterman, K. Wilson, M. Winn, and M. Wojdyr. 2018. CCP 4 i 2: The new graphical user interface to the CCP 4 program suite. *Acta Crystallogr. Sect. Struct. Biol.* 74:68–84.

doi:10.1107/S2059798317016035.

Salje, J., F. van den Ent, P. de Boer, and J. Löwe. 2011. Direct Membrane Binding by Bacterial Actin MreB. *Mol. Cell.* 43:478–487. doi:10.1016/j.molcel.2011.07.008.

Sasajima, Y., and M. Miyata. 2021. Prospects for the Mechanism of Spiroplasma Swimming. *Front. Microbiol.* 12:706426. doi:10.3389/fmicb.2021.706426.

Winn, M.D., C.C. Ballard, K.D. Cowtan, E.J. Dodson, P. Emsley, P.R. Evans, R.M. Keegan, E.B. Krissinel, A.G.W. Leslie, A. McCoy, S.J. McNicholas, G.N. Murshudov, N.S. Pannu, E.A. Potterton, H.R. Powell, R.J. Read, A. Vagin, and K.S. Wilson. 2011. Overview of the CCP4 suite and current developments. 67. 235–242 pp.

Winter, G., D.G. Waterman, J.M. Parkhurst, A.S. Brewster, R.J. Gildea, M. Gerstel, L. Fuentes-Montero, M. Vollmar, T. Michels-Clark, I.D. Young, N.K. Sauter, and G. Evans. 2018. DIALS: Implementation and evaluation of a new integration package. *Acta Crystallogr. Sect. Struct. Biol.* 74:85–97. doi:10.1107/S2059798317017235.

Chapter 3: Structural analysis of ScMreB5

Some sections reprinted from: Pande et al., *Journal of Cell Biology*

DOI: [10.1083/jcb.202106092](https://doi.org/10.1083/jcb.202106092)

3.1: Introduction

In the previous chapter, we successfully purified ScMreB5 in an optimized buffer condition, crystallized the protein, and determined the structure. Previously solved crystal structures of MreB and electron microscopy of *T.maritima* and *C.crescentus* highlighted the conserved and distinguishing features of MreB compared to actins (van den Ent et al., 2014, 2001). These included domain organization, nucleotide binding pocket and polymeric assembly.

Although there is little sequence conservation between actin and MreBs, specific motifs, that are a part of nucleotide binding cleft are well conserved (Bork et al., 1992). There is functional conservation with respect to ATP binding and hydrolysis. *In vivo* mutational studies have shown that ATP-binding pocket residues are important for cell shape (Dye et al., 2011) . These mutations lead to different phenotypic defects as well as different filament dynamics of MreB (Dye et al., 2011; Formstone and Errington, 2005). Thus, nucleotide binding and hydrolysis seem to play an important role in the MreB function.

Crystal structures from *C. crescentus* (Cc), *T. maritima* (Tm), and more recently *S. eriocheris* (Se) have been determined for MreB (van den Ent et al., 2014, 2001; Takahashi et al., 2022). CcMreB structures in different nucleotide and filament states showed that only slight conformational change could drive MreB polymerization. Based on *in vivo* studies on MreB from *B. subtilis*, *E. coli*, and *C.crescentus*, it has been shown that the A22 drug affects cell shape by disrupting MreB polymerization (van den Ent et al., 2014; Bean et al., 2009; Awuni and Mu, 2019; Bean et al., 2009). Many of the A22-resistant mutants of MreB have residues mutated in the nucleotide-binding pocket region (Dye et al., 2011). The crystal structure of CcMreB bound to the inhibitor A22 and its less toxic analog MP265 showed the drug inhibits lateral interactions within a double protofilament. The mechanism by which MreB interacts with the membrane via a hydrophobic loop was shown biochemically for TmMreB (van den Ent et al., 2014; Salje et al., 2011). Recently, the crystal structure of SeMreB3, from another *Spiroplasma* species, *S. eriocheris*, was also determined. It was shown that subdomains IA and IB undergo conformational changes during the transition from a nucleotide-free state to a nucleotide-bound state (Takahashi et al., 2022).

In this chapter, I have analyzed the sequence and structure of ScMreB5 and compared it with other MreBs and actin. I have looked at the conserved MreB features which are: filament assembly as observed from crystal packing, polymerization interface, nucleotide binding pocket, and the membrane binding region. Additionally, a detailed analysis of conformational change occurring with different nucleotide and filament states has been performed for different MreBs (CcMreB, TmMreB, SeMreB3, and ScMreB5). Lastly, I have carried out the sequence analysis and structural comparison with the A22 binding pocket of ScMreB5 with CcMreB – A22 drug-bound structure.

3.2: Materials and Methods

3.2.1: Sequence and structural analysis of ScMreB5

To determine the residues involved in ATP hydrolysis and polymerization, structural and sequence analyses were performed. For structural comparison, we chose the structure of actin and *C.crescentus*, and *S.eriocheris* MreB in different nucleotide-bound conformational states. UCSF Chimera v1.13.1 (Pettersen et al., 2004) was used to perform structural analysis. Each subdomain of ScMreB5 was individually superposed on the CcMreB subdomains using the “Match Maker” command in Chimera with default settings. Root mean square deviation (RMSD) values were obtained for the C α atom pairs (these atom pairs were generated by iteratively pruning C α atom pairs until a 2 Å cutoff was reached). For comparing the nucleotide-binding pockets, the C α atom pairs of the IIA subdomain of ScMreB5 – AMP-PNP were superimposed over the C α atoms of the IIA subdomain of CcMreBs, SeMreB3, and actin structures. This was performed in UCSF Chimera v1.131. (Pettersen et al., 2004) using the “Match” command, specifying the residue range of 153 - 166 as subdomain IIA. The resulting superposed structures were further analyzed at the nucleotide-binding pocket region. The sequence alignment for the ScMreB5 with other MreBs and actin was done using Clustal Omega (Sievers et al., 2011).

3.2.2: Identification of potassium ion at the nucleotide-binding pocket

For determining the presence of potassium ion at the nucleotide-binding pocket of ScMreB5 in the crystal, X-ray fluorescence scanning was performed. Crystallization of ScMreB5-AMP-PNP devoid of potassium ion (coming from either Buffer A or from the crystallization condition) was carried out. The protein was crystallized with 2 mM AMP-PNP and 2 mM MgCl₂ in the crystallization buffer containing 0.15 M Na-phosphate and 16 % PEG 3350, pH 7.8. To remove any remnants of potassium ion before freezing, the crystal was picked and washed thrice with the drop containing 20 % glycerol cryoprotectant in the parent condition. The X-ray fluorescence scan was performed at the beamline I-04 Diamond Light Source, UK.

3.2.3: Domain-wise analysis of MreBs

For calculating the domain angles ω_1 (IB-IA-IIA) and ω_2 (IA-IIA-IIB), the centroid of each subdomain was calculated from the backbone (excluding unmodelled residues from the structure). In UCSF Chimera v. 1.31.1 (Pettersen et al., 2004), MreB structure was opened and a single subdomain was selected. From the 'Tools' tab drop down options, 'Structure Analysis' tab was chosen. The option of 'Axes/Planes/Centroid' was opened from the 'Structure Analysis'. This opened 'Structure measurement' box. Now, 'Define Centroid' option was clicked and in the dialog box "Mass weighing" option was set as 'False'. This generated a centroid for one of the sub-domain of MreB. Similarly, centroid was generated for the other three subdomains. This method has been adapted from (Takahashi et al., 2022). After determining the centroid, the axis between the centroid of IB-IB (a1), IA-IIA (a2), and IIA-IIB (a3) was determined. Two centroids between which the axis has to be defined were selected from the 'Centroid' tab in the 'Structure measurement' dialog box. From the "Axes" tab in the 'Structure measurement' dialog box axis was defined using default settings. For determining ω_1 , the angle between the axis, 'a1' and 'a2' was calculated using the command line interface (Command: angle a1, a2). For determining ω_2 , the angle between the axis 'a2' and 'a3' was calculated.

For calculating the dihedral angle (ϕ), coordinate "x, y and z" position values for the centroid of four subdomains were obtained and the dihedral angle value was determined from the python script made for calculating the dihedral angle.

For determining the distance between the centroids of IB and IIB, axis (a4) was determined from the "Structure measurement" option as described above.

3.2.4: Comparing A22 binding site

For predicting the A22 drug resistance for ScMreB5 through structure, a structural comparison with the A22 bound structure of CcMreB (PDB ID: 4CZG) was performed. ScMreB5 – AMP-PNP IIA subdomain was superposed on CcMreB – AMP-PNP (PDB ID: 4CZJ) using the “Matchmaker” command in UCSF Chimera v1.13.1. Similarly, IIA subdomains of TmMreB (PDB ID: 1JCG) and CcMreB – A22 (PDB ID: 4CZG) were also superposed on CcMreB (PDB ID: 4CZJ). After superposition, the A22 binding site of these structures was compared. The RMSD values of the loop at the A22 binding site were obtained after the structure superposition.

For the docking study, the “AutoDock Vina” option from “Surface/Binding Analysis” was used in UCSF Chimera v.1.131 (Pettersen et al., 2004). Firstly, all the water molecules and non-standard residues (except the nucleotide, Mg^{2+} and K^+) were deleted from the structures (PDB ID: 4CZG and 7BVZ). A22 3D conformer was downloaded from “PubChem” (CID 348494) and opened in UCSF Chimera v.1.131 (Pettersen et al., 2004). Then, the entire MreB structure was selected, and the “AutoDock Vina” dialog box was opened. Here, the location of the output file was defined, and ligand and the receptor models were selected. In the ‘Receptor search volume’ option, the ‘resize search volume using: cntrl button 1’ was selected. Then, over the selected protein structure, a search volume box was made, over the core of the protein structure, leaving the outer regions of the subdomains. All the other options were kept as default and the program was run. The top three A22 docked coordinates, with minimum energy and the least RMSD values, were selected for both structures and analyzed.

3.2.5: Membrane binding sequence analysis

For determining potential membrane binding regions in ScMreB5, sequence alignment was performed in Clustal Omega (as described in section 3.2.1).

For ScMreB5 extended C-terminus conservation analysis, MreB5 sequences listed in (Harne et al., 2020), were taken and aligned using Clustal Omega. The alignment result was analyzed and edited in Jal View (Clamp et al., 2004). The C-terminus residue conservation was generated using WebLogo (Crooks et al., 2004).

3.3: Results

3.3.1: Features of the crystal structures of ScMreB5

We sought to find out the molecular details of ScMreB5 by solving crystal structures in the ADP and AMP-PNP bound state of the protein (Fig 3.1 A and B). Both the structures were very similar, superimposing with an overall root mean square deviation (RMSD) of 0.87 Å. ScMreB5-ADP and ScMreB5-AMP-PNP structures have a typical actin fold. Both the structures superimpose well with the structures of *T.maritima* and *C.crescentus* MreBs. Like actins, there are two domains, I and II which are further divided into two subdomains each, IA (1-32, 76-141, 315-334) and IB (33 - 75); IIA (142 - 178, 251- 352) and IIB (179 - 250) (residue numbering as per ScMreB5). The membrane binding loop, present in the IA subdomain, was found to be disordered in the ScMreB5-ADP (residues 93-97) (Fig 3.1 B), however, this loop was observed in the ScMreB5-AMP-PNP structure due to crystal contacts. The nucleotide-binding cleft is formed at the core of the protein. The conserved motifs, namely phosphate I, phosphate II, Connect I and Connect II, are present at the nucleotide-binding pocket as shown for ScMreB5 – AMPNP (Fig 3.1 C).

No drastic conformational change was observed when the two states were compared subdomain-wise (superposition RMSD in Table 3.1). A higher RMSD value for the IA subdomain was contributed by the Phe87 – Lys97 region. This region has the putative membrane binding loop of ScMreB5. In ADP bound state, the membrane binding loop started from Met92, the entire loop could not be modelled for ScMreB5-ADP. In the case of ScMreB5-AMPNP, the helix preceding the loop in the ADP state opened, hence the loop region started from Phe87. Hence the region between Phe87-Met93 and Lys 97-Ala99 did not superpose well. This led to an increase in the RMSD of subdomain IA (Fig 3.1 D).

Clear electron density was observed for the nucleotides and Mg²⁺ ion in both ADP- and AMP-PNP-bound states (Fig 3.1 E and F).

Table 3.1: RMSD values of each subdomain upon domain-wise superposition of ScMreB5 structures

Subdomains	RMSD (Å) (Overall atom pairs)
IA	1.72 (113)
IB	0.46 (43)
IIA	0.30 (101)
IIB	0.48 (72)

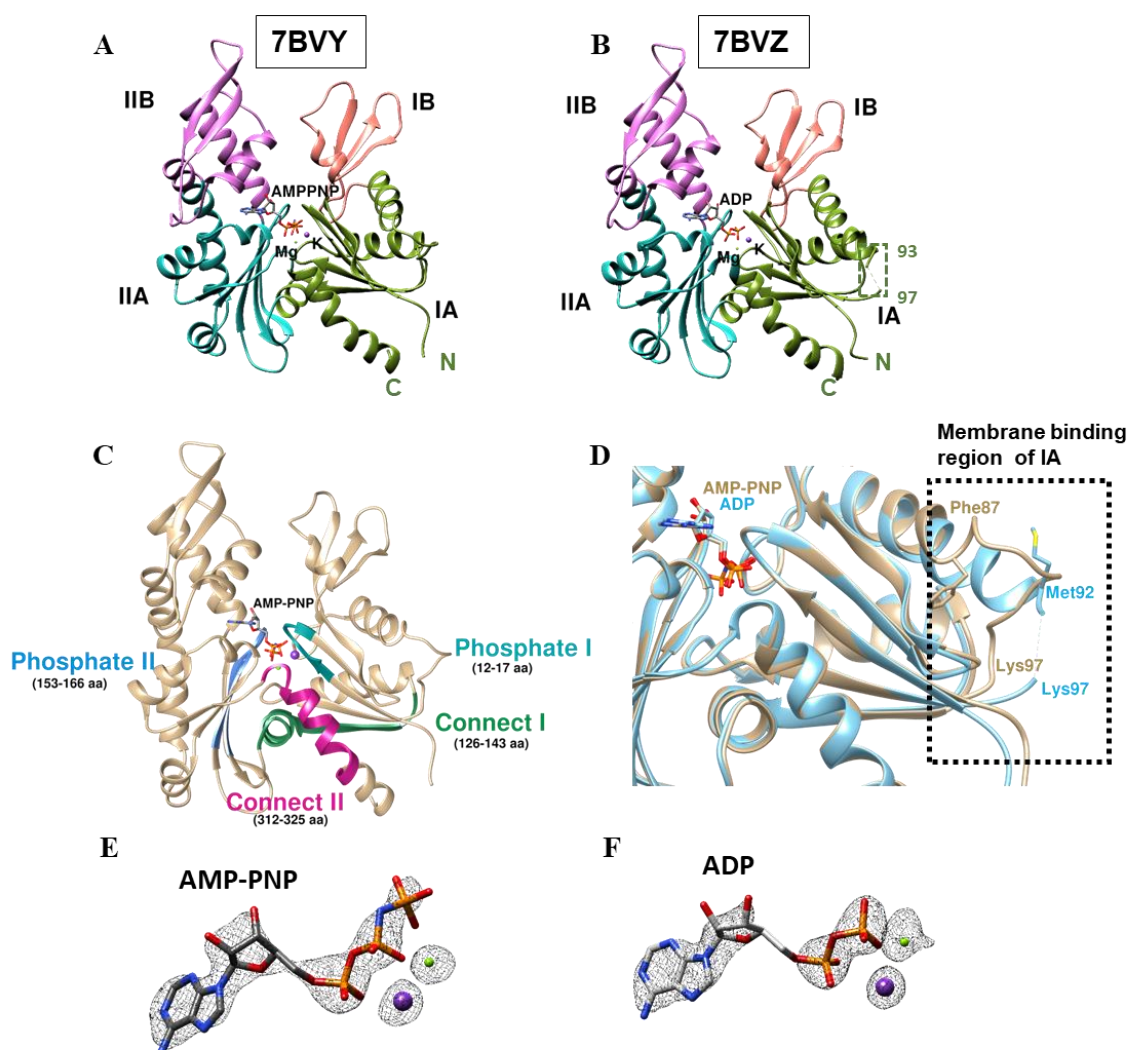


Figure 3.1: Crystal structure of ScMreB5.

(**A and B**) Crystal structures of ScMreB5 in ADP (PDB accession no. 7BVZ) and AMP-PNP (PDB ID: 7BVY) bound states. The subdomains IA, IB, IIA, and IIB are colored and labeled. N- and C-terminal ends are labeled N and C, respectively. The chain breaks in 7BVZ are also labeled by their residue numbers (93 and 97). (**C**) Conserved motifs at the nucleotide-binding pocket are shown for ScMreB5 (PDB ID: 7BVY). (**D**) The superposed IA subdomain of both crystal structures shows the membrane binding region (in the box) of ScMreB5. This region does not superpose well for ScMreB5-ADP and ScMreB5-AMPPNP. (**E and F**) Electron density for the bound ADP and AMP-PNP with Mg^{2+} and K^+ (composite omit map $F_o - F_c$ shown at 2.0σ).

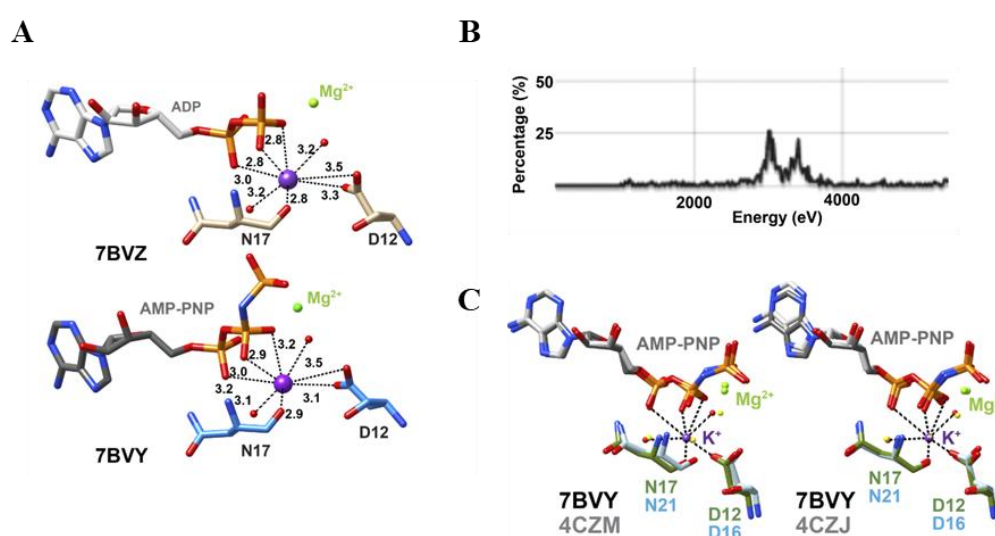


Figure 3.2: ScMreB5 is stabilized by KCl and nucleotides.

(**A**) Coordination sphere of potassium in ScMreB5-ADP (top) and ScMreB5-AMP-PNP (bottom). (**B**) X-ray fluorescence scan for ScMreB5-AMP-PNP crystals. (**C**) Asp12 and Asn17 of ScMreB5 at the potassium-binding site are compared with the corresponding residue present in monomeric (PDB ID: 4CZM) and double protofilament CcMreB (PDB ID: 4CZJ) by superposing IIA subdomain of CcMreBs onto IIA subdomain of ScMreB5-AMP-PNP structure (single protofilament conformation). The presence of a water molecule in the CcMreB at the potassium-equivalent position can be observed. The residues of ScMreB5 are colored domain-wise; those of CcMreB are light blue. The water molecules for ScMreB5 are red, and for CcMreBs, yellow.

3.3.2: Structural basis of K⁺ ion mediated stability of ScMreB5

We found the presence of strong electron density for K⁺ ion at the nucleotide-binding pockets, positioned between α and β phosphates of ADP and AMP-PNP in both the structures of ScMreB5 (Fig 3.2 A). The identity of the ion was confirmed through the X-ray fluorescence scanning of ScMreB5 – AMP-PNP crystals that were crystallized in the absence of potassium ion from the crystallization condition (Fig 3.2 B). There was a clear increase in thermal stability for the protein in the KCl-containing buffer in the presence of ADP and AMP-PNP. Additionally, the protein came bound with ADP in the presence of KCl containing buffer. There was a water molecule in the CcMreB structure at the position equivalent to the K⁺ in the ScMreB5 (Fig 3.2 C). The residues Asp12 and Asn17, which are involved in potassium ion coordination in ScMreB5, are well conserved among MreBs from different bacteria and interact with the corresponding water molecule in CcMreB (Fig 3.5). Thus, the presence of K⁺ ion provided the structural basis of the ScMreB5 stability in the KCl-containing buffer.

3.3.3: Protofilament organization of ScMreB5

The packing of ScMreB5–ADP and ScMreB5–AMP-PNP molecules in the crystal structures revealed a single-protofilament assembly (Fig 3.3 A and B). The subunit repeat distance of 51.1 Å was similar to CcMreB single protofilament (ADP bound) and antiparallel double protofilament (AMP-PNP bound) (Fig 3.3 C and D) and SeMreB3 antiparallel protofilament (AMP-PNP bound) (Fig 3.3 E) assemblies. An increase in repeat distance to 52.4 Å in the nucleotide-free antiparallel protofilament assembly of SeMreB3 was observed (Fig 3.3 F). This was probably due to a more open conformation of the protein in the unbound nucleotide state.

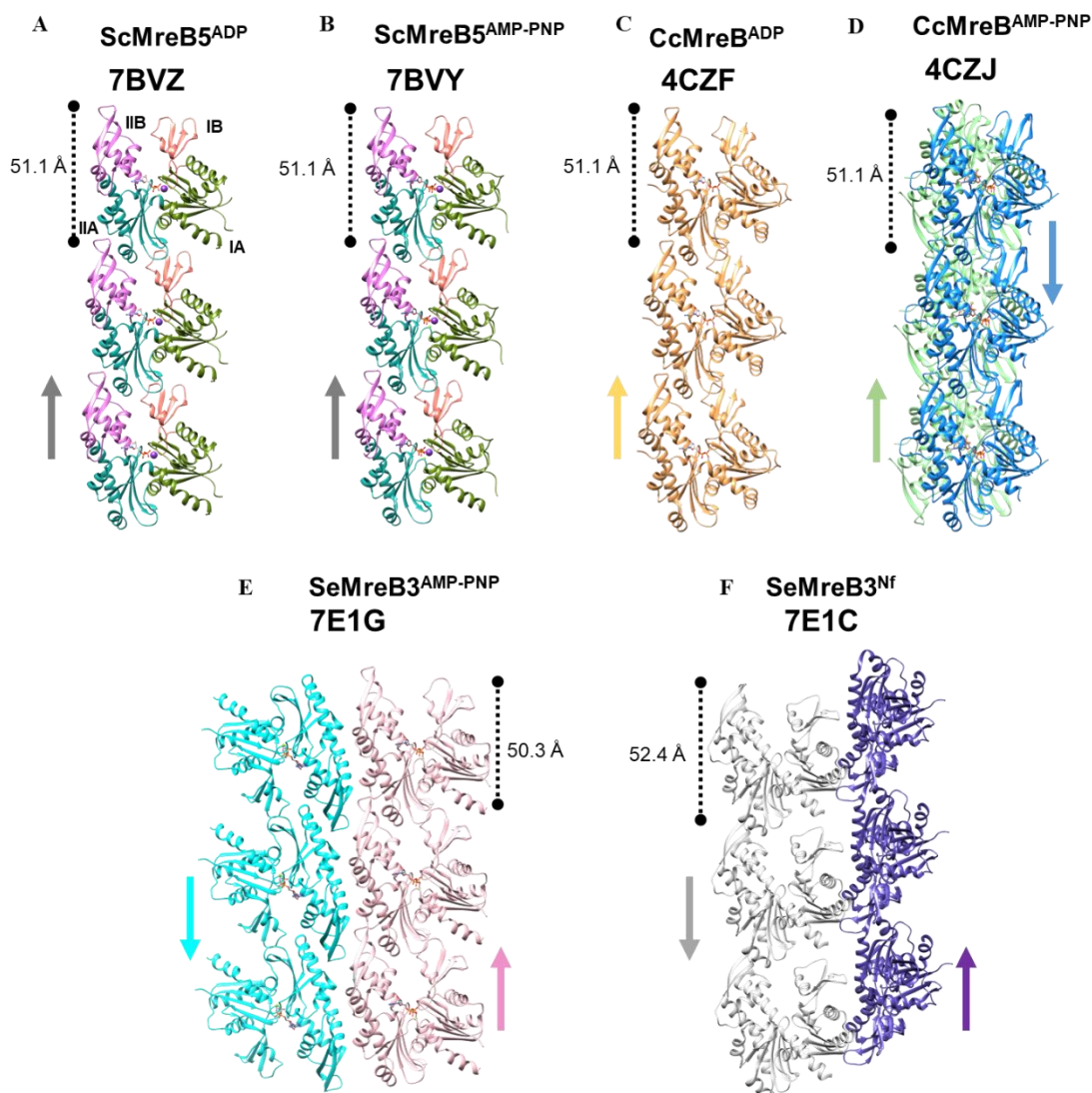


Figure 3.3: ScMreB5 possesses a conserved protofilament assembly compared to other MreBs.

(**A and B**) Protofilament structures of ScMreB5 bound to ADP (PDB ID: 7BVZ) and AMP-PNP (PDB ID: 7BVY). Individual chains are colored according to the subdomains. (**C and D**) Protofilament structure of CcMreB bound to ADP (PDB ID: 4CZF) and a double antiparallel protofilament assembly of CcMreB bound to AMP-PNP (PDB ID: 4CZJ). ScMreB5 protofilament assembly have the same subunit repeat as CcMreB (51.1 Å). (**E and F**) An antiparallel protofilament assembly of SeMreB3 bound to AMP-PNP (PDB ID: 7E1G) and a protofilament structure of nucleotide free form of SeMreB3 (PDB ID: 7E1C). Slightly different subunit repeat distances are observed in SeMreB3 assembly, indicating a crystal packing effect rather than an accurate subunit interface in a protofilament.

3.3.4: Domain-wise analysis for MreBs

To check for the subdomain-wise conformational change in different nucleotide states of the ScMreB5 protofilament, we chose four structures as reference: nucleotide-free state protofilament (PDB ID: 71EC), ADP bound protofilament (PDB ID: 4CZF), AMP-PNP bound protofilament (PDB ID: 1JCG) and AMP-PNP bound double protofilament (PDB ID: 4CZJ). Subdomains of each structure were superimposed over subdomains of ScMreB5 – ADP and ScMreB5 – AMP-PNP. No significant conformational change for any of the subdomains was observed. The RMSD values for each subdomain were within 1.5 Å (summarized in Table 3.2). Next, we wanted to know if relative subdomain movement occurs upon nucleotide binding and filament formation. For this, we calculated the angle between the three centroids of the subdomains, ω_1 (IIA-IA-IB) and ω_2 (IA-IIA-IIB) (Fig 3.4 A). The angular shift in ω_1 will correspond to movement in IB, whereas ω_2 would correspond to movement in IIB. For estimating movement between the I and II domains, we calculated the dihedral angle (ϕ) (Fig 3.4 B). This analysis was earlier done for *S. eriocheris* MreB3 (Takahashi et al., 2022). All these calculations were done for all the MreB structures determined to date (MreBs from *C. crescentus*, *T. maritima*, and *S. eriocheris*). These values are summarized in Table 3.3. We also calculated the distance between the centroids of the subdomains IB and IIB (IB-IIB) (Fig 3.4 A).

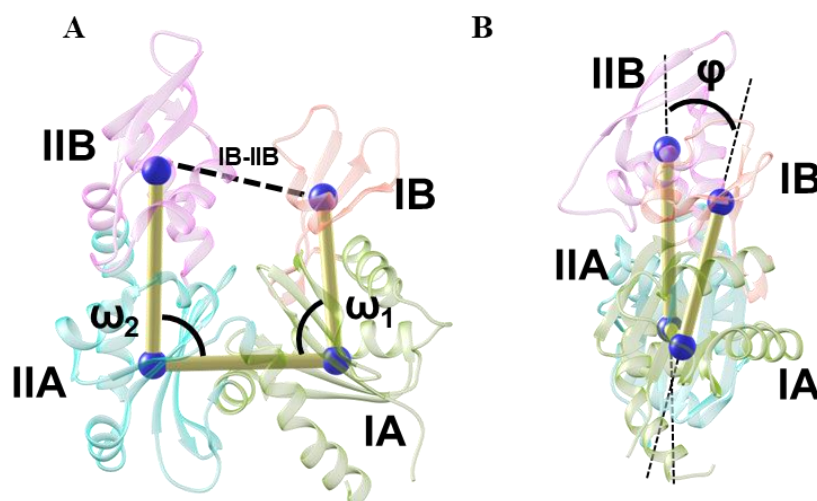


Figure 3.4: Domain wise analysis for MreB structures.

(A) Subdomain movement is determined using ω_1 and ω_2 . The values for these angles were determined by calculating the angles between the centroids (Blue spheres), Centroid for each subdomain is defined only by the protein backbone. The angle was determined between the axis formed between the two centroids (yellow lines), IB-IA-IIA centroids forms ω_1 and IA-IIA-IIB forms ω_2 . The distance between the centroids of IB and IIB (IB-IIB) was also determined. (B) Dihedral angle (φ) was calculated between the centroid of the subdomains IB, IA, IIA and IIB. The ScMreB5 – AMP-PNP is colored according to the subdomains.

Table 3.2: Subdomain wise comparison of ScMreB5 structures with other MreBs

	ScMreB5	IA	IB	IIA	IIB
PDB IDs		Overall RMSD (Pruned atom pairs)			
7E1C (empty, single protofilament)	ADP	1.04 (79)	0.95 (30)	0.82 (101)	0.66 (72)
	AMP-PNP	1.07 (91)	0.92 (30)	0.92 (93)	0.58 (72)
1JCG (AMP-PNP, single protofilament)	ADP	1.13 (79)	1.00 (43)	0.94 (95)	0.69 (67)
	AMP-PNP	1.11 (73)	1.10 (43)	0.99 (95)	0.73 (67)
4CZF (ADP, single protofilament)	ADP	0.90 (76)	0.93 (36)	1.00 (99)	0.64 (63)
	AMP-PNP	0.84 (77)	1.11 (35)	1.04 (97)	0.64 (65)
4CZJ (AMP-PNP, double protofilament)	ADP	1.00 (83)	1.37 (37)	0.98 (98)	0.54 (53)
	AMP-PNP	1.08 (80)	1.02 (32)	0.99 (96)	0.51 (55)

Table 3.3: Subdomain angular movement and distance difference for MreBs

(Values in bracket corresponds to the difference in ω_1 and ω_2 with respect to *C.crescentus* structure, PDB ID: 4CZJ)

Organism	PDB ID	Filament Type, Bound Ligand	Molecules in an asymmetric unit	ω_1 (IIB-IA-IB) (°)	ω_2 (IA-IIA-IIB) (°)	Dihedral angle ϕ	IB-IIB (Å)
<i>C.crescentus</i>	4CZL	monomeric, ADP	1	89.2 (11.5)	88.6 (6.1)	29.2	26.1
	4CZM	monomeric, AMP-PNP	1	89.2 (11.5)	89.6 (7.1)	22.8	25.5
	4CZI	single protofilament, empty	1	85.6 (8.5)	80.8 (1.4)	19.3	22.5
	4CZF	single protofilament, ADP bound	1	87.7 (10)	86.5 (4)	19.3	22.9
	4CZJ	double protofilament, antiparallel, AMP-PNP bound	2	77.7	82.5	14.1	24.2
	4CZE	double protofilament, antiparallel, empty	2	81.8 (4.1)	82.1 (0.4)	18.1	24.3
<i>T.maritima</i>	1JCE	single protofilament, empty	1	83.3 (5.6)	85.3 (2.8)	14.7	24.2
	1JCG	single protofilament, AMP-PNP	1	86.1 (8.4)	87.3 (4.8)	17.9	24.2
<i>S.eriocheris</i>	7E1C	two protofilament filament, antiparallel, empty	1	86.3 (8.6)	88.5 (6)	26	28.4
	7E1G (Chain A)	two protofilament filament, antiparallel, AMP-PNP	2	87.2 (9.5)	89.3 (6.8)	20.8	25.6
	7E1G (Chain B)	two protofilament filament, antiparallel, AMP-PNP		89.2 (11.5)	88.7 (6.2)	22.2	26.7
<i>S.citri</i>	7BVZ	single protofilament, ADP	1	87.1 (9.4)	87.9 (5.5)	23.6	24
	7BVY	single protofilament, AMP-PNP	1	86.8 (9.1)	87.8 (5.3)	22.6	23.9

In *C. crescentus* MreB (CcMreB), as the AMP-PNP bound state transitioned from a monomer (PDB ID: 4CZM) to a double protofilament state (PDB ID: 4CZJ), IB subdomain moved inwards, as observed from a decrease in the ω_1 from 89.2° (monomeric, AMP-PNP structure) to 77.7° (double protofilament, AMP-PNP structure). Only in the double protofilament state, either empty or AMP-PNP bound, ω_1 was minimum. Therefore, in a double protofilament state, irrespective of nucleotide, the IB subdomain moves inwards, towards the core of the structure. The IIB subdomain conformation was relatively more open than the IB subdomain since the change in ω_2 is 7.1° upon change to double protofilament state from monomeric state. Interestingly, to reach a functional antiparallel double protofilament state, a step-wise decrease in dihedral angle was observed, monomeric (22.8°) to single protofilament (19.3°) and then to a double protofilament (14.1°). Hence, as the CcMreB reaches a double protofilament state, CcMreB adopts a closed conformation. Thus upon nucleotide binding and reaching a double protofilament state, IB and IIB subdomains move toward the core of the protein. This further leads to a compact/closed state of MreB as seen from the decrease in the dihedral angle ϕ .

For *T. maritima* MreB (TmMreB), we compared empty (PDB ID: 1JCE) and an AMP-PNP bound (PDB ID: 1JCG) single protofilament structures. Interestingly, when a nucleotide is bound in a protofilament, there is a slight opening of the IB and IIB subdomain (approximately 3°), as seen from the increase in ω_1 and ω_2 . This observation is consistent with CcMreB protofilament structures (PDB IDs: 4CZI and 4CZF). Thus, to accommodate a nucleotide in a protofilament within a crystal, a slight opening of the structure is required.

We further analyzed MreB structures from *Spiroplasma*, SeMreB3, and ScMreB5 respectively. *S. eriocheris* SeMreB3, empty, and AMP-PNP protofilament were analyzed. As observed for TmMreB and CcMreB, subdomain IB and IIB opening was also observed upon AMP-PNP binding. For *S. citri*, ScMreB5, ADP, and AMP-PNP bound crystal structures, the values for ω_1 , ω_2 , and ϕ are similar to those obtained for the nucleotide single protofilament crystal structure from CcMreB, TmMreB, and SeMreB3. Thus, it shows that the opening of IB and IIB subdomains is required for nucleotide binding in a protofilament assembly.

3.3.5: Nucleotide-binding pocket of ScMreB5

The pairwise sequence identities for MreBs is tabulated in Table 3.4. Residues that are at the nucleotide-binding pocket are well-conserved with respect to MreBs and actin (Fig 3.5).

Table 3.4: Sequence percentage identity with ScMreB5

ScMreB4	54.9%
ScMreB3	46.7%
ScMreB2	64.6%
ScMreB1	53.8%
BsMreB	40.9%
EcMreB	37.3%
TmMreB	35.5%
CcMreB	38.8%
Yeast_Actin	14.1%

For our analysis, we chose residues that were either involved in coordinating Mg^{2+} ion or involved in direct interaction with the catalytic water near the γ - phosphate (Fig 3.6 A and Fig 3.7 A and B). This selection was based on the structure and sequence alignment with actins and other MreBs (as shown in Fig. 3.5). Based on structure, side chain oxygen atoms ($O\delta 1/O\delta 2$ or $O\epsilon 1/O\epsilon 2$) of Asp12, Asp156, and Glu134 (Fig 3.6 B and Fig 3.7 A) in ScMreB5 are involved in interacting with the water molecules that form coordination sphere for Mg^{2+} . In our structure, electron density for the catalytic water molecule, expected to be in line with the γ - phosphate moiety, was missing.

Hence, it was not modeled in the structure. Based on the sequence and structural alignment, two residues, Glu134 and Thr161 could potentially interact with the catalytic water (Fig 3.7 C). Interestingly, in SeMreB3, Thr161 (ScMreB5) is replaced by Lys174, which no longer interacts with the catalytic water (Fig 3.7 B). This Lys is conserved in all the *Spiroplasma* MreB3 (Takahashi et al., 2022). The other residue that we chose for our study was Asp 70, which is away from the nucleotide-binding pocket. This residue is well conserved for MreBs. His73 replaces Asp70 in actins (Fig 3.5 and Fig 3.7 C). In actins, His73 is important for polymerization and regulating phosphate release upon hydrolysis of ATP (Nyman et al.,

Chapter 3: Structural analysis of ScMreB5

2002). Based on the conservation of the nucleotide-binding pocket residues for MreBs, we chose to carry out in vitro characterization for the same which is described in chapter 4.

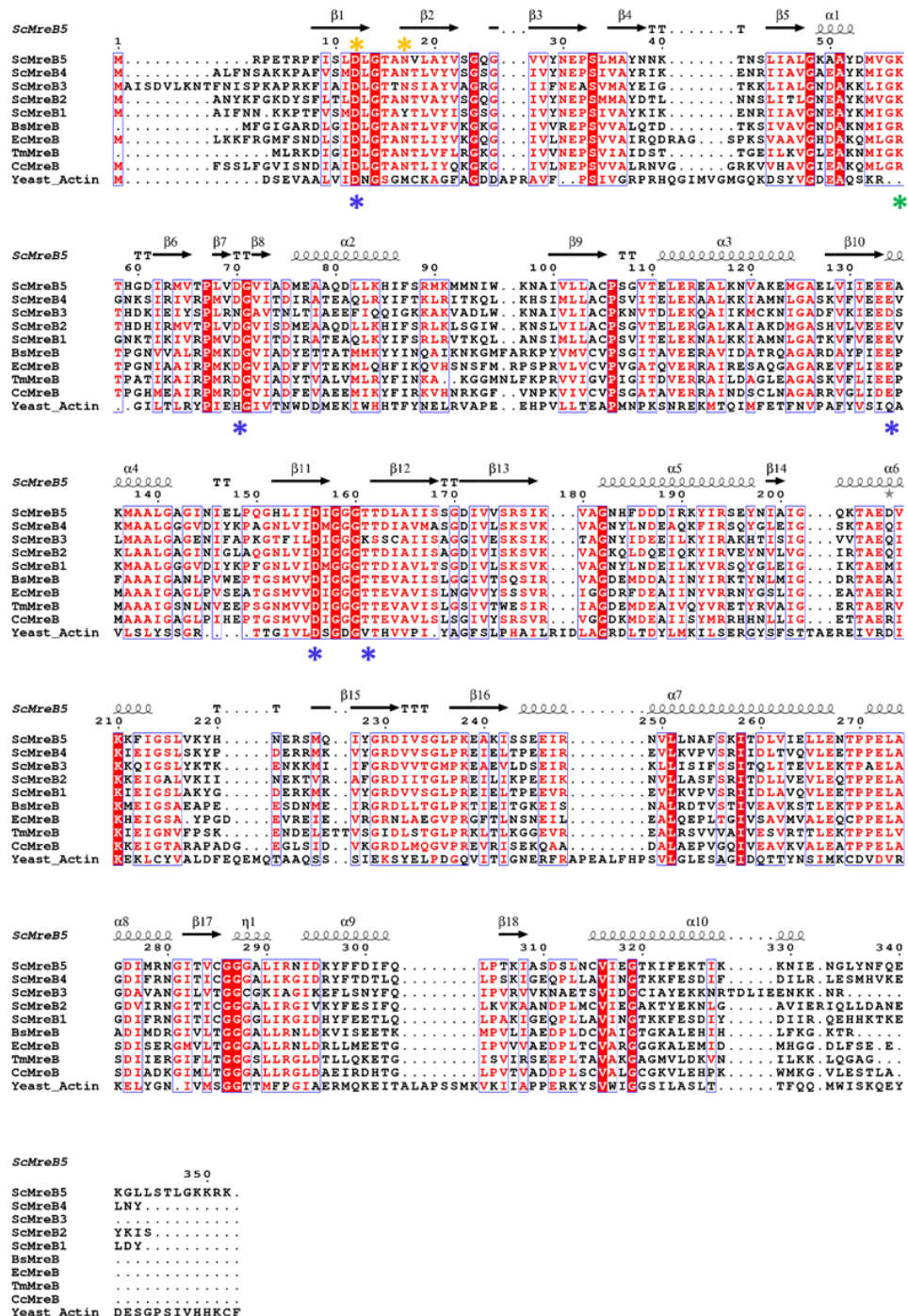


Figure 3.5: Residues at nucleotide-binding pocket are well conserved in ScMreB5.

Sequence alignment of ScMreB5 (ScMreB5) with other *S. citri* MreBs (ScMreB1, ScMreB2, ScMreB3, and ScMreB4), *C. crescentus* MreB (CcMreB), *T. maritima* (MreB) TmMreB, *E. coli* MreB (EcMreB), *B. subtilis* MreB (BsMreB), and yeast actin. Residues involved in ATP hydrolysis (blue asterisk), K^+ coordination (yellow asterisk), and polymerization interface (green asterisk) are marked.

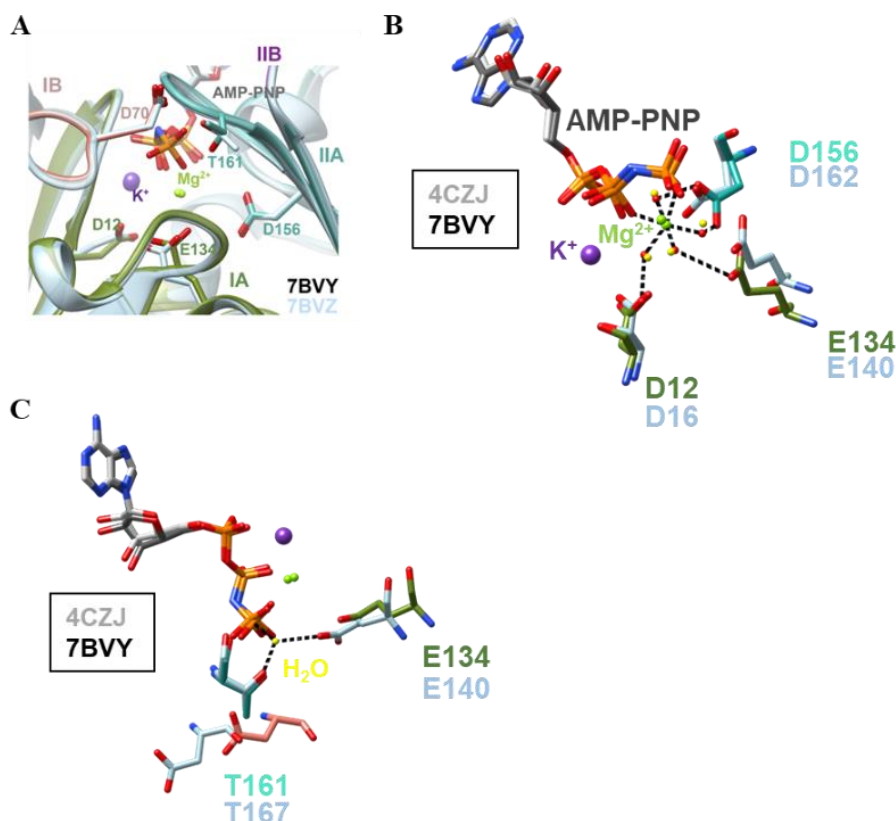


Figure 3.6: Nucleotide binding pocket of ScMreB5 is conserved.

(A) Zoomed-in view of the residues at the nucleotide binding pocket. Residues of ScMreB5–AMP-PNP (PDB ID: 7BVY; domain-wise colors) are shown superimposed with corresponding residues in ScMreB5–ADP (PDB ID: 7BVZ; blue-gray). (B) Residues involved in Mg^{2+} coordination in ScMreB5 (Asp156, Glu134, and Asp12). Distances for Mg^{2+} coordination are marked by dotted lines for ScMreB5–AMP-PNP. (C) Residues adjacent to the γ -phosphate, Glu134 and Thr161, at the nucleotide-binding pocket. Distances with the catalytic water are marked by dotted lines for CcMreB structure.

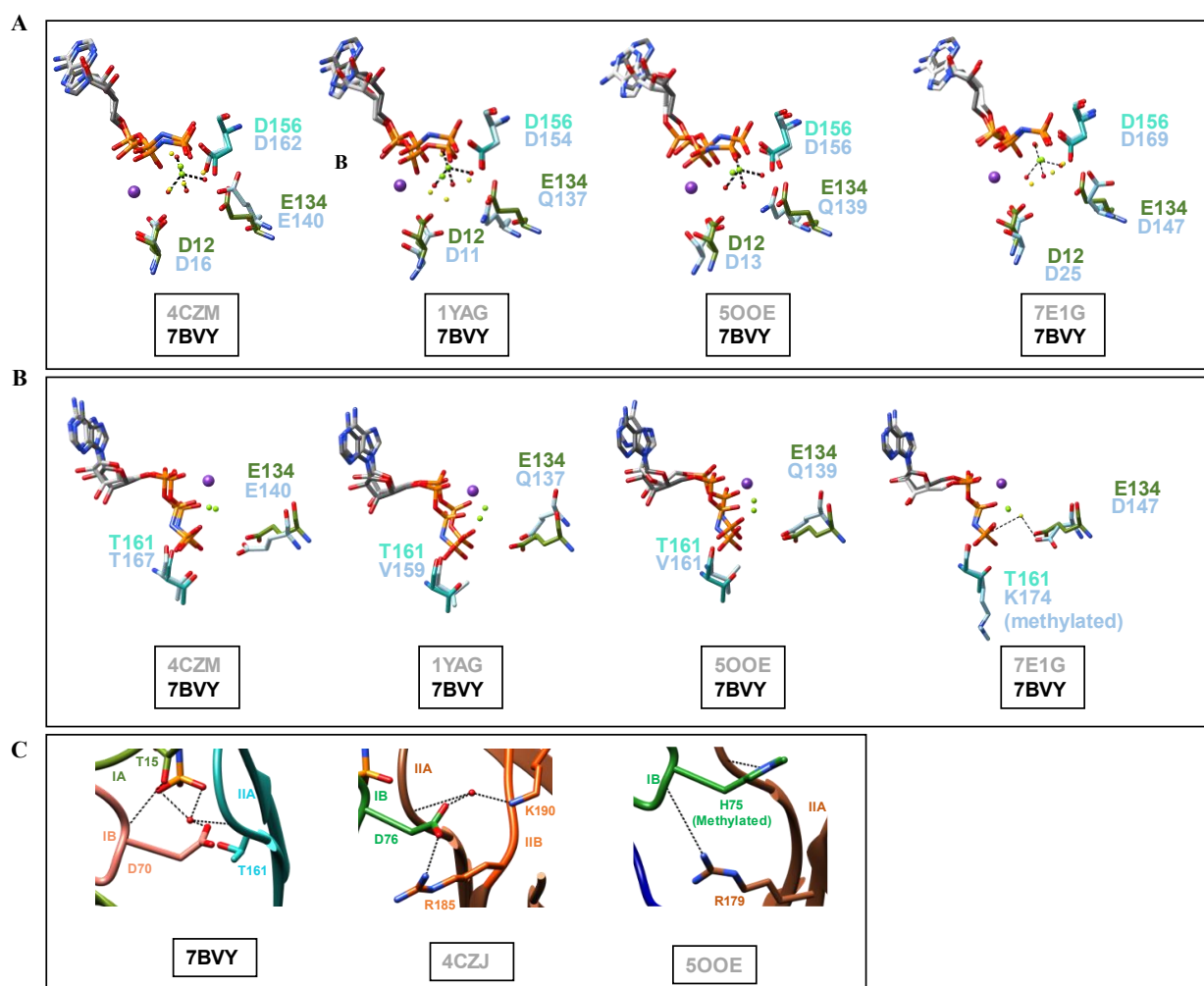


Figure 3.7: Comparison of active site geometry of ScMreB5 with other MreBs and actins.

Residues of ScMreB5 at the active site are compared with the monomeric CcMreB (PDB ID: 4CZM), monomeric yeast actin (PDB ID: 1YAG), and actin filament (PDB ID: 5OOE) and antiparallel protofilament SeMreB3 (PDB ID: 7E1G) by superposing IIA domain of each structure onto IIA domain of ScMreB5–AMP–PNP structure (single protofilament conformation). The color of the residues are subdomain wise, for ScMreB5–AMP–PNP, IB (pink), IA (green), and IIA (sea green). For the other MreBs and actin structures, residues in subdomains are colored light blue. All distances marked by black dotted lines are <3.5 Å.

(A) Superimposed active site residues holding the Mg^{2+} coordination sphere. Asp12, Glu134, and Asp156 residues of ScMreB5 are compared with the corresponding residues in monomeric CcMreB, monomeric actin, actin filament and antiparallel protofilament SeMreB3. **(B)** Superimposed active site residues at the catalytic water interface. Glu134 and Thr161 residues of ScMreB5 are compared with the corresponding residues in monomeric CcMreB, monomeric actin, actin filament and antiparallel protofilament SeMreB3. **(C)** Interacting interface for Asp70 of ScMreB5–AMP–PNP is shown with respect to corresponding residues present in double-protofilament CcMreB (PDB ID: 4CZJ) and actin filament (PDB ID: 5OOE).

3.3.6: Membrane binding sequence of ScMreB5

Filaments of MreB bind the lipid membrane. In vitro and in vivo studies on MreB of *E. coli* and *T. maritima* have shown membrane binding. This binding is facilitated through the hydrophobic loop and/or through N terminal amphipathic helix (Salje et al., 2011). The N-terminal and hydrophobic loop are the part of IA subdomain. Based on the sequence alignment of ScMreB5 with that of other MreBs, there is the presence of a hydrophobic region (92 – 98 amino acid) that could be involved in ScMreB5 - lipid interaction (Fig 3.8 A and 3.8 B). This loop was captured in the crystal structure of ScMreB5 – AMP-PNP which was disordered in the ScMreB5 – ADP. N-terminal amphipathic helix is absent in ScMreB5 (Fig 3.8 C).

Interestingly, based on the sequence alignment of all the *Spiroplasma* MreB5s, there is a presence of a longer C-terminal tail, which is rich in positively charged residues (Fig 3.8 D and E). The longer C-terminal tail is absent in other *Spiroplasma* MreBs as well as MreBs from the cell-walled bacteria. The C-terminal tail could not be modelled in the structure due to the absence of electron density. The C-terminal tail could also be part of the membrane binding region of the MreB, and have a role in facilitating the interaction of ScMreB5 with the membrane.

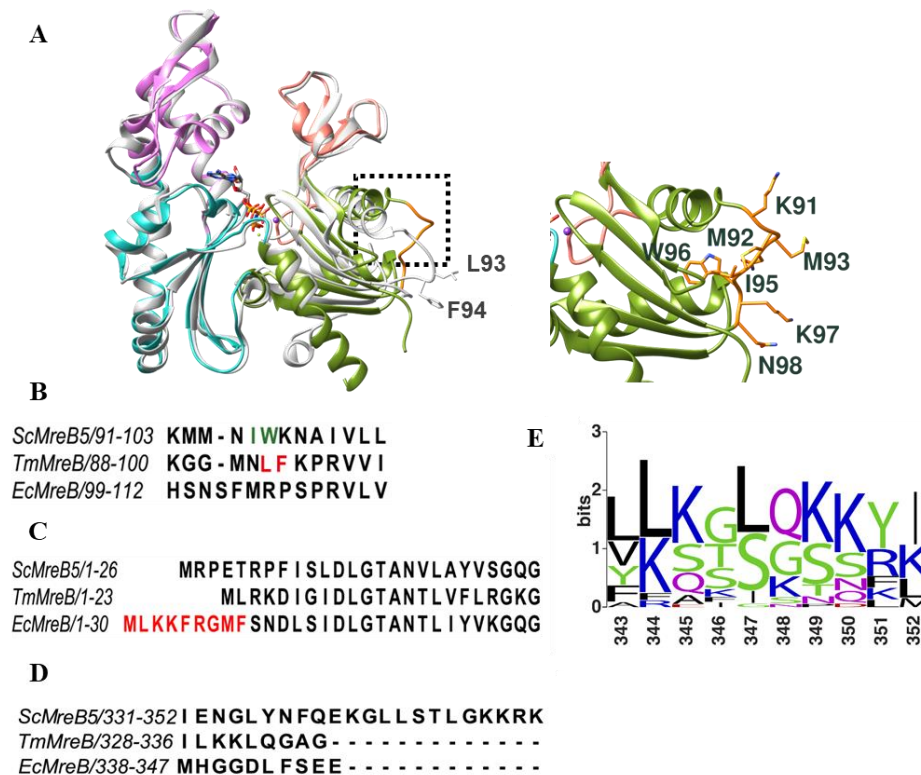


Figure 3.8: Membrane binding region of ScMreB5.

(A) Crystal structure of AMP-PNP-bound ScMreB5 (PDB ID: 7BVY), with proposed membrane insertion loop (orange) in domain IA (green). Inset: Zoomed-in view of the loop. ScMreB5 is superposed with TmMreB. TmMreB membrane binding residues are highlighted (L93 and F94). (B) Sequence alignment of ScMreB5 with TmMreB and EcMreB in the region of hydrophobic loop. The residues interacting with the membrane for TmMreB and predicted residues for ScMreB5 are highlighted in red and green, respectively. (C) Sequence alignment of ScMreB5 with TmMreB and EcMreB, showing the absence of amphipathic helix at the N-terminus. Amphipathic helix of EcMreB is highlighted in red. Secondary structures are labeled on top of the alignment. (D) Sequence alignment of C-terminal region of ScMreB5 with TmMreB and EcMreB shows longer C-terminal tail enriched with positively charged residues (highlighted with blue stars). The N- and C-terminal ends of ScMreB5 are labeled N and C, respectively. (E) Weblogo of C-terminal end, showing the presence of lysine and arginine in *Spiroplasma* MreB5s. The numbering on the x axis is with respect to the last 10 residues of ScMreB5.

3.3.7: A22 binding pocket of ScMreB5

A22 is a drug that affects the cell shape of bacteria. It functions by affecting the polymerization of MreB (Bean et al., 2009; Awuni and Mu, 2019). From the crystal structure of the *C.crescentus* MreB bound to A22 and its less cytotoxic analog MP265, it was shown that it might affect the stability of the double protofilament formed by lateral interaction between the two protofilaments (van den Ent et al., 2014), which is the functional form of MreB (Fig 3.3 D). In the A22 bound CcMreB structure, the drug interacts with Glu140 (Fig 3.9 A). This sequesters the interaction of Glu with the catalytic water.

We carried out a comparative structural study for ScMreB5 – AMP-PNP with CcMreB structures to predict if the A22 drug can bind to ScMreB5. For this, we analyzed two structures of CcMreB. First is the double protofilament CcMreB structure bound to AMP-PNP (PDB ID: 4CZJ). Second, is the single protofilament structure of CcMreB bound to A22 and ADP (PDB ID: 4CZG). Third, is the single protofilament structure of TmMreB bound to AMP-PNP (PDB ID: 1JCG) (Fig 3.9 B). We superimposed MreB structures (ScMreB5 – AMP-PNP and CcMreB – A22) with respect to the IIA subdomain of CcMreB double protofilament. Then, we looked at the A22 binding site that is near the nucleotide-binding pocket of MreB (Fig 3.9 C – E). The loop connecting the IA to IIA interacts with A22 in the CcMreB structure. This loop moves away from the A22 binding site in the double protofilament AMP-PNP bound CcMreB structure. In CcMreB – AMP-PNP structures, the

residues that hold the loop are Arg72, Arg75, and Asp76. Upon A22 binding, only Arg72 interaction remains while the entire loop moves toward the A22 binding pocket.

In the ScMreB5 structure, the residues that hold up the loop in the conformation that facilitate the binding of the A22 drug, are not conserved. Arg72 and Arg75 from CcMreB is replaced by Thr66 and Val69 in ScMreB5 (Fig 3.9 C, F, and G). This breaks the interaction and changes in loop conformation. This further moves the loop away from the A22 binding pocket. The RMSD values for the loop with respect to the CcMreB double protofilament structure are given in Table 3.5. The RMSD value for the loop movement for A22 bound CcMreB and ScMreB5 are similar, showing that the loop moved away in ScMreB5. This might lead to A22 resistance for ScMreB5.

Analyzing the sequence conservation of this loop for all the MreB5s from *Spiroplasma* shows that Thr66 position has Thr/Val and Val69 position has Val/Lys/Arg in other MreB5s (Fig 3.9 F and G). We also attempted a preliminary docking study for A22 over the ScMreB5 – ADP structure. To ensure that docking in “AutoDock Vina” worked correctly, we also used CcMreB – ADP (PDB ID: 4CZF) as a control. A22 did not dock for ScMreB5 whereas it got perfectly localized for CcMreB – ADP structure (Fig 3.10 A and B). The three highest affinity structures, with the least energies (-5.8 to -5.3 kcal/mol), docked on ScMreB5 lie far away from the actual A22 binding pocket (Fig 3.10 B). Further in silico and mutational study will be performed for this to conclusively state ScMreB5 – A22 resistance. Preliminary work on ScMreB5 for A22 resistance was performed in yeast, which has been discussed in Chapter 4.

Table 3.5: Comparison of RMSD values of A22 binding loop of CcMreB, double protofilament (PDB ID: 4CZJ) with other structures

PDB ID	Filament type	RMSD (C α)	Atom pairs
4CZG	A22 and ADP bound, single protofilament (CcMreB)	3.7	10
1JCG	AMP-PNP bound, single protofilament (TmMreB)	1.0	10
7BVY	AMP-PNP bound, single protofilament (ScMreB5)	3.3	10

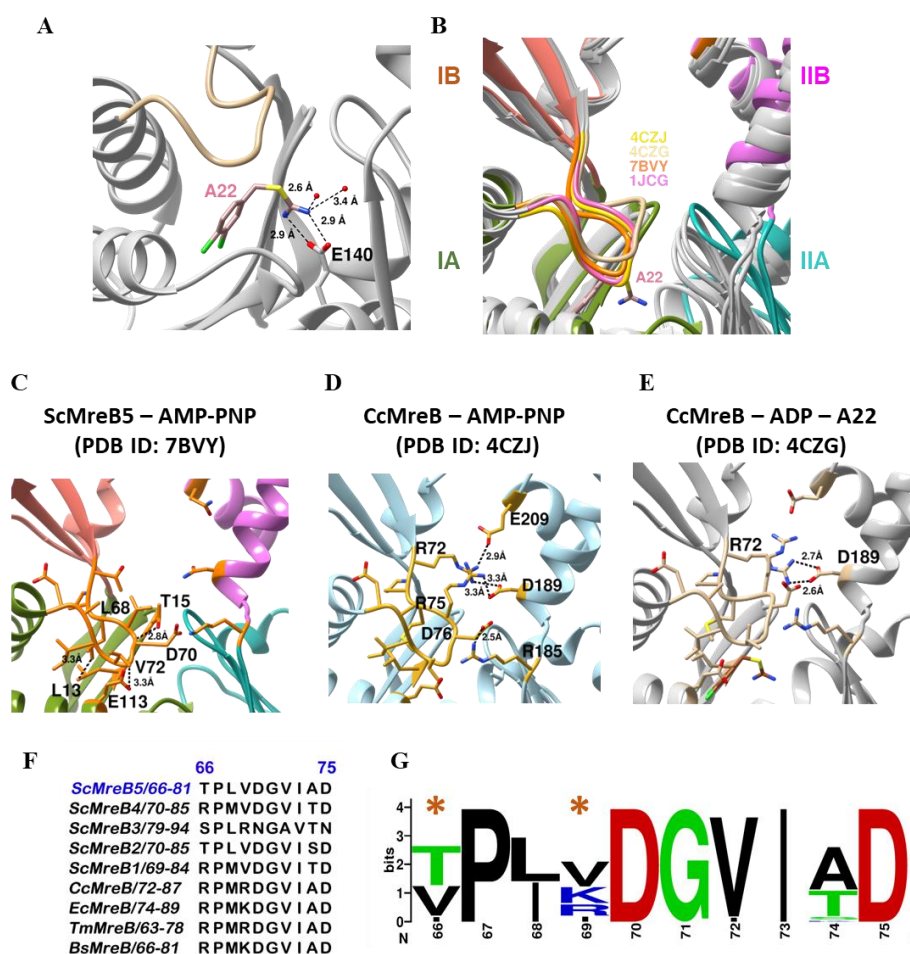


Figure 3.9: Structure and sequence comparison of A22 binding site in ScMreB5.

The A22 binding site is compared by superposing IIA domain of each structure onto IIA domain of CcMreB–AMP-PNP structure (PDB ID: 4CZJ).

(A) A22 interaction with Glu140 in CcMreB-ADP–A22 (PDB ID: 4CZG) structure. **(B)** Superposed loop A22 binding region of CcMreB bound to A22 (PDB ID: 4CZJ) with double protofilament CcMreB (PDB ID: 4CZJ), single protofilament of TmMreB (1JCG) and ScMreB5 (PDB ID: 7BVY). ScMreB5 is coloured subdomain wise and labelled. The loop interacting with A22 drug (light pink) are coloured: yellow for CcMreB – AMP-PNP double protofilament, tan colour for CcMreB bound to A22, orange colour for ScMreB5 – AMP-PNP and pink for TmMreB – AMP-PNP. **(C, D and E)** Loop residues interaction that allows A22 binding at the pocket formed by IA and IIA subdomains for ScMreB5 and CcMreB structures. The interactions that hold the loop are labelled and distances between the interacting residues are shown. **(F)** Sequence alignment of the loop interacting with the A22 for all the *S.citri* MreBs with other A22 sensitive cell-walled bacterial MreBs. **(G)** Web – Logo showing the conservation of the loop residues across all MreB5s from *Spiroplasma* species. The residues T66 and V69 analysed in the study are marked (orange asterisk).

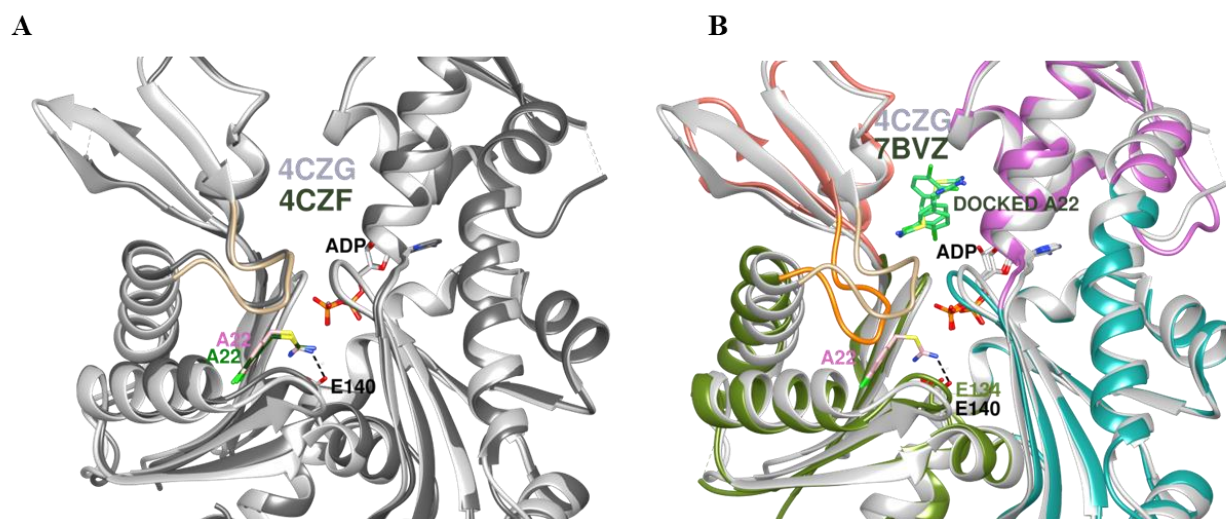


Figure 3.10: Docking A22 does not lead to the binding at the A22 site in ScMreB5.

(A) Superposed structure of CcMreB – ADP (PDB ID: 4CZF, dark grey) with CcMreB – ADP – A22 (PDB ID: 4CZG, light grey), shows localization of docked A22 (dark green), in correct orientation, over crystallized A22 (pink). (B) Superposed structure of CcMreB – ADP (PDB ID: 4CZF, dark grey) with ScMreB5 – ADP (PDB ID: 7BVZ, subdomain wise colored), shows localization of docked A22 (light green), away from the A22 binding site.

3.4: Discussion

This chapter gives a detailed analysis of the structural features of ScMreB5 and other MreBs known so far. Structural analysis of ScMreB5 revealed that the conserved features of MreB and other actin family members are also well conserved for ScMreB5. Interestingly, ScMreB5 has K^+ ion at the nucleotide-binding pocket that renders the stability to natively bound ADP. A similar subunit repeats as observed for other MreB structures is also the same for ScMreB5. Although our crystal structures capture single protofilament assembly, the functional state of MreB is an antiparallel double protofilament organization, which had been captured only in one of the structures of CcMreB, where the membrane interacting surface of the two protofilaments is on the same side. Recent structures of SeMreB3, show antiparallel protofilament organization in their crystal packing as well. However, they do not represent the functional assembly of MreB double protofilament.

To understand the conformational change occurring upon nucleotide binding and hydrolysis, we looked at the structures of all the MreBs in different nucleotide states. Subdomain-wise comparison showed that not much drastic movement occurs in different nucleotide bound and

different filament states within MreBs. From our domain angle analysis, we demonstrate that the double protofilament AMP-PNP bound state of CcMreB is the most compact state of the protein. Subdomains IB and IIB move closer to the nucleotide-binding pocket which further decreases the dihedral angle to a minimum. Hence, it could be postulated that as an ATP-bound monomeric MreB transitions from a single protofilament to an antiparallel double protofilament, there is an eventual decrease in the subdomain angles. This would orient the nucleotide for an optimal orientation of the active site residues, eventually leading to hydrolysis.

The active site residues, including the residues coordinating Mg^{2+} and those required for optimal orientation of the catalytic water, are highly conserved in MreBs, actins and across the Hsp70 superfamily members. Interestingly, for all MreB3s of *Spiroplasma*, highly conserved active site residues such as catalytic glutamate and threonine (equivalent to Glu134 and Thr161 of ScMreB5) are not conserved. This has provided different catalytic and polymerization properties to SeMreB3 (Takahashi et al., 2022). ATPase activity characterization of these residues has been discussed in Chapter 4.

Membrane interaction is a unique feature of MreBs, that further facilitate the interaction with the cell membrane and peptidoglycan synthesis machinery. From sequence analysis of all MreB5s, we observe a positively charged C-terminal extension, absent in other cell-walled and *Spiroplasma* MreBs. This region would also face the membrane binding side and hence might play a role in membrane binding. This motivated us to perform membrane binding studies for ScMreB5 and its mutants, which will be detailed in Chapter 5.

Lastly, our sequence and preliminary structural comparison studies, supplemented with basic molecular docking show that ScMreB5 could be resistant to A22 drug. This could hint at a distinctive feature of MreBs, and help in understanding the existence of A22-resistant variants of MreBs across different bacterial species and also the emergence of resistant variants.

3.5: References

- Awuni, E., and Y. Mu. 2019. Effect of A22 on the Conformation of Bacterial Actin MreB. *International Journal of Molecular Sciences*. 20:1304. doi:10.3390/ijms20061304.
- Bean, G.J., S.T. Flickinger, W.M. Westler, M.E. McCully, D. Sept, D.B. Weibel, and K.J. Amann. 2009. A22 disrupts the bacterial actin cytoskeleton by directly binding and inducing a low-affinity state in MreB. *Biochemistry*. 48:4852–4857. doi:10.1021/bi900014d.
- Bork, P., C. Sander, and A. Valencia. 1992. An ATPase domain common to prokaryotic cell cycle proteins, sugar kinases, actin, and hsp70 heat shock proteins. *PNAS*. 89:7290–7294. doi:10.1073/pnas.89.16.7290.
- Clamp, M., J. Cuff, S.M. Searle, and G.J. Barton. 2004. The Jalview Java alignment editor. *Bioinformatics*. 20:426–427. doi:10.1093/bioinformatics/btg430.
- Crooks, G.E., G. Hon, J.-M. Chandonia, and S.E. Brenner. 2004. WebLogo: a sequence logo generator. *Genome Res*. 14:1188–1190. doi:10.1101/gr.849004.
- Dye, N.A., Z. Pincus, I.C. Fisher, L. Shapiro, and J.A. Theriot. 2011. Mutations in the nucleotide binding pocket of MreB can alter cell curvature and polar morphology in *Caulobacter*. *Molecular Microbiology*. 81:368–394. doi:10.1111/j.1365-2958.2011.07698.x.
- van den Ent, F., L.A. Amos, and J. Löwe. 2001. Prokaryotic origin of the actin cytoskeleton. *Nature*. 413:39–44. doi:10.1038/35092500.
- van den Ent, F., T. Izoré, T.A.M. Bharat, C.M. Johnson, and J. Löwe. 2014. Bacterial actin MreB forms antiparallel double filaments. *eLife*. doi:10.7554/eLife.02634.
- Formstone, A., and J. Errington. 2005. A magnesium-dependent mreB null mutant : implications for the role of mreB in *Bacillus subtilis*. 55:1646–1657. doi:10.1111/j.1365-2958.2005.04506.x.
- Harne, S., S. Duret, V. Pande, M. Bapat, L. Béven, and P. Gayathri. 2020. MreB5 Is a Determinant of Rod-to-Helical Transition in the Cell-Wall-less Bacterium *Spiroplasma*. *Current Biology*. doi:10.1016/j.cub.2020.08.093.
- Nyman, T., H. Schüler, E. Korenbaum, C.E. Schutt, R. Karlsson, and U. Lindberg. 2002. The role of MeH73 in actin polymerization and ATP hydrolysis11Edited by R. Huber. *Journal of Molecular Biology*. 317:577–589. doi:10.1006/jmbi.2002.5436.

Pettersen, E.F., T.D. Goddard, C.C. Huang, G.S. Couch, D.M. Greenblatt, E.C. Meng, and T.E. Ferrin. 2004. UCSF Chimera--a visualization system for exploratory research and analysis. *J Comput Chem.* 25:1605–1612. doi:10.1002/jcc.20084.

Salje, J., F. van den Ent, P. de Boer, and J. Löwe. 2011. Direct Membrane Binding by Bacterial Actin MreB. *Molecular Cell.* 43:478–487. doi:10.1016/j.molcel.2011.07.008.

Sievers, F., A. Wilm, D. Dineen, T.J. Gibson, K. Karplus, W. Li, R. Lopez, H. McWilliam, M. Remmert, J. Söding, J.D. Thompson, and D.G. Higgins. 2011. Fast, scalable generation of high-quality protein multiple sequence alignments using Clustal Omega. *Mol Syst Biol.* 7:539. doi:10.1038/msb.2011.75.

Takahashi, D., I. Fujiwara, Y. Sasajima, A. Narita, K. Imada, and M. Miyata. 2022. ATP-dependent polymerization dynamics of bacterial actin proteins involved in Spiroplasma swimming. *Open Biology.* doi:10.1098/rsob.220083.

Chapter 4: ATPase activity and polymerization dynamics of ScMreB5

Some sections reprinted from: Pande et al., *Journal of Cell Biology*, 2022

DOI: [10.1083/jcb.202106092](https://doi.org/10.1083/jcb.202106092)

4.1: Introduction

MreB filaments possess an antiparallel double-protofilament assembly (van den Ent et al., 2014), as opposed to the parallel protofilament arrangement in most actin family members such as eukaryotic actin (Chou and Pollard, 2019; Fujii et al., 2010) and ParM (Gayathri et al., 2013), an actin-like protein in plasmid segregation. In vitro polymerization and hydrolytic activity studies for MreB has been limited to a few organisms, *T. maritima* (Bean and Amann, 2008), *C. crescentus* (van den Ent et al., 2014), *E. coli* (Nurse and Marians, 2013) and very recently, *S. eriocheris* (Takahashi et al., 2023).

MreB possesses conserved ATP hydrolysis residues. Due to the geometry of the nucleotide-binding pocket, it can also accommodate and hydrolyze GTP (Esue et al., 2006). Light scattering assay from the *E.coli*, *T.maritima* and *B.subtilis* MreBs have shown MreB polymerization in the presence of nucleotides, ATP, ADP, GTP, and AMP-PNP (Bean and Amann, 2008; Nurse and Marians, 2013; Mayer and Amann, 2009; Gaballah et al., 2011). Interestingly, for *B.subtilis*, MreB can also undergo polymerization in a nucleotide-independent manner (Mayer and Amann, 2009). Therefore, the significance of nucleotide binding or hydrolysis in filament formation and dynamics for MreB function is ambiguous. Mutational defects in the ATP binding pocket of MreB alter the filament localization, cell morphology and chromosome segregation in *B.subtilis* and *C.crescentus* (Defeu Soufo and Graumann, 2006). The spatial regulation of MreB filaments in response to cellular curvature is hypothesized to depend on hydrolytic activity (Errington, 2015). Though ATP-hydrolysis-dependent dynamics appear to be important for MreB function, the nature of filament dynamics and its exact role is unknown. The observation of filament dynamics through an in vitro reconstitution approach has not been successful for MreB, probably due to challenges with imaging the short filaments using light microscopy. Despite the ambiguity with respect to the role of ATP hydrolysis, it is intriguing to observe that active site residues and nucleotide-binding motifs are conserved across all MreBs (Chapter 4).

With this background, we aimed to understand the role of nucleotide hydrolysis in ScMreB5 filament assembly. We carried out *in vitro* mutational studies of the ATP hydrolysis residues and polymerization interface, and their biochemical characterization through ATP hydrolysis assay. This was followed by attempts to study polymerization dynamics using light scattering assay, and yeast expression system. Additionally, cryoEM was performed to observe filaments

under different nucleotide states. We have also performed preliminary work on understanding A22 resistance of ScMreB5 using the yeast expression system.

4.2: Materials and Methods

4.2.1 Phosphate release assay for estimating ATPase activity

The release of inorganic phosphate during ATP hydrolysis was measured by malachite green assay (Feng et al., 2011). Protein was pre-spun at 22,000 g at 4°C for 20 min. Concentration estimation was done with Bradford reagent using bovine serum albumin (0 – 1 mg/mL) as standards.

For determining Michaelis – Menten constants, protein was added at a final concentration of 10 μ M to the master mix of buffer containing varying concentrations of ATP (0 – 3 mM) and 3 mM MgCl₂ in buffer A (300 mM KCl , 50 mM Tris, pH 8) and mixed. For comparative study of wildtype and the mutants, protein was added at a final concentration of 10 μ M to the master mix of buffer containing ATP and MgCl₂ to achieve final concentrations of 1 mM ATP and 1 mM MgCl₂ in buffer A (300 mM KCl and 50 mM Tris, pH 8) and mixed.

To stop the reactions for a 0-time point reading, 20 μ l reaction was immediately mixed with 5 μ l of 0.5 M EDTA in a 96-well plate. The rest of the master mix was incubated at 25°C for 60 min. After 60 min, the reaction was stopped with 0.5 M EDTA in the same manner.

Simultaneously, phosphate standards (0, 25, 50, 75, 100 ,150, 200, 250 and 300 μ M) were freshly diluted from 400 μ M NaH₂PO₄. To measure the amount of phosphate release, malachite green solution was freshly prepared using 800 μ l of 3.5 mM Malachite Green (38800; Sigma-Aldrich) dissolved in 3N H₂SO₄, 16 μ l of 11% Tween 20 (P-1379; Sigma-Aldrich), and 200 μ l of 7.5% wt/vol ammonium molybdate (277908; Sigma-Aldrich). 50 μ l of malachite green solution was added to the stopped reactions and phosphate standards. Absorbance of malachite green was measured in Varioskan Flash (4.00.53) within 5 – 8 min after addition at 630 nm wavelength.

For calculating the k_{obs} (min^{-1}) (for wildtype and mutants) and Michaelis - Menten constants (for wildtype), first, the slope was calculated from the phosphate standards. The absorbance of protein containing reaction was calculated by subtracting the blank reaction absorbance (without protein). The amount of phosphate release (in μ M) after 60 min was calculated by dividing the subtracted absorbance by the slope. The rate of phosphate release, ($\mu\text{M min}^{-1}$),

was calculated by dividing the amount of phosphate release by 60 mins. The Michaelis – Menten plot was generated with amount of phosphate released per min ($\mu\text{M min}^{-1}$) on y – axis and increasing ATP concentrations on x – axis. The curve was fitted with the Michaelis Menten equation $V_0 = V_{\text{max}} ([S]/([S] + K_M))$. For calculating the phosphate release per min (k_{obs}) for wildtype and mutants at 1 mM ATP concentration, the rate of phosphate release ($\mu\text{M min}^{-1}$) was divided by the protein concentration used, i.e., 10 μM .

Prism v5.00 for Windows was used for statistical analysis and plotting the graphs. Statistical significance was estimated by unpaired t test, two tailed. The data in the graph are expressed as mean \pm SEM.

4.2.2: Light scattering assay with the purified protein

For performing polymerization assay for ScMreB5 in the presence of different nucleotides, protein was pre-spun at 100,000 g at 4°C for 20 min. Concentration estimation was done using Bradford reagent and BSA as standards (0.1 – 1 mg/mL). In a 96 well UV transparent plate (Corning), 200 μl reaction was made by mixing 50 μM (final concentration) of protein with buffer A (300 mM KCl, 50 mM Tris, pH 8) and 2 mM MgCl_2 . Initial absorbance (without nucleotide) readings were taken at 400 nm at every 20 secs intervals in Varioskan Flash (4.00.53) at 25 °C for 45 mins. After 45 mins, 2 mM (final concentration) of nucleotide (ATP, ADP, AMP-PNP) was maintained in the respective wells. Further readings were taken for 60 mins. Data was analysed and averaged in Microsoft Excel and plotted using Prism v5.00 for Windows.

4.2.3: Light scattering assay complemented with gel filtration

Protein was prespun at 22,000 g at 4°C for 20 min. Around 4 mg/ml of 300 μl of protein was injected into Superdex 75 (GE Life Sciences) that was pre-equilibrated with buffer A (50 mM Tris, pH 8, and 300 mM KCl). 200 μl of eluted monomeric fraction of protein was immediately taken for light scattering measurement. Measurement was performed in FluoroMax-4 (Horiba), with excitation and emission slit widths of 2 nm each and excitation and emission wavelength of 400 nm at 25°C. Readings were taken for 1,000 s for WT and 2,500 s for the polymerization mutant K57A. Simultaneously, protein estimation of the fraction subjected for light scattering was performed using Bradford reagent and BSA standards (0.1 – 1 mg/mL).

4.2.4: Cryo-EM

For visualizing the filaments of ScMreB5^{WT} and the ATPase mutant ScMreB5^{E134A}, cryo-EM was carried out. Quantifoil Au 1.2/1.3 grids that were glow discharged for 90 s were used. Protein was ultra-centrifuged at 100,000 g for 25 min at 4°C. Nucleotide (AMP-PNP, ADP, or ATP) and MgCl₂ (at 5 mM final concentrations for both) were added to a final concentration of 50 μM protein and incubated at 25°C for 10–15 min. 3 μl of the sample was put on the grid and incubated for 5 – 10 s before blotting for 3 s, followed by plunge-freezing into liquid ethane for vitrification using an FEI Vitrobot. For image acquisition, grids were mounted on a Titan-Krios 300 KeV electron microscope with Falcon-3 direct electron detector, and images were taken at a magnification of 59,000×. Images of the filaments were generated in ImageJ 1.52n (Rueden et al., 2017).

4.2.6: Cloning of N- terminal GFP ScMreB5 and ATPase mutant

ScMreB5^{WT} and ScMreB5^{E134A} cloned in pHis17 vector were used as a template for cloning these genes into pREP41NGFP_CD1476 vector. The vector has GFP tag was before the *NdeI* and *BamHI* site. *scmreb5*^{WT} was cloned between *NdeI* and *BamHI* restriction sites using restriction free (RF) cloning (van den Ent and Löwe, 2006) using the primers given in the table 4.1. *scmreb5*^{E134A} was cloned using pREP-NGFP-ScMreB5^{WT} as a template and specific primers for incorporating E134A mutation, as given in table 2.1.

Table 4.1: List of primers and clones obtained

Primer name	Sequence	Clones Obtained
pREP_S cM5-F	GGCATGGATGAACTATACAAAC ATATGATGAGACCAGAACTAG ACCATTTATTTC	pREP-NGFP-ScMreB5 ^{WT} and pREP-NGFP-ScMreB5 ^{E134A}
pREP_S cM5-R	GGCAAGGGAGACATTCCTTTTA CCCGGGGATCCTTATTTICTTTT TTTACCTAATGTTG	

4.3: Results

4.3.1: ATPase activity of ScMreB5^{WT} and its mutants

By measuring the amount of phosphate release using a colorimetric assay, ATPase activity for the wildtype and mutants of ScMreB5 were determined. For the assay discussed in this section, both the wildtype and the mutants were purified by affinity chromatography followed by dialysis and concentration (as discussed in Chapter 2). Protein concentration of 10 μ M was used, since below this concentration, phosphate release could not be detected for ScMreB5.

Firstly, ATPase activity assay was performed with the increasing concentrations of ATP (0 to 3 mM). For getting the kinetic parameters, Michaelis – Menten plot was obtained (Fig 4.1 A). By fitting the plot to the equation, $V_0 = V_{max} ([S]/([S] + K_M)$, kinetic parameters were calculated (Table 4.2).

We further performed comparative ATPase activity measurements of ScMreB5^{WT} and active site residue mutants. ScMreB5^{WT} showed ATPase activity which was also comparable ATPase activity of the other MreBs shown in Table 4.3. The ATPase activity measurement was done for, ScMreB5^{D12A}, ScMreB5^{D156A}, ScMreB5^{E134A}, and ScMreB5^{T161A} and ScMreB5^{D70A}. The structural and sequence analysis of these residues are discussed in result section of Chapter 3. All these mutants showed a decrease in ATPase activity, compared with WT (Fig 4.1 B). k_{obs} (min^{-1}) values for ScMreB5^{WT} ($0.15 \pm 0.007 \text{ min}^{-1}$) and the mutants (ScMreB5^{D12A}, 0.02 ± 0.008 ; ScMreB5^{D156A}, 0.08 ± 0.014 , ScMreB5^{E134A}, 0.01 ± 0.004 ; ScMreB5^{T161A}, 0.0005 ± 0.001 ; ScMreB5^{D70A}, 0.05 ± 0.002). Table 4.3 gives a comparative ATPase activity value for ScMreB5^{WT} and other MreBs.

Crystal structures of the various states of CcMreB showed that conformational changes upon polymerization affect the positioning of the catalytic residues at the active site (van den Ent et al., 2014). Hence, in addition to mutants of the ATP binding pocket residues, we checked the ATPase activity of a polymerization interface mutant, ScMreB5^{K57A}. ATPase activity of ScMreB5^{K57A} was slightly lower than the wildtype (ScMreB5^{K57A}, $0.1 \pm 0.01 \text{ min}^{-1}$).

Although, complete abrogation of activity was not observed, this indicates an allosteric communication between the polymerization interface and the active site.

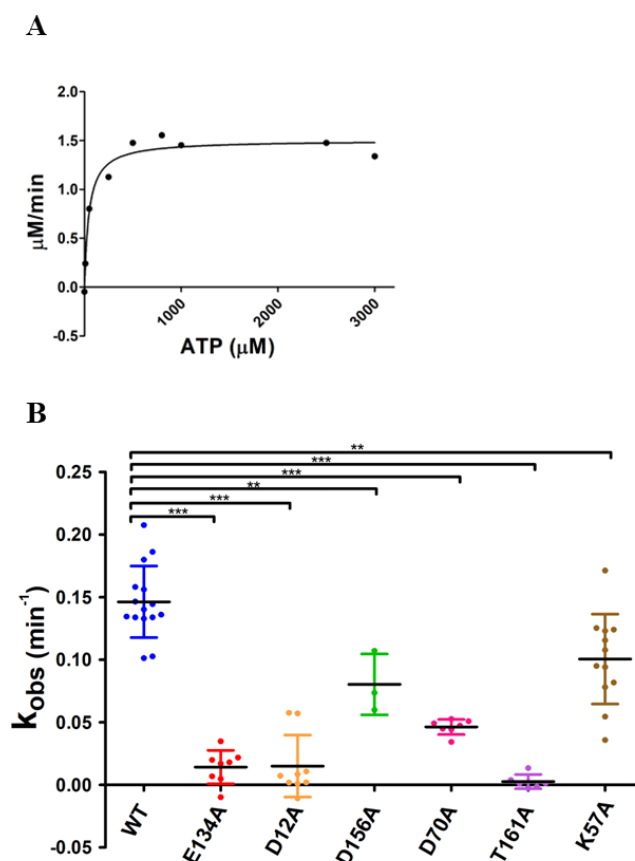


Figure 4.1: ScMreB5 is an active ATPase.

(A) ATPase activity ($\mu\text{M}/\text{min}$) of ScMreB5^{WT} was measured by increasing ATP concentration, the curve was fitted with the Michaelis-Menten equation ($V_0 = V_{\text{max}} ([S]/([S] + K_M))$), (N = 1, n = 1). (B) ATPase activity characterization of ScMreB5. Apparent specific activity k_{obs} (min^{-1}) for the ScMreB5^{WT}, active site mutants, and the polymerization mutant (ScMreB5^{WT} [WT; N = 3; n = 15], ScMreB5^{E134A} [E134A; N = 3; n = 8], ScMreB5^{D12A} [D12A; N = 2; n = 7], ScMreB5^{D156A} [D156A; N = 2; n = 3], ScMreB5^{D70A} [D70A; N = 2; n = 7], ScMreB5^{T161A} [T161A; N = 1; n = 8], and ScMreB5^{K57A} [K57A; N = 2; n = 12]; N, number of independent protein purification batches; n, total number of repeats). The error bar denotes mean with SEM; unpaired t test, two-tailed; ***, P < 0.0001; **, P = 0.001–0.002. 10 μM protein, 1 mM ATP, and 1 mM MgCl_2 were used in both the assays.

Table 4.2: Kinetic parameters for ScMreB5^{WT} from Michaelis –Menten plot

Parameters	ScMreB5 ^{WT}
V _{max} (μM/min)	1.503 ± 0.05
K _m (μM)	47.26 ± 0.05
k _{cat} (min ⁻¹)	0.15 (calculated) 0.15 ± 0.007 (observed)

Table 4.3: Comparison of ATPase activity for different MreBs

Protein	Organism	Activity [k _{obs} (min ⁻¹)]	Temperature	Assay used	Reference
ScMreB5	<i>Spiroplasma citri</i>	0.15 ± 0.007	25° C	Colorimetric (Malachite Green Assay)	(Pande et al., 2022)
EcMreB	<i>Escherichia coli</i>	0.17 ± 0.01	37° C	Radiolabelled [γ- ³² P]ATP	(Nurse and Marians, 2013)
TmMreB	<i>Thermotoga maritima</i>	0.10 ± 0.01	65° C	Colorimetric (Malachite Green Assay)	(Esue et al., 2004)
SeMreB5	<i>Spiroplasma eriocheris</i>	0.09 ± 0.01	-	EnzChek kits (Thermo Fisher Scientific)	(Takahashi et al., 2023)
GsMreB	<i>Geobacillus stearothermophilus</i>	0.08 ± 0.004 0.032 ± 0.002	53° C 37° C	Colorimetric (Malachite Green Assay)	(Mao et al., 2022)

4.3.2: Light scattering assays

Our initial polymerization study involved pelleting assay and light scattering assay in studying the nucleotide dependence for ScMreB5 polymerization. However, filaments of ScMreB5 did not pellet in any nucleotide condition, hence we were unable to use this assay further.

For light scattering assay, we measured the increase in A_{400} (absorbance at 400 nm) under different nucleotide conditions for ScMreB5^{WT}. For this assay as well, we used protein that was not subjected for size exclusion chromatography, since higher concentration of protein was required to see the scattering initially. Nucleotide addition was done after 45 mins (time for absorbance stabilization). Post ATP addition, a sharp increase in light scattering was observed after 500 secs, reaching saturation at 1300 secs. In no nucleotide condition, there was continuous increase in the absorbance (Fig 4.2 A). In both ADP and AMP-PNP condition, no further increase in absorbance was observed post-nucleotide addition (Fig 4.2 A).

To confirm that the purified protein polymerizes without nucleotide addition, we performed size exclusion combined with light scattering of the eluted monomeric fraction. ScMreB5^{WT} and polymerization mutant ScMreB5^{K57A} were tested. We observed that as soon as the protein elutes as a monomer (according to the elution volume in SEC), it undergoes polymerization, as seen from the increase in absorbance after 500 secs (Fig 4.2 B) in light scattering measurements. Hence, ScMreB5^{WT} in solution might exist as a dynamic filament. Despite a mutation at the polymerization interface, ScMreB5^{K57A} underwent polymerization post elution (Fig 4.2 C).

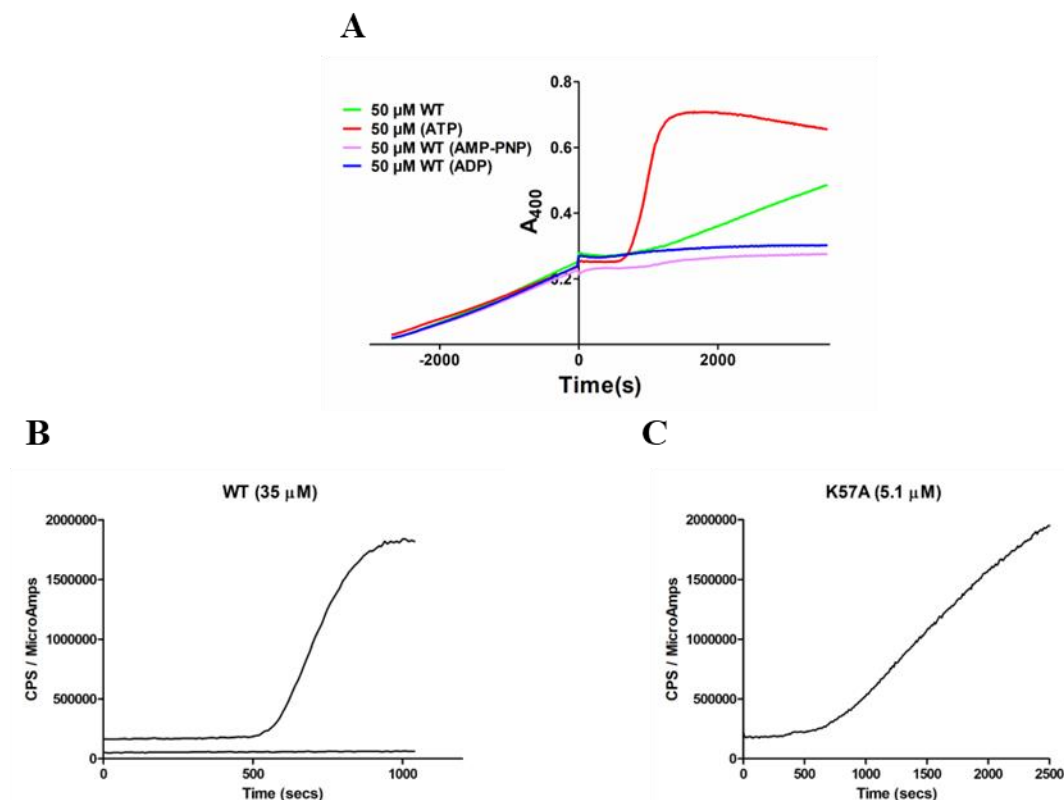


Figure 4.2: ScMreB5^{WT} polymerizes without addition of nucleotide.

(A) Averaged light scattering assay plot (N = 2 and n = 3) performed at 400 nm absorbance at 25 °C shows polymerization of ScMreB5^{WT} (50 μ M) under different nucleotide conditions. Polymerization was observed prior to any nucleotide addition. Polymerization was maximum in the presence of ATP, followed by without nucleotide. Polymerization was least in the presence of AMP-PNP and ADP. Before adding nucleotide and Mg²⁺ (1 mM each), readings are taken for 45 mins, after which Mg²⁺ and nucleotide were added and scattering was monitored till 60 mins. (B and C) Light scattering intensity (immediately post gel filtration) was measured for ScMreB5^{WT} and ScMreB5^{K57A} (polymerization mutant) undergoing polymerization independent of nucleotide addition. Concentration of proteins ScMreB5^{WT} and ScMreB5^{K57A} monitored for light scattering were 35 and 5 μ M, respectively at 400 nm wavelength.

4.3.3: Cryo-electron microscopy study

We attempted to study the nucleotide dependence of filament formation for ScMreB5^{WT} and its ATP hydrolysis mutant ScMreB5^{E134A} by observing the presence of filaments in vitro using cryo-

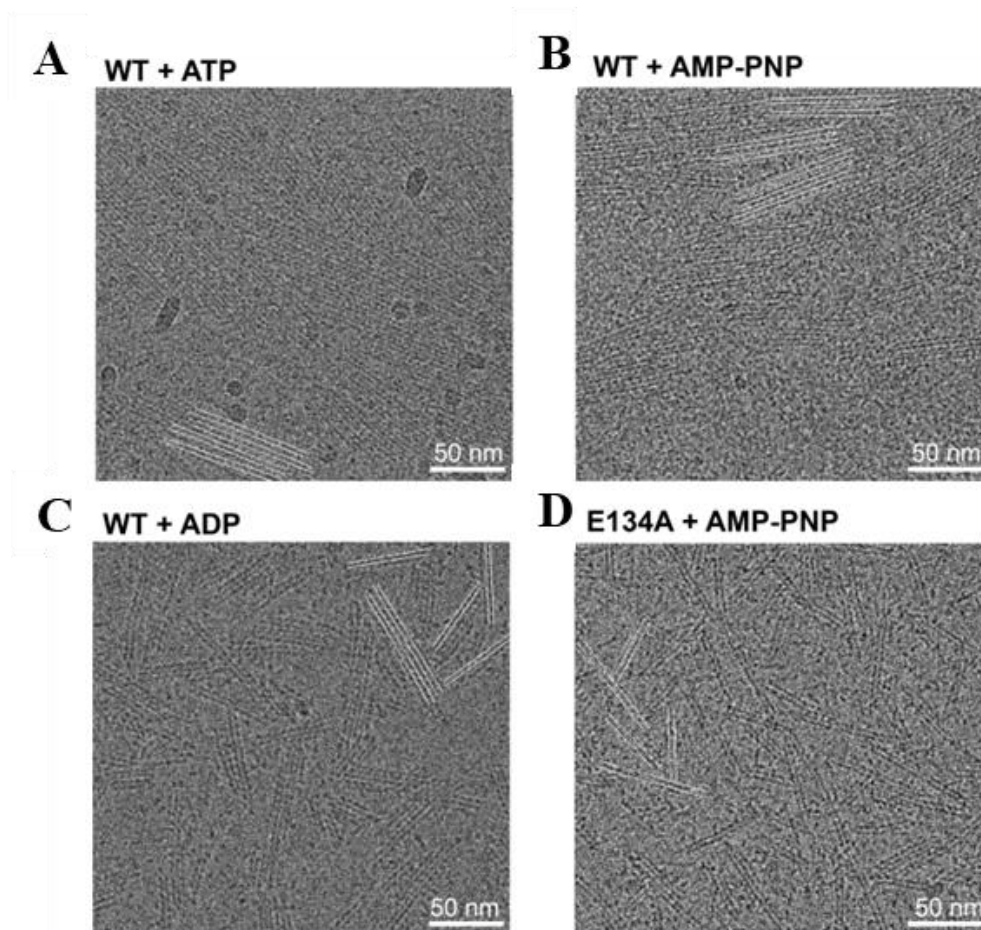


Figure 4.3: ScMreB5 filaments form double-protofilament assemblies independent of nucleotide hydrolysis.

(A–D) Cryo-electron micrographs showing filaments of ScMreB5^{WT} in the presence of 5 mM ATP and MgCl₂ (A); ScMreB5^{WT} in the presence of 5 mM AMP-PNP and MgCl₂ (B); ScMreB5^{WT} in the presence of 5 mM ADP and MgCl₂ (C); and ScMreB5^{E134A} mutant (hydrolysis deficient) in the presence of 5 mM AMP-PNP and MgCl₂ (D). A few double protofilaments are highlighted by pairs of parallel white lines to enable easy visualization of the filament distribution. Concentration of protein used was 50 μM. Scale bar denotes 50 nm.

EM. ScMreB5^{WT} in the presence of ATP (Fig. 4.3 A) and AMP-PNP (Fig. 4.3 B) formed a high density of double protofilament assemblies having a sheet-like appearance of laterally

associated filament bundles. We also observed filaments of ScMreB5^{WT} in the presence of ADP (Fig. 4.3 C) and ScMreB5^{E134A} in the presence of AMP-PNP (Fig. 4.3 D). This implied that despite the absence of increased light scattering (Fig. 4.2 A), the protein existed as filaments in solution. However, very few sheet-like bundles were observed in ScMreB5^{WT}-ADP and ScMreB5^{E134A}-AMP-PNP compared with ScMreB5^{WT}-ATP and -AMP-PNP (Fig. 3, A-D). While filaments observed for ScMreB5^{WT}-ADP and ScMreB5^{E134A}-AMP-PNP demonstrated that ATP hydrolysis was not required for filament formation in vitro. This was in contrast to our results from light scattering assay. Lower filament bundles in these conditions is suggestive of lower filament density or defective bundling or both.

4.3.4: ScMreB5 polymerization dynamics study in yeast

This work was performed in collaboration with the lab of Dr. Srinivasan Ramanujam, NISER, Bhubaneswar. Preliminary experiments and observations were done by me and further standardization and quantitative work was carried forward by Nivedita. Mitra in the lab. All the yeast experiments lab pertaining to the publication were performed by Nivedita. The main results of which, citing the figures from the paper (Pande et al., 2022) are briefly discussed below.

With an aim to visualize the polymerization dynamics of ScMreB5 filaments, I cloned ScMreB5^{WT} and ScMreB5^{E134A} as an GFP fusion construct in a yeast expression vector (details of which are discussed in the materials and methods section). Subsequently, to check whether the N-terminal GFP does not affect the protein activity, we cloned and expressed ScMreB5^{Nt-GFP} in pHis17 vector for the wildtype (Cloning discussed in the materials and methods section of Chapter 6). The protein was purified as a monomer (Fig 6.5 B) and exhibited ATPase activity (Table 6.6, Chapter 6) and membrane binding ability (Fig 6.5 D, Chapter 6) similar to wildtype. This confirmed that the N-terminal GFP fusion construct for ScMreB5 was functional, hence we further proceeded with our yeast microscopy experiments to observe polymerization dynamics.

N-terminal GFP-fusion constructs of ScMreB5^{WT} and ScMreB5^{E134A}, were expressed in fission yeast and filament assembly were monitored. Dynamics of EcMreB polymerization in fission yeast with a similar N-terminal GFP fusion has been reported (Srinivasan et al., 2007). It served as a useful system to observe the effect of the mutation on filament dynamics and bundling. ScMreB5^{WT} showed long filaments which were parallel to the longitudinal axis

(Fig 4.1 A in Pande et al., 2022) . These filaments eventually bundled up (Pande et al., 2022). However, for ScMreB5^{E134A} fewer and shorter filaments were visible that were unable to undergo bundling. This difference was observed more prominently by super resolution imaging (Fig 4.1 B in Pande et al., 2022). Additionally, lesser number of cells expressing ScMreB5^{E134A} had filaments in comparison to ScMreB5^{WT} expressing cells that had higher filaments.

Polymerization dynamics was further studied through time-lapse imaging of filament formation for ScMreB5^{WT} and ScMreB5^{E134A}. It confirmed that the polymerization and lateral association of filaments were efficient in ScMreB5^{WT} compared to ScMreB5^{E134A} (Fig 5.1 A and E in Pande et al., 2022). Cells expressing ScMreB5^{WT} started polymer formation in ~ 26 mins compared to ScMreB5^{E134A}, where filament started to assemble in ~ 69 mins (Fig 5.1 B in Pande et al., 2022). Hence, from these results it was confirmed that the hydrolytic mutant Glu134 exhibited impaired filament dynamics, lag in polymerization and inefficient bundling.

4.3.5: A22 resistance of ScMreB5

This preliminary work was performed in collaboration with the lab of Dr. Srinivasan Ramanujam, NISER, Bhubaneswar. The yeast experiments were performed by Nivedita Mitra in the lab.

A22 drug inhibits filament formation of N-terminal GFP tagged *E.coli* MreB (EcMreB^{WT}) (Srinivasan et al., 2007). From our structural analysis discussed in Chapter 3, we hypothesized that ScMreB5 could be resistant to A22. A22 binds to monomeric MreB and prevents polymerization (Awuni and Mu, 2019; van den Ent et al., 2014). Therefore, light scattering experiments could not be performed for ScMreB5 in the presence of A22, since protein existed in a polymerized (or dynamic) state as concluded from our light scattering assay data. Hence, to test our hypothesis we expressed the N-terminal GFP tagged EcMreB^{WT} and ScMreB5^{WT} in *S.pombe* cells. Our preliminary observation showed that, indeed, ScMreB5 was resistant to A22 (Fig 4.4 A). ScMreB5^{WT}, could form filaments even at dosage above EcMreB filament formation inhibitory concentration (Fig 4.4 A and B).

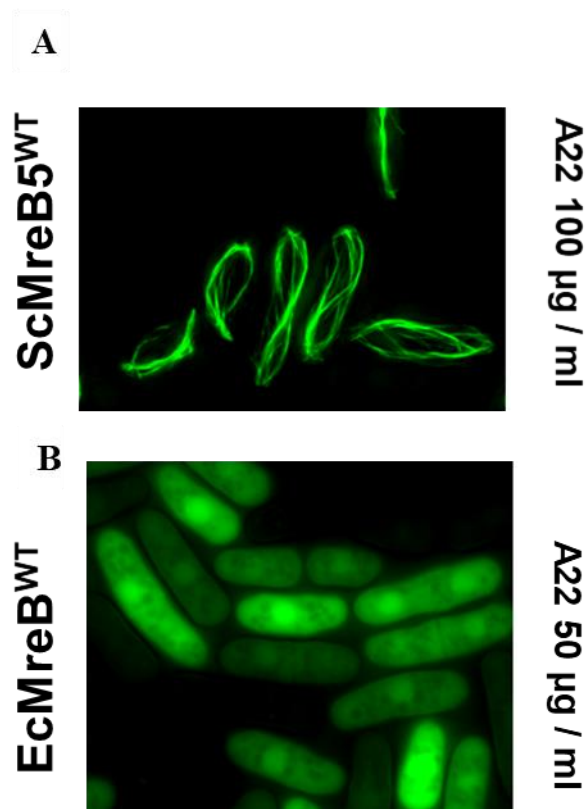


Figure 4.4: A22 does not inhibit the filament formation of N-terminal GFP tagged ScMreB5 expressed in yeast.

(A) ScMreB5^{WT} and with N-terminal tagged GFP expressed in *S. pombe* cells. Representative images are shown for the GFP channel. Filament formation is not inhibited at 100 µg/ml of A22 for ScMreB5, (B) For EcMreB, diffused fluorescence is observed even at 50 µg/ml A22 concentration. Preliminary experiment performed by Nivedita Mitra, NISER.

4.4: Discussion

In this chapter we carried out ATP hydrolysis and polymerization dynamics studies for ScMreB5. We show that these features are conserved for ScMreB5, like other MreBs from the cell – walled bacteria studied so far. The active site residues, including the residues coordinating Mg²⁺ and those required for optimal orientation of the catalytic water, are highly conserved in MreBs and actins and across the Hsp70 superfamily members. Our ATPase activity measurements point out a role for these residues in ATP hydrolysis, emphasizing that ATP hydrolysis is an inevitable feature for MreB (as well as ScMreB5) function. Effects of the polymeric interface mutant ScMreB5^{K57A} and the inter-subdomain contact mutant ScMreB5^{D70A} on ATPase activity suggest allosteric communication between the ATP-binding

pocket and the polymerization interface in MreB too, a conserved feature of many characterized actin family members (Chu and Voth, 2005; Vorobiev et al., 2003). The role of nucleotide identity and hydrolysis in MreB polymerization is still unclear. Our light scattering assay data shows that ScMreB5, in solution, exists in a dynamic state, probably because of pre-bound to ADP at the nucleotide binding pocket. Thus, nucleotide dependence in filament formation in vitro is could not be tested for ScMreB5. The electron microscopy studies of MreB filaments of cell-walled bacteria have shown that there is dependence on monovalent salt concentration, bivalent cation, pH and nucleotide identities in filament formation (Bean and Amann, 2008; Mayer and Amann, 2009; Popp et al., 2010). These properties are specific for different cell-walled bacterial MreBs. For SeMreB3 and SeMreB5 from cell-wall less bacteria *S.eriocheris*, polymerization has been shown in presence of ATP (Takahashi et al., 2022). Based on the observation of electron microscopy and pelleting assay to determine polymerization, both the protein could polymerize in presence of NaCl (1M) and KCl (100 mM) (Takahashi et al., 2022). Cryo-electron microscopy study has shown the presence of antiparallel double protofilament assembly as sheets and individual filaments for ScMreB5. This further indicates the conservation of antiparallel protofilament arrangement for ScMreB5 as reported for SeMreB3 (Takahashi et al., 2023) and CcMreB (van den Ent et al., 2014).

From our yeast microscopy experiment, we show that the residue Glu134 is essential for efficient polymerization as well as filament bundling. In-depth analysis of nucleotide-binding pocket of the structures of CcMreB, show that catalytic Glu (Glu140 in CcMreB and Glu134 in ScMreB5) functions as an interaction hub, forming a network of interactions with γ -phosphate of the nucleotide, catalytic water, and residues from all four MreB subdomains. The entire network of interactions (labeled i–vii in Fig. 4.5) with all four subdomains was observed only in the double-filament conformation (PDB accession no. 4CZJ; Fig. 4.5) and not in the single-protofilament or monomeric states (PDB accession nos. 4CZI, 4CZF, or 4CZM in Fig. 4.5). The γ -phosphate of the nucleotide and Glu140Cc side chain play key role in the network. Thus, the residue may act as the sensor for the ATP-bound state and trigger the transition to the double-protofilament conformation—an important feature of nucleotide state-dependent polymerization. Additionally, the requirement of Glu140Cc in providing an optimal active site geometry for ATP hydrolysis hints that the residue might also trigger efficient ATP hydrolysis, suggesting a crucial role in nucleotide-dependent polymerization dynamics. Our preliminary data on A22 polymerization inhibition for ScMreB5 indicates that

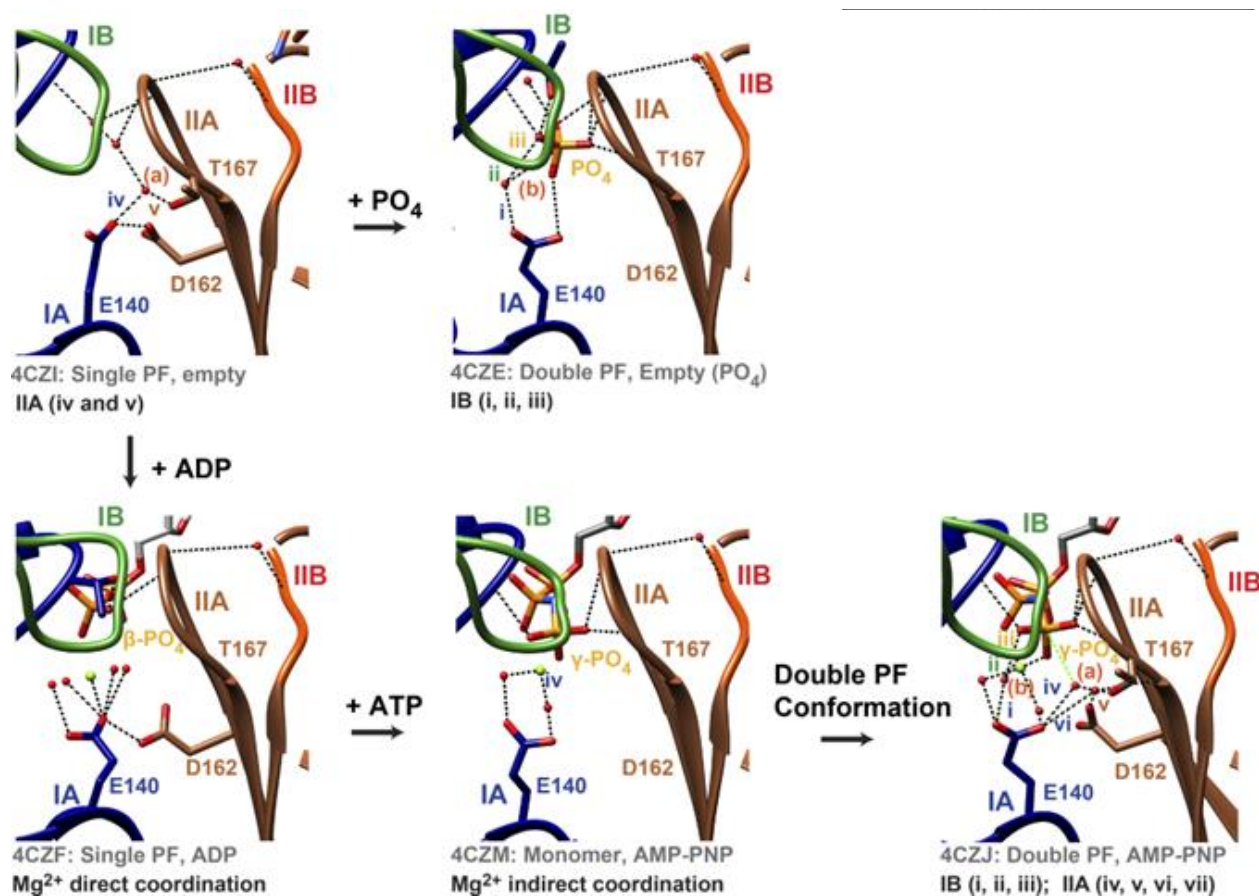


Figure 4.5: Mechanism of ATP dependence of MreB function.

Glu140^{Cc} (CcMreB numbering) plays a pivotal role in ATP-dependent conformational change of MreB. Schematic (box): Glu140^{Cc} in the double-protofilament AMP-PNP-bound state (PDB accession no. 4CZJ) holds the IB and IIA subdomain via water-mediated interactions, (a) and (b). These water-mediated interactions are not present for ADP single filament (PDB accession no. 4CZF) and AMP-PNP monomeric state (PDB accession no. 4CZM), where Glu140^{Cc} functions only in Mg²⁺ coordination.

the protein might be resistant to A22 drug. Based on our structural analysis, this further supports our hypothesis that the residues Thr66 and Val69 could contribute to A22 resistance. Further experiments are planned, where we will mutate these residues to corresponding CcMreB residues and test if ScMreB5 gains A22 sensitivity. It will be the part of our future work.

4.5: References

- Awuni, E., and Y. Mu. 2019. Effect of A22 on the Conformation of Bacterial Actin MreB. *International Journal of Molecular Sciences*. 20:1304. doi:10.3390/ijms20061304.
- Bean, G.J., and K.J. Amann. 2008. Polymerization properties of the *Thermotoga maritima* actin MreB: Roles of temperature, nucleotides, and ions. *Biochemistry*. 47:826–835. doi:10.1021/bi701538e.
- Chou, S.Z., and T.D. Pollard. 2019. Mechanism of actin polymerization revealed by cryo-EM structures of actin filaments with three different bound nucleotides. *Proceedings of the National Academy of Sciences*. 116:4265–4274. doi:10.1073/pnas.1807028115.
- Chu, J.-W., and G.A. Voth. 2005. Allostery of actin filaments: molecular dynamics simulations and coarse-grained analysis. *Proc Natl Acad Sci U S A*. 102:13111–13116. doi:10.1073/pnas.0503732102.
- Defeu Soufo, H.J., and P.L. Graumann. 2006. Dynamic localization and interaction with other *Bacillus subtilis* actin-like proteins are important for the function of MreB. *Molecular Microbiology*. 62:1340–1356. doi:10.1111/j.1365-2958.2006.05457.x.
- van den Ent, F., T. Izoré, T.A.M. Bharat, C.M. Johnson, and J. Löwe. 2014. Bacterial actin MreB forms antiparallel double filaments. *eLife*. doi:10.7554/eLife.02634.
- van den Ent, F., and J. Löwe. 2006. RF cloning: A restriction-free method for inserting target genes into plasmids. *Journal of Biochemical and Biophysical Methods*. 67:67–74. doi:10.1016/j.jbbm.2005.12.008.
- Errington, J. 2015. Bacterial morphogenesis and the enigmatic MreB helix. *Nature Reviews Microbiology*. 13:241–248. doi:10.1038/nrmicro3398.
- Esue, O., M. Cordero, D. Wirtz, and Y. Tseng. 2004. The Assembly of MreB, a Prokaryotic Homolog of Actin*. doi:10.1074/jbc.M410298200.
- Esue, O., D. Wirtz, and Y. Tseng. 2006. GTPase Activity, Structure, and Mechanical Properties of Filaments Assembled from Bacterial Cytoskeleton Protein MreB. *J Bacteriol*. 188:968–976. doi:10.1128/JB.188.3.968-976.2006.

- Feng, J., Y. Chen, J. Pu, X. Yang, C. Zhang, S. Zhu, Y. Zhao, Y. Yuan, H. Yuan, and F. Liao. 2011. An improved malachite green assay of phosphate: Mechanism and application. *Analytical Biochemistry*. 409:144–149. doi:10.1016/j.ab.2010.10.025.
- Fujii, T., A.H. Iwane, T. Yanagida, and K. Namba. 2010. Direct visualization of secondary structures of F-actin by electron cryomicroscopy. *Nature*. 467:724–728. doi:10.1038/nature09372.
- Gaballah, A., A. Kloeckner, C. Otten, H.-G. Sahl, and B. Henrichfreise. 2011. Functional Analysis of the Cytoskeleton Protein MreB from *Chlamydomonas reinhardtii*. *PLOS ONE*. 6:e25129. doi:10.1371/journal.pone.0025129.
- Mao, W., L.D. Renner, C. Cornilleau, I.L. de la Sierra-Gallay, S. Benlamara, Y. Ah-Seng, H.V. Tilbeurgh, S. Nessler, A. Bertin, A. Chastanet, and R. Carballido-López. 2022. Polymerization cycle of actin homolog MreB from a Gram-positive bacterium. 2022.10.19.512861. doi:10.1101/2022.10.19.512861.
- Mayer, J.A., and K.J. Amann. 2009. Assembly properties of the bacillus subtilis actin, MreB. *Cell Motility and the Cytoskeleton*. 66:109–118. doi:10.1002/cm.20332.
- Nurse, P., and K.J. Mariani. 2013. Purification and characterization of Escherichia coli MreB protein. *Journal of Biological Chemistry*. 288:3469–3475. doi:10.1074/jbc.M112.413708.
- Pande, V., N. Mitra, S.R. Bagde, R. Srinivasan, and P. Gayathri. 2022. Filament organization of the bacterial actin MreB is dependent on the nucleotide state. *Journal of Cell Biology*. 221:e202106092. doi:10.1083/jcb.202106092.
- Popp, D., A. Narita, K. Maeda, T. Fujisawa, U. Ghoshdastider, M. Iwasa, Y. Maéda, and R.C. Robinson. 2010. Filament structure, organization, and dynamics in MreB sheets. *Journal of Biological Chemistry*. 285:15858–15865. doi:10.1074/jbc.M109.095901.
- Rueden, C.T., J. Schindelin, M.C. Hiner, B.E. DeZonia, A.E. Walter, E.T. Arena, and K.W. Eliceiri. 2017. ImageJ2: ImageJ for the next generation of scientific image data. *BMC Bioinformatics*. 18:529. doi:10.1186/s12859-017-1934-z.
- Srinivasan, R., M. Mishra, M. Murata-Hori, and M.K. Balasubramanian. 2007. Filament Formation of the Escherichia coli Actin-Related Protein, MreB, in Fission Yeast. *Current Biology*. 17:266–272. doi:10.1016/j.cub.2006.11.069.

Takahashi, D., I. Fujiwara, Y. Sasajima, A. Narita, K. Imada, and M. Miyata. 2022. ATP-dependent polymerization dynamics of bacterial actin proteins involved in Spiroplasma swimming. *Open Biology*. doi:10.1098/rsob.220083.

Takahashi, D., M. Miyata, and I. Fujiwara. 2023. Assembly properties of Spiroplasma MreB involved in swimming motility. 2023.01.26.525654. doi:10.1101/2023.01.26.525654.

Vorobiev, S., B. Strokopytov, D.G. Drubin, C. Frieden, S. Ono, J. Condeelis, P.A. Rubenstein, and S.C. Almo. 2003. The structure of nonvertebrate actin: Implications for the ATP hydrolytic mechanism. *Proceedings of the National Academy of Sciences*. 100:5760–5765. doi:10.1073/pnas.0832273100.

Chapter 5: Membrane binding features of ScMreB5

Some sections reprinted from: Pande et al., *Journal of Cell Biology*, 2022 and Harne et al.,
Current Biology, 2020

DOI: [10.1083/jcb.202106092](https://doi.org/10.1083/jcb.202106092) and [10.1016/j.cub.2020.08.093](https://doi.org/10.1016/j.cub.2020.08.093)

5.1: Introduction

MreB of cell-walled bacteria binds lipid membrane (Salje et al., 2011). Cryo-EM studies have also shown that filaments of MreB bound to lipid monolayer and also liposomes in the presence of ATP and AMP-PNP. Structural and sequence based studies have shown the presence of hydrophobic loop and N-terminal helix (only in Gram-negative bacteria) which enable membrane binding (Salje et al., 2011). Liposome pelleting assays also confirmed that the binding is mediated by the hydrophobic loop residues (Leu93 and Phe94) in TmMreB. In the chapter 3, we showed that ScMreB5 had Ile95 and Trp96 in the hydrophobic loop region based on sequence alignment. The above loop was ordered in the ScMreB5 – AMP-PNP crystal structure, while in the ScMreB5-ADP structure, it could not be modeled. ScMreB5 has an extended C-terminal tail that is rich in Lys residue. N-terminal amphipathic helix was absent in ScMreB5. Hence, we proceeded to characterize the membrane binding ability of ScMreB5. For this we carried out liposome pelleting assays with liposomes containing lipids that constituted *S.citri* lipid composition, in the size range of 100 nm diameter. We have characterized the membrane binding ability, the residues responsible for binding and the mode of membrane interaction by ScMreB5.

Until now, membrane-binding studies on MreB has been performed in the absence of nucleotide. However, dependence of nucleotide state on membrane binding by MreB has not been explored systematically. We also checked for the effect of membrane binding on the hydrolysis activity by MreB5. The liposome binding experiments were also carried out using the active site mutants ScMreB5^{T161A} and ScMreB5^{E134A} to validate the role of transition between nucleotide states in membrane binding. These two mutant were chosen for study because: (a) Thr161 play a role in ATP hydrolysis; (b) Glu134 play a role in ATP sensing as well as hydrolysis. We have carried out a series of liposome pelleting assays with nucleotides or nucleotide analogs that would mimic different stages of hydrolytic cycle of ScMreB5. Our results provide novel insights into a novel mode of membrane binding as well as nucleotide dependence of ScMreB5 in membrane binding.

5.2: Material and methods

5.2.1: Liposome preparation

All the lipids used in the experiments, namely, DOPC (850375C), DOPG (840475C), porcine brain sphingomyelin, SM (860062C), and Cardiolipin, CL (710335C), were purchased from Avanti Polar Lipids. For performing pelleting assays with liposomes mimicking *S. citri* lipid composition (Davis et al., 1985), working concentration of 2 mM containing the lipid mix was prepared. 0.28 mM of DOPC, 0.76 mM of DOPG, 0.66 mM of brain SM and 0.30 mM of *E. coli* CL chloroform solutions were aliquoted in a clean test tube and dehydrated to remove the chloroform. A stock concentration of 2 mM lipids in chloroform was made only DOPG, only DOPC, and varying percentage ratios of DOPC: DOPG lipids in the same manner. The chloroform solution of lipids was aliquoted in a clean test tube and dried using filtered air. It is essential to ensure the complete removal of chloroform. The dehydrated lipid mix was resuspended in buffer A (50 mM Tris, pH8, and 300 mM KCl) and 1 mM MgCl₂. The lipids in buffer will form multilamellar vesicles of micrometer range. To obtain liposomes of homogenous size range, the lipid solution was extruded through a 100 nm polycarbonate membrane (Avanti Polar Lipids) to get liposomes of 100 nm range. These liposomes were further used in the charge specificity and nucleotide-dependent liposome pelleting assays.

5.2.2: Liposome pelleting assay

Protein was spun at 22,000 g at 4°C for 20 min to remove any precipitation. Concentration of the protein was estimated using Bradford reagent using BSA solution (0.1 – 1 mg/mL) as standards.

2 μM (final concentration) protein was added to the reaction mixture of 100 μl containing buffer A (300 mM KCl, and 50 mM Tris, pH 8), 1 mM MgCl₂, and liposomes (varying concentrations ranging from 0 - 1 mM). The reaction was set up in an ultracentrifugation tube compatible with TLA 120.2 Beckman rotor. This mixture was further incubated at 25°C for 15 mins and spun at 100,000 g for 25 mins at 25°C in the Beckman Coulter Optima MAX-XP tabletop ultracentrifuge. Supernatant was carefully removed and the tube base was once washed with 50 μl buffer A. The pellet was resuspended in 50 μl buffer A. 20 μl supernatant and the pellet were mixed with 15 μl of 2 X Laemmli buffer. 15 μl of supernatant and 7.5 μl of the resuspended pellet was loaded onto the 12 % SDS-PAGE gel made in 1.5 mm spacer plate – short plate set up. This ensured that both equal amounts were loaded in the gel for

comparison later. This protocol was followed for the following assays: (a) to compare the binding of ScMreB5^{WT} and mutants with liposome composition resembling *Spiroplasma* membrane composition at a concentration of 1 mM liposome; (b) to determine the charge-based binding specificity of ScMreB5^{WT} and the mutants with liposomes prepared from 1 mM DOPG and 1 mM DOPC, respectively; (c) to determine the binding curves of ScMreB5^{WT} with increasing liposome concentration (0 – 1 mM); (d) to estimate the binding properties for ScMreB5^{WT} and mutants at 600 μ M liposome concentration at varying ratios of DOPG and DOPC in the liposome mix; (e) to determine the binding specificity for ScMreB5^{WT} and the mutants at 600 μ M (80% DOPG and 20% DOPC) liposome concentration; and (f) to determine the binding specificity for the ScMreB5^{WT} and the ATPase mutants in the presence of 1 mM ADP/ ATP/AMP-PNP/ ADP-AlF_x at 600 μ M (80% DOPG and 20% DOPC) liposome concentration (here the protein was preincubated for 5 min at 25°C with the nucleotides before liposome addition).

Note: For preparing 1 mM ADP-AlF_x in a 100 μ l reaction, 1 μ l of 100 mM ADP, 1 μ l of 100 mM Al(NO₃)₃ and 1 μ l of 1M NaF in (1:1:10) molar ratio were mixed in buffer A. It is important to make this mixture fresh every time for the experiment. NaF and Al(NO₃)₃ solutions in Milli-Q water are to be made fresh for preparing ADP-AlF_x.

The intensity analysis of the protein band was performed in ImageJ 1.52n (Rueden et al., 2017). For calculating the fraction of protein in the pellet, band intensity in the pellet fraction was divided by the sum of band intensities in pellet and supernatant. The data in the graph were expressed as the mean \pm SEM. Statistical significance was estimated by unpaired t test, two-tailed. Prism v5.00 for Windows was used for plotting the graphs.

5.2.3: PLiMAP assay

Principle: PLiMAP (proximity-based labeling of membrane-associated proteins) assay is a recently developed assay (Jose and Pucadyil, 2020; Jose et al., 2020) that utilizes photoactivable bifunctional fluorescent lipid, such as BODIPY-diazirine phosphatidylethanolamine (BDPE) as a reporter to determine the membrane binding of the protein of interest. BDPE has a diazirine group at the head and fluorescent dye at the tail of the lipid (Fig 5.1 A). The diazirine group, when exposed to UV, undergoes photolysis. The photolysis generates the reactive carbene that undergoes biomolecular conjugation (West et al., 2021). So, when a protein of interest interacts the liposomes doped with BDPE, upon UV exposure, the interacting protein conjugates with BDPE (Fig 5.1 B). The binding affinity of

the protein to the liposome is directly proportional to the level of conjugation. This is determined by running the reaction on an SDS-PAGE gel and estimating in-gel fluorescence, since the BDPE has a fluorescent probe attached.

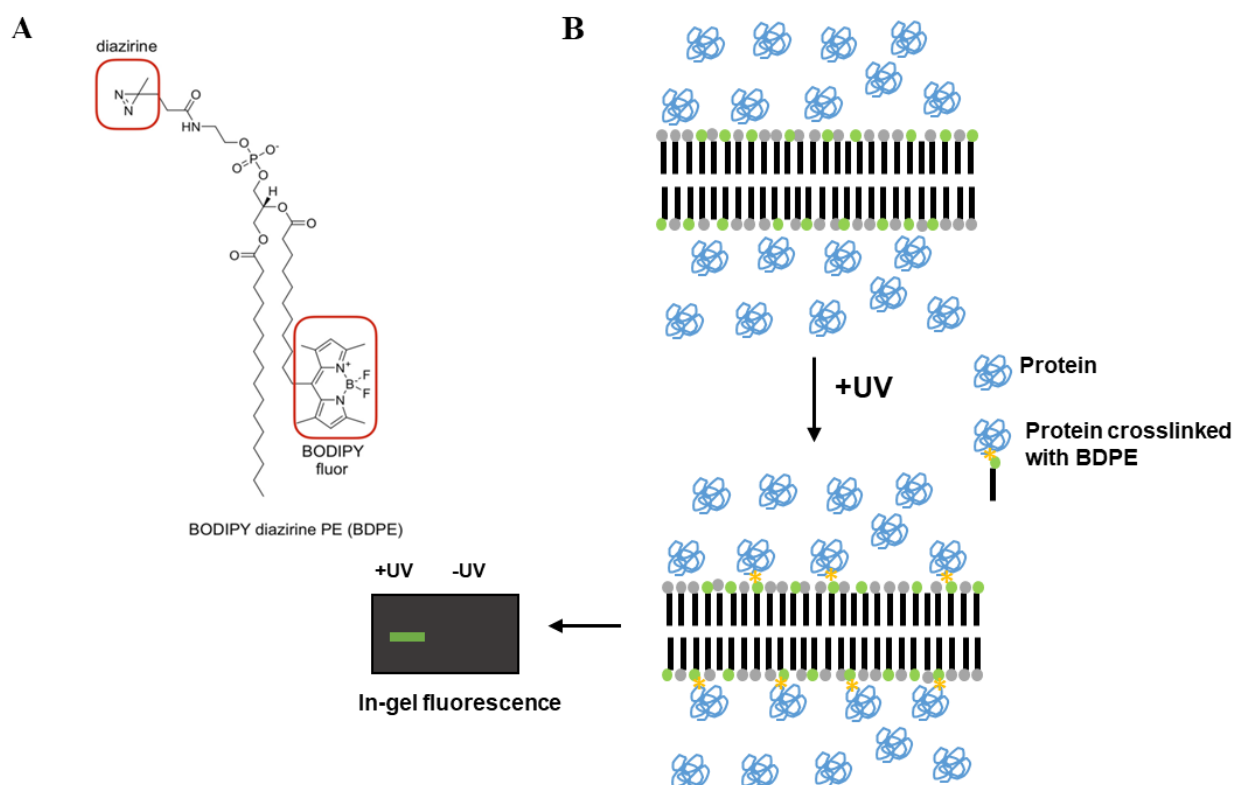


Figure 5.1: Design of PLiMAP assay (Proximity-based labeling of membrane-associated proteins)

(A) Chemical structure of BODIPY diazirine phosphatidyl ethanolamine (BDPE). Image adapted from (Jose and Pucadyil, 2020). (B) Flowchart of PLiMAP assay. The protein of interest is incubated with BDPE doped membrane. Upon UV exposure, protein interacting with the membrane gets crosslinked with BDPE. The cross-linked protein is visualized by in-gel fluorescence.

BDPE synthesis: Protocol described in (Jose and Pucadyil, 2020) was followed to prepare BDPE. BDPE was made in a sterile glass vial by mixing the chloroform stocks of 1.4 mM of TopFluor PE (1-palmitoyl-2-[dipyrrrometheneboron difluoride] undecanoyl-sn-glycero-3-phosphoethanolamine, Avanti Polar Lipids, Catalog number: 810282) with 14 mM of SDA (succinimidyl 4,4'-azipentanoate, Sigma, Catalog number 803413). The pH of the reaction was adjusted to pH 8.0 using triethanolamine. The vial was covered with aluminum foil to prevent any photodegradation. The vial was incubated for 14 hrs at 37°C in the dark. To confirm the BDPE formation, the reaction was resolved by using thin layer chromatography

on silica gel using a solvent mix of chloroform: acetone: acetic acid: methanol: water (9:2:1:1.6:0.5; v/v/v/v/v). After confirmation of BDPE formation, this stock (which was 1.4 mM concentration) was stored at $-30\text{ }^{\circ}\text{C}$ until further use.

Performing PLiMAP: Protein was spun at 22,000 g at $4\text{ }^{\circ}\text{C}$ for 20 min to remove any precipitation. Concentration of the protein was estimated using Bradford reagent using BSA solution (0.1 – 1 mg/mL) as standards.

A stock concentration of 2 mM lipids doped with 1 mol% of BDPE (1.4 mM) was prepared for the following lipid mixes: DOPC liposome (99% DOPC: 1% BDPE; in mol %), DOPG liposome (99% DOPG: 1% BDPE; in mol %) and DOPG: DOPC: BDPE (79% DOPG:20 % DOPC:1 % BDPE; in mol %). Liposome preparation for PLiMAP was done in the same way as described in section 5.2.1 above. 2 μM (final concentration) of ScMreB5^{WT} was added to the reaction mixture of 100 μl containing buffer A (300 mM KCl, and 50 mM Tris, pH 8), 1 mM MgCl_2 , and 600 μM liposomes. The reaction was incubated at $25\text{ }^{\circ}\text{C}$ for 10 mins in the dark. After incubation, the reaction was transferred into a 96-well UV transparent plate and placed inside UVP crosslinker CL-1000L. The plate was placed on a setup that provided a distance of 3 cm from the lamp. The reaction was exposed to 200 mJ/cm^2 of 366 nm UV light for 1 min for crosslinking. After the crosslinking, 20 μL of the sample was mixed with 3 μL of 5X SDS dye that does not contain bromophenol blue. The reaction is heated at $99\text{ }^{\circ}\text{C}$ for 5 – 10 mins and immediately loaded on the 12 % SDS-PAGE gel. Since our reaction buffer has 300 mM KCl, the SDS in the 5 X loading dye reacts with KCl to form KDS (potassium dodecyl sulfate) that tends to aggregate (Hejazi et al., 2013). Heating the sample prevents precipitation. Therefore, each sample should be loaded immediately after heating for 5 mins. The gel was run at 120 V until the unreacted BDPE that is running along with the dye front leaves the gel. The gel was imaged for a fluorescent signal using the GFP filter (iBrightTM FL1500 Imaging System) for visualizing the conjugated protein that interacted with the liposomes. After determining in-gel fluorescence, the gel is stained with Coomassie Brilliant Blue to visualise the total protein amount in the reaction mix. The gel was analyzed using ImageJ 1.52n (Rueden et al., 2017).

5.2.4: Malachite green assay in the presence of liposome

The release of inorganic phosphate during ATP hydrolysis was measured by malachite green assay (Feng et al., 2011). Protein was prespun at 22,000 g at 4°C for 20 min. Concentration estimation was done with Bradford reagent using Bovine serum albumin (0 – 1 mg/mL) as standards.

For comparative study of wild type with and without liposomes, protein was added at a final concentration of 10 μ M to the master mix of buffer containing ATP and MgCl₂ to achieve final concentrations of 1 mM ATP and 1 mM MgCl₂ in HK buffer (150 mM KCl and 20 mM Tris, pH 8) and mixed. For the liposome containing reaction, 0.6 mM liposome mix (38 PG: 15 CL:46 PC, in mol%) was also added. Liposome was prepared as described in the section 5.2.1. The master mix sufficient for six time points (5, 15, 20, 30, 40 and 60 mins) was made with and without the liposome. To stop the reaction at each time point, 20 μ l reaction was immediately mixed with 5 μ l of 0.5 M EDTA in a 96-well plate. Simultaneously, phosphate standards were freshly diluted from 400 μ M NaH₂PO₄. To measure the amount of phosphate release, malachite green solution was freshly prepared as described in the Chapter 4 “Material and Methods” section. 50 μ l of malachite green solution was added to the stopped reactions and phosphate standards. Absorbance of malachite green was measured in CLARIOstar at 630 nm wavelength.

For calculating the μ M of phosphate released per μ M of protein (for wild type, with and without liposomes). The absorbance of the reaction was calculated by subtracting the respective blank reaction absorbance (without protein). The amount of phosphate released (in μ M) at each time point was calculated by dividing the subtracted absorbance by the slope. The μ M of phosphate released per μ M of protein (μ M PO₄ μ M⁻¹) was calculated by dividing the amount of phosphate release by protein concentration which is 10 μ M for each time point. Prism v5.00 for Windows was used for statistical analysis and plotting the graphs. The data in the graph were expressed as mean \pm SEM.

5.3: Results

5.3.1: ScMreB5 binds liposomes

We wanted to study if ScMreB5, like other MreBs (CcMreB and TmMreB), can interact with liposomes. For this, we performed a liposome pelleting assay with an increasing concentration of liposomes (Fig. 5.2 A and B). Earlier membrane-binding studies on MreBs – have used *E.coli* lipid extract. Since *Spiroplasma* membrane composition differs from *E.coli*, the liposome composition we used for our study mimicked *S. citri* lipid composition given in Table 5.1.

Table 5.1: Comparison of *S.citri* lipid composition with *E.coli*

Organism	PC (mol%)	PG (mol%)	CL (mol%)	SM (mol%)	PE (mol%)	References
<i>S. citri</i>	14	38	15	33	-	(Davis et al., 1985)
<i>E. coli</i>	-	18	8	-	74	(Rowlett et al., 2017)

In liposome pelleting assay, liposomes and protein are mixed and centrifuged to pellet down the liposomes. If there is interaction with the liposomes, the protein will come in the pellet fraction, whereas if interaction is absent, the protein will remain in the supernatant. The binding of ScMreB5^{WT} increased with increasing liposome concentrations (Fig 5.2 A and B). Liposome pelleting assay with 2 μ M RNase protein as a negative control confirmed that the binding of ScMreB5^{WT} was not a non-specific membrane protein interaction (Fig 5.2 C).

We conducted sequence and structural analysis to determine plausible membrane binding regions of ScMreB5 (discussed in chapter 3). Based on our analysis, we made single (ScMreB5^{I95A} and ScMreB5^{W96A}) and double (ScMreB5^{I95A, W96A}) mutant constructs of these residues and tested their binding using liposome composition resembling the *S.citri* membrane (Davis et al., 1985). In comparison to ScMreB5^{WT}, the mutations did not abrogate liposome binding significantly. The single and double mutant proteins were found in the pellet fraction.

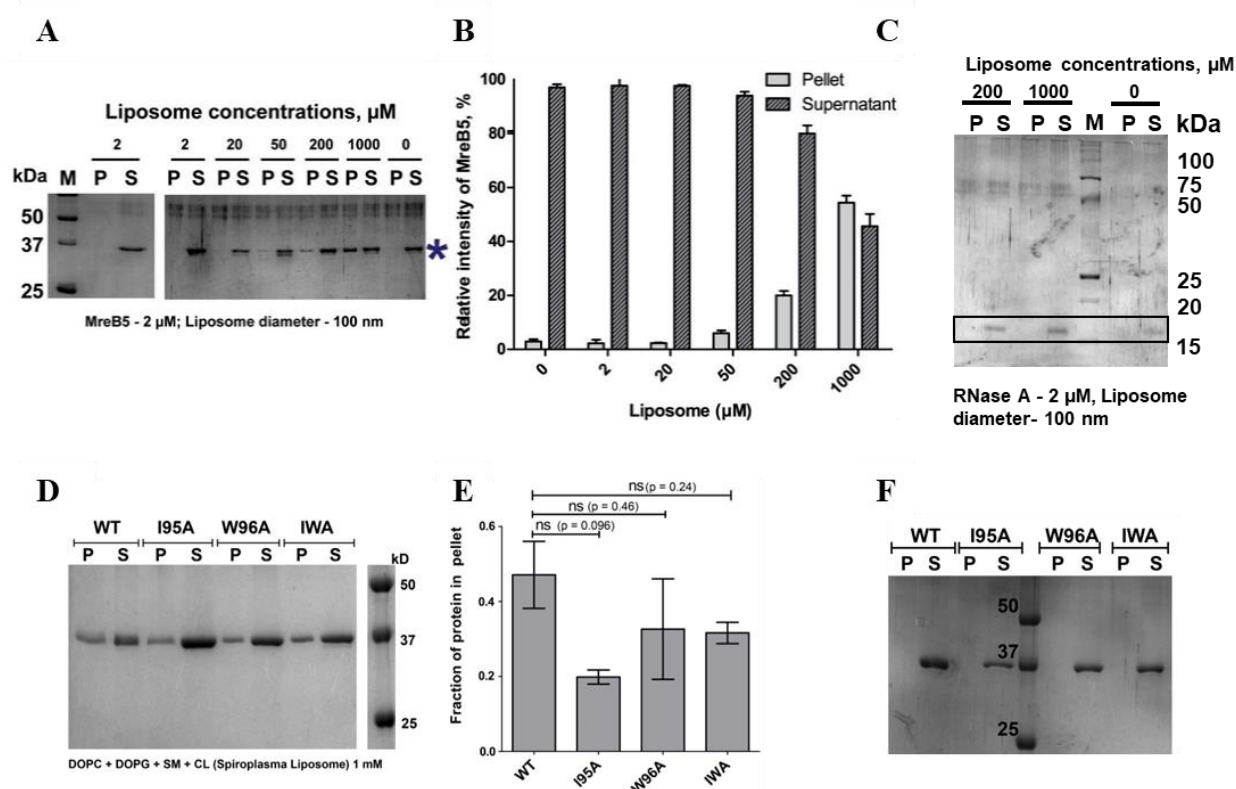


Figure 5.2: ScMreB5 binds liposomes.

(A) A representative 12% SDS-PAGE gel showing sedimentation of ScMreB5^{WT} upon adding increasing concentrations of liposomes. (B) A plot showing relative mean intensities (expressed in percentage) of bands corresponding to ScMreB5^{WT} position in the SDS-PAGE gels from 3 independent experiments, as shown in (A). The relative intensities of pellet (or supernatant) fractions at the position corresponding to ScMreB5^{WT} band were calculated as intensity of pellet (or supernatant) at the position corresponding to ScMreB5^{WT} band divided by sum of the two intensities and represented in the graph as a percentage. (C) A representative 12% SDS-PAGE gel of liposome pelleting assay with RNase A as negative control. No binding is observed at high liposomes concentration. (D) A representative 12% SDS-PAGE gel of liposome pelleting assay for comparing membrane binding of ScMreB5^{WT} (denoted WT), with the hydrophobic loop mutants (single mutants ScMreB5^{I95A} and ScMreB5^{W96A} and double mutant ScMreB5^{I95A, W96A}, denoted as I95A, W96A, and IWA, respectively). P and S represent the pellet and supernatant fractions of the reaction. (E) Plot showing relative intensities of the fraction of protein in the pellet corresponding to ScMreB5^{WT} and hydrophobic loop mutants calculated from the SDS-PAGE gels (representative gel shown in E) from three independent experiments. The error bar denotes mean with SEM; unpaired two-tailed Student's t test; ns, $P > 0.20$). (F) A representative 12% SDS-PAGE gel of ScMreB5^{WT} and membrane binding loop mutants in the absence of liposomes. In all the gels, P and S, respectively, represent pellet and supernatant fractions

upon sedimentation at 100,000 $\times g$. Concentrations of liposomes of composition mimicking *S. citri* lipids and protein used in the assay were 1 mM and 2 μM , respectively.

(Fig. 5.2 D and E). This suggested that the hydrophobic loop might not serve as the sole membrane anchor for ScMreB5, contrary to what was observed for TmMreB (Salje et al., 2011). Pelleting assays of the reaction mix without liposomes served as negative controls for the liposome binding experiments (Fig. 5.2 F). The control runs showed that the protein does not pellet on its own in the absence of liposome, irrespective of its polymerization state.

5.3.2: ScMreB5 binds to negatively charged lipids

We conducted a phospholipid specificity study to decipher the mechanistic details of ScMreB5–liposome interaction. *S. citri* membrane has the maximal amount of phosphatidylglycerol (an anionic lipid) and the lowest amount of phosphatidylcholine (a neutral lipid) as shown in Table 5.1.

Hence, we tested whether liposome binding by ScMreB5 could be charge specific.

ScMreB5^{WT} and the hydrophobic loop mutants did not bind 100% 1,2-dioleoyl-sn-glycero-3-phosphocholine (DOPC) liposomes (Fig. 5.3 A and B), whereas binding was observed with 100% 1,2-dioleoyl-sn-glycero-3-phospho-(19rac-glycerol) (DOPG, an anionic lipid) liposomes (Fig. 5.2 A and B). PLiMAP assay for ScMreB5^{WT} with 100 % DOPC and DOPG liposomes also confirmed the binding specificity for negatively charged lipids (Fig 5.3 C).

5.3.3: C-terminal tail of ScMreB5 facilitates membrane binding

Presence of positively charged residues suggested that the C-terminal tail might mediate a charge-based interaction. Therefore, we designed a construct with the last 10 residues deleted (ScMreB5^{ΔC10}) and tested binding to 100% DOPG and DOPC liposomes (Figs. 5.3 B and D). ScMreB5^{ΔC10} showed decreased binding, an effect similar to the hydrophobic loop mutants. To comparatively analyze liposome binding by the mutants, we chose a fixed concentration of liposomes based on a binding curve obtained for ScMreB5^{WT} with increasing concentrations of liposomes (Fig. 5.3 E). 600 μM , a concentration just below saturation in the binding curve (Fig. 5.3 E), was maintained as a constant liposome concentration for further assays. Next, we repeated the pelleting assays for ScMreB5^{WT} by varying DOPC: DOPG in the liposome preparation to tease out the contributing factors of lipid composition specificity (Fig. 5.3 F). Based on this, in further experiments, 80% DOPG at 600 μM of liposomes was used for the pelleting assays. ScMreB5^{ΔC10} and ScMreB^{5195A} exhibited reduced binding of the

protein to 600 μM liposomes containing 80% DOPG (Fig. 5.3 G and H). The above result showed that membrane binding by ScMreB5 is driven by positively charged and hydrophobic residues on the membrane-binding surface. The surface potential of the membrane binding face of the modeled ScMreB5 double protofilament is also consistent with this hypothesis, which is either positively charged or hydrophobic (Fig. 5.4).

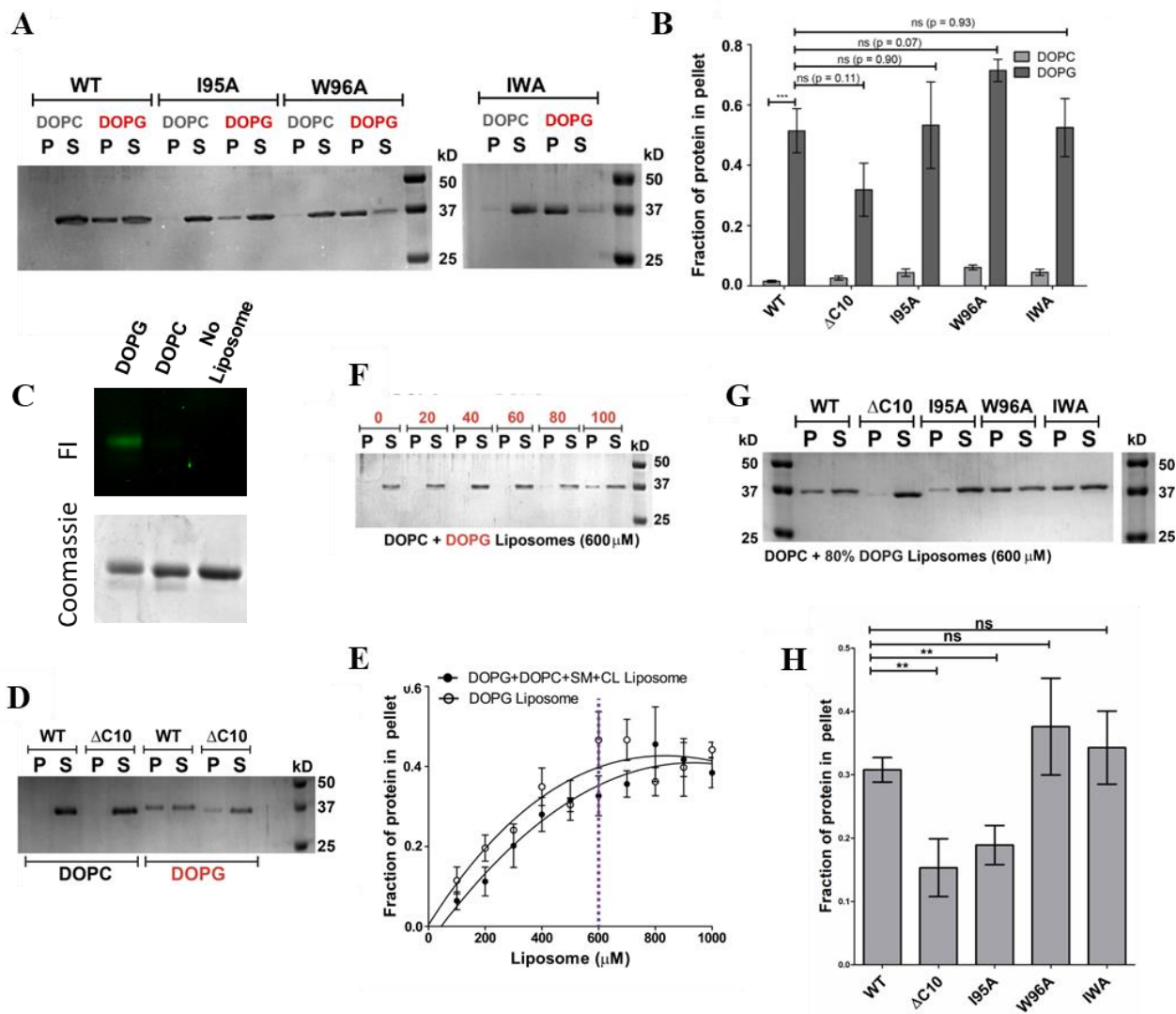


Figure 5.3: ScMreB5 binding is modulated by charged lipids.

(A) A representative 12% SDSPAGE gel of liposome pelleting assay for determining membrane binding of ScMreB5^{WT} and the hydrophobic loop mutants with a neutral lipid DOPC and an anionic lipid DOPG. P and S represent the pellet and supernatant fractions of the reaction. Concentrations of DOPG and DOPC liposomes and protein used in the assay are 1 mM and 2 μ M, respectively. (B) Plot showing relative intensities of the fraction of protein in the pellet corresponding to ScMreB5^{WT} and mutant constructs in the SDS-PAGE gels from five independent experiments. The binding is specifically observed for liposome composed of the anionic lipid DOPG for the ScMreB5^{WT} as well as the mutants. Negligible binding is seen for both ScMreB5^{WT} and the mutants for the liposome made from neutral lipid DOPC. The error bar denotes the mean with SEM; unpaired two-tailed Student's t test; ns, $P > 0.05$; ***, $P < 0.0001$). (C) A representative PLiMAP experiment gel showing in-gel fluorescence (FI) and Coomassie Brilliant blue staining (Coomassie) of ScMreB5^{WT} on DOPG and DOPC liposomes. Concentration of protein and liposomes used are 2 μ M and 0.6 mM respectively. (D) A representative 12% SDS-PAGE gel of liposome pelleting assay with C-terminal deletion mutant (ScMreB5 ^{Δ C10}) shows binding with the charged liposome, DOPG. Concentrations of DOPG and DOPC liposomes used in the assay are 1 mM each, and that of protein is 2 μ M. (E) Liposome-binding curves showing the increase in the fraction of ScMreB5^{WT} in the pellet (liposome-bound fraction) at 2 μ M protein concentration, with increasing concentration of the liposomes mimicking *Spiroplasma* lipid composition and 100% DOPG liposomes. The purple dotted line marks the 600- μ M liposome concentration chosen for further liposome-binding assays. (F) A representative 12% SDS-PAGE gel of liposome pelleting assay showing the binding specificity of ScMreB5^{WT} by varying the DOPC and DOPG ratios at 600 μ M liposome concentration. Protein in the pellet is observed at the higher DOPG percentages. (G) A representative 12% SDS-PAGE gel of liposome pelleting assay showing a decrease in binding for ScMreB5^{WT} and mutants (ScMreB5 ^{Δ C10}, ScMreB5^{I95A}, ScMreB5^{W96A}, ScMreB5^{I95A,W96A}, and ScMreB5^{E134A}, denoted Δ C10, I95A, W96A, IWA, and E134A, respectively) at 20%:80% (DOPC:DOPG) liposome ratio. P and S represent the pellet and supernatant fractions of the reaction. Concentrations of liposomes and protein used in the assay are 600 and 2 μ M, respectively. (H) Plot showing relative intensities of the fraction of protein in the pellet calculated from the SDS-PAGE gels from at least four independent experiments (representative image in G).

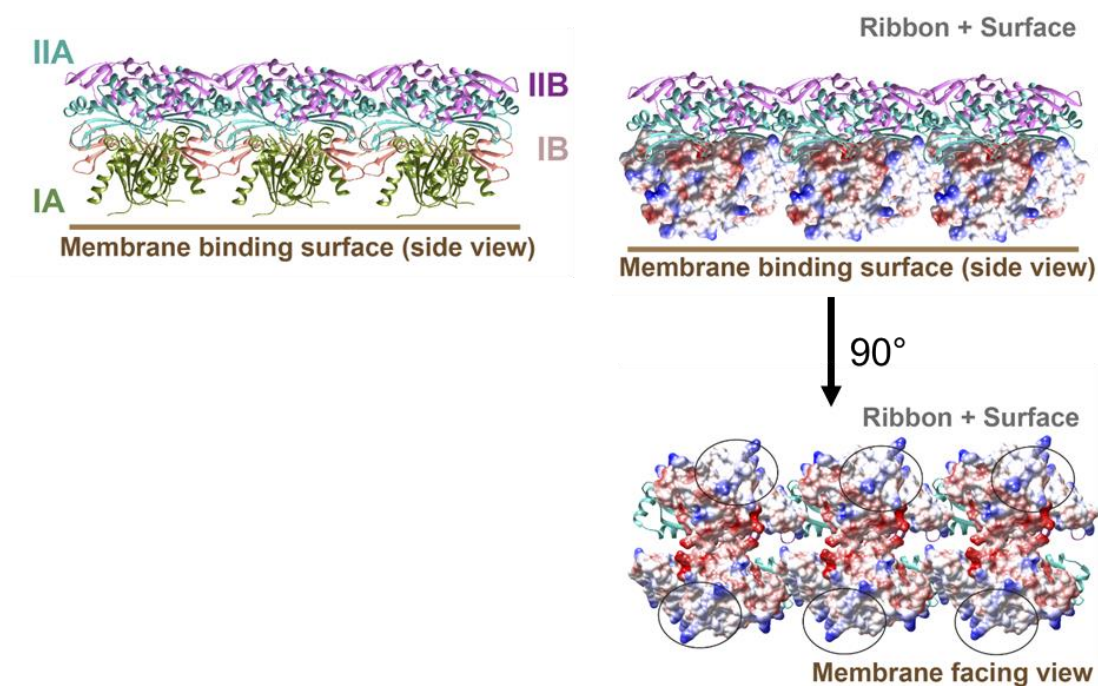


Figure 5.4: Electrostatic potential surface of ScMreB5 double protofilament model.

Different views of membrane-binding face of double-protofilament ScMreB5. Electrostatic surface potential of the membrane-binding face (IA and IB subdomains; middle and right subpanels) of double protofilament of ScMreB5 is shown corresponding to the ribbon views of the double protofilament (left). Circled regions within the surface show the regions of positive and neutral charge for the membrane-binding face of the filament. The double protofilament of ScMreB5 was modeled using CcMreB double protofilament, PDB accession no. 4CZE. Subdomains IA and IB are colored pink and light green.

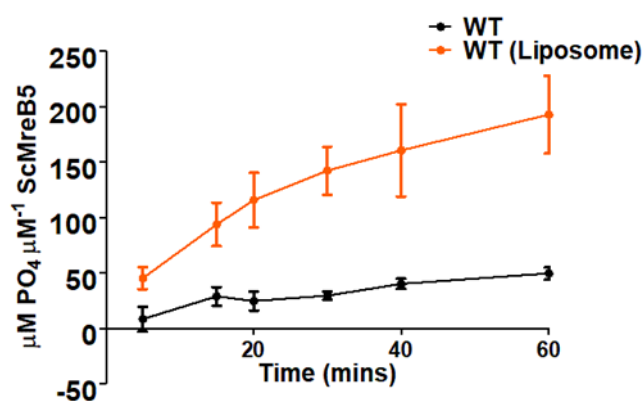


Figure 5.5: Liposome stimulates ScMreB5^{WT} ATPase activity.

Time-dependent ATPase activity characterization of ScMreB5^{WT} in the presence and absence of liposomes. In the assay, 10 µM protein, 1 mM ATP and 1 mM MgCl₂ and 0.6 mM of liposomes (composition: 38 % PG, 15 % CL and 47 % PC) were used in the assay. The buffer used in the reaction was HK buffer (150 mM KCl, 20 mM HEPES, pH 7.5).

5.3.4: ScMreB5 activity is stimulated in the presence of liposomes

The filament of MreB interacts with the lipid bilayer (Salje et al., 2011; Hussain et al., 2018; Maeda et al., 2012). To understand if the nucleotide state of the filament modulates membrane binding, we first tested the lipid bilayer's effect on the ATP hydrolysis rate of ScMreB5. ScMreB5^{WT} ATPase activity was stimulated in the presence of 600 μ M liposomes in the reaction (Fig 5.5). At 60 mins time point, the amount of phosphate release was 4 times higher in the presence of liposomes ($49.6 \pm 5.2 \mu$ M without liposomes versus $192.8 \pm 32.9 \mu$ M with liposomes). k_{obs} in the presence of liposomes increased to $0.32 \pm 0.05 \text{ min}^{-1}$. Our results indicated that the membrane interaction could affect the nucleotide-binding and hydrolysis rates for ScMreB5^{WT}.

5.3.5: ScMreB5 liposome binding is nucleotide-dependent

ATPase activity stimulation in the presence of liposomes encouraged us to study the interdependence between the nucleotide state and liposome binding. We carried out liposome pelleting assays of ScMreB5^{WT} upon addition of ADP, ATP, AMP-PNP or ADP-AlFx (a transition state analog of ATP hydrolysis cycle) in the reaction mix. Pelleting assays with liposomes suggest that there was a differential binding for ScMreB5^{WT} based on the nucleotide state (Fig 5.6 A and B). Binding was observed without addition of any excess nucleotide, and in the presence of AMP-PNP and ADP-AlFx states compared to negligible binding upon addition of excess of ATP or ADP (Fig 5.6 A and B). PLiMAP assay for the ScMreB5^{WT} in the presence of nucleotide showed a similar result (Fig 5.5 C). Thus, indeed the nucleotide state determined the membrane binding. Pelleting assays of the reaction mix without liposomes showed that the protein did not pellet upon the addition of nucleotide (Fig 5.6 H and I).

For deciphering the mechanism of nucleotide dependence, we characterized the hydrolysis mutants ScMreB5^{E134A} and ScMreB5^{T161A} for nucleotide-dependent membrane binding. From our structural analysis we know that ScMreB5^{E134A} could be involved in sensing the ATP binding and driving the ATP hydrolysis (Fig 3.6 B and C). ScMreB5^{T161A} could only be involved in driving the ATP hydrolysis (Fig 3.6 B and C). These two mutations could

therefore shed light on the dependency of membrane binding on nucleotide binding and hydrolysis.

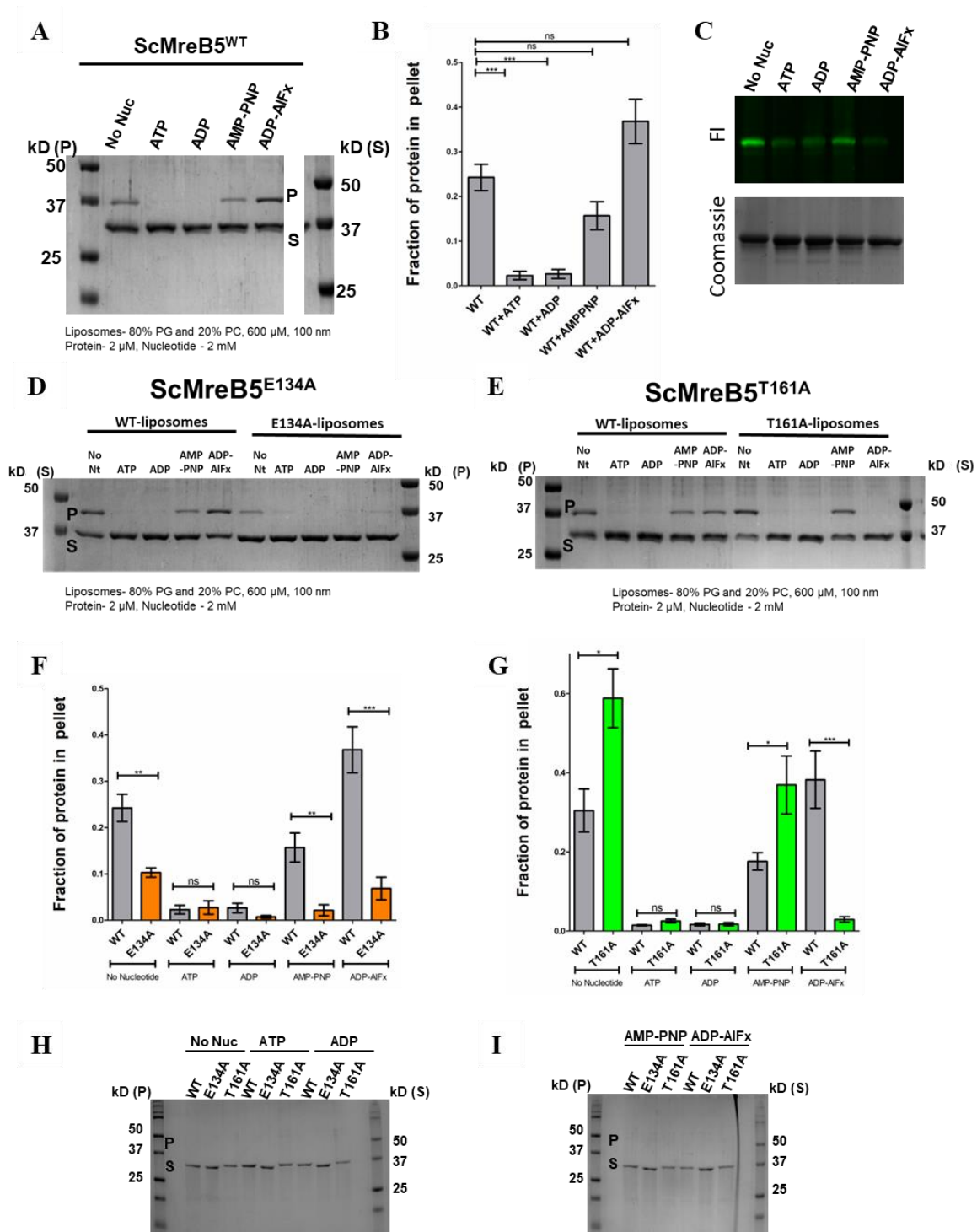


Figure 5.6: ScMreB5 binding to liposomes is nucleotide-dependent.

(A) A representative 12% SDS-PAGE gel of liposome pelleting assay showing binding for ScMreB5^{WT} in different nucleotide states at 20%:80% (DOPC: DOPG) liposome ratio. P and S represent the pellet and supernatant fractions of the reaction. (B) Plot showing relative intensities of the protein fraction in the pellet in different nucleotide conditions calculated from the SDS-PAGE gel from at least four independent experiments (representative image in A). The error bar denotes the mean with SEM; unpaired two-tailed Student's t test; ns, P = 0.09; ***, P ≤ 0.0001). (C) A representative PLiMAP experiment gel showing in-gel fluorescence (FI) and Coomassie Brilliant blue staining (Coomassie) of ScMreB5^{WT} on DOPC: DOPG: BDPE (79%:20%:1%) liposomes in the presence of different nucleotides. (D) A representative 12% SDS-PAGE gel of liposome pelleting assay showing binding for ScMreB5^{E134A} in different nucleotide states at 20%:80% (DOPC:DOPG) liposome ratio. P and S represent the pellet and supernatant fractions of the reaction. (E) A representative 12% SDS-PAGE gel of liposome pelleting assay showing binding for ScMreB5^{T161A} in different nucleotide states at 20%:80% (DOPC: DOPG) liposome ratio. P and S represent the pellet and supernatant fractions of the reaction. (F) A comparison plot showing intensities of the protein fraction in the pellet in different nucleotide conditions for ScMreB5^{WT} and ScMreB5^{E134A} calculated from the SDS-PAGE gel from at least three independent experiments (representative image in D). The error bar denotes the mean with SEM; unpaired two-tailed Student's t test; **, P = 0.002-0.007; ***, P = 0.0006 and ns, P = 0.8). (G) A comparison plot showing relative intensities of the protein fraction in the pellet in different nucleotide conditions for ScMreB5^{WT} and ScMreB5^{T161A} calculated from the SDS-PAGE gel from at least three independent experiments (representative image in D). The error bar denotes the mean with SEM; unpaired two-tailed Student's t test; *, P = 0.01 – 0.04; **, P = 0.001 and ns, P = 0.05-0.9). (H and I) A representative 12% SDS-PAGE gel of a pelleting assay at 100,000 g with ScMreB5^{WT}, ScMreB5^{E134A} and ScMreB5^{T161A} under different nucleotide conditions in the absence of liposomes. The concentration of nucleotides and MgCl₂ used in the assays above are 1 mM each. The concentration of protein and liposomes used in the assays above are 2 μM and 0.6 mM, respectively.

Irrespective of the nucleotide condition, ScMreB5^{E134A} exhibited significantly reduced binding (Fig 5.6 D and F). Significant reduction in binding in the AMP-PNP state for ScMreB5^{E134A} state shows that ATP sensing is essential for membrane interaction. ScMreB5^{T161A}, bound similarly as wild type in all conditions except in the ADP-AlFx state (Fig 5.6 E and G). Thus, showing that the transition state might facilitate membrane binding.

5.4: Discussion

In this chapter we characterized ScMreB5 membrane binding and role of nucleotide state on membrane binding. ScMreB5 was able to bind liposomes resembling the *Spirioplasm* cell width (100- 150 nm) and lipid composition. Earlier studies have shown that the binding of MreB to the membrane is mediated by hydrophobic loop and N-terminal amphipathic helix. Our study shows that, unlike for other MreBs, the binding of ScMreB5 is mediated by both hydrophobic and electrostatic interaction. A novel binding mode has been established in which an entire filament surface binds to the membrane. Within *Spirioplasm*, this mechanism of interaction could be essential in the absence of accessory transmembrane protein like Rod Z (Colavin et al., 2018) that also help in MreB localization onto the cell membrane.

MreBs studies so far show that it can undergo nucleotide dependent polymerization (Bean and Amann, 2008; Takahashi et al., 2022; Mayer and Amann, 2009). But the regulation of polymerization and its effect on membrane binding is unknown. Our interpretation of the wild-type and ATPase mutant pelleting assay data is based on the following finding and supposition: (a) The liposome-induced increase of ATPase activity; (b) Assuming that filaments can exist in different nucleotide states. These filaments may exhibit a variety of conformations at different nucleotide states. Certain conformations may affect the affinity to the membrane.

From our observations of the wildtype and the mutant, ATP binding and transition state might facilitate the compatible filament conformation for binding to liposomes. Whereas no binding in the ADP state for the wildtype and the ATPase mutant's probable incompatible protein conformation in the ADP state for membrane interaction. Thus, our comparative liposome pelleting assay study of ScMreB5^{WT} with ScMreB^{E134A} (ATP sensor and hydrolysis driving residue) and ScMreB5^{T161A} (ATP hydrolysis driving residue) show that the conformational change on ATP binding and transition state determine membrane binding. Thus, there could an allostery between nucleotide binding pocket and the membrane binding site in ScMreB5 filaments. The role of filament bundling and polymerization on membrane binding is still yet to be deciphered.

5.5: References

- Bean, G.J., and K.J. Amann. 2008. Polymerization properties of the *Thermotoga maritima* actin MreB: Roles of temperature, nucleotides, and ions. *Biochemistry*. 47:826–835. doi:10.1021/bi701538e.
- Colavin, A., H. Shi, and K.C. Huang. 2018. RodZ modulates geometric localization of the bacterial actin MreB to regulate cell shape. *Nat Commun*. 9:1280. doi:10.1038/s41467-018-03633-x.
- Davis, P.J., A. Katznel, S. Razin, and S. Rottem. 1985. Spiroplasma membrane lipids. *Journal of Bacteriology*. 161:118–122.
- Feng, J., Y. Chen, J. Pu, X. Yang, C. Zhang, S. Zhu, Y. Zhao, Y. Yuan, H. Yuan, and F. Liao. 2011. An improved malachite green assay of phosphate: Mechanism and application. *Analytical Biochemistry*. 409:144–149. doi:10.1016/j.ab.2010.10.025.
- Hejazi, S.M., M. Erfan, and S.A. Mortazavi. 2013. Precipitation Reaction of SDS and Potassium Salts in Flocculation of a Micronized Megestrol Acetate Suspension. *Iran J Pharm Res*. 12:239–246.
- Hussain, S., C.N. Wivagg, P. Szwedziak, F. Wong, K. Schaefer, T. Izoré, L.D. Renner, M.J. Holmes, Y. Sun, A.W. Bisson-Filho, S. Walker, A. Amir, J. Löwe, and E.C. Garner. 2018. MreB filaments align along greatest principal membrane curvature to orient cell wall synthesis. *eLife*. 7:e32471. doi:10.7554/eLife.32471.
- Jose, G.P., S. Gopan, S. Bhattacharyya, and T.J. Pucadyil. 2020. A facile, sensitive and quantitative membrane-binding assay for proteins. *Traffic*. 21:297–305. doi:10.1111/tra.12719.
- Jose, G.P., and T.J. Pucadyil. 2020. PLiMAP: Proximity-Based Labeling of Membrane-Associated Proteins. *Current Protocols in Protein Science*. 101:e110. doi:10.1002/cpps.110.
- Maeda, Y.T., T. Nakadai, J. Shin, K. Uryu, V. Noireaux, and A. Libchaber. 2012. Assembly of MreB filaments on liposome membranes: A synthetic biology approach. *ACS Synthetic Biology*. 1:53–59. doi:10.1021/sb200003v.
- Mayer, J.A., and K.J. Amann. 2009. Assembly properties of the bacillus subtilis actin, MreB. *Cell Motility and the Cytoskeleton*. 66:109–118. doi:10.1002/cm.20332.

Rowlett, V.W., V.K.P.S. Mallampalli, A. Karlstaedt, W. Dowhan, H. Taegtmeier, W. Margolin, and H. Vitrac. 2017. Impact of Membrane Phospholipid Alterations in *Escherichia coli* on Cellular Function and Bacterial Stress Adaptation. *J Bacteriol.* 199:e00849-16. doi:10.1128/JB.00849-16.

Rueden, C.T., J. Schindelin, M.C. Hiner, B.E. DeZonia, A.E. Walter, E.T. Arena, and K.W. Eliceiri. 2017. ImageJ2: ImageJ for the next generation of scientific image data. *BMC Bioinformatics.* 18:529. doi:10.1186/s12859-017-1934-z.

Salje, J., F. van den Ent, P. de Boer, and J. Löwe. 2011. Direct Membrane Binding by Bacterial Actin MreB. *Molecular Cell.* 43:478–487. doi:10.1016/j.molcel.2011.07.008.

Takahashi, D., I. Fujiwara, Y. Sasajima, A. Narita, K. Imada, and M. Miyata. 2022. ATP-dependent polymerization dynamics of bacterial actin proteins involved in *Spiroplasma* swimming. *Open Biology.* doi:10.1098/rsob.220083.

West, A.V., G. Muncipinto, H.-Y. Wu, A.C. Huang, M.T. Labenski, L.H. Jones, and C.M. Woo. 2021. Labeling Preferences of Diazirines with Protein Biomolecules. *J. Am. Chem. Soc.* 143:6691–6700. doi:10.1021/jacs.1c02509.

Chapter 6: Membrane remodelling dynamics of ScMreB5

6.1: Introduction

Membrane curvature is an important feature of a cell and its organelles. It ranges from a scale of nanometer to micrometer. Curvature can act as a geometric cue for localization of many proteins of nanometer in size range. In rod shaped bacteria, micronscale curvature exists at the cell pole, cytokinetic furrow, cell branches, etc (Updegrave and Ramamurthi, 2017).

There are different curvature sensing proteins that recognize such regions, and might recruit downstream effector proteins. Examples of such proteins in bacteria are SpoVM, MreB and DivIVA (Updegrave and Ramamurthi, 2017). SpoVM recognizes the positive curvature of forespore in *B.subtilis* at the time of sporulation (Gill et al., 2015). DivIVA recognizes the area of negative curvature of the cell division septum at the cell poles at the time of onset of sporulation (Updegrave and Ramamurthi, 2017; Lenarcic et al., 2009). Recognition by these nanometer sized proteins is mediated by cooperative interaction, molecular crowding or by forming multimeric structures at the site of binding (Updegrave and Ramamurthi, 2017).

As discussed previously, MreB interacts with the membrane through membrane binding regions on the surface of the protein. MreB also has the ability to sense areas of positive and negative curvature by sensing the difference in the greatest principal curvature (Hussain et al., 2018). It can localize along the rod and exclude from the cell pole by sensing the curvature difference. In vitro, MreB is able to induce curvature by causing membrane deformations and tubulation of micron scale (1 – 5 μm) liposomes (Hussain et al., 2018; Ursell et al., 2014; Salje et al., 2011; Libchaber et al., 2011). Using molecular simulations, it has also been shown that rather recognizing a micron scale curvature, the nanometer size range of MreB filaments recognize local areas of negative curvature present throughout the rod length (Ursell et al., 2014). This in turn would lead to cell wall synthesis in these local areas. Hence, filaments of MreB can sense and generate curvature within rod-shaped bacteria and liposomes. For MreB to efficiently bind to the membrane surface, it would have to be in a polymeric state. Our liposome pelleting assay data showed the role of nucleotide state in membrane binding of ScMreB5 (Chapter 5). We further hypothesized that the nucleotide state of MreB would also determine membrane remodelling ability. To study this we used an in-vitro reconstitution approach. This part of the work is in the preliminary stage and was done in collaboration with Prof. Thomas Pucadyil's lab at IISER Pune. Membrane remodelling was visualized in presence of MreB under different nucleotide states. Each state represented a step in the ATP hydrolysis cycle. Remodelling was visualized in two membrane systems: (a) supported lipid membrane tubes (SMrT tubes), with nanometer range tube

diameter, (b) supported lipid bilayers (SLBs). Both these membrane systems have been used to study membrane fission and remodelling events of well characterized eukaryotic dynamin (Dar et al., 2015) and EHD1 (Kamerkar et al., 2019). We show that ScMreB5 can remodel both the SLBs and SMrT tubes in a nucleotide dependent manner. This further highlights the features of curvature sensing and conformational change that the protein would undergo during the cycle of ATP hydrolysis and polymerization that might drive the membrane remodelling.

6.2: Materials and Methods

6.2.1: SMrT (Supported membrane tubes) template – ScMreB5 activity assay

1 mM chloroform lipid mix consisting of 0.38 mM of DOPG, 0.46 mM of DOPC, 0.15 mM of CL and 0.01 mM of p-Texas Red DHPE (1,2-Dihexadecanoyl-sn-Glycero-3-Phosphoethanolamine) (or 0.01 mM of DiO, a lipophilic carbocyanine dye) was prepared in a clean glass vial with PTFE lined screw cap. The SMrT template was made as reported earlier (Dar et al., 2017, 2015). 40 mm coverslip was PEGylated with PEG 400 (Sigma). The procedure of PEGylation was followed as described in (Dar et al., 2017) . Before spotting the lipid mix, the PEGylated coverslip was washed sequentially with 1% SDS, water, methanol, and water. Around 1 - 2 μ L (~ 1 nmol) of the lipid mix was spread as a band (around 1 – 1.5 cm away from the coverslip edge) over a 40 mm PEGylated (PEG 400) coverslip. The coverslip was left for drying to remove chloroform and then assembled in a flow cell (FCS2 system from Biopetechs). The coverslip was placed over a 0.1 mm silicone spacer that separated the coverslip from the ITO- coated glass slide. The flow cell was filled with filtered and degassed HK buffer (20 mM Hepes, pH 7.5 and 150 mM KCl) to hydrate the lipids to form large vesicles. The outlet of the chamber was connected to a peristaltic pump and around 3 – 4 mL of buffer was passed at a high flow rate. The flowing of buffer led to extrusion of nanometer diameter size range tubes from the large vesicle reservoir. Once most of the reservoir was extruded out into tubes, the flow was stopped. The SMrT templates formed was pinned to the coverslip surface at distinct sites. The schematic flow chart of the setup is shown in Fig 6.1 A.

After the SMrT templates formation, the chamber was equilibrated by passing 200 μ L of HK buffer containing 1 mM ATP/ADP/AMP-PNP/ADP-AlF_x , 1 mM MgCl₂ and oxygen scavenger mix ((2 μ L glucose oxidase (20 mg/mL), 2 μ L catalase (3.5 mg/mL) and 2 μ L

glucose (450 mg/mL)) and 1 mM DTT (Dar et al., 2017). After equilibration, a maximum of 8 "before" fields were fixed. After setting the areas, 200 μ L reaction containing 1 μ M of ScMreB5^{WT}, 1 mM ATP/ADP/AMP-PNP/ADP-AIF_x, 1 mM MgCl₂, oxygen scavenger mix (2 μ L glucose oxidase (20 mg/ml), 2 μ L catalase (3.5 mg/ml) and 2 μ L glucose (450 mg/ml), and 1 mM DTT was made. The reaction mix was flown in at the lowest flow rate setting and incubated at room temperature for 10 mins. After 10 mins, "after" images of the fixed fields were acquired.

For calculating the percentage of tubes cuts, the total number of tubes were counted from "after" field. Then, number of tubes that underwent cutting were counted. This was done for all the "after" fields. To get the percentage of tube cuts from all the analyzed fields, the total number of cut tubes was divided by the total number of tubes. The fraction of cut tubes was multiplied by 100 to get the percentage. The data was plotted on Graph Pad prism.

6.2.2 SLB (Supported lipid bilayer) assay

Around 5 - 8 μ L of the lipid mix (prepared as discussed in the SMrT assay section: 5.2.4) was spotted over a pre-cleaned 40 mm PEGylated (PEG 400 or PEG 8000) coverslip (refer Dar et al., 2017 for PEGylation steps) by spin disc method. The coverslip was stuck using double-sided tape on the cap of 35*10 mm size petri dish. The petri dish cap was further stuck to a magnetic bead. This set up was placed over a magnetic stirrer and spun at 400 rpm. Using a 10 μ L Hamilton syringe, 5 - 8 μ L of the lipid mix was spotted at the center of the rotating coverslip. Due to rotation, the lipid mix was spread over the coverslip as spots (Fig 5.2 B). The coverslip was left for drying to remove all the chloroform. The coverslip was assembled and hydrated in the flow cell as described for the SMrT template above (section 5.2.4). This generated the islands of bilayers over the passivated coverslip. (Important note: For PEG8000 coverslip, 1 – 2 mL of HK buffer is passed at a slower flow rate for hydrating the dried lipid spots, as the PEG8000 coverslip is more passivated. PEG8000 coverslip was only used for ScMreB5^{WT} and ScMreB5^{Nt-GFP} mix reaction). The schematic flow chart of the setup is shown in Fig 6.1 B.

After the SLBs were formed, the chamber was equilibrated by passing 200 μ L of HK buffer containing 1 mM ATP/ADP/AMP-PNP/ADP-AIF_x, 1 mM MgCl₂, and oxygen scavenger mix (2 μ L glucose oxidase (20 mg/ml), 2 μ L catalase (3.5 mg/ml) and 2 μ L glucose (450 mg/ml), and 1 mM DTT. After equilibration, a maximum of 8 "before" fields were fixed. After setting the areas, 200 μ L reaction containing 1 μ M of ScMreB5^{WT}, 1 mM ATP/ADP/AMP-

PNP/ADP-ATF_x, 1 mM MgCl₂, oxygen scavenger mix and 1 mM DTT was made. The reaction mix was flown in at the lowest flow rate setting and incubated at room temperature for 10 mins. After 10 mins, "after" images of the fixed fields were acquired.

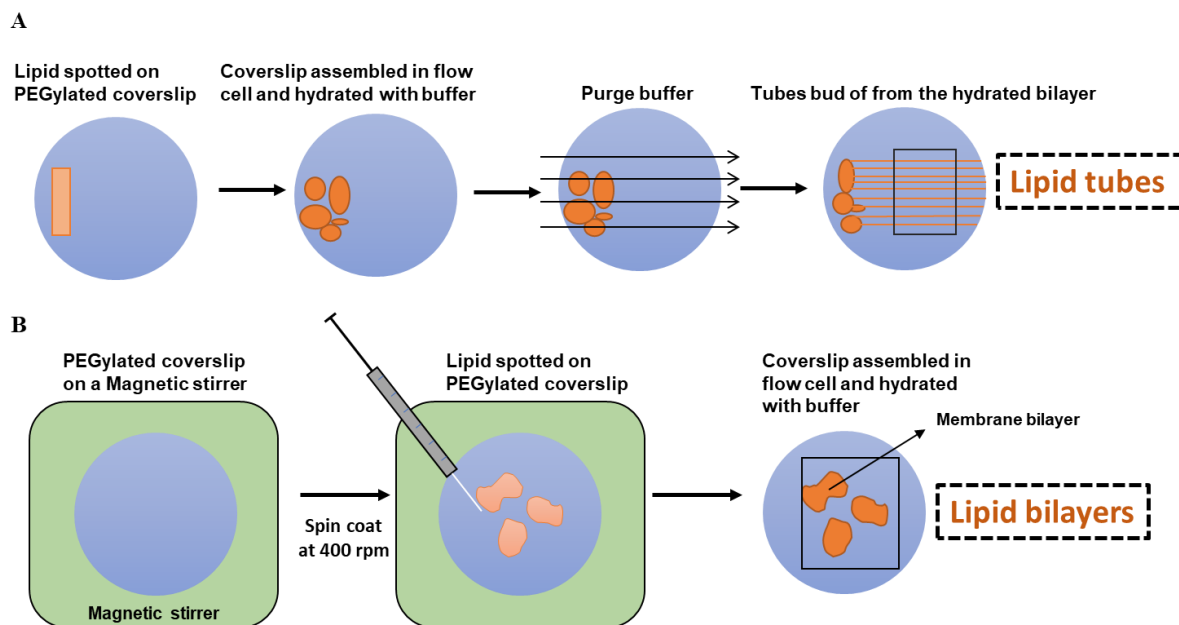


Figure 6.1: Schematic of preparing SMrT (Supported Membrane Tubes) and SLB (Supported lipid bilayer) templates. **(A)** Work flow of generating SMrT templates over a PEGylated coverslip **(B)** Work flow of generating SLB templates over a PEGylated coverslip.

6.2.3: Fluorescence microscopy of SMrT and SLBs templates

Fluorescence imaging of the SMrT and SLB templates were carried out on Olympus IX83 inverted microscope that was equipped with a stable LED light source (CoolLED), and an Evolve 512 EMCCD camera (Photometrics). The imaging was performed through a 100X, 1.4 NA oil-immersion objective. For image acquisition, Micro-Manager software was used and rendered using Fiji (Schindelin et al., 2012).

6.2.4: Cloning and purification of ScMreB5 mutants and GFP fusion constructs

Cloning

For this study, new constructs for various strategies of fluorescent labeling of ScMreB5^{WT} were created. ScMreB5^{Cys221} (Fig 6.2) were generated by RF cloning strategy (RF cloning is discussed in Chapter 2 section of "Materials and Methods"). Primers are listed in Table 6.1. Cloning of ScMreB5^{Nt-GFP} and ScMreB5^{UT} (UT - Untagged) was done by restriction digestion-ligation method. ScMreB5^{UT} was cloned in pET28A vector that has a SUMO tag at the N-terminal of protein. For cloning these constructs, 'insert' was generated by one-step PCR using ScMreB5^{NdeI} as a template. ScMreB5^{NdeI} construct was generated by RF cloning. This construct had a silent mutation for the internal *NdeI* site (59th basepair, near the N – terminus) of *scmreb5* gene. Hence, this construct generated a PCR product (*scmreb5*^{NdeI}) with *NdeI* and *BamHI* restriction sites flanking at the ends. The PCR product was further subjected to restriction digestion.

For generating pET28a – SUMO- ScMreB5^{UT}, pET28A –SUMO-*ftsA* was used as a vector. *ftsA* was replaced with the digested *scmreb5*^{NdeI} PCR product between *NdeI* and *BamHI* sites. For generating pHis17- ScMreB5^{Nt-GFP}, pHis- SmFtsZ^{Nt-GFP} was used as a vector. *ftsZ* was replaced with the digested *scmreb5*^{NdeI} PCR product between *NdeI* and *BamHI* sites. A schematic of the generated constructs is shown in Fig 6.2.

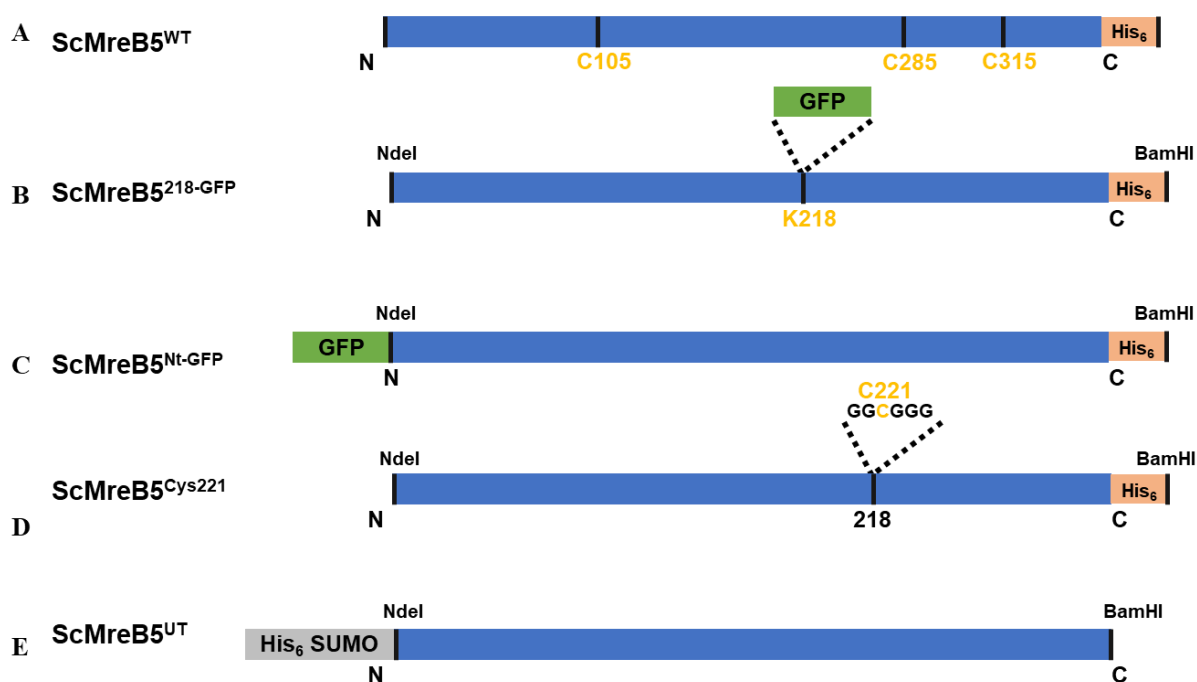


Figure 6.2: Constructs for visualizing ScMreB5 on membrane.

(A) ScMreB5^{WT}, (B) ScMreB5^{218-GFP}, (C) ScMreB5^{Nt-GFP}, (D) ScMreB5^{Cys221} and (E) ScMreB5^{UT}

The list of primers and generated constructs is provided in Table 6.1.

ScMreB5^{218-GFP} was cloned in the lab earlier by Dr. Shrikant Harne in pHis17 vector between *NdeI* and *BamHI* restriction sites.

Table 6.1: List of primers and clones/inserts generated

Primer name	Sequence ('5 → 3')	Template vector for PCR (Vector-construct name)	Clones/Inserts generated (Vector-construct name)
ScM5-Nde-del-f	GGAAGTCTAAT GTTTTAGCATAcG TTTCAGGACAAG GTGTAGTC		
ScM5H6-r	GATGATGATGAT GATGGGATCCTTT TCTTTTTTTACCT AATGTTGATAATA ATCC	pHis17-ScMreB5 ^{WT}	pHis17-ScMreB5 ^{NdeI}
T7-Fwd	TAATACGACTCAC TATAGGG		PCR product for restriction digestion cloning in pHis-SmFtsZ ^{Nt-GFP}
T7-Rev	GCTAGTTATTGCT CAGCGG	pHis17-ScMreB5 ^{NdeI}	
ScM5-F	CTTTAAGAAGGA GATATACATATG AGACCAGAAACT AGACCATTATT TC		PCR product for restriction digestion cloning in pET28a-SmFtsA
pREP_ScM5-R5-R	GGCAAGGGAGA CATTCTTTTACC CGGGGATCCTTA TTTTCTTTTTTTA CCTAATGTTG	pHis17-ScMreB5 ^{NdeI}	
	CATTGGTTCATT AGTTAAAggcggctca tcaccatcatcatagcg	pHis17-ScMreB5 ^{NdeI}	pHis17-ScMreB5 ^{Cys221}

ScM5_Sandwich218 H6	gcTACCATAACGA AAGATCAATGC		
ScM5H6-r	GATGATGATGAT GATGGGATCCTTT TCTTTTTTTACCT AATGTTGATAATA ATCC		

Expression and Purification

ScMreB5^{Cys221}, ScMreB5^{Nt-GFP} and ScMreB5^{218-GFP} constructs were expressed and purified with the same protocol as standardized for ScMreB5^{WT} (described in Chapter 2 "Materials and Methods" section).

For overexpression of the pET28a-SUMO-ScMreB5^{UT} construct, different strategy was followed. In the pET28A vector, the gene of interest to be overexpressed is under the *lacI* promoter. In the Rosetta strain (which is a derivative of BL21 bacterial expression strain), the T7 polymerase expression is under the tight regulation of *lacUV5* promoter (Tegel et al., 2010). Inducing the transformed culture of Rosetta cells with IPTG leads to the overexpression of our gene of interest.

scmreb5^{UT} in pET28A vector was transformed in competent Rosetta cells by Heat shock method and spread on LB Agar plate containing kanamycin (50 µg/mL) and chloramphenicol (35 µg/mL) as the antibiotic. The plate was incubated for 12 hrs at 37 °C. 5 – 8 colonies were inoculated in 15 mL of LB broth containing kanamycin (50 µg/mL) and chloramphenicol (35 µg/mL) and incubated under shaking conditions at 37 °C until OD₆₀₀ of 1.0 was reached This served as the primary culture. 1 L of LB media containing kanamycin (50 µg/mL) and chloramphenicol (35 µg/mL) as the antibiotic was inoculated with the 10 mL of primary culture. The culture was grown until OD₆₀₀ reached to 0.8-1.0 at 37 °C under shaking conditions. The culture was induced with 0.5 mM IPTG and further incubated under shaking conditions at 18°C for 12 - 14 hrs. After protein expression, the culture was pelleted down at 4000 xg, and the stored at -80 °C until further use.

For purification, the pellet was thawed and cells were homogenized in lysis buffer (300 mM KCl, 50 mM Tris, pH 8, and 10 % glycerol). The resuspended pellet was sonicated (Total time - 2 min, 1 sec ON, 3 secs OFF, 60% amplitude, 2 cycles). The lysate was centrifuged at

44,082 xg for 45 mins, 4 °C in JA 25.5 rotor. The supernatant was loaded on a 5 mL Ni-NTA column (HisTrap, GE Healthcare) pre-equilibrated with buffer A (50 mM Tris pH 8, 300 mM KCl). Hexa-histidine tag present in the N-terminus of the protein facilitated binding to the Ni-NTA column. Bound protein was eluted using a step gradient of 5 %, 10 %, 20 %, 50 %, and 100 % of buffer B (50 mM Tris pH 8, 300 mM KCl, and 500 mM Imidazole). Fractions containing the purest protein were identified using 12 % SDS-PAGE gel. These fractions were pooled together in a sterile Falcon tube and concentration was estimated by Bradford reagent and BSA (0.1-1 mg/mL) as standards. Ulp protease was added to the protein falcon in ~ 1: 100; Ulp: protein molar ratio. Ulp protease (28 kDa) would cleave off the SUMO tag (13 kDa) that will remove the hexa-histidine and SUMO tag from the N-terminus of the protein. The Ulp protease-protein mix was set up for digestion during dialysis (10 kDa molecular weight cut off) against buffer A (50 mM Tris pH 8, 300 mM KCl) for 1.5 hrs at 4°C. Post digestion, the protein was centrifuged at 44,082 xg for 20 mins, 4 °C in JA 25.5 rotor. The supernatant was loaded onto the pre-equilibrated Ni-NTA column and flow-through was collected. The flow-through should have the ScMreB5^{UT}. The column was washed with 50 mL buffer A, and then the bound HexaHis-SUMO was eluted with 100 % Buffer B. The samples of the second Ni-NTA were run on the 12% SDS-PAGE gel. The ScMreB5^{UT} was surprisingly bound to the column and eluted along with the Hexa-His SUMO tag at 100 % Buffer B. The protein is concentrated to 800 µL in 10 kDa centricons and injected into pre-equilibrated Superdex 75. The protein-containing fractions were run on the 12 % SDS-PAGE gel. The purest fraction corresponding to the 37 kDa molecular weight were concentrated, aliquoted, flash frozen, and stored at -80°C until further use.

6.2.5: Cystine residue labelling

Labelling of ScMreB5^{WT} native Cys (ScMreB5^{Cys105,285,315}) and ScMreB5^{Cys221} was done with Alexa 488 C₅ Maleimide (Catalog number A10254, Invitrogen). A small amount of dye powder was taken from a 10 µL tip and dissolved in 100 % DMSO. For obtaining the absorption maxima value at 280 nm (protein) and 488 nm (dye), the DMSO dye solution was diluted to 4000 X in methanol. The spectrum (200 – 700 nm) was obtained in the spectrophotometer, and absorption corresponding to 280 nm and 488 nm for the dye were noted. The concentration "c" of the dye solution was calculated using the equation corresponding to the Beer- Lambert law :

$$A = \epsilon_{\text{dye}} \cdot c \cdot l$$

(A = Absorption of protein (A_{280}) or dye (A_{488}); ϵ = molar extinction coefficient ($M^{-1}cm^{-1}$); l = path length, 1 cm). The molar extinction " ϵ_{dye} " values for the dye is $72,000 M^{-1}cm^{-1}$.

Around 10-fold excess of protein was taken depending on the dye concentration obtained. The dye- DMSO solution and the protein were mixed in a 0.5 mL Eppendorf and incubated at room temperature in the dark for around 1 hr for labelling. The labelling reaction was quenched with 1 mM DTT. The labelled protein was desalted to remove the excess dye using the pre-equilibrated (with buffer A) desalting column (5 mL, Cytiva). 2 mL fractions were collected and run on 12 % SDS PAGE gel. The fractions containing protein were pooled and further concentrated. The absorption values at 280 nm (protein) and 488 nm (dye) were obtained by spectrophotometer. The protein concentration was estimated from the equation given below (Nanda and Lorsch, 2014).

$$\text{Protein Concentration (M)} = ((A_{280} - A_{488}) \div \epsilon_{\text{protein}}) \times \text{Dilution factor of the protein}$$
$$\epsilon_{\text{protein}} = 20,400 M^{-1}cm^{-1}$$

For estimating the labelling efficiency, values of absorption of the labelled protein at A_{488} , ϵ_{dye} value of the dye and concentration of the labelled protein are put into the following equation (Nanda and Lorsch, 2014):

$$\text{Moles dye per mole of protein} = (A_{488} \text{ of labeled protein} \div (\epsilon_{dye} \times \text{protein conc (M)})) \times \text{dilution factor}$$

6.2.6: Electron microscopy

Transmission electron microscopy of negatively stained samples was carried out to visualize the ScMreB5^{WT} filaments and liposomes. 1 mM liposomes in buffer A of composition DOPG:CL: DOPC (38%:15%:47%; in mol%) were prepared as described above. For only liposomes, carbon film (only on 200 mesh) (Ted Pella, Catalog number: 01840) grid was used. Grids were glow discharged for 25 secs glow time and 10 secs hold time. 4 μ L of HK buffer was added onto the grid and blotted out. 4 μ L of 400 μ M liposome was added to the grid, incubated at room temperature for 5 mins, and blotted out. 4 μ L of HK buffer was added to the grid for washing and blotted out. The grid was stained with 0.5 % uranyl acetate for 30 secs and blotted out. The grid was placed over a parafilm inside a petriplate for drying overnight.

For liposome-protein samples, carbon-formvar grid, 200 mesh (Ted-Pella, Catalog number: 01800) grid was used. Grids were glow discharged for 25 secs glow time and 10 secs hold time. 5 μ L of reaction mix containing 400 μ M liposome, 5 μ M ScMreB5^{WT} and 2 mM MgCl₂ was added to the grid, incubated at room temperature for 5 mins, and blotted out. 4 μ L of Milli-Q was added to the grid for washing and blotted out. The grid was stained with 0.5 % of uranyl acetate for 30 secs and blotted out. The grid was placed over a parafilm inside a petriplate for drying overnight. Images of the liposomes were generated in ImageJ 1.52n (Rueden et al., 2017).

Cryo- EM was carried out to visualize the ScMreB5^{WT} filaments and liposomes. 1 mM liposomes in buffer A of composition DOPG:CL: DOPC (38%:15%:47%; in mol%) were prepared as described above. In a 50 μ L reaction mix, 40 μ M of ScMreB5^{WT}, 2 mM MgCl₂ and 2 mM AMP-PNP were mixed and incubated at room temperature for 5 mins. 400 μ M liposome was added to the mix and incubated at room temperature until loading onto the glow discharged grid. For only liposome condition, 400 μ M liposomes solution was directly added onto the glow discharged grid. Quantifoil grid R2/2 (Ted Pella) glow discharged for 25 secs were used. Inside the FEI Vitrobot chamber (temperature = 15°C and humidity =100 %), 4 μ l of the sample (only liposome or liposome-ScMreB5^{WT} in AMP-PNP conditions) was put on the grid and incubated for 7 – 10 mins before blotting out for 4 s. 4 μ l of HK buffer was put on the grid and incubated for 15 secs before blotting out for 3 secs. The second blotting was done in order to facilitate the liposome to enter inside the grid hole. This protocol was modified from (Lige and Ligu Wang, 2020) paper. The grid was plunge-frozen into liquid ethane for vitrification using an FEI Vitrobot. For image acquisition, grids were mounted on a Tecnai™ G2 20, 200 KeV electron microscope with 4K x 4K Eagle CCD Camera with a 4-port readout and 15 μ m pixel size. The magnification ranges of 50,000X - 62,000X was used. Images of the liposomes were generated in ImageJ 1.52n (Rueden et al., 2017)

6.2.7: Field emission scanning electron microscopy (FE-SEM)

SLBs templates of ScMreB5^{WT} in ATP and ADP-ALF_x conditions were prepared as described in the section 5.2.5 above. After 10 mins, of protein and nucleotide incubation, templates were fixed with 3 % w/v glutaraldehyde for 10 mins, followed by washing with HK buffer. The fixed templates were sequentially dehydrated by passing 200 μ L of 10 %, 20%, 40%, 60%, 80% and 100 % of ethanol. The flow cell was disassembled and the coverslip was

placed under vacuum overnight. For FE-SEM, fixed coverslip was coated with gold using a Q150T Turbo-Pumped Sputter Coater. The imaging was performed on an Ultra Plus Field Emission Scanning Electron Microscope (Zeiss) using a 3.00 keV electron beam and secondary electron detector. The images obtained were analyzed in ImageJ 1.52n (Rueden et al., 2017).

6.3: Results

6.3.1: ScMreB5 can remodel lipid membrane in a nucleotide-dependent manner

This work is currently being carried out in collaboration with Prof Thomas Pucadyil. Himani Khurana helped in the standardization of the microscopy experiments.

Our liposome pelleting assay showed the dependence of nucleotide state on membrane binding. For visualizing the nucleotide-dependent dynamics and localization of ScMreB5 on the membrane, we performed fluorescence microscopy of *in vitro* reconstituted membrane and ScMreB5. We studied the effect of ScMreB5 over a planar membrane (SLB; Supported Lipid Bilayer) and lipid tubes (SMrT; Supported membrane nanotubes). These templates have earlier been used to study membrane fission events (on nanotubes) and bilayer remodelling by proteins such as dynamin and EHD1 (Dar et al., 2015; Deo et al., 2018).

Both the templates were made using lipid composition, 38:15:46:1 (DOPG:CL: DOPC: Tx-Red DHPE; in mol%) in the 20 mM Hepes pH 7.5 and 150 mM KCl buffer environment and had curvature insensitive fluorescent lipid, *p*-Texas Red DHPE incorporated for visualization. The lipid composition was similar to *Spiroplasma* in terms of membrane charge (38 mol% and 15 mol% of PG and CL). We used them to study the effect of ScMreB5 in the presence of different nucleotides over two different curvature ranges (SMrT tubes and SLBs).

SLBs and the SMrT templates were pre-equilibrated with nucleotide and MgCl₂ in HK buffer. After pre-equilibration, unlabelled ScMreB5^{WT}, nucleotide and MgCl₂, were flowed in, incubated for 10 mins, and imaged. ScMreB5^{WT} displayed the capacity to remodel both templates. The extent of remodelling was dependent on nucleotide used.

6.3.1a: ScMreB5 severs SMrT templates in nucleotide-dependent manner

In the absence of nucleotide and $MgCl_2$, ScMreB5^{WT} was able to do extensive remodelling, which is seen from the tubes getting severed (Fig 6.3 A). No such observation was made in the presence of only $MgCl_2$ (Fig 6.3 B). In the presence of constant ATP-bound state (AMP-PNP, non-hydrolysable analog), the tubes severing and events of constrictions over the tubes (Fig 6.3 C). Few severing events occur in the presence of ATP, but the number of constriction events was not significant (Fig 6.3 D). Interestingly, in the presence of the transition state analog ADP-AIFx, the tubes underwent drastic bending, with no events of constriction or severing observed (Fig 6.3 E). In the ADP state, no tube remodelling was observed (Fig 6.3 F). Preliminary quantification of the percentage of tubes cut is shown (Fig 6.3 G). The summary of the effect on SMrT tubes under different nucleotide conditions with a plausible hypothesis on the mechanism is summarized in the Table 6.2. Our preliminary observation of ScMreB5^{WT} on SMrT templates shows that, indeed there is a role of nucleotide hydrolysis and transition state that affects remodelling.

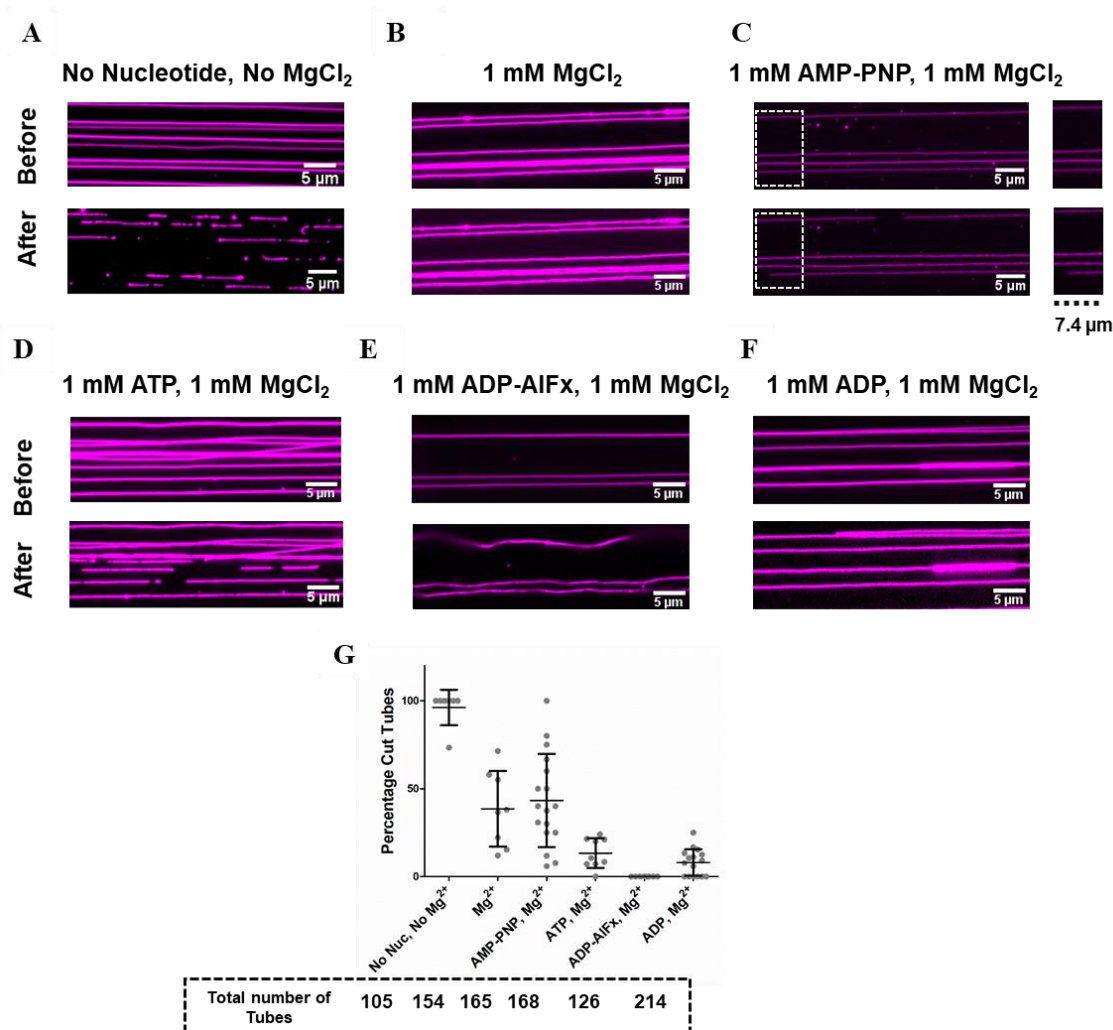


Figure 6.3: ScMreB5 remodels supported membrane nanotubes (SMrT) in nucleotide dependent manner.

Represented images of supported lipid tube labeled with 1 % Texas Red DHPE in the presence of ScMreB5^{WT} in the presence of different nucleotide and MgCl₂. **(A)** No Nucleotide, No MgCl₂, **(B)** 1 mM MgCl₂, **(C)** 1 mM AMP-PNP, 1 mM MgCl₂ **(D)** 1 mM ATP, 1 mM MgCl₂, **(E)** 1 mM ADP-AlF_x, 1 mM MgCl₂ and **(F)** 1 mM ADP, 1 mM MgCl₂. Lipid tube is composed of DOPG:CL: DOPC: TxRed DHPE (38%:15%:46%:1%). Scale bar is 10 μm. **(G)** Quantitation of the percentage of tubes cuts by ScMreB5^{WT} under different nucleotide conditions. Data represent the mean ± SD tubes cut in multiple fields across single experiment. The data represent analysis from the single preparation of SMrT templates. All the experiments were conducted with 1 μM of C-terminal Hexa-His tagged ScMreB5^{WT} in HK buffer (150 mM KCl, 20 mM Hepes pH 7.5).

Table 6.2: Summary of the effects of different nucleotide states on ScMreB5 remodelling of lipid tubes

Condition	Effect on Lipid tubes	Hypothesis
No Nucleotide, No MgCl ₂	Extensive cuts	Membrane facilitates removal of bound ADP leading to change in conformation of the filaments and remodelling of the bound membrane
MgCl ₂	Very few cuts	Incompatible filament conformation for efficient binding to lipid tubes, excess MgCl ₂ keeps the protein in ADP bound state
AMP-PNP, MgCl ₂	Cuts and Constrictions	Filament conformation facilitating constriction only
ATP, MgCl ₂	Very few cuts, few constrictions	Conformational changes of the filament accompanying hydrolysis initiates cuts of constricted tube
ADP-AlF _x , MgCl ₂	No cuts, no constrictions, bend tubes	Transition state conformation is unable to cut/constrict tubes, but pulls the membrane
ADP, MgCl ₂	No cuts, no constrictions	Incompatible conformation

6.3.1b: ScMreB5 remodels Supported lipid bilayer templates in nucleotide-dependent manner

We next wanted to explore if ScMreB5 can remodel the planar surface, such as the SLB (Supported lipid bilayer). In the absence of nucleotide and MgCl₂, as well as in the presence of AMP-PNP, ScMreB5 could not remodel the membrane (Fig 6.4 A and B). Interestingly, ScMreB5 could remodel the membrane with ATP, which was seen as a spike-like lipid bilayer structure (Fig 6.4 C). The appearance and activity of remodelling became even more apparent in the transition state, ADP-AlF_x condition (Fig 6.4 D). But no remodelling was observed in the presence of ADP (Fig 6.4 E). The summary of the effect on SLBs under different nucleotide conditions with a plausible hypothesis on the mechanism is summarized in the Table 6.3. Our preliminary data on SLB remodelling indicates that the transition state achieved upon ATP hydrolysis might facilitate the bilayer remodelling for ScMreB5.

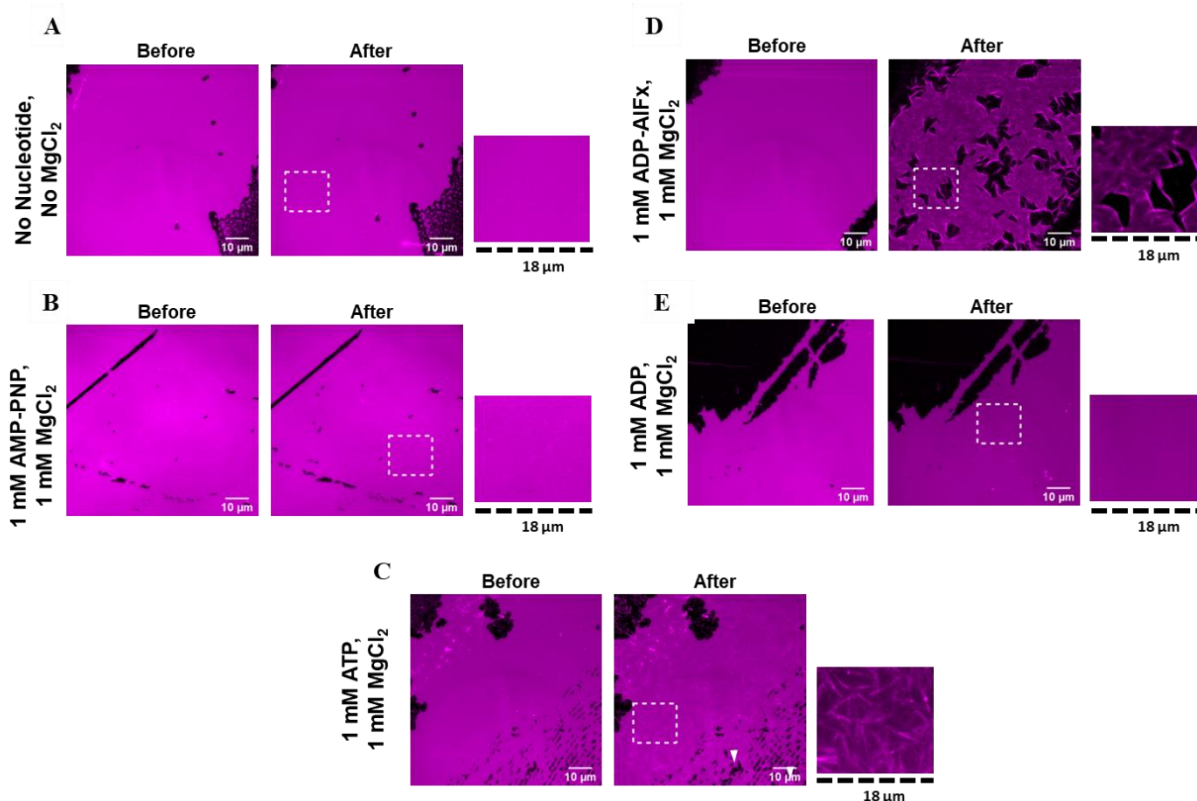


Figure 6.4: ScMreB5 remodels lipid bilayer in the presence of different nucleotides.

Representative fluorescence micrographs of supported lipid tube labeled with 1 % DHPE Texas Red DHPE in the presence of ScMreB5^{WT} under different nucleotides and MgCl₂. (A) No nucleotide and MgCl₂ (B) 1 mM AMP-PNP, 1 mM MgCl₂ (C) 1 mM ATP, 1 mM MgCl₂, (D) 1 mM ADP-AlF_x, 1 mM MgCl₂ and (E) 1 mM ADP, 1 mM MgCl₂. SLB (Supported Lipid Bilayer) comprises DOPG:CL:DOPC:TxRed DHPE (38%:15%:46%:1%). Scale bar =

10 μ m. All the experiments were conducted with 1 μ M of C-terminal Hexa-His tagged ScMreB5^{WT} in HK buffer (150 mM KCl, 20 mM Hepes pH 7.5).

Table 6.3: Summary of the effects of different nucleotide states on ScMreB5 remodelling of supported lipid bilayers

Condition	Effect on Bilayer	Hypothesis
No Nucleotide, No MgCl ₂	No membrane activity, intact bilayer	Incompatible filament conformation
MgCl ₂	Not attempted	-
AMP-PNP, MgCl ₂	No membrane activity, intact bilayer	Compatible filament conformation for binding but no remodelling
ATP, MgCl ₂	Bilayer remodelling, observation of spike like structure on bilayer	Compatible filament conformation for binding, remodelling is initiated
ADP-AIFx, MgCl ₂	Drastic bilayer remodelling	Compatible filament conformation (in transition state), remodelling occurs
ADP, MgCl ₂	No membrane activity, intact bilayer	Incompatible filament conformation for binding

6.3.2: Visualizing ScMreB5 on a membrane bilayer

Our preliminary data on the bilayer templates showed how the tubes or planar membrane undergo remodelling. But since we were using unlabelled protein, we did not have any information on protein localization and dynamics on the bilayer. Several attempts are being made to visualize protein on these structures as described below and summarized in Table 6.4.

Table 6.4: Summary of the trials done for ScMreB5 visualization over supported lipid bilayer

Construct	Feature of the protein	ATPase Activity (k_{obs})	ATPase Activity post labelling	ATPase Activity (in presence of liposomes)	Bilayer Remodelling (in presence of ATP)
ScMreB5^{Cys}_{105,285,315}	Native Cys are labelled (Cys105, Cys 285 and Cys315)	0.13 min ⁻¹	Inactive	Not checked	Did not proceed
ScMreB5²²¹_{Cys}	Native Cys and Cys221 inserted at the 218 th position (sandwich loop) are labelled	0.40 min ⁻¹	Inactive	Not checked	Did not proceed
ScMreB5^{218-GFP}	GFP inserted at 218 th position of ScMreB5	0.76 min ⁻¹	-	Not checked	Not observed, Did not proceed
ScMreB5^{NtGFP}	GFP inserted at N-terminal of ScMreB5	0.10 min ⁻¹	-	0.40 min ⁻¹	Not observed
ScMreB5^{UT}: ScMreB5^{NtGFP} (1:1)	Untagged ScMreB5 wildtype and ScMreB5 ^{Nt-GFP} mixed in 1:1 molar ratio	0.20 min ⁻¹	-	0.40 min ⁻¹	Observed, Under progress

Firstly, the maleimide derivative of Alexa Fluor™ 488 fluorescent dye was used for labelling the native Cys of ScMreB5^{WT} (ScMreB5^{Cys105,285,315}). However, post-labelling protein did not show any ATPase activity (Table 6.4). In parallel, we also designed constructs that had Cys incorporated after the 218th amino acid, which is the exposed loop (ScMreB5^{221Cys}) on the IIB subdomain. The loop is on the non-membrane binding face of ScMreB5. We expected that the exposed Cys would increase the labelling efficiency without hampering the ATPase activity of the protein. ScMreB5^{221Cys} did not elute as a monomer during purification (Fig 6.5 A) and had four times higher ATPase activity than the wildtype (Table 6.4). We went ahead with maleimide labelling, but post labelling the protein became inactive (Table 6.4). Hence, we did not proceed further with fluorescence microscopy for both conditions.

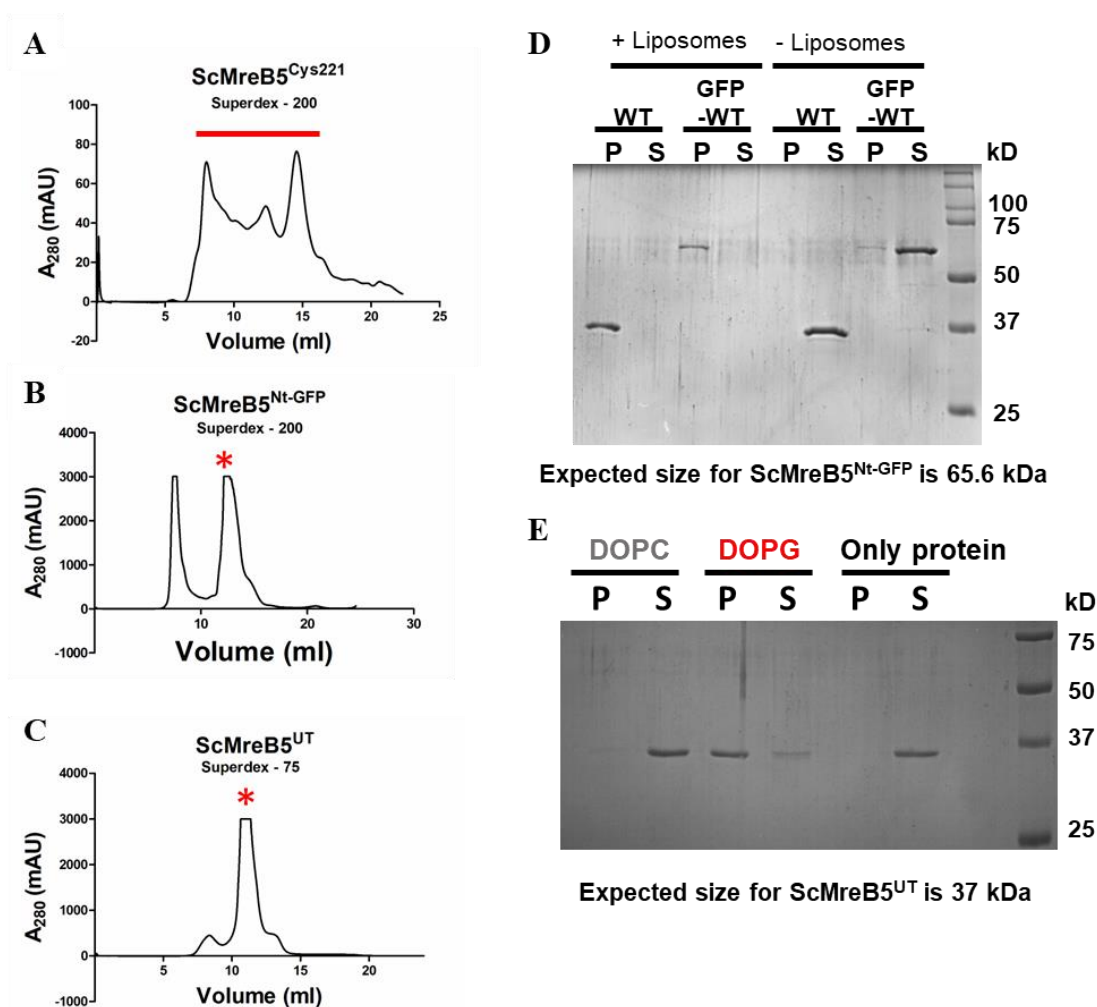


Figure 6.5: Purification profile and liposome pelleting assay of fusion construct and untagged ScMreB5.

(A) Superdex 200 gel filtration profile of ScMreB5^{Cys221}. The proteins start eluting from the void up until the monomer. The entire eluted protein (marked with the red line) is

concentrated and used for all the experiments. **(B)** Superdex 200 gel filtration profile of ScMreB3^{Nt-GFP}. The monomeric fraction (marked as asterisk) is used in all the experiments. **(C)** Superdex 75 gel filtration profile of ScMreB5^{UT}. The monomeric fraction (marked as asterisk) is used in all the experiments. **(D)** A representative 12% SDS-PAGE gel of liposome pelleting assay for determining membrane binding of ScMreB5^{Nt-GFP} with liposome made from DOPC: DOPG (20%:80%, mol %). P and S represent the pellet and supernatant fractions of the reaction. Concentrations of liposomes and protein used in the assay are 600 μ M and 2 μ M, respectively. **(E)** A representative 12% SDS-PAGE gel of liposome pelleting assay for determining membrane binding of ScMreB5^{UT} with a neutral lipid DOPC and an anionic lipid DOPG. P and S represent the pellet and supernatant fractions of the reaction. Concentrations of DOPG and DOPC liposomes and protein used in the assay are 600 μ M and 2 μ M, respectively.

Next, we used GFP fusion constructs of ScMreB5 to visualize the protein over the bilayer. ScMreB5^{218-GFP}, has GFP inserted after 218th amino acid residue (same region as for ScMreB5^{Cys221}). The protein had 7 times higher ATPase activity than the wildtype (Table 6.4). However, we did not see much remodelling on the bilayer in the presence of ATP (Fig 6.6 A), compared to ScMreB5^{WT}. Hence, we did not proceed further. The other GFP construct we used was ScMreB5^{Nt-GFP}; monomeric elute of ScMreB5^{Nt-GFP} was used for the study (Fig 6.5 B). This construct had ATPase activity similar to wildtype, both in the presence and absence of liposomes (Table 6.4). It also bound to the liposomes (Fig 6.5 D). Though ScMreB5^{Nt-GFP} bound to bilayer, it could not remodel the membrane in the presence of ATP (Fig 6.6 B).

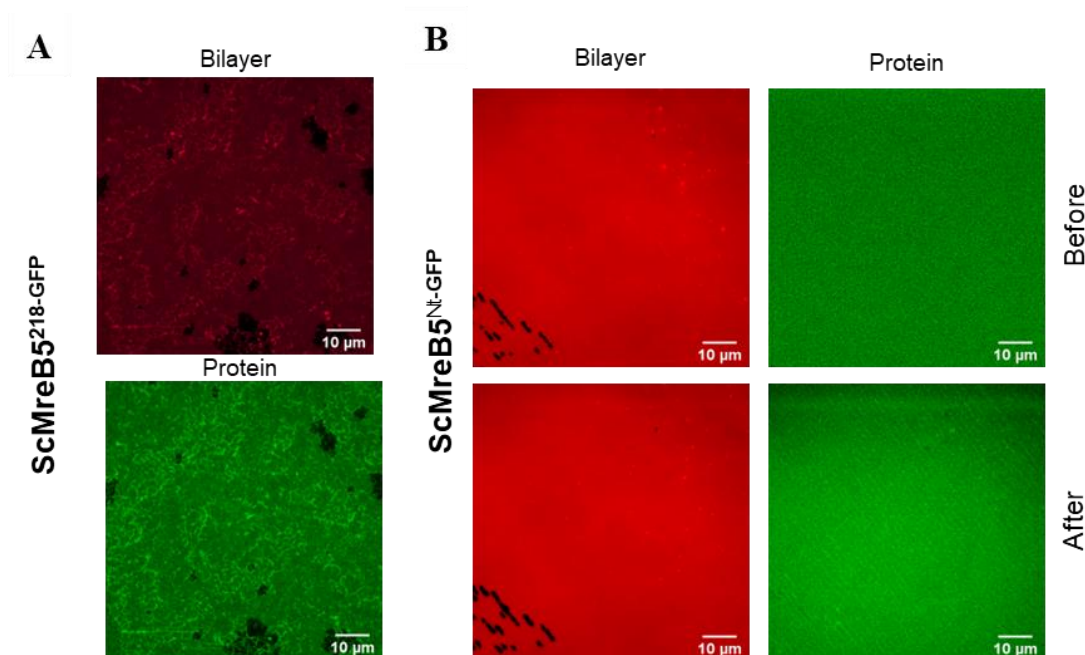


Figure 6.6: Visualizing ScMreB5 on the Supported lipid bilayer.

(A) Representative fluorescence micrograph of supported lipid bilayer (SLBs) containing 38% DOPG:15% CL:46% DOPC:1% DHPE-TxRed (in mol %) imaged after (10 mins) of addition of ScMreB5^{218-GFP} with ATP and MgCl₂. Spike like structures are not observed. (B) Representative fluorescence micrograph of supported lipid bilayer (SLBs) containing 38% DOPG:15% CL:46% DOPC:1% DHPE-TxRed (in mol %) imaged before and after (10 mins) of addition of ScMreB5^{Nt-GFP} with ATP and MgCl₂. No bilayer remodelling is observed. Scale bar =10 μm.

6.3.3: Mix of ScMreB5 N-terminal GFP and untagged constructs remodels bilayer

Untagged ScMreB5 construct (ScMreB5^{UT}) was designed for studying membrane remodelling. ATPase activity with and without liposome was similar to the wildtype Hexa His tagged ScMreB5, ScMreB5^{WT}, Table 6.4. Charge-specific liposome binding was also observed (Fig 6.5 E). We further went ahead to study remodelling of SLB in the presence of ATP and ADP-AIF_x (Fig 6.7 A and B). In both conditions, bilayer remodelling was observed as for the Hexa-His wildtype construct.

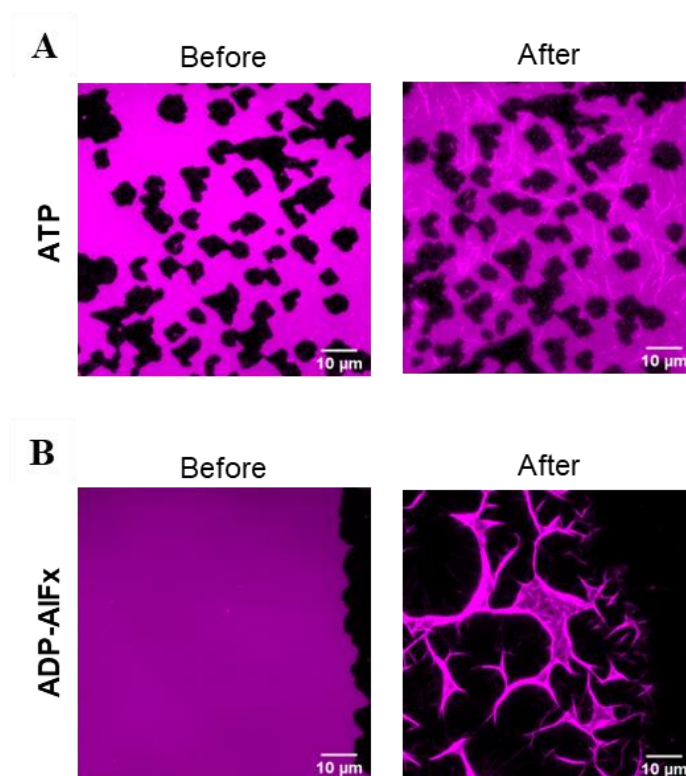


Figure 6.7: Visualizing ScMreB5^{UT} mediated remodelling of Supported lipid bilayer.

(A) Representative fluorescence micrograph of supported lipid bilayer (SLBs) containing 38% DOPG:15% CL:46% DOPC:1% DHPE-TxRed (in mol %) imaged before and after (10 mins) of addition of ScMreB5^{UT} with ATP and MgCl₂. Spike-like structures are observed. (B) Representative fluorescence micrograph of supported lipid bilayer (SLBs) containing 38% DOPG:15% CL:46% DOPC:1% DHPE-TxRed (in mol %) imaged before and after (10 mins) of addition of ScMreB5^{UT} with ADP-AlFx and MgCl₂. Extensive remodelling is observed. Above experiments were performed using 1 μM protein, 1 mM nucleotide and 1 mM MgCl₂. HK buffer (20 mM HEPES, pH 7.5 and 150 mM KCl). Scale bar = 10 μm.

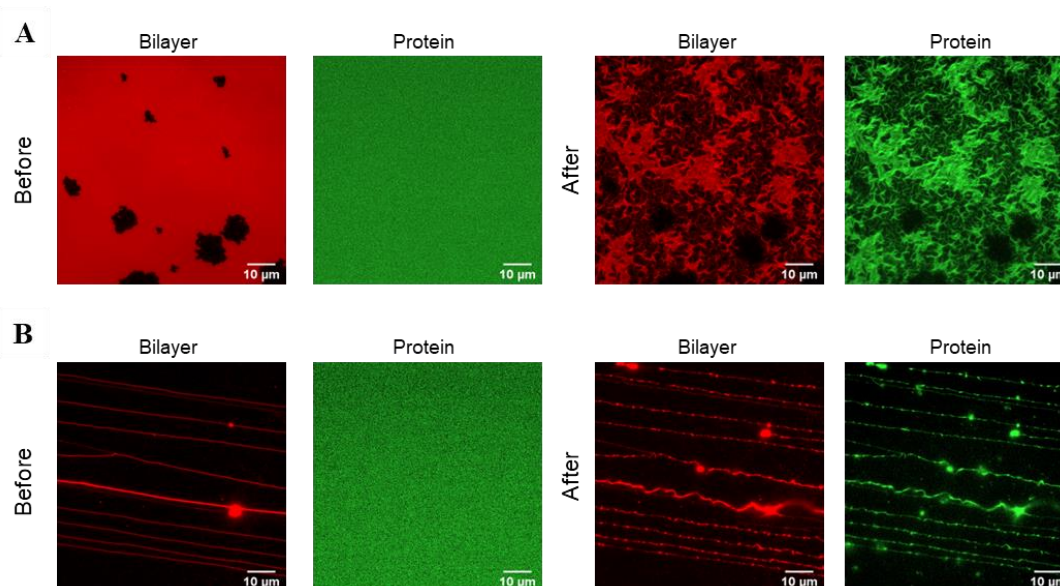


Figure 6.8: Visualizing ScMreB5^{UT} and ScMreB5^{Nt-GFP} mix mediated remodelling of supported lipid bilayer.

(A) Representative fluorescence micrograph of supported lipid bilayer (SLBs) imaged before and after (10 mins) of addition of ScMreB5^{UT} : ScMreB5^{Nt-GFP} mix with ADP-AlFx and MgCl₂. Spike like structures are observed in both the protein and lipid channels. (B) Representative fluorescence micrograph of supported membrane nanotubes (SMrT) imaged before and after (10 mins) of addition of ScMreB5^{UT} : ScMreB5^{Nt-GFP} mix with ADP-AlFx and MgCl₂. Nanotube tubes seem to undergo bending and constriction. The above experiments used 2 μM protein (1 μM ScMreB5^{UT} and 1 μM ScMreB5^{Nt-GFP}), 1 mM ADP-AlFx and 1 mM MgCl₂ in HK buffer (20 mM HEPES, pH 7.5 and 150 mM KCl). Lipid mix used contained 38% DOPG:15% CL:46% DOPC:1% DHPE-TxRed (in mol %). Scale bar = 10 μm.

We then went ahead to check whether a mix of ScMreB5^{UT} and ScMreB5^{Nt-GFP} could be used for visualizing the filament dynamics and membrane remodelling. ATPase activity measurement with and without liposomes, were similar to wildtype in 1:1 molar ratio of the protein in the reaction (Table 6.4). We used the same ratio to visualize remodelling on the SLB and the SMrT templates. Initially, we checked the remodelling in the ADP-AlFx condition, which gives the most extreme level of remodelling. Remodelling was observed in both the bilayer and the tubes (Fig 6.8 A and B). We could observe the protein localizing over the remodelled membrane structures in the GFP channel (Fig 6.8 A and B). Hence, this strategy worked for determining protein localization and dynamics. Further standardization is underway using protein mix and different nucleotide conditions. It will provide a handle to study the time-dependent membrane remodelling and quantifying the protein dynamics on the SLBs and SMrTs.

6.3.4: Electron microscopy of ScMreB5 with liposomes and Supported lipid bilayer (SLB)

We performed negative staining electron microscopy and cryo-electron microscopy on liposomes and protein filaments in the presence and absence of AMP-PNP. Preliminary negative stain data of ScMreB5 in the absence of any nucleotide showed that protein filaments can bind to the liposome (Fig 6.9 A and B). Preliminary cryo-EM data on ScMreB5 show that in AMP-PNP presence, liposomes distort from a spherical shape (Fig 6.9 C) to a pleomorphic structure (Fig 6.9 D). Hence, ScMreB5 can also sense the curvature and remodel the liposomes.

We performed scanning electron microscopy to visualize the remodelled structures formed after remodelling in ATP and ADP-AlFx conditions (Fig 6.10 A and B). In both the states, we could see the tube-like structures and folded bilayer (Fig 6.10 A and B). These structures might be a complex of both the protein and the bilayer. Not much difference in the structures were observed between the two nucleotide states.

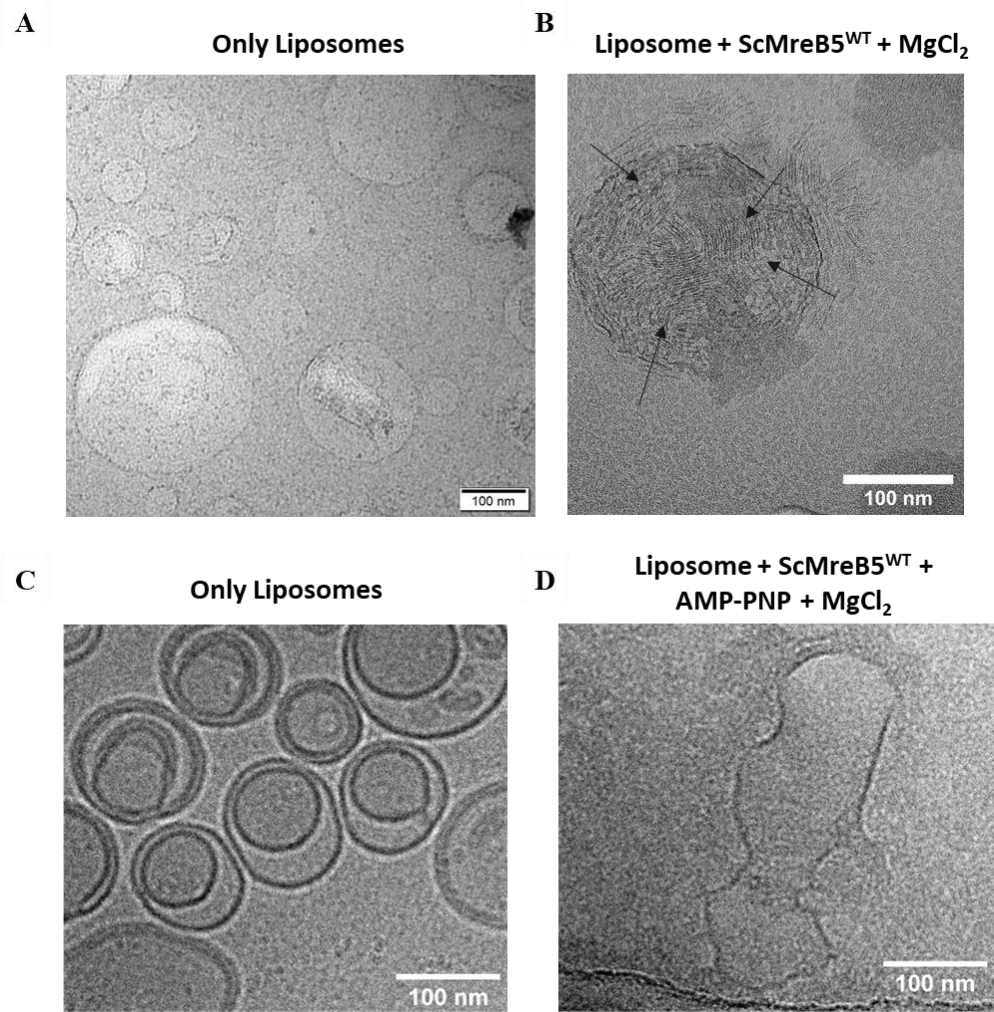


Figure 6.9: ScMreB5^{WT} can bind and deform liposomes

(A) A representative negative stain of only liposomes shows retention of liposome shape. (B) A representative negative stain of liposome and ScMreB5^{WT} filaments (Black arrows) in the absence of any nucleotide show that it binds to liposome (C) Cryo-electron micrograph of only liposomes show liposomes retaining their shape and are multilamellar. (D) Cryo-electron micrograph of liposome in the presence of ScMreB5^{WT} with AMP-PNP and MgCl₂. Liposomes undergo deformation in the presence of ScMreB5. Liposomes (100 nm) are made from 38% DOPG:15% CL: 47% DOPC lipids. Scale bar =100 nm.

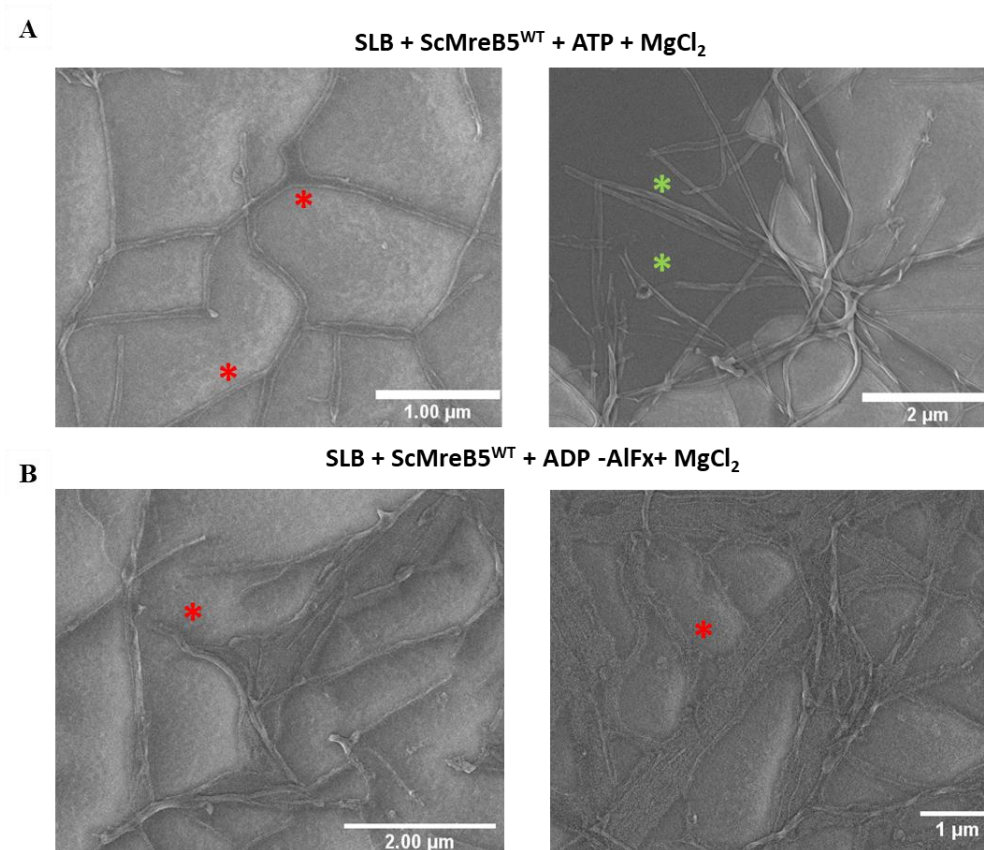


Figure 6.10: FE-SEM of ScMreB5^{WT} on SLBs show remodelled bilayer structures

(A) Scanning electron micrograph of SLB (Supported Lipid Bilayer) with ScMreB5^{WT} in the presence of ATP and MgCl₂. (B) Scanning electron micrograph of SLB (Supported Lipid Bilayer) with ScMreB5^{WT} in the presence of ADP-AlFx and MgCl₂. Remodelled bilayer-protein structures are seen in A and B. Tube-like and folded bilayer structures are marked in red and green asterisks, respectively. SLB are made from composition of 38% DOPG:15% CL: 47% DOPC lipids.

6.4: Discussion

This chapter focussed on understanding how ScMreB5 in different nucleotide state remodels different membrane curvature. Cryo-EM studies on MreBs from *T.maritima* and *C.crescentus* showed it could deform micron-scale liposomes (1 – 2 μm) (Hussain et al., 2018; Wong et al., 2019; Salje et al., 2011). The liposome deformation was observed when protein was enclosed within the liposome as well as when present outside the liposomes. Curvature sensing and tubulation studies performed using molecular dynamics simulations and micron

scale (1 – 5 μm) liposomes showed it can sense a range of micron scale curvature (Hussain et al., 2018; Wong et al., 2019).

Preliminary negative staining on TEM and cryo-EM shows that ScMreB5 can bind to liposomes even without excess nucleotide. It can cause liposomes to undergo deformation in the AMP-PNP conditions, similar to TmMreB (Hussain et al., 2018). Thus, ScMreB5 displays conserved features of membrane binding and liposome deformations. Whether ScMreB5 can deform liposomes when enclosed within the liposomes remain to be tested.

MreBs studies so far show that it can undergo nucleotide-dependent polymerization (Bean and Amann, 2008; Takahashi et al., 2022; Mayer and Amann, 2009). But the regulation of polymerization and its effect on membrane binding is unknown. In the previous chapter, we showed nucleotide-dependent membrane remodelling using ATP/ADP/AMP-PNP/ADP-AIF_x.

To visualize the effect of ScMreB5 in different nucleotide states, we performed fluorescence microscopy on two extreme curvature systems, nanotube (SMrT tubes) and planar membrane (SLBs). ScMreB5 was able to remodel both surfaces irrespective of the curvature, however under different nucleotide states. In a planar surface, remodelling was maximum during the transition state of the ScMreB5 filament. The constriction and severing might have occurred in nanotubes due to the conformational change in different nucleotide states. After optimizing the construct for visualizing ScMreB5 over nanotubes and planar membranes, we can monitor the filament dynamics as it causes membrane remodelling. This part of will be carried out further in the future.

6.5: References

- Bean, G.J., and K.J. Amann. 2008. Polymerization properties of the *Thermotoga maritima* actin MreB: Roles of temperature, nucleotides, and ions. *Biochemistry*. 47:826–835. doi:10.1021/bi701538e.
- Dar, S., S.C. Kamerkar, and T.J. Pucadyil. 2015. A high-throughput platform for real-time analysis of membrane fission reactions reveals dynamin function. *Nat Cell Biol*. 17:1588–1596. doi:10.1038/ncb3254.
- Dar, S., S.C. Kamerkar, and T.J. Pucadyil. 2017. Use of the supported membrane tube assay system for real-time analysis of membrane fission reactions. *Nat Protoc*. 12:390–400. doi:10.1038/nprot.2016.173.
- Deo, R., M.S. Kushwah, S.C. Kamerkar, N.Y. Kadam, S. Dar, K. Babu, A. Srivastava, and T.J. Pucadyil. 2018. ATP-dependent membrane remodeling links EHD1 functions to endocytic recycling. *Nat Commun*. 9:5187. doi:10.1038/s41467-018-07586-z.
- Gill, R.L., J.-P. Castaing, J. Hsin, I.S. Tan, X. Wang, K.C. Huang, F. Tian, and K.S. Ramamurthi. 2015. Structural basis for the geometry-driven localization of a small protein. *Proceedings of the National Academy of Sciences*. 112:E1908–E1915. doi:10.1073/pnas.1423868112.
- Hussain, S., C.N. Wivagg, P. Szwedziak, F. Wong, K. Schaefer, T. Izoré, L.D. Renner, M.J. Holmes, Y. Sun, A.W. Bisson-Filho, S. Walker, A. Amir, J. Löwe, and E.C. Garner. 2018. MreB filaments align along greatest principal membrane curvature to orient cell wall synthesis. *eLife*. 7:e32471. doi:10.7554/eLife.32471.
- Kamerkar, S.C., K. Roy, S. Bhattacharyya, and T.J. Pucadyil. 2019. A Screen for Membrane Fission Catalysts Identifies the ATPase EHD1. *Biochemistry*. 58:65–71. doi:10.1021/acs.biochem.8b00925.
- Lenarcic, R., S. Halbedel, L. Visser, M. Shaw, L.J. Wu, J. Errington, D. Marenduzzo, and L.W. Hamoen. 2009. Localisation of DivIVA by targeting to negatively curved membranes. *EMBO Journal*. 28:2272–2282. doi:10.1038/emboj.2009.129.
- Libchaber, A., J. Shin, T. Nakadai, Y.T. Maeda, V. Noireaux, and K. Uryu. 2011. Assembly of MreB Filaments on Liposome Membranes: A Synthetic Biology Approach. *ACS Synthetic Biology*. 1:53–59. doi:10.1021/sb200003v.

- Lige, T., and Ligu Wang. 2020. Cryo-EM sample preparation method for extremely low concentration liposomes. *Ultramicroscopy*. 208:112849. doi:10.1016/j.ultramic.2019.112849.
- Mayer, J.A., and K.J. Amann. 2009. Assembly properties of the bacillus subtilis actin, MreB. *Cell Motility and the Cytoskeleton*. 66:109–118. doi:10.1002/cm.20332.
- Nanda, J.S., and J.R. Lorsch. 2014. Chapter Seven - Labeling of a Protein with Fluorophores Using Maleimide Derivatization. In *Methods in Enzymology*. J. Lorsch, editor. Academic Press. 79–86.
- Rueden, C.T., J. Schindelin, M.C. Hiner, B.E. DeZonia, A.E. Walter, E.T. Arena, and K.W. Eliceiri. 2017. ImageJ2: ImageJ for the next generation of scientific image data. *BMC Bioinformatics*. 18:529. doi:10.1186/s12859-017-1934-z.
- Salje, J., F. van den Ent, P. de Boer, and J. Löwe. 2011. Direct Membrane Binding by Bacterial Actin MreB. *Molecular Cell*. 43:478–487. doi:10.1016/j.molcel.2011.07.008.
- Schindelin, J., I. Arganda-Carreras, E. Frise, V. Kaynig, M. Longair, T. Pietzsch, S. Preibisch, C. Rueden, S. Saalfeld, B. Schmid, J.-Y. Tinevez, D.J. White, V. Hartenstein, K. Eliceiri, P. Tomancak, and A. Cardona. 2012. Fiji: an open-source platform for biological-image analysis. *Nat Methods*. 9:676–682. doi:10.1038/nmeth.2019.
- Takahashi, D., I. Fujiwara, Y. Sasajima, A. Narita, K. Imada, and M. Miyata. 2022. ATP-dependent polymerization dynamics of bacterial actin proteins involved in Spiroplasma swimming. *Open Biology*. doi:10.1098/rsob.220083.
- Tegel, H., S. Tourle, J. Ottosson, and A. Persson. 2010. Increased levels of recombinant human proteins with the Escherichia coli strain Rosetta(DE3). *Protein Expr Purif*. 69:159–167. doi:10.1016/j.pep.2009.08.017.
- Updegrave, T.B., and K.S. Ramamurthi. 2017. Geometric protein localization cues in bacterial cells. *Current Opinion in Microbiology*. 36:7–13. doi:10.1016/j.mib.2016.12.001.
- Ursell, T.S., J. Nguyen, R.D. Monds, A. Colavin, G. Billings, N. Ouzounov, Z. Gitai, J.W. Shaevitz, and K.C. Huang. 2014. Rod-like bacterial shape is maintained by feedback between cell curvature and cytoskeletal localization. *Proceedings of the National Academy of Sciences*. 111:E1025–E1034. doi:10.1073/pnas.1317174111.

Chapter 6: Membrane remodelling dynamics of ScMreB5

Wong, F., E.C. Garner, and A. Amir. 2019. Mechanics and dynamics of translocating MreB filaments on curved membranes. *eLife*. 8:e40472. doi:10.7554/eLife.404

Chapter 7: Conclusions and Future prospect

7.1: Summary of major findings

Cell-wall synthesis and its maintenance determines the shape of the bacteria. An important scaffold protein that is responsible for cell shape in bacteria is the cytoskeleton protein MreB. Filaments of MreB align as dynamic patches by sensing the greatest principal curvature in bacteria and further crosstalk with the cell wall synthesis machinery (Shi et al., 2018). Thus, this interaction reinforces the bacterial cell shape. Recent findings have shown the relevance of MreBs in cell shape and motility in cell-wall less bacteria like *Spiroplasma* (Lartigue et al., 2022; Kiyama et al., 2022; Masson et al., 2021). In vitro characterization of MreBs from *S. citri* can highlight the fundamental and distinct features of the protein required for cell shape maintenance independent of cell wall synthesis.

In my thesis I have characterized one out of five MreBs, ScMreB5 of *S. citri*. The major finding of the thesis is that the nucleotide state of ScMreB5 determines filament organization, membrane binding and membrane remodeling abilities. We show that the fundamental structural features of MreB that are important for cell-wall mediated cell shape maintenance are also important for ScMreB5 mediated maintenance of cell-shape in the absence of cell-wall.

The major findings from our work are briefly summarized here.

Crystal structures of ScMreB5 provide the structural basis of K⁺ mediated stability of ScMreB5

Optimization of purification condition revealed that the presence of K⁺ and nucleotide enhances the protein stability. ScMreB5 crystal structures (PDB IDs: 7BVY and 7BVZ) had a unique K⁺ ion binding site at the nucleotide-binding pocket that improved protein stability by facilitating the stabilization of ADP via K⁺ mediated interaction.

Conserved structural features of actins and MreBs from cell-wall bacteria are well-conserved in ScMreB5

Structural comparison with other MreBs and actins show the conservation of structural features and active site motifs for ScMreB5. Sequence analysis revealed the conservation of ATP hydrolysis residues that were also characterized experimentally through ATPase activity measurements. A thorough analysis of the relative subdomain movements by calculating subdomain angles (IB-IA-IIA and IIB-IIA-IA) and dihedral angle of all the available MreB

structures was performed. To reach a functional double protofilament state, a sequential decrease in both the dihedral and subdomain angles occur. Our sequence and structural analysis for membrane binding region in ScMreB5 showed the presence of a hydrophobic loop and a unique extended and positively charged C-terminal tail, both of which could contribute to the membrane binding. Analysis of the A22 binding pocket of ScMreB5 led to the hypothesis that the protein could resist the polymerization inhibitory drug A22, which was further proved experimentally through yeast expression based experiments for observation of MreB filaments.

ScMreB5 is an active ATPase

Our ATPase activity measurements for the wild type and hydrolysis mutants show that residues are functionally well conserved as for actins and other MreBs. Our ATPase activity assay for the polymerization mutant hint to the interface's role in the protein's hydrolytic activity, a conserved feature of the actin family of proteins.

ScMreB5 polymerization properties are dependent on the nucleotide state

Our cryo-EM and light scattering assay show that ScMreB5 can undergo polymerization without the requirement of nucleotide hydrolysis. A polymerization dynamics was performed in collaboration with Dr. Srinivasan Ramanujam (NISER Bhubaneswar). GFP fusion constructs of ScMreB5^{WT} and ATP hydrolysis mutant ScMreB5^{E134A} in yeast *S. pombe* were expressed. A comparison of filament dynamics and filament bundling showed that Glu134 is important for efficient filament formation and bundling. Glu134 can act as sensor for ATP binding and hydrolysis, further determining polymerization properties. Though Glu134 is known to affect hydrolysis, its role as a switch for triggering ATP-dependent conformational change and polymerization has not been stated earlier.

ScMreB5 membrane binding is charge-based and dependent on the nucleotide state

ScMreB5 binds to liposomes that mimic *S.citri* membrane composition. Unlike for other MreBs where binding is through a specific region by hydrophobic interaction, our data suggested a surface-level interaction for ScMreB5, that involves both charge-based and hydrophobic residue-mediated interaction. We further show that the nucleotide state drives ScMreB5 membrane binding. It is the first evidence for MreBs, where nucleotide state plays a role in membrane binding and stimulates hydrolytic activity for MreBs.

ScMreB5 nucleotide state determines membrane remodeling ability

ScMreB5 can also deform liposomes, as observed for TmMreB and CcMreB (van den Ent et al., 2014; Salje et al., 2011). Further, for the first time we provide evidence of the membrane remodeling ability of ScMreB5 in different nucleotide states. This part of the work is done in collaboration with Prof. Thomas Pucadyil (IISER, Pune). Based on our results on the effect of MreB5 on lipid bilayer and lipid tubes, we hypothesize that the filament conformation is sensitive to curvature. Conformational changes of the filament accompanying the ATP hydrolysis cycle could drive the membrane remodeling by the bound ScMreB5 filaments.

7.2: Major implications from the work

Glu134 plays important role in nucleotide dependent polymerization

Glu134 in the ScMreB5 is mostly conserved in actins and MreBs (Bork et al., 1992). Based on our structural and biochemical analysis of this residue, we propose that Glu has a dual role (a) sensing ATP, which further drives conformational change at the nucleotide-binding pocket. (b) ATP hydrolysis. As the ATP binds at the pocket, Glu undergoes a conformational change that facilitates the interaction of each subdomain with the nucleotide-binding pocket (Fig 7.1). This might further help in further attaining a conformation that drives the formation of the MreB antiparallel double protofilament state. After achieving a double protofilament state, the catalytic Glu functions as a catalytic residue to drive ATP hydrolysis. Hence, it plays an important function of determining efficient polymerization dynamics and ATP hydrolysis.

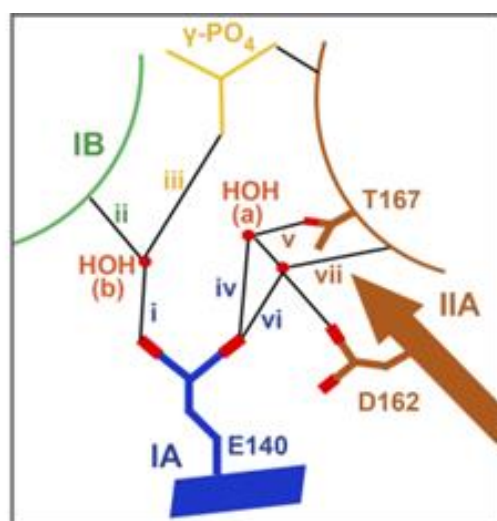


Figure 7.1: Schematic of Glu-mediated subdomain conformational change.

Glu140 in *C.crescentus* MreB (Glu134 in ScMreB5) holds the conformation of the subdomains in a conformation that facilitates the double protofilament conformation of the

MreB, which might further undergo ATP dependent hydrolysis. In the schematic, Glu140 in a double-protofilament AMP-PNP bound state interacts with the other subdomains via water (a and b) mediated interaction represented as i to vii. This further positions Glu140 near the catalytic water (a), leading to ATP hydrolysis. Post hydrolysis some of these interaction breaks lead to a conformational change in the filament assembly.

Surface-mediated interaction of the ScMreB5 filament under different nucleotide conditions determines liposome binding

We show that, unlike TmMreB, ScMreB5 binding to liposomes depends on charge and hydrophobic interactions. Thus, filaments of ScMreB5 would interact with the lipid membrane through the membrane-facing surface of the protein. Further, our study shows that ScMreB5 filament binding depends on different nucleotide states (Fig 7.2). Hence, the sensing of nanometre scale curvature (100 nm size liposomes) by ScMreB5 is dependent on the nucleotide state of the protein. Different nucleotide states can also lead to membrane deformations by ScMreB5.

Membrane remodelling of ScMreB5 is dependent on the nucleotide state of the protein

ScMreB5 filaments can sense and remodel curvatures of different ranges, from a nanometre-size tube to planar membrane surfaces. Interestingly, the remodelling extent of ScMreB5 on the surface of two different curvatures depends on the nucleotide state. This could mean that different filament conformation of ScMreB5 in different nucleotide states can remodel the

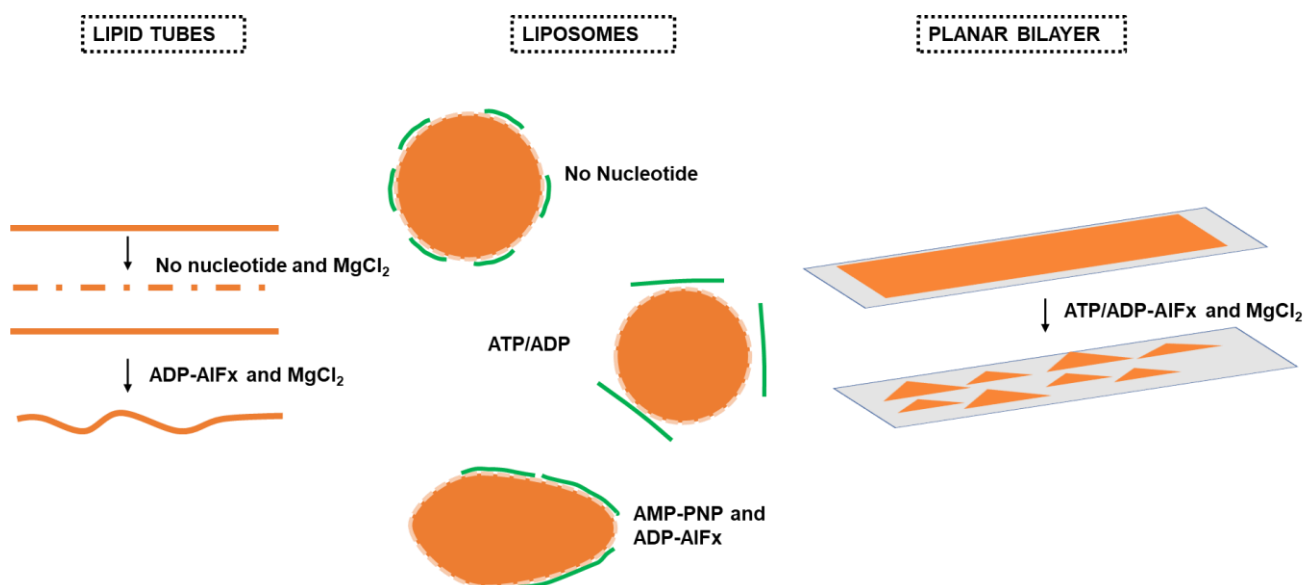


Figure 7.2: Schematic of nucleotide-dependent differential binding and remodelling of the membrane.

Shown here are the membrane surface of differential curvatures, lipid tubes (< 100 nm size), liposomes (~ 100 nm size range) and planar membrane. ScMreB5 is able to sense membranes of different curvatures. Membrane sensing is dependent on the nucleotide state of the protein. The nucleotide state might determine the filament conformation. Different filament conformations would further define the membrane remodelling ability of ScMreB5. Orange coloured structures is the lipid bilayer, and the green lines represent ScMreB5 filaments bound to liposomes.

membrane differently. Hence, different filament conformation of ScMreB5 determines curvature sensing and remodelling capability.

Our results propose a model for ScMreB5 membrane interaction. Dynamic antiparallel double-protofilaments of ScMreB5 recognize the charged membrane surface. This interaction further facilitates a stimulated ATPase activity of ScMreB, leading to a conformational change of the filaments. This conformational change drives the membrane remodelling. The event of ATP hydrolysis is essential to drive the conformational change that provides the necessary force for membrane remodeling (Fig 7.1). This feature hints towards an allosteric mechanism where conformational change at the nucleotide-binding pocket drives changes at membrane binding region of ScMreB5. In addition to membrane interaction, ScMreB5 interact with Fibril filaments (Harne et al., 2020). This interaction has also been observed to be dependent on the nucleotide states (based on the work of Mrinmayee Bapat, unpublished results). Thus, ScMreB5 might play a central role in membrane binding and remodelling with the Fibril filament. Recent studies also support the role of ScMreB5 in helical shape and motility revival in spherical synthetic cells and Mycoplasma (Lartigue et al., 2022; Kiyama et al., 2022). Our study provides a mechanistic insight into how ScMreB5 might generate this helicity (membrane remodelling) by nucleotide dependent conformational change. Thus, the conformational change driven by ATP hydrolysis and membrane binding ability have an allosteric link to determine the helical shape of *Spiroplasma*.

7.3: Future Prospects

Recent studies on *Spiroplasma* MreBs have shown the interaction between multiple MreB paralogs. MreB5 comes as the significant MreB for determining the helicity and swimming of *Spiroplasma* (Lartigue et al., 2022; Kiyama et al., 2022; Harne et al., 2020). To determine the role of ATP hydrolysis and polymerization for MreB5 function, expressing hydrolysis and polymerization mutants of ScMreB5 in the non-helical, non-motile *S.citri* strain, ASP-I will be further carried out. The exact role of other MreBs in driving the helical shape and motility remains to be elucidated. Role of MreBs in determining *Spiroplasma* such as cell length, kinking motility, chemotaxis and cell division etc, role of MreBs and Fibril is still unknown. Although the interaction studies of *Spiroplasma* MreBs and Fibrils show their role in helicity and swimming, the role of polymerization dynamics, ATP hydrolysis and membrane binding features remains to be understood for each MreB. Biochemical characterization of *Spiroplasma* MreBs and interaction studies using purified protein under different nucleotide states can help understand interaction between different MreBs. This would shed light on how the nucleotide state of the filament would determine interactions between MreBs and Fibril. This can be further taken forward by characterizing membrane binding and remodelling study of different MreBs in the presence of different nucleotide.

7.4: References

- Bork, P., C. Sander, and A. Valencia. 1992. An ATPase domain common to prokaryotic cell cycle proteins, sugar kinases, actin, and hsp70 heat shock proteins. *PNAS*. 89:7290–7294. doi:10.1073/pnas.89.16.7290.
- van den Ent, F., T. Izoré, T.A.M. Bharat, C.M. Johnson, and J. Löwe. 2014. Bacterial actin MreB forms antiparallel double filaments. *eLife*. doi:10.7554/eLife.02634.
- Harne, S., S. Duret, V. Pande, M. Bapat, L. Béven, and P. Gayathri. 2020. MreB5 Is a Determinant of Rod-to-Helical Transition in the Cell-Wall-less Bacterium *Spiroplasma*. *Current Biology*. doi:10.1016/j.cub.2020.08.093.
- Kiyama, H., S. Kakizawa, Y. Sasajima, Y.O. Tahara, and M. Miyata. 2022. Reconstitution of a minimal motility system based on *Spiroplasma* swimming by two bacterial actins in a synthetic minimal bacterium. *Science Advances*. 8:eabo7490. doi:10.1126/sciadv.abo7490.

Chapter 7: Conclusions and Future Prospects

Lartigue, C., B. Lambert, F. Rideau, Y. Dahan, M. Decossas, M. Hillion, J.-P. Douliez, J. Hardouin, O. Lambert, A. Blanchard, and L. Béven. 2022. Cytoskeletal components can turn wall-less spherical bacteria into kinking helices. *Nat Commun.* 13:6930. doi:10.1038/s41467-022-34478-0.

Masson, F., X. Pierrat, B. Lemaitre, and A. Persat. 2021. The wall-less bacterium *Spiroplasma poulsonii* builds a polymeric cytoskeleton composed of interacting MreB isoforms. *iScience.* 24:103458. doi:10.1016/j.isci.2021.103458.

Salje, J., F. van den Ent, P. de Boer, and J. Löwe. 2011. Direct Membrane Binding by Bacterial Actin MreB. *Molecular Cell.* 43:478–487. doi:10.1016/j.molcel.2011.07.008.

Shi, H., B.P. Bratton, Z. Gitai, and K.C. Huang. 2018. How to Build a Bacterial Cell: MreB as the Foreman of *E. coli* Construction. *Cell.* 172:1294–1305. doi:10.1016/j.cell.2018.02.050.

Permissions



Vani Pande <vani.pande@students.iiserpune.ac.in>

Request to reprint paper as part of thesis

2 messages

Vani Pande <vani.pande@students.iiserpune.ac.in>
To: permissions@rockefeller.edu

Mon, Feb 6, 2023 at 9:42 PM

Dear Sir/Ma'am

I needed permission to reprint an article published in the Journal of Cell Biology on April 4, 2022, as a part of my thesis. I am one of the authors of the publication.

The title for the same is "Filament organization of bacterial actin MreB is dependent on the nucleotide state"

DOI: <https://doi.org/10.1083/jcb.202106092>

Could you kindly guide me through the process of getting permission for reprinting the article?

Thank you,

Kind regards

Vani Pande

Int PhD Biological sciences

IISER Pune

20162013

RU Press Permiss <permiss@mail.rockefeller.edu>
To: Vani Pande <vani.pande@students.iiserpune.ac.in>

Mon, Feb 13, 2023 at 10:26 PM

Hi Vani,

Thank you for publishing with JCB! As one of the authors of the paper, you retain copyright and can freely reuse the article in your thesis, with citation. Let me know if you need anything else.

Best,

Laura



Submit Log in Register Subscribe Claim Q ☰

There is no charge for publishing in a *Trends* journal, and there are no charges for color figures.

Copyright

Upon acceptance of an article, authors will be asked to transfer copyright. This transfer will ensure the widest possible dissemination of information. A form facilitating transfer of copyright will be provided upon acceptance of the manuscript. After transfer of copyright, authors retain rights as discussed below.

Authors' rights

As an author, you (or your employer or institution) may do the following:

- Make copies (print or electronic) of the article for your own personal use, including for your own classroom teaching use.
- Make copies and distribute such copies (including through e-mail) of the article to known research colleagues for the personal use by such colleagues (but not for commercial purposes, as described below).
- Post a revised personal version of the final text (including illustrations and tables) of the article (to reflect changes made in the peer review and editing process) on your personal or institutional website or server, with a link (through the relevant DOI) to the article as published, provided that such postings are not for commercial purposes, as described below. Please note: Depositing in or posting to special repositories (such as PubMed Central or institutional repositories) is permitted only under specific agreements between Elsevier and the repository and only when consistent with Elsevier's policies concerning such repositories.
- Present the article at a meeting or conference and distribute copies of the article to the delegates attending such meeting.
- Allow your employer to use all or part of the information in the article for other intracompany use (e.g., training) if the article is a "work for hire" made within the scope of your employment.
- Retain patent and trademark rights and rights to any process or procedure described in the article.
- Use the article or any part thereof in a printed compilation or your works, such as collected writings or lecture notes (subsequent to publication of the article in the journal).
- Prepare other derivative works that extend the article into book-length form or otherwise re-use portions or excerpts in other works, with full acknowledgment of its original publication in the journal.

All copies (print or electronic) or other use of the paper or article must include the appropriate bibliographic citation for the article's publication in the journal. However, you should not indicate in the citation that the version that you are reproducing or posting is the final published version as published in the journal. For example, it may be appropriate to indicate, "This paper has been submitted to [Journal] for consideration."

Commercial purposes include: the posting by companies or their employees for use by customers (e.g., pharmaceutical companies and physician prescribers); commercial exploitation such as associating advertising with such posting (including the linking to advertising by search engines); the charging of fees for document delivery or access; or the systematic distribution to others via e-mail lists or list servers (to parties other than known

Activate Windows
Go to Settings to activate Windows.